Institute for Materials Science and Engineering

NONDESTRUCTIVE EVALUATION

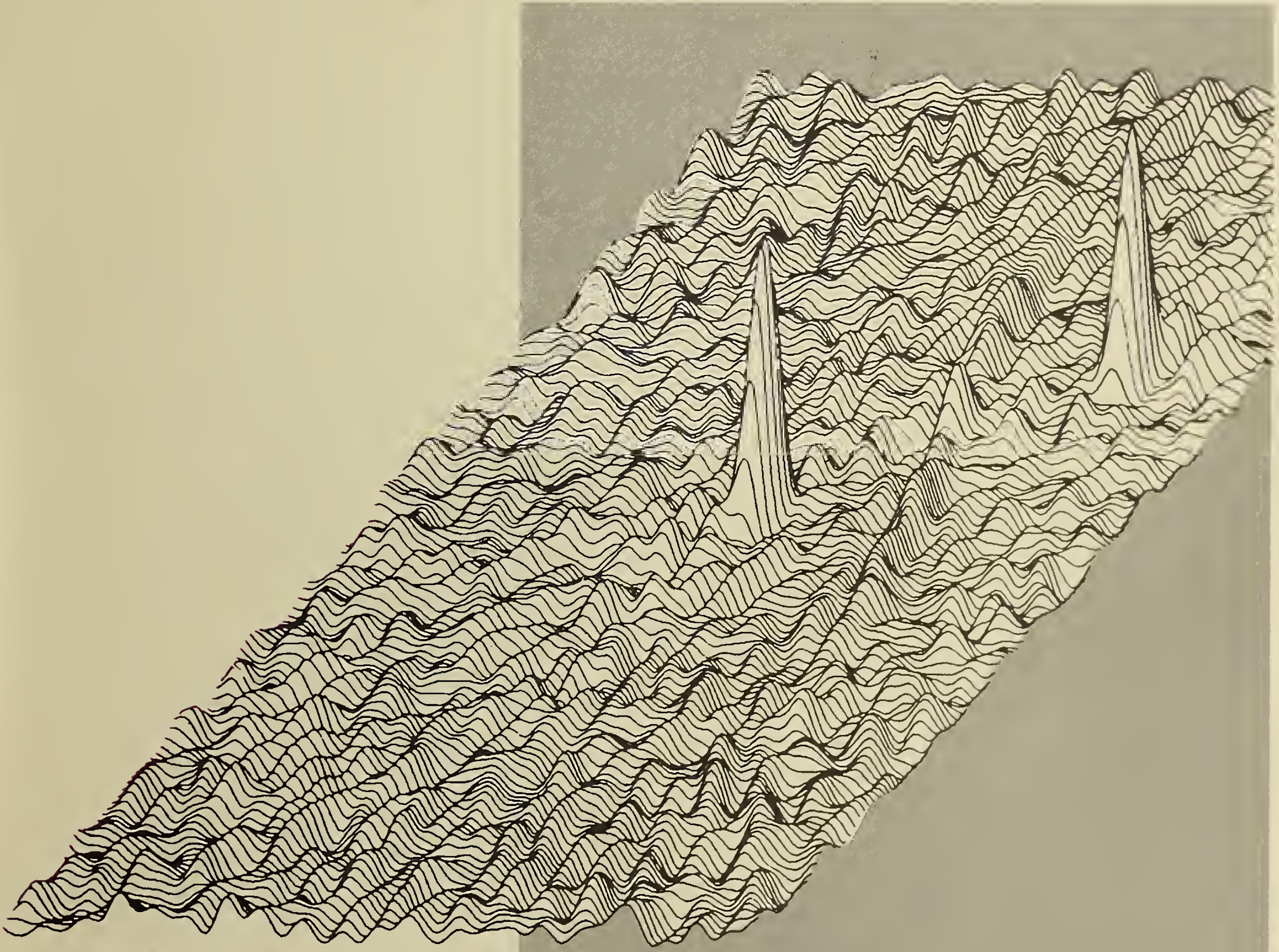

NBSIR 85-3187
U.S. Department of Commerce
National Bureau of Standards

Technical Activities 1985

Reconstruction of two simulated acoustic emission point sources in the presence of noise.

S. J. Norton and M. Linzer

Institute for Materials Science and Engineering

NONDESTRUCTIVE EVALUATION

H. T. Yolken, Chief
L. Mordfin, Deputy

NBSIR 85-3187
U.S. Department of Commerce
National Bureau of Standards

Technical Activities 1985

TECHNICAL ACTIVITIES

Table of Contents

I. NDE STANDARDS

II. NDE METHODS FOR INTERNAL FLAW CHARACTERIZATION

III. NDE FOR INTERFACES AND COMPOSITES

IV. NDE FOR PROCESS CONTROL

APPENDICES

INTRODUCTION

This report provides brief reviews of the technical activities in nondestructive evaluation (NDE) that were carried out by or for the National Bureau of Standards (NBS) in fiscal year 1985 (October 1, 1984 through September 30, 1985). In addition to reports on work supported by the Office of Nondestructive Evaluation (ONDE), a number of reports are included on related NBS work not supported by ONDE. Collectively, these technical activities constitute the Bureau's NDE Program, which is managed programmatically and administered on a Bureau-wide basis by ONDE.

The most common application of NDE is the characterization of cracks, voids, inclusions, and other kinds of flaws in materials, components, assemblies, and structures. This usage of NDE is the basis of modern in-service inspection procedures as applied, for example, to aircraft, bridges, pipelines, and pressure vessels. Recognizing that NDE measurements must be reproducible and that modern NDE must be quantitative, a principal mission of the NBS NDE Program has been to provide traceability for NDE measurements to national measurement standards. To this end, research must be carried out to achieve an adequate understanding of the physical basis of the NDE measurement techniques and procedures that require standardization. Furthermore, the results of the Bureau's research and development work on NDE measurements must be applied to several specific and meaningful problems in order to demonstrate the validity of the results and to help disseminate them to the user communities. Thus it is possible to think of the NDE Program as comprising three types of activities: research, standardization, and applications.

During the last several years quantitative NDE has been applied by industry to the measurement of material properties and characteristics such as residual stress, texture, and various other microstructural features. Such applications have been receiving increased attention because of the nationwide effort to raise the quality of manufactured products. Clearly, the ability to monitor important material properties and characteristics during a manufacturing process can often be used to guide or to control the process and, thus, to help avoid the manufacture of subquality products or materials. In response to these developments, the Bureau's NDE Program has for a number of years sponsored work on the application of NDE to the measurement of materials properties and characteristics and more recently has placed major emphasis on such measurements in regard to on-line monitoring and process control in manufacturing. The reviews in this annual report are arranged in the following major areas as a useful way to focus upon and to summarize the Program: (1) NDE Standards, (2) NDE Methods for Internal Flaw Characterization, (3) NDE for Interfaces and Composites, and (4) NDE for Process Control. Each of these sections is preceded by an introduction. The area of NDE standards, a cornerstone of the NBS NDE Program, includes calibration techniques, measurement procedures, document standards, and artifact standards. The work in area (2) deals with improving or developing new NDE methods for quantitative flaw evaluation and to determine suitability and reliability for specific applications. Projects dealing with the measurement of properties for process control appear in (3) and (4), where the motivation is primarily to provide a research base for application to process control. Area (3) deals with interfaces (solid surfaces, near surfaces, and coatings) and composites. Research on interfaces and composites has been highlighted because of the substantial technical importance of these subjects to industry. In addition, this focus was selected because of the difficulty that is usually encountered in utilizing NDE techniques in these applications. Area (4) deals, in general, with bulk properties for materials process control. For example, ultrasonics in metallurgical processing and NDE for ceramic processing appear in area (4).

Reports such as this one have been issued on an annual basis since 1978 and are commonly referred to as the "NBS NDE Annual Reports." A parallel series of reports, also issued annually, presents bibliographies and abstracts for the Bureau's technical reports and publications on NDE and its supporting technologies. The purpose of both of these report series is to serve as an introduction to the Bureau's NDE Program. Many readers will want further details on specific aspects of the work or its outputs, and such inquiries are welcomed and encouraged, both by the principal NDE investigators (whose names and affiliations precede each of the articles in the report) and by ONDE. Either can be addressed in care of NBS, Gaithersburg, Maryland 20899, or reached by telephone via (301) 921-1000. Requests for further information and suggestions regarding the Program always receive prompt and careful attention.

I. NDE STANDARDS

The first section of this annual report covers activities on NDE standards and includes work on calibration techniques, artifact standards, measurement methods, and document or written standards. The articles in this section are arranged by technique and include, for example, reports on eddy currents, ultrasonics, acoustic emission, x-ray radiography, and optical, thermal, and magnetic techniques. Although many of the research activities described in the nineteen articles in this section will have a positive effect on NDE technology, the first two reports on eddy currents are of particular interest and importance. This research has been very productive and should lead to a substantial improvement in eddy current techniques.

MEASUREMENT METHODS, CALIBRATION PROCEDURES, AND STANDARDS FOR QUANTITATIVE EDDY CURRENT NDE

J. C. Moulder and J. C. Gerlitz

Fracture and Deformation Division

Institute for Materials Science and Engineering

and

B. A. Auld and S. R. Jefferies

Edward L. Ginzton Laboratory

Stanford University

INTRODUCTION

The objectives of this research program are to develop measurement methods, calibration procedures, and standards appropriate to quantitative eddy current NDE. Experimental studies at NBS-Boulder are carried out in close collaboration with theoretical studies at Stanford University, a cooperative effort that has continued for four years.

Past efforts have included the development of high-frequency, broadband eddy current probes for inspection of high-resistivity aerospace alloys, ref. 1, 2; studies on methods for calibrating eddy current measurement systems, ref. 3; development of a new measurement technique that uses a precision impedance analyzer to measure changes in eddy current probe impedance caused by surface flaws, ref. 3, 4; design and construction of an automated eddy current scanner operating in the 30-60 MHz frequency range, ref. 4; and detailed comparisons of experimental eddy current flaw signals with predictions of the Stanford model for the interaction of a nonuniform probe-field with surface flaws, ref. 5.

During the past year we have extended our studies comparing theory and experiment in eddy current testing to more practical situations. The aim has been to introduce new features into the theoretical model to reproduce more realistic situations and then test the modified theory against controlled experiments. In particular, we extended theory and experiment to the case of low-conductivity materials and began more extensive studies of real fatigue cracks, as opposed to artificial flaws.

A number of other studies were also undertaken this year. A new calibration method was devised and tested for uniform-field eddy current probes. The influence of probe characteristics on eddy current flaw signals was studied in cooperation with researchers in CEEE's Electromagnetic Technology Division. The use of electrical-discharge-machined (EDM) notches for artifact standards in eddy current testing was considered from both experimental and theoretical perspectives. Finally, a new method for monitoring fatigue crack growth has been developed in the course of preparing fatigue cracks for our own use.

NEW THEORETICAL AND EXPERIMENTAL STUDIES

Extension of Theory and Experiment to Low-Conductivity Materials

In the present probe-flaw interaction theory, the assumption is made in calculating the magnetic field inside the flaw that the walls are perfectly conducting. Finite conductivity is then introduced later, in evaluating the electric field inside the flaw. The same method is used in analyzing transmission lines and waveguides with high-, but finite-conductivity walls.

In many practical situations, the conductivity of the workpiece is relatively low and the predictions of the present theory are open to question. Theory indicates that the magnitude of the flaw signal, ΔZ, is inversely proportional to specimen conductivity. Thus, flaw signals from low-conductivity materials are expected to be larger than those from high-conductivity materials for equal skin depths and similar flaws.

To match the assumptions of theory as closely as possible, our past studies were limited to highly conducting materials such as aluminum. This year, we extended the comparison of theory with controlled experiments to flaws in a titanium alloy. Experimental flaw scans were obtained for both EDM notches and fatigue cracks in Ti-6Al-4V using air core and ferrite core probes. Similar-size flaws in aluminum alloy were measured for comparison.

The results of one such comparison are shown in Figures 1 and 2, where the magnitudes and phases of the flaw signals from similar-size, semicircular EDM notches in titanium and aluminum alloys are compared. These measurements were taken with a ferrite core probe operating at 550 kHz scanned along the length of the flaw. The magnitude of the signal is larger for the flaw in titanium, despite the fact that the skin depth is about six times larger in the titanium specimen. This result confirms the predictions of theory qualitatively.

To make quantitative comparisons of theory and experiment it is necessary to know the intensity and spatial distribution of the probe's magnetic field. This information, used to compute the flaw signal, can be calculated from existing theory for air core probes, ref. 6. (Analytical expressions for the magnetic field of ferrite core probes are not yet available, although numerical methods have been devised.) When the results of similar flaw signal measurements made with air core probes were compared to the predictions of the nonuniform-probe-field theory, we found quantitative agreement, within the uncertainty of the experimental measurements, ref. 7,8.

Another prediction of the theory is confirmed by the results shown in Fig. 2. In this figure we observe that the phase of the flaw signal for the aluminum specimen does not vary significantly as the probe is scanned along the flaw's length, but the phase varies continuously for the titanium specimen. As shown by theoretical calculations, this effect is related to the ratio of flaw depth to skin depth, a/δ. When $a/\delta \gg 1$, as is the case for the aluminum specimen, the phase of ΔZ varies little with flaw depth. But as a/δ approaches unity, as occurs for the titanium specimen, the effect of varying flaw depth on the phase of ΔZ becomes as strong as the effect on the magnitude of ΔZ.

Calibration Method for Uniform-Field Probes

Calibration methods for eddy current probes are vitally important for obtaining quantitative results from measurements. Especially important are methods for determining a probe's magnetic field intensity, since this quantity enters into every calculation of probe response. Relatively few of the probes actually used for practical inspections are amenable to calculation of the field strength; we therefore must turn to measurement.

A new calibration method for uniform-field eddy current probes was devised and tested this year in collaboration with Dr. E. Smith of United Technologies Research Center. The method consists of measuring the impedance change, ΔZ, induced in a probe by a cylindrical recess of known volume in the surface of a specimen of known conductivity. These quantities can be related to the value of H/I for the probe, the magnetic field strength per unit current, according to the expression.

$$\Delta Z = i \left(\frac{H}{I}\right)^2 \frac{2}{\sigma} \left(\frac{Ad}{\delta^2}\right)$$

where σ is conductivity, A is the surface area of the recess, d its depth, and $i = \sqrt{-1}$.

To test this calibration method, three cylindrical recesses 1.6 mm in diameter with depth of 0.013, 0.127, and 1.27 mm were fabricated by electrical-discharge machining in a specimen of IN-100 (a nickel super alloy whose nominal composition composition is 60% Ni, 15% Co, 10% Cr, 5.5% Al, 4.7% Ti, 3% Mo, and 1% Va). The specimen was then sent to Dr. Smith at UTRC to be tested with a new uniform field probe he developed. His measurements on these calibration recesses showed that, except for the deepest recess, he could obtain consistent calibration factors that subsequently enabled him to compare experimental flaw measurements to the predictions of Auld's uniform-field theory, ref. 9. For the deepest recess, the depth far exceeded the skin depth so that the field could no longer be considered uniform.

Eddy Current Probe Characterization

We have already mentioned the importance of characterizing the intensity and spatial distribution of a probe's magnetic field for quantitative eddy current NDE. This fact has influenced our strategy of using air core probes in experimental studies, since magnetic fields can be calculated for this type of probe, permitting the results to be compared with theory. The theory of Dodd and Deeds that is used in calculating probe fields, ref. 6, although widely accepted as accurate, has not been compared directly to measured fields before. This year we have made such a comparison for the first time in collaboration with T. Capobianco and F. Fickett of the Electromagnetic Technology Division.

The impetus for such a study is illustrated in Fig. 3, which compares experimental measurements made using two nominally identical air core probes with theoretical predictions for a rectangular EDM notch in 6061 aluminum. The figure shows that the two probes give results that differ by about 30 percent, the theoretical prediction falling between the two experimental curves. No explanation for this discrepancy could be found in measurements of the probes' electrical parameters such as inductance, impedance, or resonant frequency. X-rays revealed no difference in the physical construction of the probes.

The magnetic fields of these two eddy current probes were mapped using techniques developed by Fickett and Capobianco. The results showed that differences in the flaw signals produced by the probes for the same flaw could be traced to a ten percent difference in their field strengths, ref. 10. The measured field distributions were compared to the predictions of the Dodd and Deeds theory, with reasonably good quantitative agreement being observed.

In another experiment, field mapping was performed for a probe with a ferrite core. The measured field profile was then used as an input for calculating flaw signals using the nonuniform-probe field theory. Calculated flaw signals were in good qualitative agreement with measured flaw profiles. This is the first time that this has been attempted, and it is a very important step in extending quantitative techniques to practical probe designs.

EDM Notches as Artifact Standards for Eddy Current Testing

In many industrial NDE applications, eddy current test instruments are calibrated with artifact standards -- artificial flaws especially fabricated to approximate the size and shape of actual flaws that are expected to occur. Often these artificial flaws are made by electrical-discharge machining (EDM). The EDM process produces a flaw with a relatively larger opening and smoother walls than real fatigue cracks.

Despite the fact that the artificial flaws differ markedly from actual flaws, many practitioners assert that EDM notches are "conservative" calibration standards, meaning that such calibration flaws produce a signal that is smaller than the signal from a real crack of the same length and depth. Yet theoretical and experimental results we have obtained this year show that in general, the exact opposite is the case: EDM notches have larger flaw signals than real fatigue cracks. This point is illustrated in Fig. 4, which shows the magnitudes of flaw signals from two closely matched flaws in Ti-6Al-4V, one an EDM notch and the other a fatigue crack.

However, it must be recalled that most eddy current instruments do not measure the absolute magnitude of the flaw signal, but rather, the magnitude of the signal in quadrature to liftoff in order to discriminate against liftoff. In this case, it might indeed be possible for the signal from an EDM notch to be smaller than one from a fatigue crack, but clearly the matter requires a careful, critical examination. We have performed such a study this year in cooperation with Mr. Ward Rummel of Martin Marietta Denver Aerospace.

The results of our study suggest that a great deal of caution must be exercised when using EDM notches to calibrate eddy current instruments. We found that for aluminum alloys, the conventional belief was reasonable: the quadrature signal from an EDM notch was smaller than the quadrature signal from a similar size fatigue crack. However, for titanium alloys, this was no longer true. The difference in these two cases stems from the fact that the phase of the flaw signal depends upon the value of a/δ, the ratio of flaw depth to skin depth, whereas the phase of the liftoff signal depends on r/δ, the ratio of the mean radius of the probe coil to the skin depth. Therefore, for any given probe there will always be some value of flaw depth below which an EDM notch no longer gives a "conservative" calibration.

Eddy Current Monitoring of Fatigue Crack Growth

To provide well characterized fatigue cracks for our own studies, we developed methods for growing fatigue cracks in a predictable, reliable fashion this year. We have shown that a reflection-type eddy current probe can be used to monitor the growth of the crack, rather than the customary crack mouth opening displacement (CMOD) gauge, which is less sensitive and requires very large starter notches. The reflection probe used was demonstrated to have an output that is linear with flaw cross-sectional area. The length of the flaw can be determined by scanning the probe along its length. Having the length and area of the flaw permits determination of the depth more reliably than can be done from CMOD measurements.

SUMMARY

This year we have extended comparisons of theory and experiment in eddy current testing to low-conductivity specimens and fatigue cracks to more accurately model real test situations. In collaboration with our colleagues in the Electromagnetic Technology Division, new studies were undertaken showing that characterization of eddy current probes by magnetic field mapping is a useful adjunct to experimental flaw measurements. The use of EDM notches for eddy current calibration standards was investigated both experimentally and theoretically, demonstrating that such standards must be used with caution. In addition, a new calibration method for uniform field probes was developed and a new method for monitoring fatigue crack growth was demonstrated.

Future studies will focus on comparing theory and experiment for reflection probes, a much different type of eddy current probe than the absolute probes we have studied to date. We also plan further studies on the uniform-field calibration method to determine its accuracy and limitations.

REFERENCES

1. C. M. Fortunko and S. A. Padget, "High-Frequency, Broadband Eddy Current Probes for Improved Flaw Characterization," in "Technical Activities 1982 Office of Nondestructive Evaluation," H. T. Yolken, editor, NBSIR 82-2617 (Dec. 1982).

2. C. M. Fortunko, J. C. Moulder, J. C. Gerlitz, A. C. Bennett, B. A. Auld, and F. G. Muennemann, "High-Frequency, Broadband Eddy Current Probes for Improved Flaw Characterization," in "Technical Activities 1983 Office of Nondestructive Evaluation," L. Mordfin, editor, NBSIR 84-2815 (Dec. 1983).

3. J. C. Moulder, J. C. Gerlitz, B. A. Auld, M. Riaziat, S. Jefferies, and G. McFetridge, "Calibration Methods for Eddy Current Measurement Systems," Review of Progress in Quantitative Nondestructive Evaluation 4A, pp. 411-420 (Plenum, 1985).

4. J. C. Moulder, J. C. Gerlitz, B. A. Auld, M. Riaziat, S. Jefferies, and G. McFetridge, "Eddy Current Characterization of Surface Flaws," in "Technical Activities 1984 Office of Nondestructive Evaluation," L. Mordfin, editor, NBSIR 84-2944 (Nov. 1984).

5. B. A. Auld, G. McFetridge, M. Riaziat, and S. Jefferies, "Improved Probe-Flaw Interaction Modeling, Inversion Processing, and Surface Roughness Clutter,"Review of Progress in Quantitative Nondestructive Evaluation 4A, pp. 623-634 (Plenum, 1985).

6. C. V. Dodd and W. E. Deeds, "Analytical Solutions to Eddy-Current Probe-Coil Problems, "J. Appl. Phys. 39, No. 6, pp. 2829-2838 (May 1968).

7. B. A. Auld and S. Jefferies, "Semi-Elliptical Surface Flaw EC Interaction and Inversion: Theory," Review of Progress in Quantitative Nondestructive Evaluation 5, to be published.

8. J. C. Moulder, J. C. Gerlitz, B. A. Auld, and S. Jefferies, "Semi-Elliptical Surface Flaw EC Interaction and Inversion: Experiment," Review of Progress in Quantitative Nondestructive Evaluation 5, to be published.

9. Eugene Smith, "Application of Uniform Field Eddy Current Technique to 3-D EDM Notches and Fatigue Cracks," Review of Progress in Quantitative Nondestructive Evaluation 5, to be published.

10. T. E. Capobianco, F. R. Fickett, and J. C. Moulder, "Mapping Eddy Current Probe Fields with a SQUID Magnetometer," Review of Progress in Quantitative Nondestructive Evaluation 5, to be published.

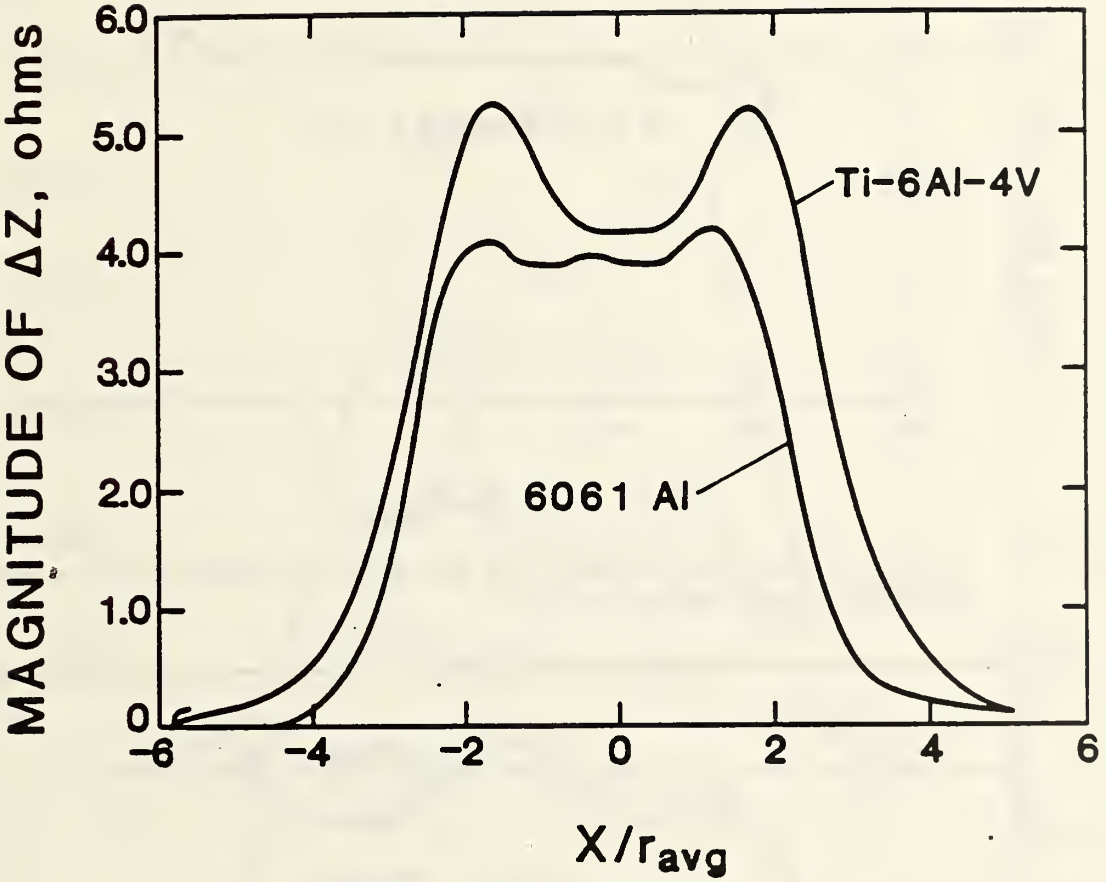

Figure 1. Magnitudes of the flaw signals obtained by scanning a ferrite core eddy current probe along the lengths of two semicircular artificial flaws, one in Ti-6Al-4V and one in 6061 Al. The flaw in the titanium specimen was 3.15 mm long, 1.58 mm deep, and 0.43 mm wide. The flaw in aluminum was 3.48 mm long, 1.74 mm deep, and 0.25 mm wide. The abscissa represents the position of the probe relative to the flaw center, normalized by the mean probe radius. Measurements were taken at 550 kHz.

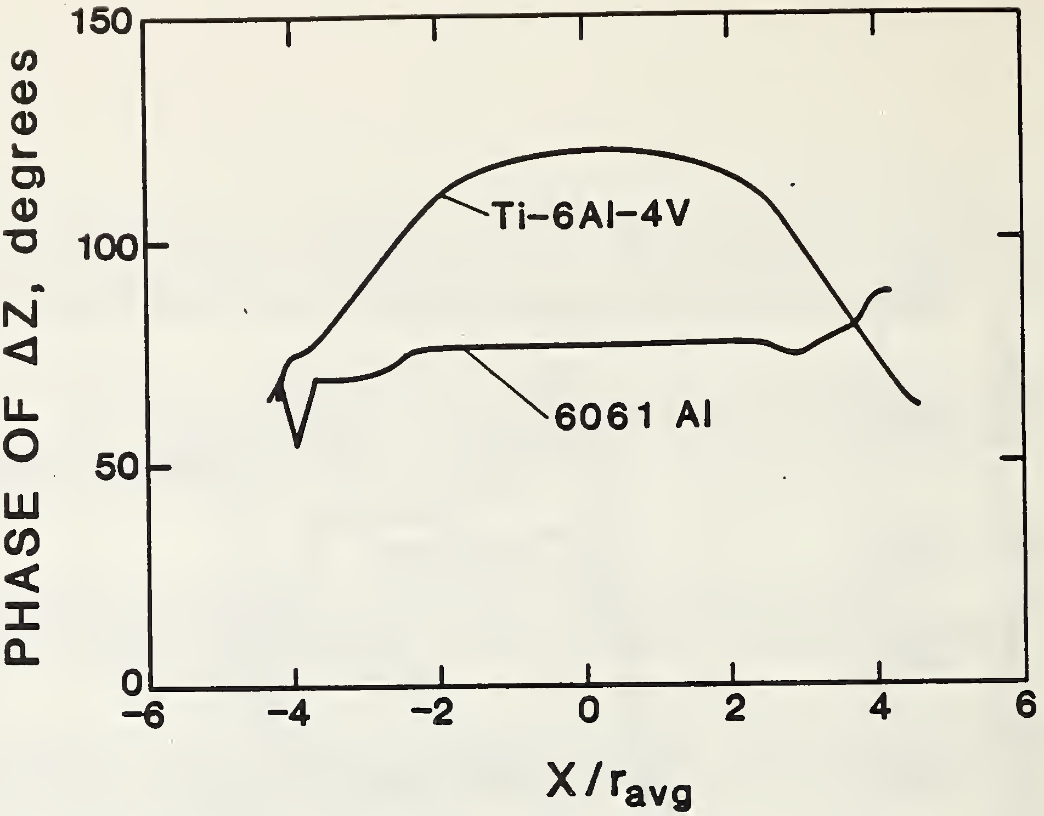

Figure 2. Phases of the flaw signals from the same two flaws in titanium and aluminum alloys shown in Fig. 1.

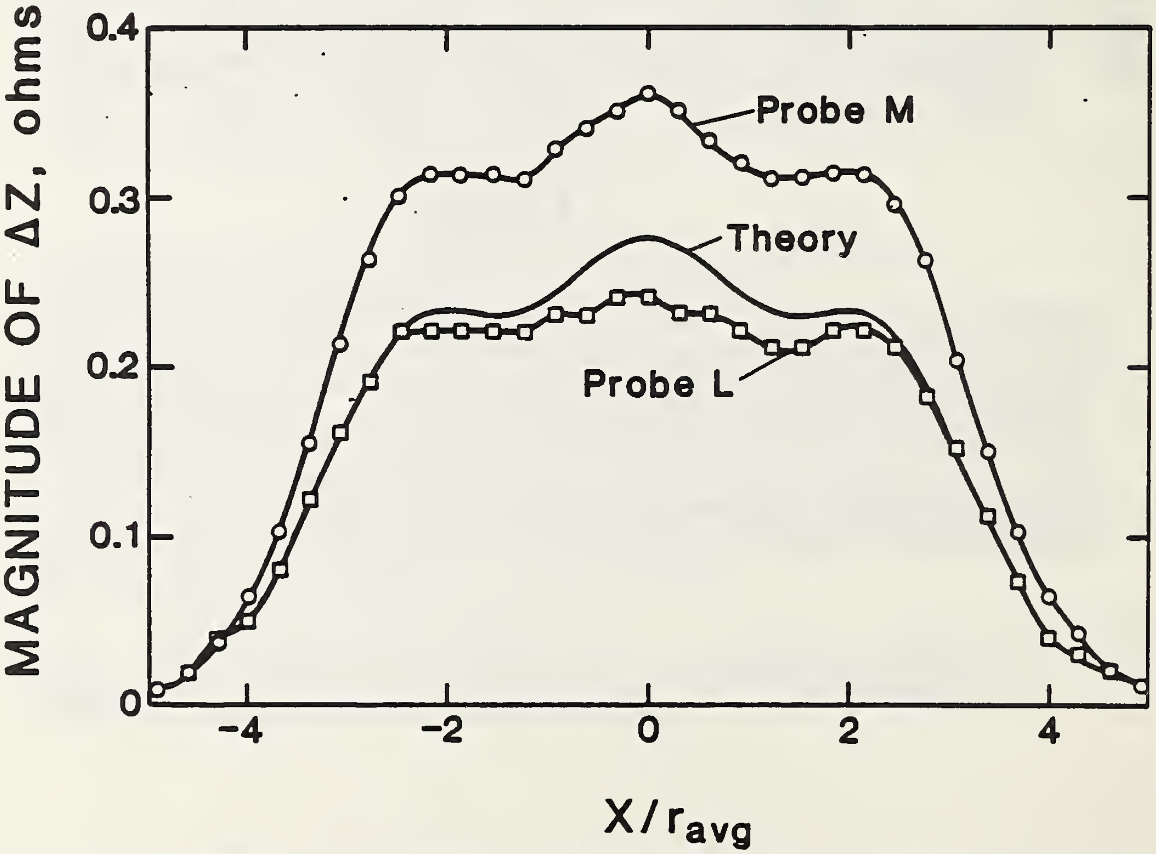

Figure 3. Comparison of theoretically predicted eddy current flaw signal (solid line) with experimental measurements made with nominally identical air core probes. The flaw was a rectangular EDM notch in 6061 Al, 3.90 mm long, 1.17 mm deep, and 0.20 mm wide.

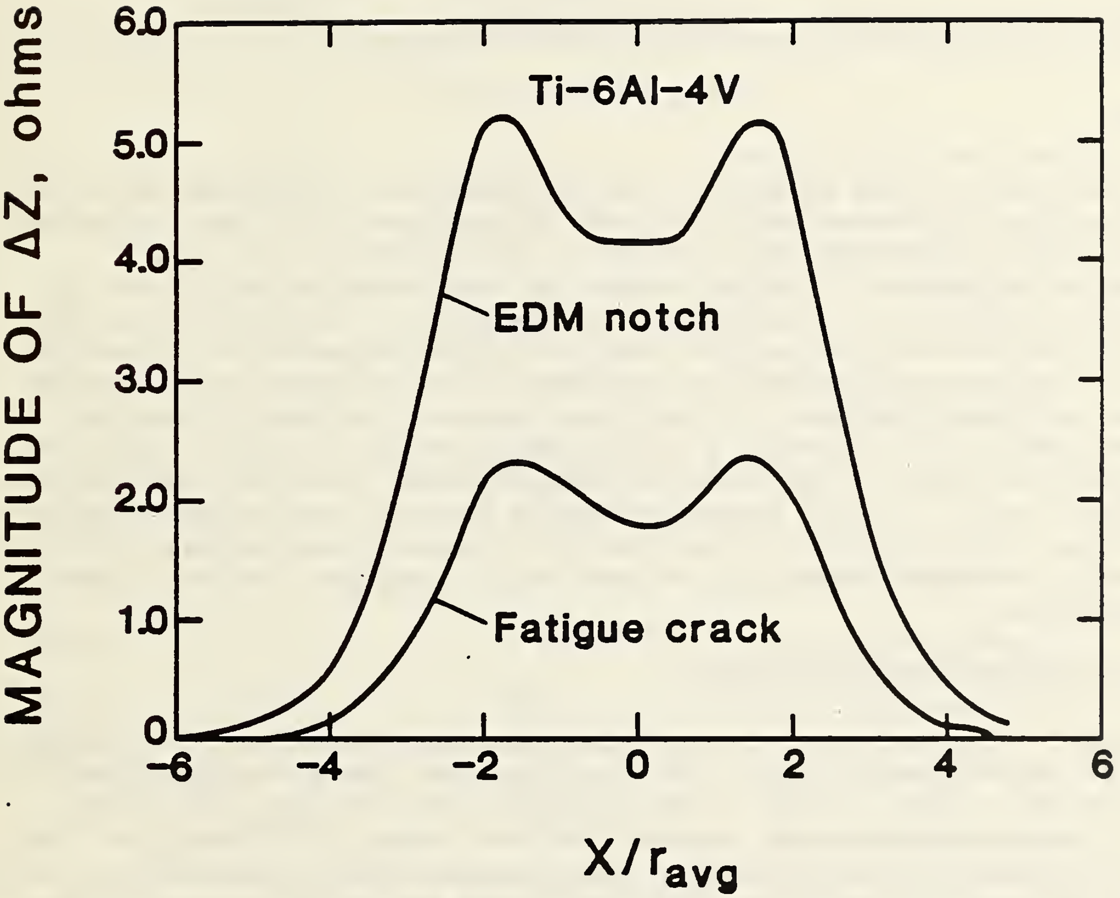

Figure 4. Magnitudes of experimental flaw signals for a semicircular fatigue crack and an EDM notch of similar size in Ti-6Al-4V. Measurements were made with a ferrite core probe operating at 550 kHz.

EDDY CURRENT COIL CHARACTERIZATION

T. E. Capobianco and F. R. Fickett

Electromagnetic Technology Division

Center for Electronics and Electrical Engineering

INTRODUCTION

The major goal of this program is the investigation of experimental techniques for accurate characterization of eddy current test coils and determination of the effect of various coil defects or disturbances on the coil's electromagnetic signature. A unique feature of this characterization is that it is made independent of the presence of a work piece. Such information is necessary in two areas of eddy current NDE, the field evaluation of commercial coils and the more esoteric problem of determining the interaction between an eddy current coil and a defect. In the first instance, we hope to develop a standard test method and, perhaps, a field-usable system for rapid prediction of coil performance and, in the second, a technique for accurately mapping the near field of a coil. In this report we briefly describe our accomplishments in both of these areas in FY 85 along with other interactions related to the project. More technical details on the work can be obtained from the referenced publications.

ELECTRICAL PARAMETER CHARACTERIZATION

Last year's efforts were concerned with measuring variations in electrical parameters in production run coils. We concluded that these variations were not large enough to cause a probe to be unusable so we now have turned our attention to examining commercial probes which are known to be defective. We obtained a collection of these defective eddy current probes from the Air Force. We then measured the inductance, resistance and self-resonance of the probes. As part of this evaluation we constructed a test circuit to run the probes near their normal operating frequency and to allow measurement of resonant frequency and impedance. This last test appears to be a promising one for predicting coil sensitivity and is being evaluated further. The data for the 5/16" bolt hole probes could indicate a connection between resonance amplitude and defect sensitivity, but the sample population is too small and the documentation is insufficient. The test circuit has been incorporated into an automated system in anticipation of receiving more probes for evaluation. We are now trying to obtain more sample probes, both defective and acceptable, for these measurements. Preliminary resonance measurements are tabulated in Table 1 and compared to the comments in the Air Force documentation received with the defective probe samples.

All of these probes are run close to resonance in service. It should be pointed out that a rejected probe does not necessarily have poor sensitivity to flaws. Defects in its physical construction can also be a cause for rejection. The probes that we tested were all such that the coil can be seen. Other designs frequently encase the coil in a plastic rod and then non-optical methods must be used to look for misalignment or other mechanical defects.

Table 1. Resonant frequency and amplitude measurements of defective probes

PROBE	RESONANT FREQ. (kHz)	IMPEDANCE AT RES. (ohms)	A. F. DOCUMENTATION
		5/16" bolt hole probes	
6	135	194	"sensitivity very poor"
16	157	195	"unacceptable due to insensitivity"
18	141	227	"too insensitive"
misc	90	338	"noisy"(no comments about sensitivity)
		3/16" bolt hole probes	
20	93	393	"excellent sensitivity"
52a	87	391	no documentation
52b	88	298	no documentation
52c	71	401	no documentation
52d	89	296	no documentation

One issue we have discussed with workers in the field but have not yet addressed in our research is the claim of "polarity" problems with some ferrite core probes. Our speculation is that there may be a capacitive coupling effect between the turns of the coil immediately adjacent to the ferrite and the core itself. If the coupled lead is not connected to instrument ground, this undesirable coupling could be showing up as noise in the output. The services have apparently a de facto instrument for day-to-day eddy current work. It is not especially elaborate in design in light of modern electronics, but it has proven to be dependable and is relatively inexpensive. We have made numerous attempts to borrow one of these for our test program with no success. We feel that certainly some of the problems causing the rejection of large numbers of probes may have to do with interfacing to this instrument. There is an indication from our interactions in recent months that the services are tending to increase the sophistication of their NDE techniques to a significant degree with the addition of computer controlled systems. Many of the probe problems may be resolved by this change; or they may become even more severe as the demands on the probes increase.

FIELD MAPPING STUDIES

Our work this year has been concentrated on producing very small inductive pickup coils and on making instrumentation improvements. The reduction in the size of the search coils from that of our earlier work [1] has been considerable and this is reflected in the turns-area product (nA) of the coils. The search coil used in the work previously reported has an nA of 226 mm^2. The coils we are currently using have an nA of 0.823 mm^2. This is good news from the standpoint of scanning resolution, but it has required significant advances in our electronics because of much smaller signal levels.

In our efforts to develop the smallest possible hand-wound search coils we encountered the problem that, as the coil size decreased, stray electromagnetic interference approached the expected signal size and, in some cases, could completely obscure the signal. Our noise studies showed that two factors were the largest contributors to this pickup. They were the presented area between the leads and the presented area at soldered joints in the leads. In order to minimize these problems two major improvements in coil design were implemented: (1) the leads are wound with a very tight twist pitch; and (2) no joints are allowed between the leads and the coil. The leads from these small coils are 25 cm twisted pairs of #44 copper wire with a twist pitch of five turns per millimeter. The outside diameter of the coils is 0.43 mm and the inside diameter is 0.20 mm.

Shielding studies were also made on the SQUID system in order to improve the detection sensitivity. RF interference is a serious problem with these devices under the best of conditions and, in our application where we are introducing the signal from room temperature, the problems are greatly magnified. Our work showed that by careful shielding of input leads to the dewar, use of superconducting shields for the SQUID pickup transformer, and proper adjustment of the input coupling to the SQUID itself, we could increase our sensitivity by more than an order of magnitude over that reported last year.

Measurements were made comparing the improved SQUID system to more conventional electronics with our new small coils as input. We found that, while the SQUID system offered some advantages in sensitivity, its limited dynamic range and frequency response, coupled with the requirement of liquid cryogens makes the system cumbersome and difficult to use. It is our (somewhat surprising) conclusion that, with its present limitations the SQUID is probably not the instrument of choice for measuring the relatively large ac magnetic fields used in NDE at frequencies in the kilohertz range or greater. Simpler, more conventional, methods are available. We should mention that SQUID technology is still in its infancy and the electronics is being improved and expanded in frequency range at a great rate. Unfortunately, delivery of the newly purchased upgraded state-of-the-art electronics package for our system has once again been delayed by a few months.

On the other hand, there are applications such as low frequency ac or dc field detection with multi-axis gradiometer coils or detection at large distances from the testpiece which would be difficult if not impossible to do with any device except a SQUID. These areas are still unexplored territory in NDE.

All of the data presented here were taken with a very sophisticated (and expensive) lock-in amplifier system, although the SQUID-based system would have served as well. With the lock-in system we have also had to make improvements over our original design including using differential inputs to the amplifier and extensive shielding of the leads and all joints.

Two field mapping sensors were built. One is positioned to sense the field parallel (tangential field) to the face of the eddy current probe and the second measures the field perpendicular to the face (axial field). Separate scans are required for each component. In each case the leads have the same orientation with respect to the axis of the probe holder. This allows us to scan two orthogonal components of the magnetic field of the eddy current probes without changing the orientation of the search coil leads in the eddy current probe field. As expected, this makes the lead pickup signal nearly the same for the two coils. The positioner developed for these measurements is a stepping motor scanning system developed jointly with CMS. The positioner itself allows us to radially scan a given eddy current coil at a any number of angles. The usual scan sequence is: first from the center of the coil to beyond the outer radius; the eddy current coil is then rotated through 180 degrees and the radial scan repeated; a 90 degree rotation and scan is then followed by another 180 degree rotation and scan. When this is done with both field sensors, a fairly comprehensive field profile is achieved. Computer drive of the scanner and processing of the input data greatly reduces the time involved.

Another device built in our laboratory is used to calibrate the pickup coils. This is a relatively simple, but carefully constructed, Helmholtz pair with a coil radius of 2.9 cm and a field constant of 384 ± 4 m^{-1} (4.83 $Oe \cdot A^{-1}$) which allows calibration of our pickup coils in uniform fields at the operating frequencies. The coils just mentioned have calibration constants near 6.4×10^{-2} $\mu V \cdot m \cdot A^{-1}$ (5.1 $\mu V \cdot Oe^{-1}$) at 10 kHz.

In our latest series of measurements we mapped the fields produced by the following four eddy current probes:

2 air core absolute probes;
1 ferrite core absolute probe;
1 differential or gradiometer probe with ferrite core pickup coils.

The two air core absolute probes were nominally of the same construction, but during use it was found that the response of the two probes varied by as much as 30% when they were scanned over the same defects [2]. Field profiles of the probes showed no significant differences in the spatial distribution of the field, but the magnitude of the tangential field component varied by 10% for the same level of probe excitation current. The tangential field profiles are shown in Fig. 1. The variation of the axial component was 23%, but this large effect is probably partially the result of liftoff differences of the sensor coil during the two scans. At present our positioning system lacks precision in this dimension and the fields fall off very rapidly with increasing liftoff.

The tangential field data for the two air core probes were compared to values calculated using the theory of Dodd and Deeds [3] with the results shown in Fig. 2. The theoretical calculation was made for a liftoff of 0.7 mm which is the built in liftoff of the coils of each eddy current probe (0.5 mm) plus one sensor coil radius (0.2 mm). The figure shows good agreement in the field distribution between theory (dashed) and experiment (solid). The peak values of the two experimental curves vary by 10% and the peak of the lower experimental curve is within 20% of the calculated value. We consider the agreement to be quite good given the uncertainties involved. We compared the field distribution of the ferrite core probe to that of the two air core probes. The average radius of the ferrite core coil is 1.9 mm. This is slightly larger than the radius of the air core coils which is 1.6 mm. Fig. 3 is the plot of the normalized data. The sensor positional data (R) is normalized to the individual coil dimensions (R ave) and the radial field [H(r) in A/mm] is given per unit of coil excitation current (A). The peak field strength of the air core probes occurs at 1.41. The field concentrating effect of the ferrite is evident in the larger magnitude and also the tighter field pattern of the ferrite core probe. Its peak value occurs at 0.90.

The last probe in this group is a differential, or gradiometer, probe. Its construction is shown in Fig. 4. It consists of an outer air core excitation coil and two inner ferrite core pickup coils which are connected in series opposition. Field mapping results are shown in Fig. 5 for both tangential and axial field scans. On each graph, one scan is made across the face of one of the ferrite core pickup coils and the other on a path between the two. The pickup coils are open circuited for this measurement; power is to the excitation coil only. Clearly, the field produced by the air core excitation coil is distorted by the ferrite cores of the pickup coils.

SUMMARY

It is clear from this work that field mapping of eddy current probes can detect differences in probes of supposedly identical construction. Field profiles of ferrite core probes are difficult to calculate, but are necessary information for quantitative flaw inversion work. Using our techniques, these profiles can be measured directly. Better shielding methods have allowed us to use search coils with areas that are several orders of magnitude smaller than those we have used in earlier work. As a result, the resolution of our scans is improved and field maps of eddy current probes are obtained with relative ease. Greater detail on all of these topics is available in one of our recent papers [4].

COLLABORATIVE EFFORT WITH CMS

An informal joint effort was started this year with John Moulder of CMS to investigate the application of our field mapping system and techniques to the detection and sizing of actual flaws. For these experiments, we used the differential or gradiometer eddy current probe described above (Fig. 4) to measure several flaw specimens. Two well-received papers were presented at conferences earlier this year as a result of this effort [5,6]. The differential probe was found to have an accurately linear response to flaw area (length x depth) as shown in Fig. 6.

WIRE ROPE NDE

At the request of ONDE, Fred Fickett participated in a meeting at NBS (Gaithersburg) in late September with J. Kharnak of the Bureau of Mines regarding the use of magnetic techniques to detect incipient failure in the wire rope used in mining operations. As a result of that meeting, a short proposal outlining our thoughts on research needed in this area was prepared and presented to the Bureau of Mines in October. In April, at the request of OSHA and USBM, Tom Capobianco attended a meeting at the Department of Labor, Mine Safety and Health Administration, Denver office on the NDE of wire rope. The group, consisting of interested persons from both industry and government, agreed to form a committee whose purpose would be to develop retirement criteria for wire rope based on nondestructive test methods. Future meetings are being planned, but our participation is uncertain since no funding is yet forthcoming from USBM and magnetic testing is not the main thrust of our ONDE-sponsored research program.

REFERENCES

1. F. R. Fickett and T. E. Capobianco, "Magnetic Field Mapping With a SQUID Device, "Review of Progress in Quantitative Nondestructive Evaluation 4:401 (Plenum, 1985).

2. J. C. Moulder, J. C Gerlitz, B. A. Auld, and S. Jeffries, "Semi-Elliptical Surface Flaw EC Interaction and Inversion: Experiment," Review of Progress in Quantitative Nondestructive Evaluation, Vol. 5, to be published.

3. C. V. Dodd and W. E. Deeds, " Analytical Solutions to Eddy-Current Probe - Coil Problems," J. Appl. Phys. 39:2829 (1968).

4. T. E. Capobianco, F. R. Fickett and J. C. Moulder, "Mapping of Eddy Current Probe Fields," Review of Progress in Quantitative Nondestructive Evaluation, Vol. 5, (1986). To be published.

5. T. E. Capobianco, J. C. Moulder, and F. R. Fickett, "Flaw Detection with a Magnetic Field Gradiometer," Proceedings of the 15th Symposium on Nondestructive Evaluation. In press.

6. J. C. Moulder and T. E. Capobianco, "Detection and Sizing of Surface Flaws with a SQUID-Based Eddy Current Probe," Review of Progress in Quantitative Nondestructive Evaluation, Vol.5, (1986). To be published.

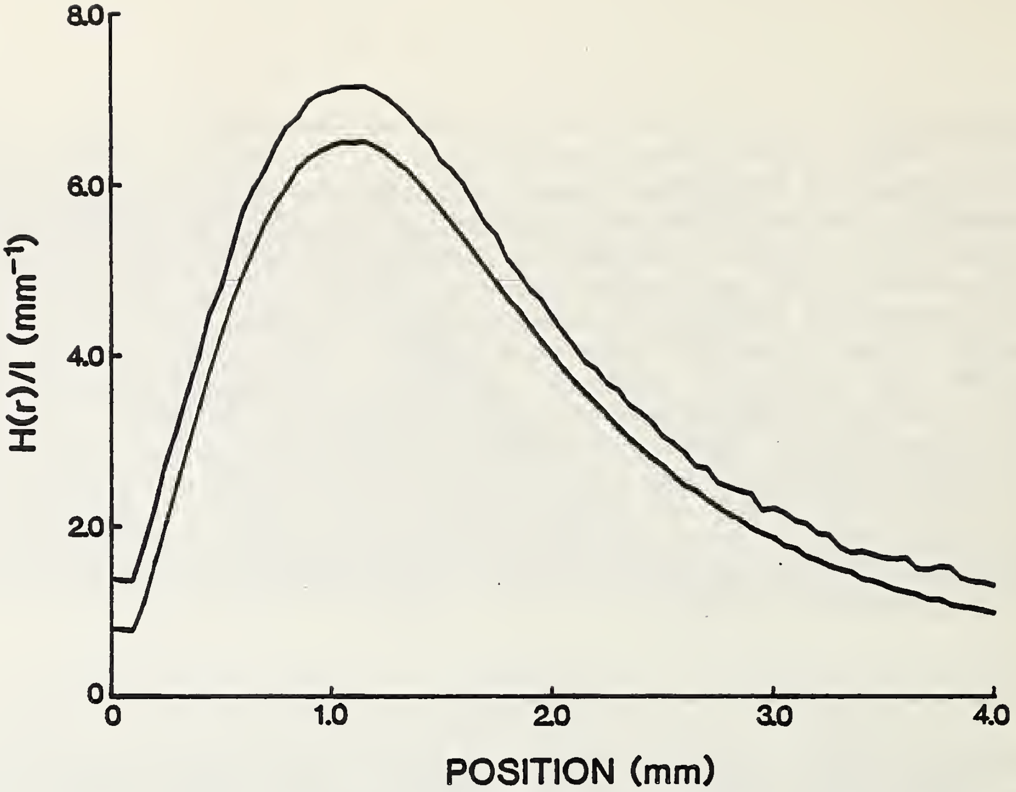

Figure 1. Reduced field parallel to the probe face for two nominally identical probes.

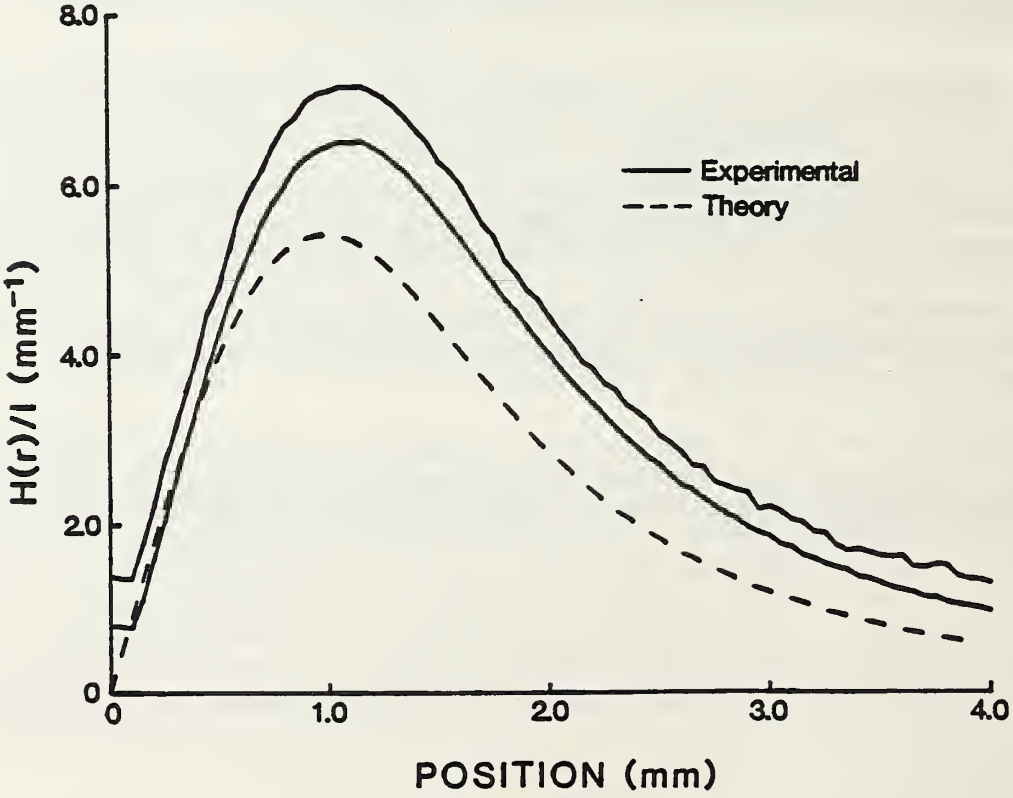

Figure 2. Comparison of a theoretical calculation of the probe fields with the experimental data of Fig. 1.

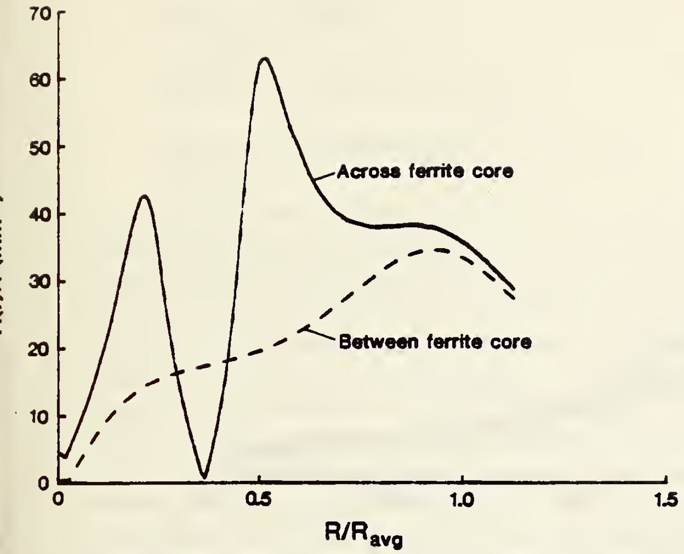

Figure 5a. Tangential field profile of the differential probe.

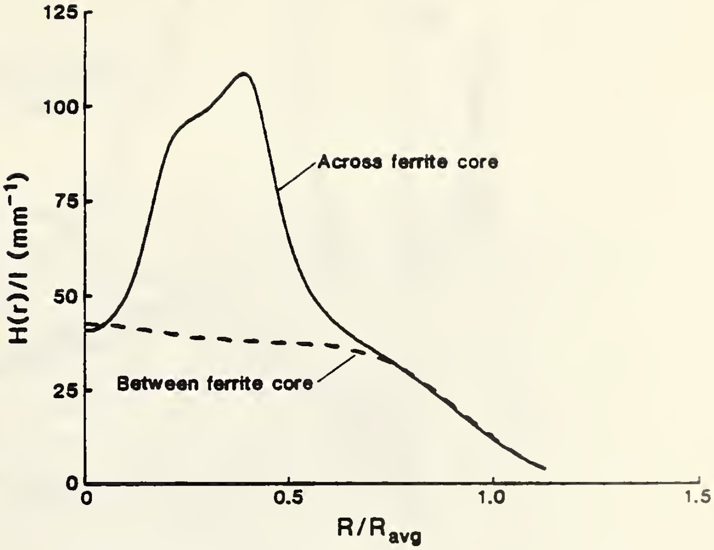

Figure 5b. Axial field profile of the differential probe.

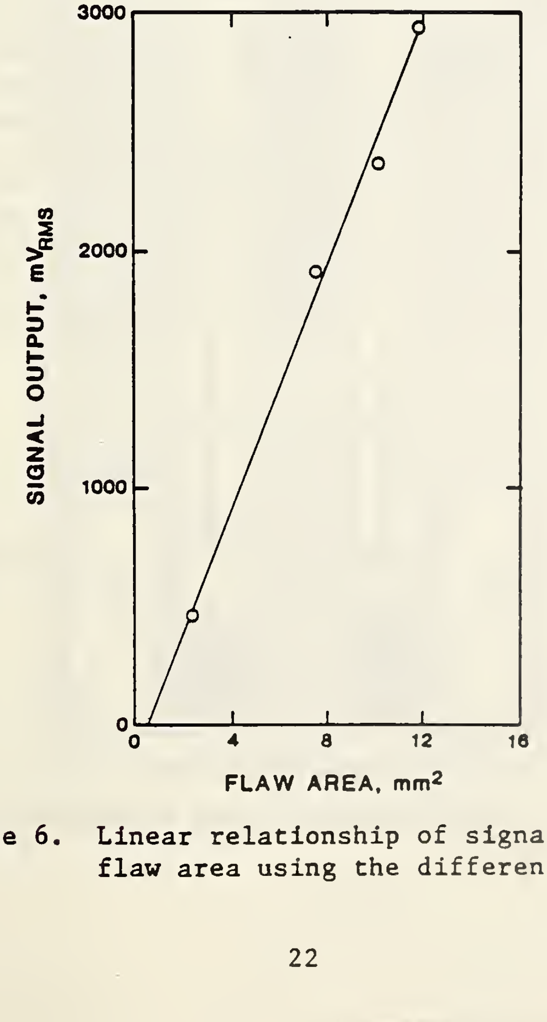

Figure 6. Linear relationship of signal amplitude to flaw area using the differential probe.

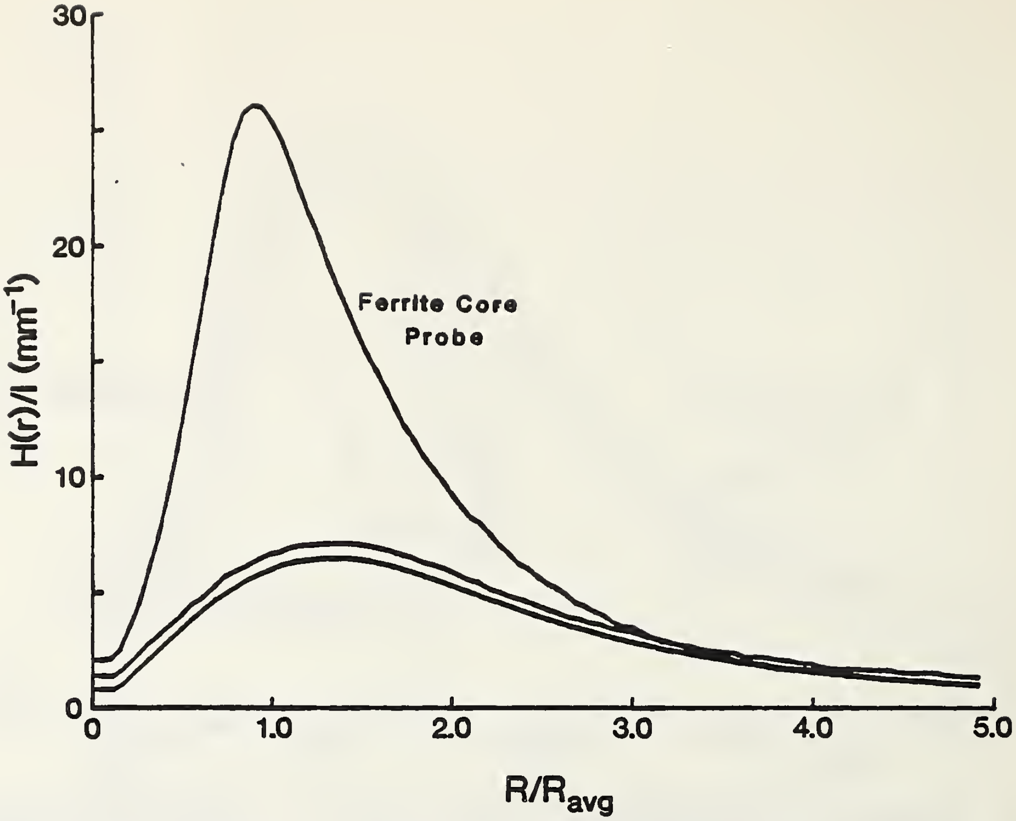

Figure 3. Comparison of field measurements of air core and ferrite core probes.

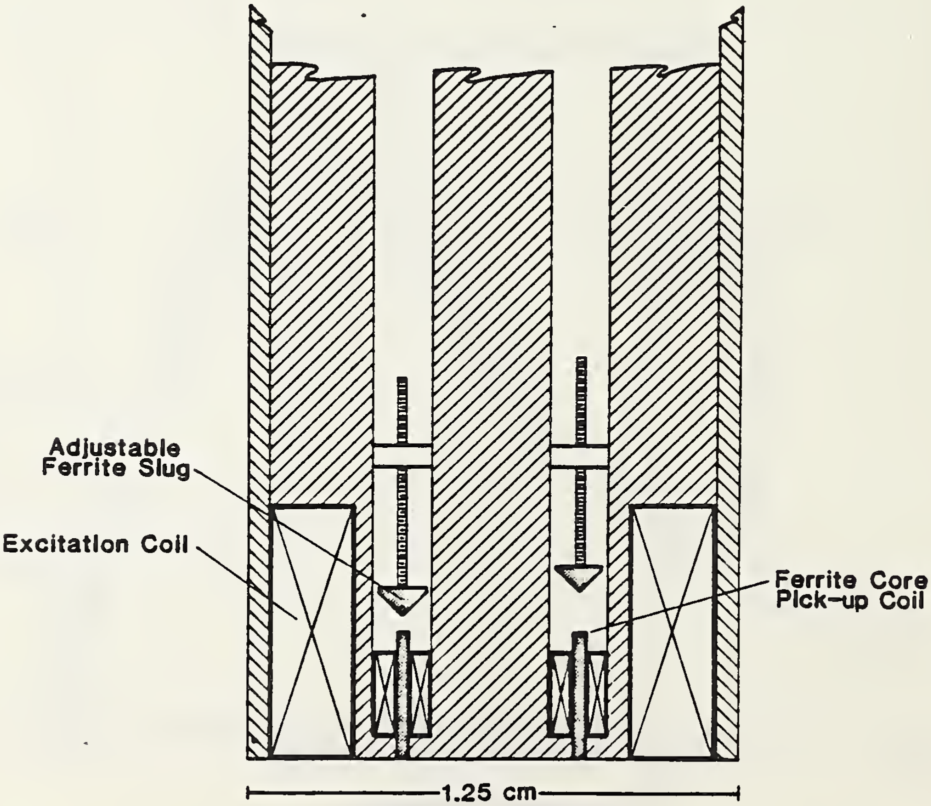

Figure 4. Cross-section of the differential probe.

STANDARDIZATION OF EDDY CURRENT CONDUCTIVITY MEASUREMENTS

George M. Free

Center for Basic Standards

National Measurement Laboratory

A program on eddy-current standards was initiated in the Office of Nondestructive Evaluation. Since April 1, 1985, the Electricity Division, Center for Basic Standards, has offered a new service in which electrical conductivity reference standards for use in calibrating eddy current conductivity meters are measured at 20°C. Standards tested at the present time are in the range from 15% IACS (International Annealed Copper Standard) to 100% IACS. The range will be extended down to 1% IACS by January 1986. Standards are measured at frequencies in the range between 10 kilohertz and 100 kilohertz, depending on their nominal IACS rating. Special arrangements can be made for calibrating standards at user-specified frequencies for the calibration of fixed-frequency conductivity meters. The standards are tested for uniformity of electrical conductivity over the surface to be calibrated and conductivity reported is that measured at the center of this surface. Standards to be tested must be non-magnetic and have a specified geometry.

The 1984 Annual Book of ASTM included for the first time E1004-84, Standard Test Method for Electromagnetic (Eddy Current) Measurements of Electrical Conductivity. This recommended practice was developed by ASTM Committee E-7 on Nondestructive Testing. The test method describes a procedure for measuring the electrical conductivity of nonmagnetic metals using the electromagnetic (eddy current) method and commercially available electrical conductivity instruments. Eddy-current measurements of electrical conductivity are widely used in industry for the sorting of metals with respect to variables such as type of alloy, aging, heat treatment, corrosion, etc. This recommended practice should go a long way towards ensuring that an individual worker makes such measurements in a reproducible manner and that the results obtained by different workers are consistent.

ULTRASONIC ABSOLUTE-POWER TRANSFER STANDARDS

F.R. Breckenridge, S.E. Fick and C.E. Tschiegg

Mechanical Production Metrology Division

Center for Manufacturing Engineering

A transfer standard comprising a new type of transducer and suitably-customized electronics has been developed[1] to optimize the transfer of NBS measurements of total radiated power in liquid media. With earlier transfer standards, procedures necessary for the transfer of calibration constituted sources of error comparable in magnitude to those of the underlying primary measurement of ultrasonic power. The new transfer standard uses a transducer with built-in rf metering circuitry; electronics embodied in the impedance-matching unit provided with each transducer allow the field user to obtain a pre-determined level of ultrasonic power by making a single measurement of dc voltage. Since the new procedure obviates the two absolute measurements of rf voltage and two calculations required by earlier procedures, the significant errors of the earlier procedures are precluded. The new transducer, unlike its predecessors, is capable of high output at high-order harmonics, so that a single unit can be used to obtain more than a watt of ultrasonic power at frequencies spanning 20 MHz in 1 MHz increments.

After the completion late in 1983 of two years of prototype testing, fabrication of transfer standards slated for eventual distribution by the Office of Standard Reference Materials (OSRM) was begun. Testing of the ten calibration systems comprising the first "production run" began in April, 1984. Each system will be tested periodically until it is dispensed by OSRM. As of March, 1985, data for the ten units indicates that errors in transferring NBS measurements of ultrasonic power to the field user should not exceed 0.5%. The comparable component of error when other methods of transfer are used is typically ten times larger. Further analysis of the results of some 1000 measurements made on prototype and production transducers over a three-year period has established that the previously-unknown long-term stability of transducers using lithium niobate is indistinguishable from the well-known high stability of quartz transducers.

SUMMARY

A new "universal" ultrasonic power transfer standard has been developed and is available from NBS. The transducer and custom electronics eliminate all of the difficult user's problems previously identified with the transfer of NBS measurements. The new device and transfer procedures also decrease the uncertainty of the transfer by an order-of-magnitude to 0.5%. Over 1000 tests have established good stability for the device.

REFERENCE

1. S.E. Fick, F.R. Breckenridge, C.E. Tschiegg, and D.G. Eitzen, "An Ultrasonic Absolute Power Transfer Standard," NBS J. Res. 89, No. 2, pp 209-212 (March-April 1984).

ULTRASONIC ARTIFACT CALIBRATION METHODOLOGY

G. V. Blessing and D. G. Eitzen

Mechanical Production Metrology Division

Center for Manufacturing Engineering

INTRODUCTION

The Ultrasonic Standards group of the National Bureau of Standards has an on-going responsibility for the improvement of ultrasonic reference block calibration methodology. As part of this project, the Office of Standard Reference Materials has supported an effort to improve block uniformity by purchasing a special lot of aluminum bar material (nominally 2 inch diameter), manufactured under specially controlled conditions which included a heat treatment process to specifically enhance wave propagation performance. Ultrasonic tests are being made on this material lot to determine the degree of (scattering and elasticity) homogeneity as a function of bar extrusion position.

DISCUSSION

Five material specimens were chosen for detailed comparison studies: four (three heat-treated and one non-heat-treated) from the special material lot, and one from a (reference) lot of known good ultrasonic material. A set of four shorter bars, varying in length from 1.25 to 6.00 inches, was sectioned from each specimen to provide the needed amplitude and elasticity data for wave propagation parallel to the bar axis. Using the pulse-echo ultrasonic system prescribed in the ASTM E127 document, metal-path-distance amplitude relationships were obtained before and after drilling the on-axis 5/64 inch diameter flat-bottom-holes that act as ultrasonic echo gages.

Prior to hole drilling, distance-amplitude data for the bars taken from the special materials lot did not show the expected monotonically decreasing amplitude relationship with increasing bar length. As a result, detailed ultrasonic scans across the bars were performed to elucidate the peculiar behavior of the special lot material, of which the heat-treated samples showed the most prominent effects. Figures 1 and 2 illustrate the difference, respectively, between the reference and heat-treated materials. The anomolous peak in the center of Fig. 2 is conjectured to be the result of material inhomogenity due to a preferred crystallite orientation that inadvertently resulted from the extrusion process. Elasticity measurements of the longitudinal wave velocity revealed a small (0.3 %) difference between the heat-treated and the other materials. This was not considered significant.

Subsequent to hole drilling (making ultrasonic blocks) the peculiar distance-amplitude relationships for the blocks fabricated from the special-lot material (expectedly) persisted. As a result, preliminary analysis of these data indicates this material lot is not suitable for the orginally intended purpose of fabricating blocks with uniform ultrasonic properties to also satisfy the requirements of ASTM E127.

SUMMARY

ASTM requested that NBS become a source of "certified" raw stock which is suitable for making flat-bottom-hole ultrasonic reference blocks to satisfy ASTM E127 Standard Practice. A large quantity of specially produced and heat treated aluminum rod was obtained and evaluated. The ultrasonic response of the raw stock was found to be anamolous and produces reference blocks with an inappropriately high reference signal.

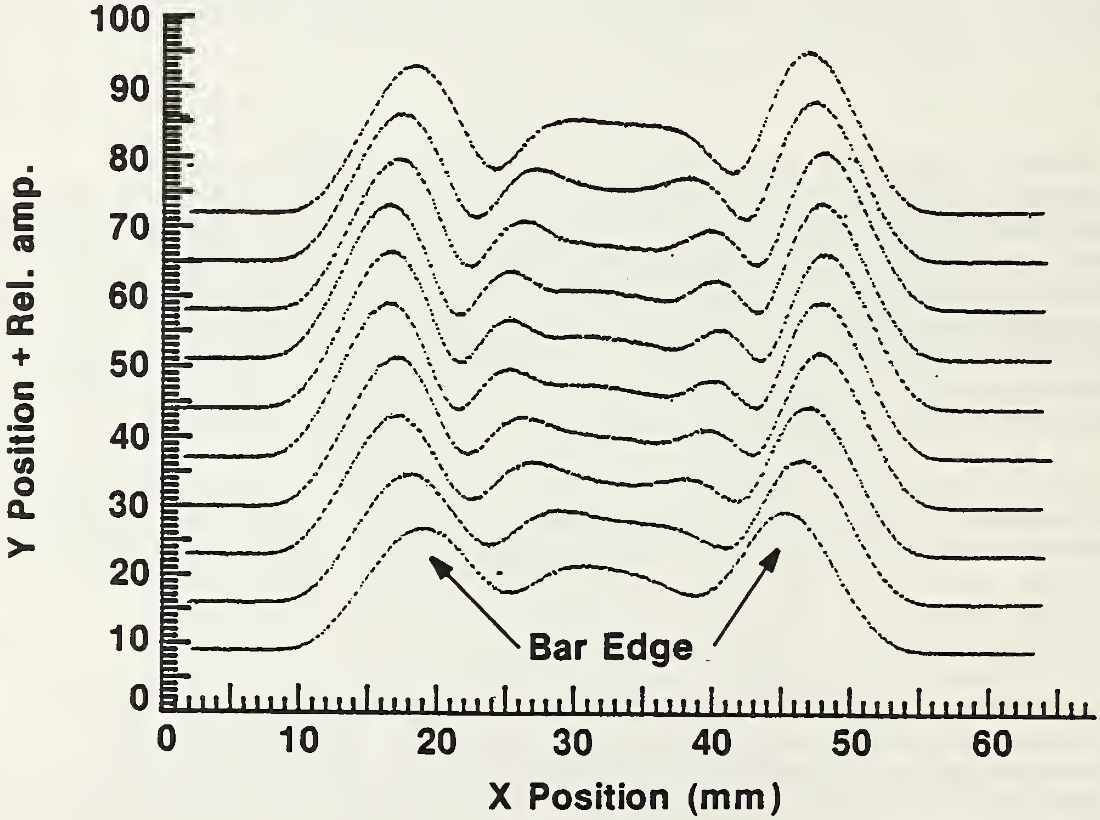

Figure 1. Ultrasonic pulse-echo amplitude data of good (reference) solid bar material six inches in length, scanning in the X-direction and incrementing in the Y-direction. Wave propagation (at 5 MHz) is parallel to the bar axis, with the relative amplitude proportional to the echo amplitude from the back surface (base) of the bar.

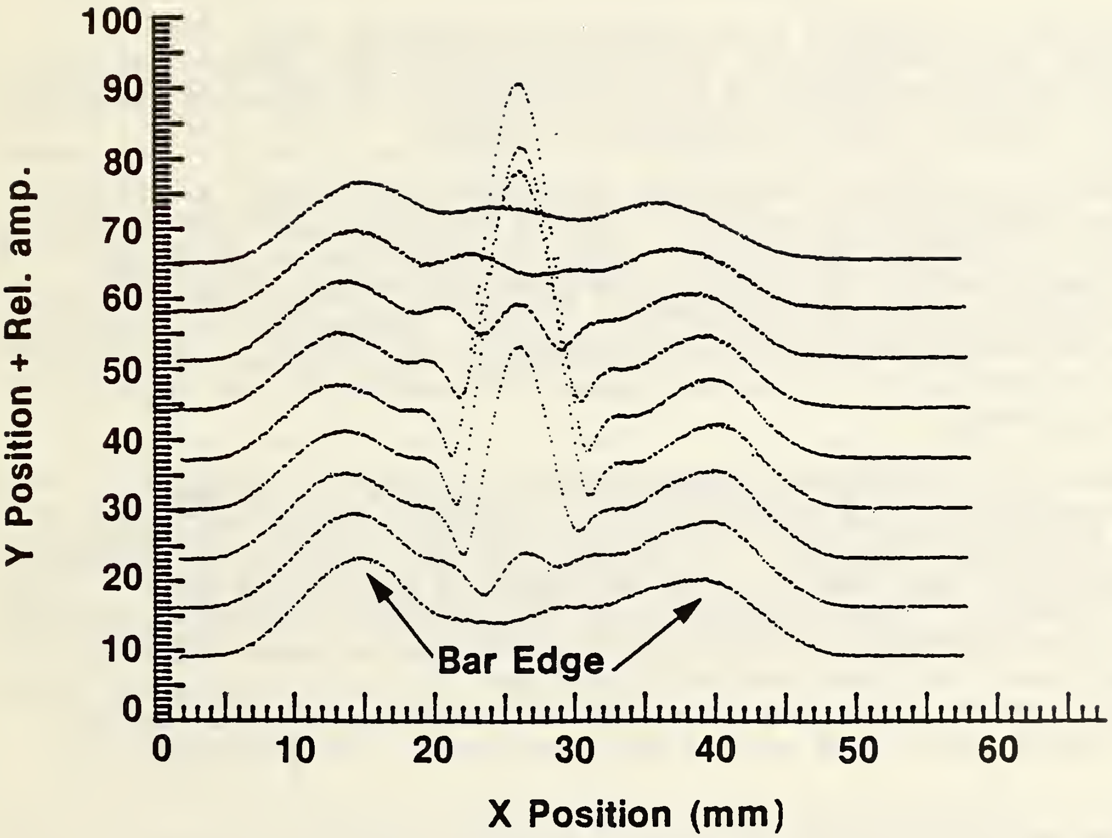

Figure 2. Same as Figure 1, but of a heat-treated bar from the special material lot.

DOCUMENT STANDARDS FOR ULTRASONICS AND ACOUSTIC EMISSION

D.G. Eitzen and F.R. Breckenridge

Mechanical Production Metrology Division

Center for Manufacturing Engineering

The goal of this project is to produce MIL-Standards and/or ASTM Standard Practices covering basic areas of ultrasonics and acoustic emission. This project has been supported by the Army Materials and Mechanics Research Center, and, recently, partially supported by Navair.

One task is to develop "precise and consistent terminology for acoustic emission test methods and procedures." Over 16 documents were used to develop a data base for terms and definitions. About 37 terms were selected and defined. These terms and definitions were successfully coordinated with the three military services. As a result MIL-STD-1945, "Glossary of Terms and Definitions for Acoustic Emission Test Procedures" was published near the end of 1984. ASTM Section E7.04.01 on AE Glossary is considering the terms for use in their glossary.

Another task is to "develop appropriate and precise terminology for ultrasonic test methods and procedures using resources such as ASNT, ASTM, ASME and military publications." In carrying out this task over 30 documents were reviewed and a data base of terms and competing definitions were organized. About 115 terms and definitions were proposed for a MIL-STD. This draft MIL-STD is undergoing a second round of coordination among the three military services. The terms and definitions are also being used as the basis for a revised ASTM E500 Standard Definition of Terms Related to Ultrasonic Testing. Some of these terms are now being balloted at the ASTM Society level.

The task on MIL-Standards on acoustic emission transducer calibration is also proceeding well. A draft MIL-document on the primary calibration of AE sensors has been delivered to the Army but alternative publication mediums are being discussed. This draft formed the basis of an ASTM Standard Method on the Primary Calibration of AE Sensors. The ASTM document is currently being balloted at the subcommittee level, having successfully passed an ASTM section ballot. A standard on the secondary calibration of AE sensors is also being developed. This document is envisioned as covering two or three alternative techniques. A technical outline of one technique has been drafted and distributed. A second technique may closely parallel the primary method.

Future plans call for the drafting of standards documents on secondary calibration of AE sensors and on the use of Hsu (pencil) AE source simulator. A MIL-document on characterization of ultrasonic transducers is also being considered.

SUMMARY

One MIL-STD has been published and two draft MIL-STD's prepared on AE ultrasonic methods. Two ASTM Standards based on this work are in the approval process.

VECTOR TRANSDUCER CALIBRATION

Christian D. Turner, H. N. G. Wadley, and J. A. Simmons

Metallurgy Division

Institute for Materials Science and Engineering

For many acoustic emission applications it is necessary to determine both the vertical and horizontal sensitivity of acoustic emission transducers. Indeed, partial knowledge of transducer sensitivity is not only incomplete, but can be misleading. A theoretical formulation was presented in last year's report for deducing the complete sensitivity of a transducer to displacement along all three coordinate axes. A simple formulation was also given which allows one to calibrate the relative horizontal to vertical sensitivity of an acoustic emission transducer assuming linear supraposition of response across the line of the transducer and a diameter of approximately 15 mm or less. This year we report on the experimental results for this simplified method.

In the configuration shown in Figure 1, the y_1 and y_2 axes lie on the plane of a plate, while the y_3 axis (not shown) is vertical to the plate. A horizontal force F is applied in y_1 direction and produces both horizontal and vertical responses in that direction, while producing only horizontal responses along the transverse, y_2, direction. For the configuration shown, the motions of the transducer and the Green's tensor components are given in the rotated x_1, x_2 coordinate system by:

$$U_1 = FG_{11} \text{ Cos } \theta$$
$$U_2 = FG_{22} \text{ Sin } \theta$$
$$U_3 = FG_{31} \text{ Cos } \theta$$

where the Heaviside Green's tensor functions are shown in Figure 2 for a 100 mm distance on a 4140 steel plate of 34.16 mm in thickness. We recall that the first Green's tensor component refers to the direction of response motion while the second component refers to the direction of an applied force. We shall be concerned, however, only with the front end or P & PP components of the signal, which are little affected by the thickness of the plate (unless the plate becomes much thinner).

Even for transducers of finite size, the vertical displacements are of opposite sign either side of $\theta = 90°$. Thus to a first approximation the vertical stimulus presented even to a finite diameter transducer at that position will be null. For a transducer which has purely vertical response, we then expect the magnitude near the P wave arrival to behave ascosine θ. A poled horizontal transducer with its pole at $\phi = 0$ will display a similar cosine θ dependence, while with the pole at $\phi = 90°$, the dependence will behave as sin θ, although the magnitude will be less due to the smaller value of G_{22} vis-a-vis G_{11}.

A schematic drawing of the experimental apparatus is shown in Figure 3. A 4140 steel disk 400 mm in diameter and 34.16 mm thick was used as the test medium. The surface of this disk was machined down leaving a pin 1.75 mm in diameter and 3 mm high in the center of the disk. The surface was then optically polished and mounted on a teflon ring in a rigid aluminum block. The disk could be fully rotated through 360°. Both the disk and the aluminum support block were marked so that the degree of rotation was known. The loading was accomplished by breaking a .5 mm lead horizontally across the pin. The lead was suspended just above the surface to minimize rotation moments.

Figure 4 shows the amplitude of the first wave arrival as detected by a capacitive transducer and plotted as a function of rotation angle. Since the transfer function of this type of transducer is easily calculable, the signal voltages were converted to absolute surface displacements in picometers. The data agrees well with the dashed theoretical curves. The curve of first wave arrival versus θ is shown in Figure 5 for an NBS type conical transducer. Within the measurement accuracy of this experiment, no horizontal sensitivity can be seen. Given the signal to noise ratio of this experiment, the vertical to horizontal sensitivity for this type of transducer appear to be greater than 20:1.

Figure 6 and 7 show similar polar plots for a commercial shear transducer with two different orientations ϕ, and $\phi_2 = \phi_1 + 90°$, where the angle ϕ was set to approximately agree with the poling direction of the transducers. These plots show first wave arrival behavior offset by nearly 90°. The discrepancy in the signal strengths for each orientation can be explained by noting that $G_{11}{}^{H} > G_{22}{}^{H}$. The ϕ_2 plot indicates that this transducer has little vertical sensitivity.

SUMMARY

We have demonstrated a simple method for estimating the vertical-to-horizontal sensitivity of an acoustic emission transducer. In order to quantitatively predict the horizontal transfer function of an AE transducer in more detail, a careful evaluation of the force function generated by the horizontally breaking lead is required. This work is in progress. The robust deconvolution methods we have implemented are relatively insensitive to the particular form of this force function and should allow us to complete a quantitative determination of the transfer function.

REFERENCES

1. J. A. Simmons and H. N. G. Wadley, "Vector Transducer Calibration," Review of Progress in Quantitative Nondestructive Evaluation, Vol. 3B, ed. by D. O. Thompson and D. E. Chimenti, pp. 699-706, Plenum Publishing Co., 1984.

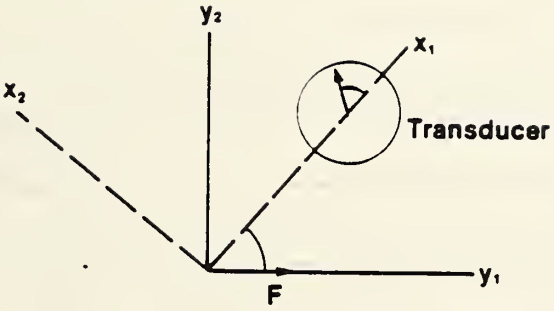

Figure 1. Geometry and notation. All vectors drawn are in the plane of the plate.

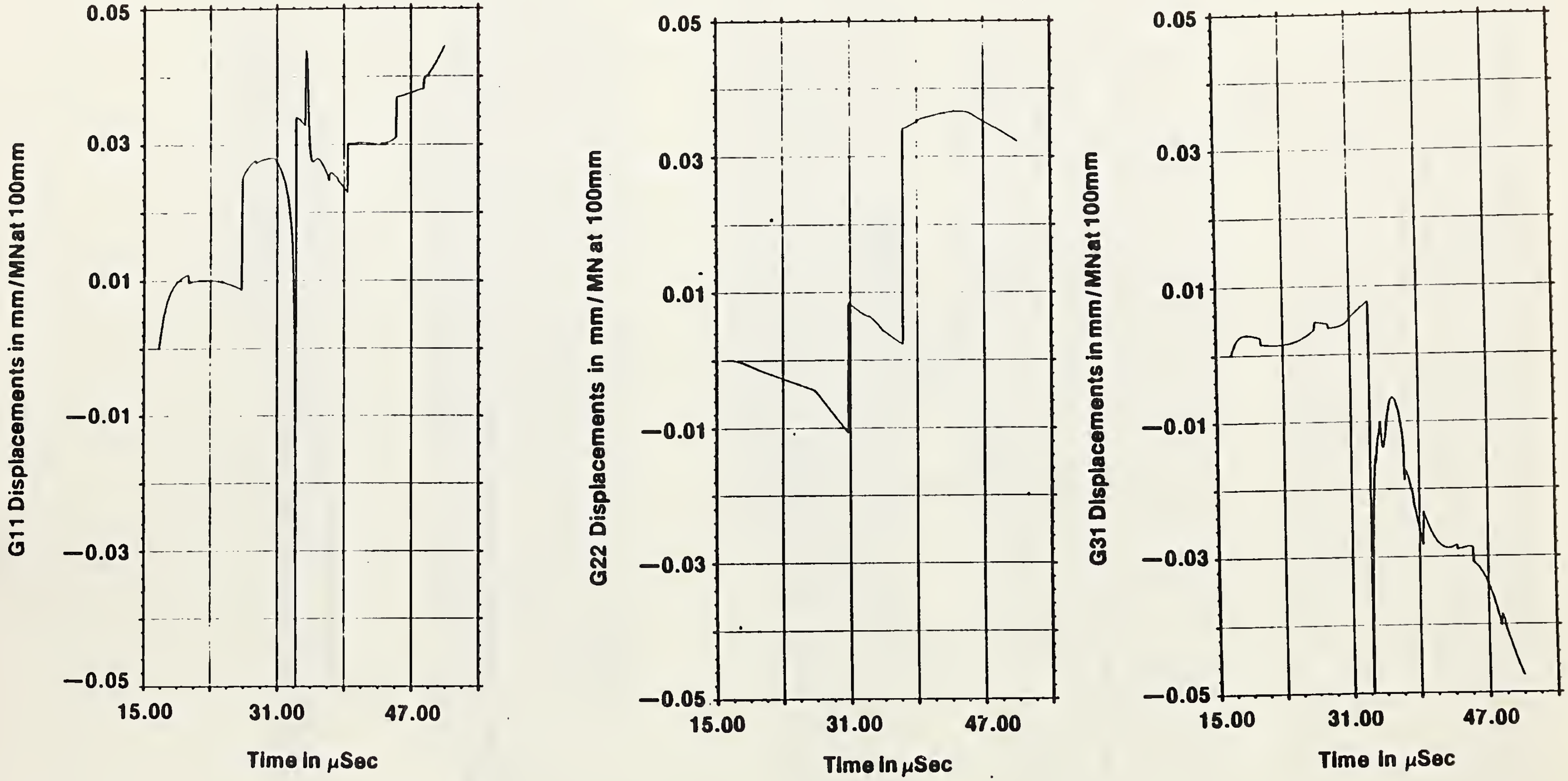

Figure 2. Heaviside green's tensor components used in this technique. The first subscript refers to the direction of the displacement and the second to the direction of the force.

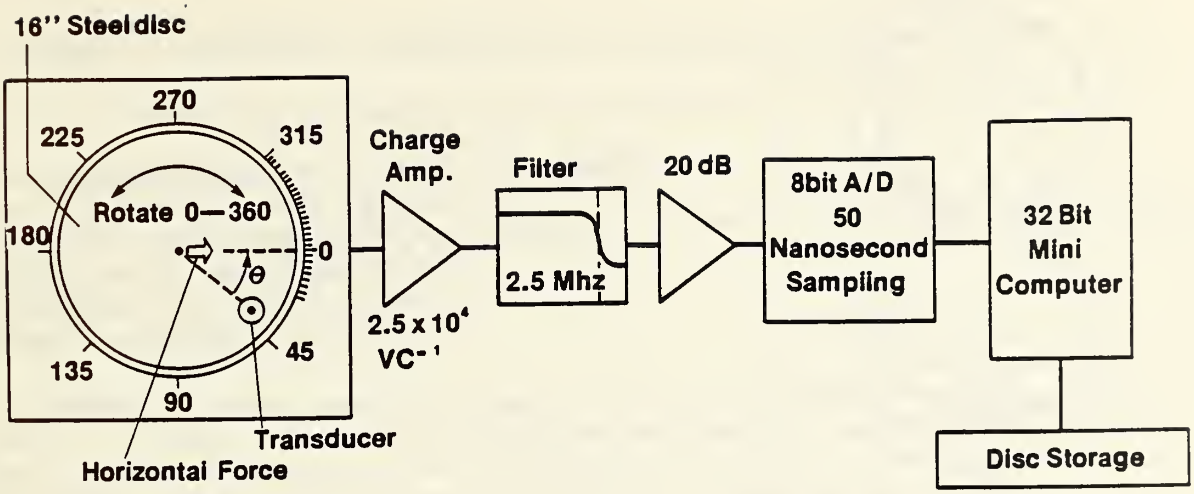

Figure 3. Schematic diagram of the experimental arrangement.

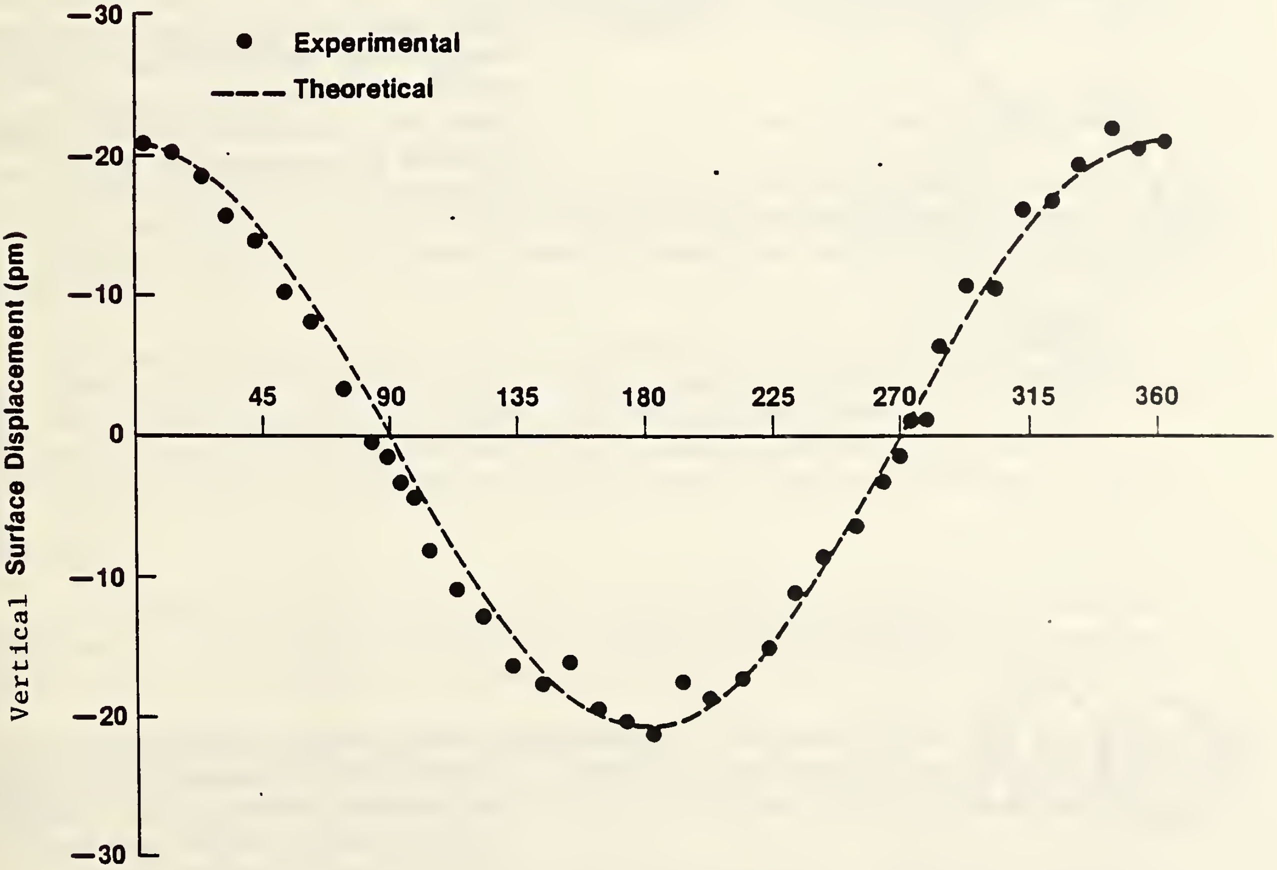

Figure 4. Magnitude of first wave arrival as a function of rotation angle, θ for a capacitive transducer.

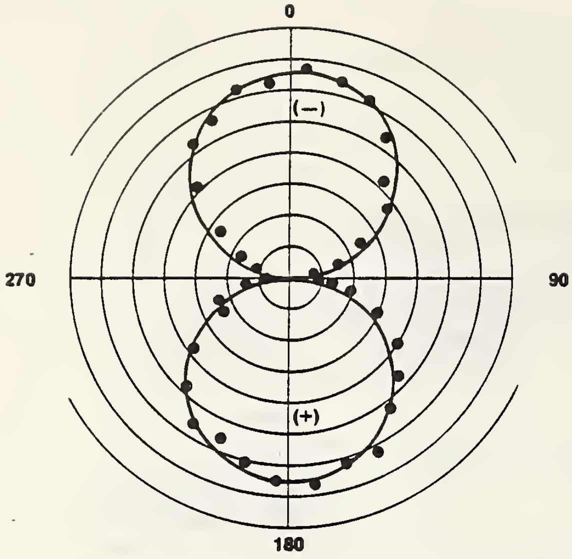

Figure 5. Polar plot of magnitude of first wave arrival versus θ for an NBS conical transducer. This plot was independent of the angle ϕ. Plus or minus signs indicate direction of motion.

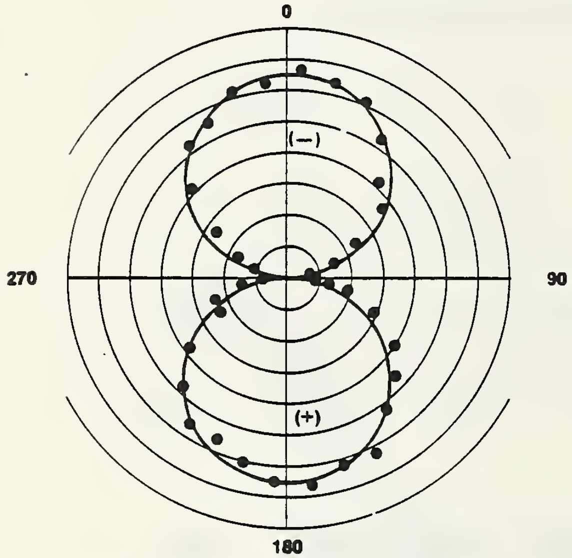

Figure 6. Polar plot of magnitude of first wave arrival versus θ for a shear transducer with $\phi = \phi_1$ oriented along the poling direction. Plus or minus signs indicate direction of motion.

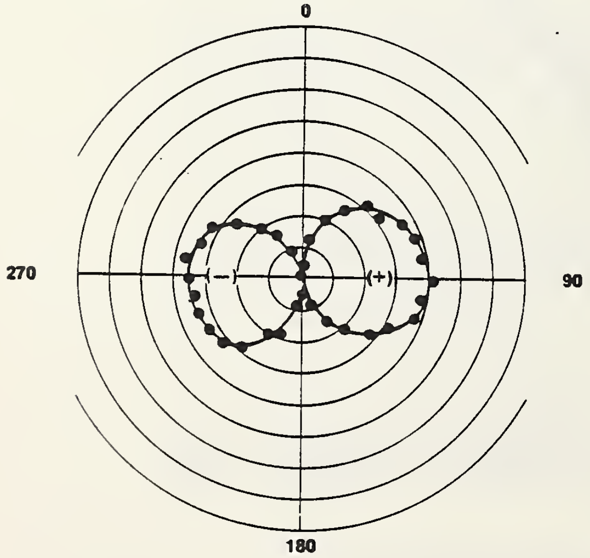

Figure 7. Polar plot of magnitude of first wave arrival versus θ for a shear transducer with $\phi = \phi_1 + 90°$. Plus of minus signs indicate direction of motion.

DYNAMIC DISPLACEMENT TRANSDUCERS FOR ACOUSTIC EMISSION

T.M. Proctor, M. Greenspan, and D.G. Eitzen

Mechanical Production Metrology Division

Center for Manufacturing Engineering

INTRODUCTION

Transducers which measure dynamic surface displacement with high sensitivity and fidelity are being developed and modeled. Such transducers are needed as transfer standards for the secondary calibration of acoustic emission sensors, as a tool in developing signal processing techniques to characterize acoustic emission sources, and as transducers for field applications. Both the normal and tangential components of motion must be measured to describe the dynamic displacement at a point on a surface. We previously had developed the NBS conical transducer which measures the normal component of displacement with a sensitivity of approximately 10^{-13} meter. This transducer is flat in frequency response from kilohertz to a few megahertz within a few dB. Transducers based on this development are now available from at least four sources including the NBS Office of Standard Reference Materials.

NORMAL DISPLACEMENT

A small level of effort was devoted to additional development of the NBS conical transducer. A new backing design was developed which is much simpler to construct than the polyhedral backing associated with the best model of the transducer.

The new backing consists of a rectangular parallelepiped in which a machined cavity is filled with tin. This composite construction provides the backing asymmetry needed to reduce back reflections and the tin improves damping. Transducers produced with this backing are equal to the best transducers using the complex, more difficult to machine polyhedral backing.

ANALYSIS

An analysis of the operation of the NBS conical transducer is nearly complete[1]. The analysis is aimed at a better understanding of the device so that it can be optimized or at least tailored for specific applications.

The analysis computes the response of a transducer from the geometry and material properties of the active element and the mechanical impedances looking into the mounting surface and into the backing block. The main problems are

(a) construction of an equivalent circuit for a conical transducer,
(b) derivation of an expression for the terminating impedances,

(c) solution of the Pochhammer-Chree problem for a cone (of finite length), and
(d) calculation of the finite-aperture effect.

The analysis resolves these problems; some approximations being necessary. The analysis is compared with response curves for conical transducers calibrated on the NBS AE calibration facility[2]. One such comparison is shown in Figure 1. The analysis predicts the general features of the measured response well. It also quantifies the importance of the smaller and larger diameters and mechanical impedances of the test surface and backing material. The results also show a modification of the Pochhammer-Chree theory would improve agreement. The roll-off at higher frequencies is, as yet, unexplained.

TANGENTIAL DISPLACEMENT

The development of a high fidelity, sensitive transducer for measuring dynamic tangential displacement continues. This problem is more difficult than the development of normal displacement sensors. In the case of normal displacement sensors, the poled direction is the same as the direction of motion and stress and, since the electrodes of the piezoelectric element are at the ends of this common axis, the element can be poled before or after machining. Preserving this symmetry in a completed transducer is relatively easy.

For tangential transducers, poling electrodes are placed so that the element is poled parallel to the tangential motion. These electrodes are subsequently removed and measuring electrodes are placed perpendicular to the poling electrodes. Then when shaping the element it is more difficult to maintain appropriate symmetries and it is not possible to pole subsequent to machining the element. These difficulties sometimes result in tangential transducers with unwanted sensitivity to normal displacement. Newly developed fabrication techniques have minimized this problem of cross sensitivity. The response of the newest tangential transducer to normal displacement is more than 20 dB below its tangential response over most of its 1 MHz bandwidth. This newest transducer has quite good fidelity. Its time domain response to a point-force step-function input to the large calibration block is shown in Figure 2 and compares well with the theoretically predicted waveform of tangential displacement shown in Figure 3. Figure 4 is the amplitude response versus frequency obtained by comparing the FFT of the measured output with that of the theoretical waveform.

SUMMARY

A new, easier to manufacture backing has been developed for the normal displacement measuring NBS conical transducer. A thorough analysis of the transducer shows good agreement with measured response and provides the tools for optimizing transducer geometry for specific applications. The most recent model of tangential transducer shows good fidelity, measuring waveforms that compare well with theory.

REFERENCES

1. M. Greenspan, "The NBS Conical Transducer: Analysis," to be submitted to J. Acoust. Soc. Am.

2. F.R. Breckenridge, "Acoustic Emission Transducer Calibration by Means of the Seismic Surface Pulse," J. Acoust. Emission 1, No. 2, 87-94; 1982.

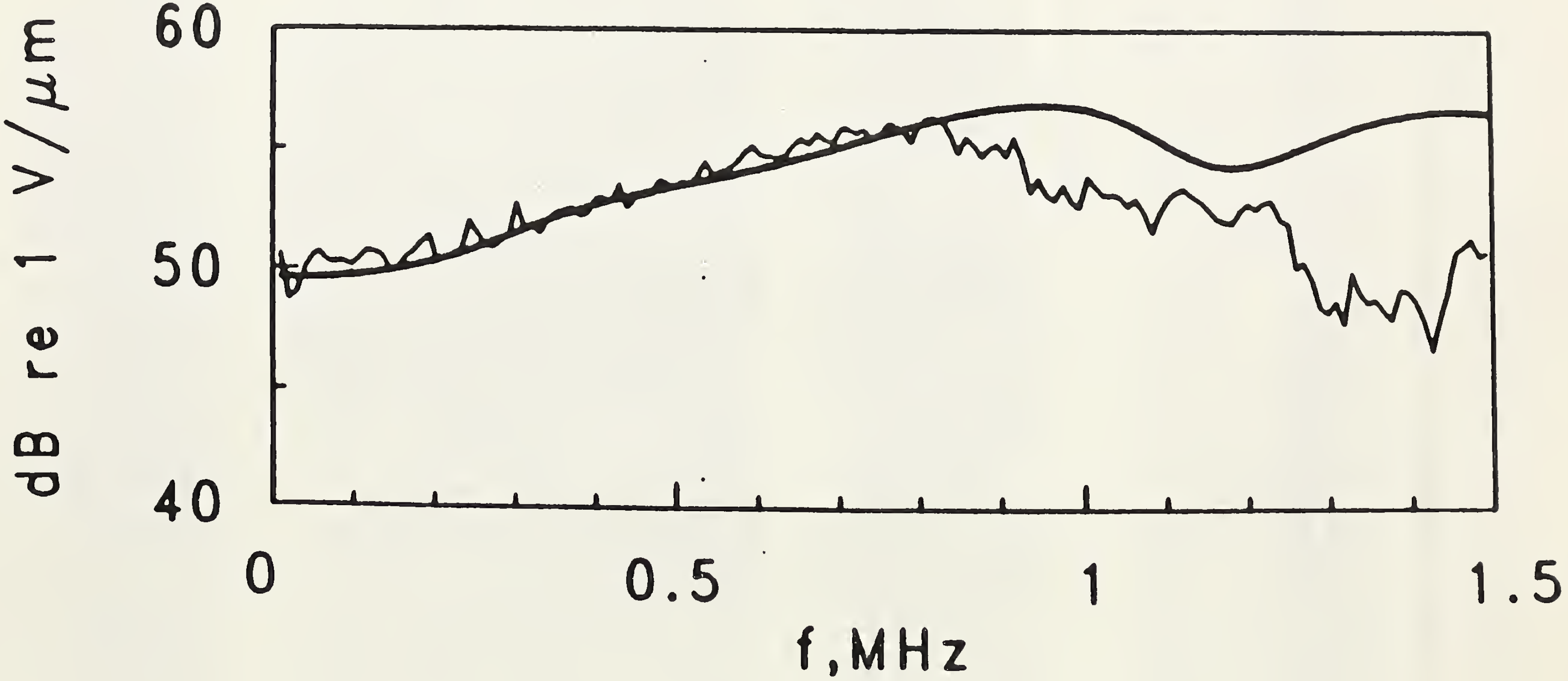

Figure 1. Amplitude versus frequency for a conical transducer with a smaller diameter of 0.62 mm, a larger diameter of 1.74 mm and a length of 1.24 mm. The thick line is from the analysis; the thin line is measured response.

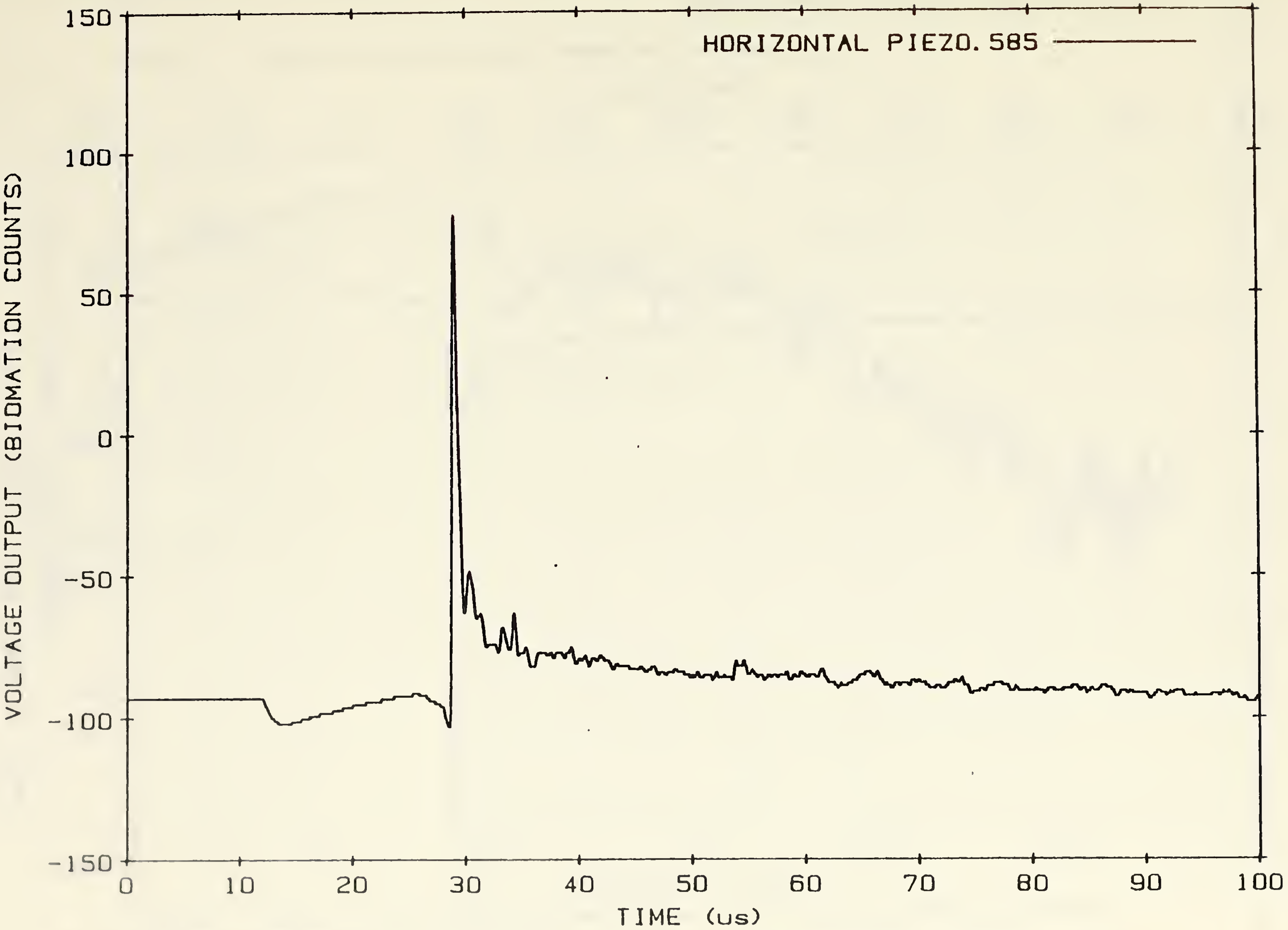

Figure 2. Measured waveform using the newest model of the NBS tangential transducer.

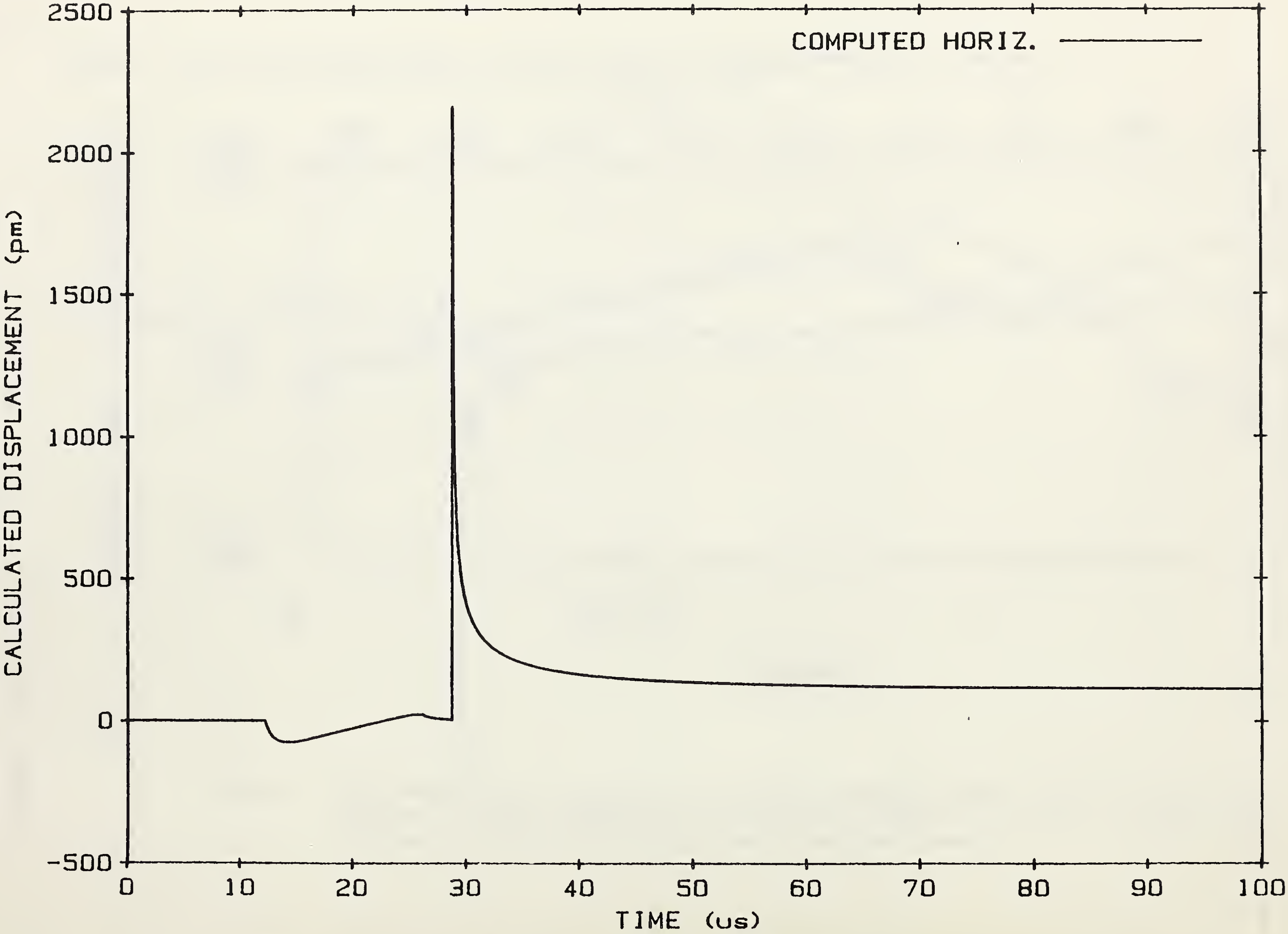

Figure 3. Theoretical waveform for tangential displacement.

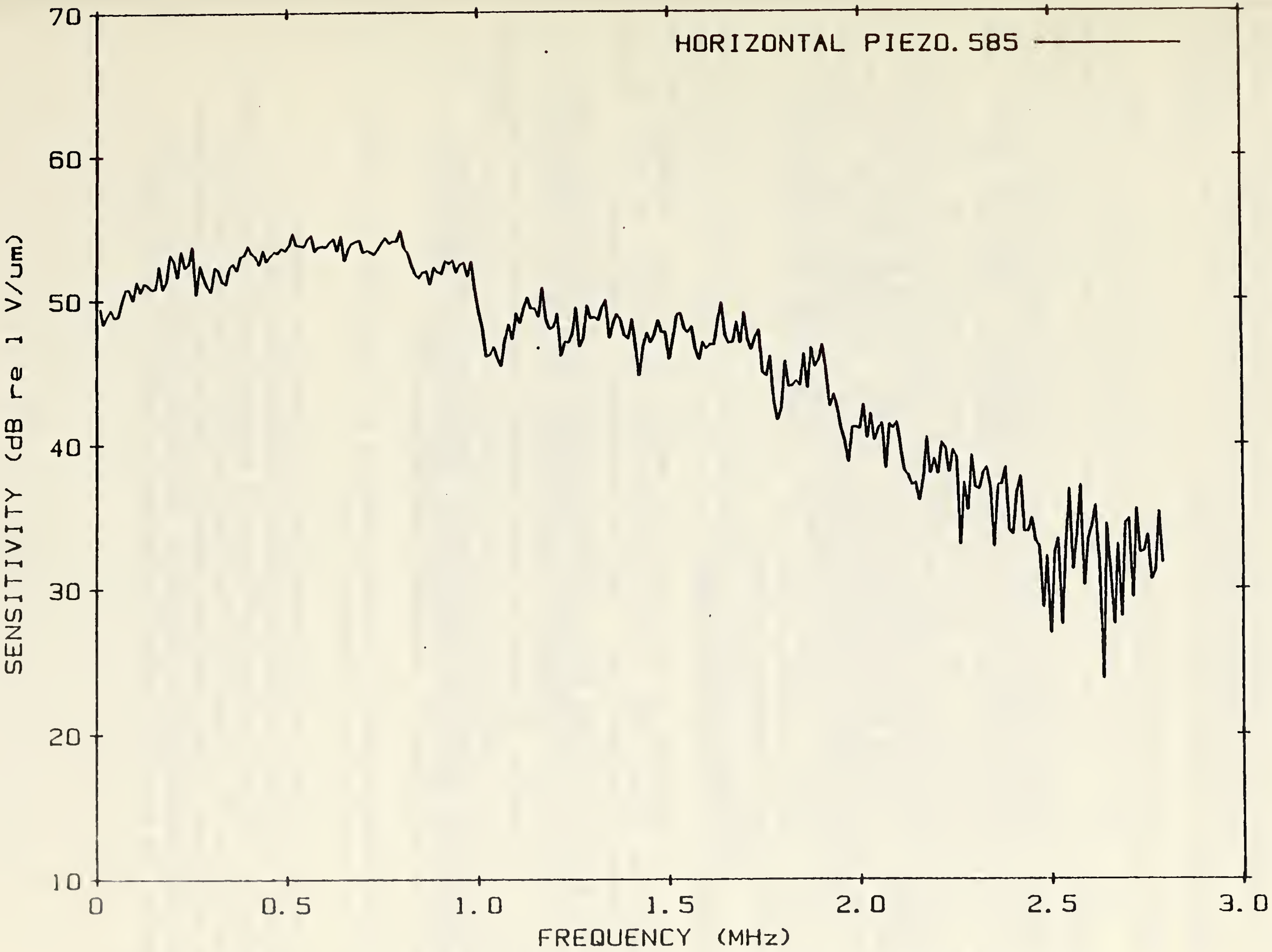

Figure 4. Amplitude of response versus frequency for the NBS tangential transducer.

CALIBRATION ACTIVITIES FOR AE TRANSDUCERS

F.R. Breckenridge and T.M. Proctor

Mechanical Production Metrology Division

Center for Manufacturing Engineering

INTRODUCTION

Based on recommendations by ASTM, ASME, and the AE Working Group a facility for the calibration of AE sensors was developed. This development was partially supported by the Electric Power Research Institute and the Office of Naval Research. The calibration subjects the device under test to a known dynamic displacement in order to determine its sensitivity as a function of frequency. The first method implemented makes use of the surface-pulse configuration[1] in which the mechanical input (a capillary-glass-break source which produces point-force step function) and the device under test are located on the same surface of a large transfer block which approximates a half-space. More recently, a through-pulse method has also been implemented; in this configuration the mechanical input and the device under are centered on the transfer block on opposite surfaces.

CALIBRATIONS AND TRANSDUCER DEVELOPMENT

Since the beginning of the calibration service for acoustic emission transducers in January 1980, we have performed 633 calibrations, of which, 82 were performed in the past year. Many of these were on experimental transducers constructed at NBS. For example, a number of calibrations have been done as part of the development of transducers specifically designed to measure the horizontal component of dynamic surface displacement with good fidelity. Calibration of these horizontal-sensing transducers has been done using the horizontal component of motion resulting from the glass-break source and referenced to the calculated horizontal displacement. Results from through-pulse calibration and surface-pulse calibration are combined to evaluate the performance of horizontal sensing transducers.

The calibration facility has been improved by installation of a better monitor for recording the glass-break force.

A batch of 20 NBS conical transducers is in the final stages of production. They will be used by AE sensor manufacturers, research laboratories, DoD, and testing services as a transfer standard for the secondary calibration of AE sensors. The transducers are being equipped with buffer amplifiers to make them more immune to loading and stray capacitance effects, thus increasing the accuracy of the calibration transfer. Other features of the amplifier system include partial shielding of the hot electrode of the transducer, gold contacts for reliability, and an equalizer network to improve the flatness of the frequency response of the transfer standards. Presently, the amplifiers have been constructed, but the transducers need to be recalibrated with the buffer amplifiers in place on the transducers.

Methods for the secondary calibration of AE sensors are being developed. An outline of a possible secondary calibration system has been made. The system would use a steel plate, 91 cm square and 3.3 cm thick. The source would be an NBS conical transducer driven by a tone-burst generator, and the calibration would be accomplished by comparing the unknown transducer against a calibrated, NBS conical transducer, both transducers being placed on the same side of the plate as the source transducer and equally distant from it.

A version of the NBS conical transducer having a scaled down active element and conical backing was constructed. An amplifier with a small amount of electrical equalization is used with this transducer to produce a somewhat improved frequency response. Figure 1 shows the time waveform of this transducer. This waveform is very close to the actual normal displacement. Figure 2 shows its amplitude sensitivity versus frequency showing it to have very good fidelity to above 2 MHz.

The calibration facility will continue to be used for the primary calibration of transducers and for evaluation of transducer development. Improvements aimed at assuring measurement process control will be developed and implemented.

SUMMARY

The AE sensor calibration facility continues to be useful for primary calibration and as a basic tool in transducer development.

REFERENCE

1. F.R. Breckenridge, "Acoustic Emission Transducer Calibration by Means of the Seismic Surface Pulse," J. Acoust. Emission 1, No. 2, pp 87-94 (1982).

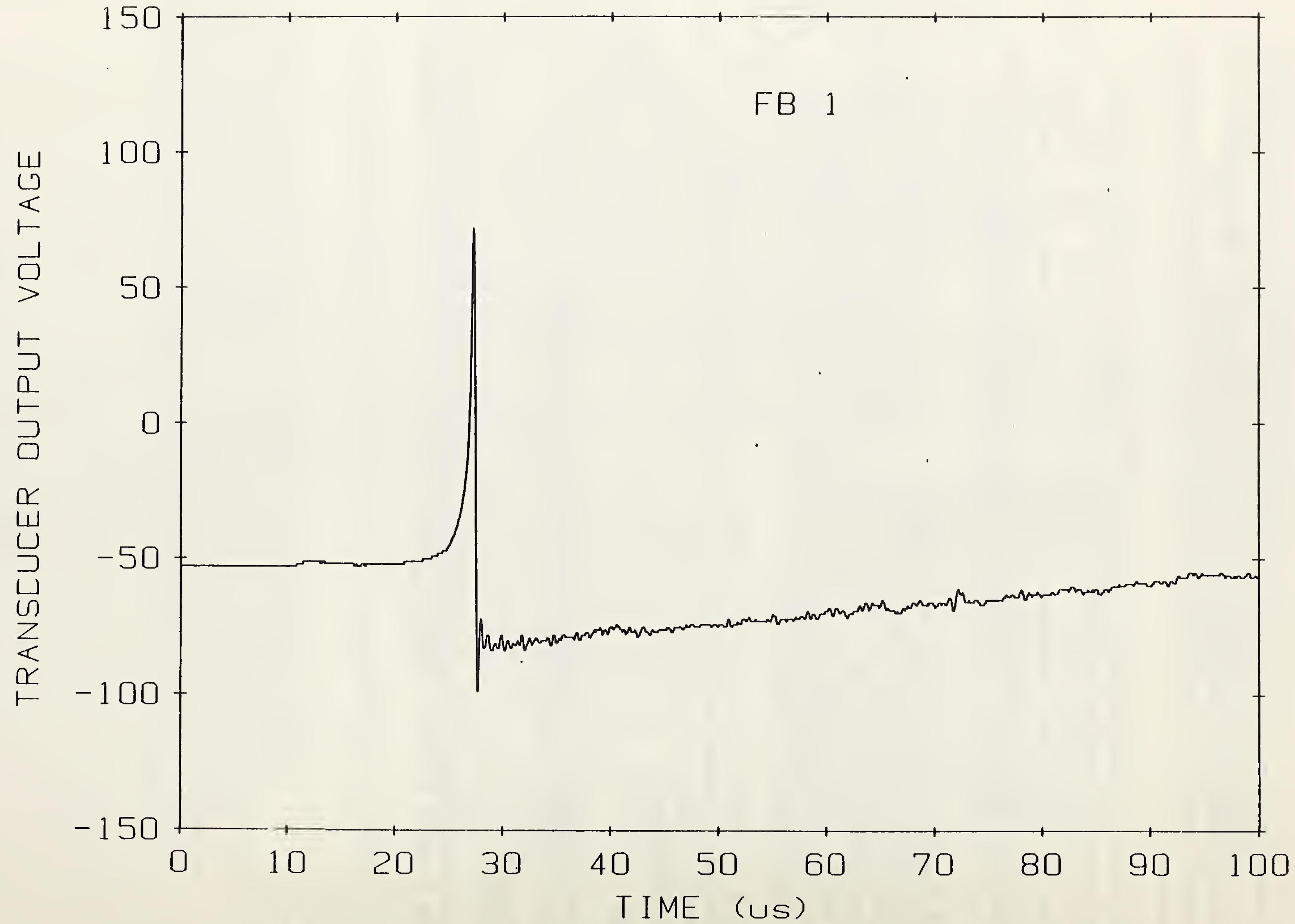

Figure 1. Surface pulse waveform as received by a modified NBS conical transducer with electrical equalizer on the steel calibration block.

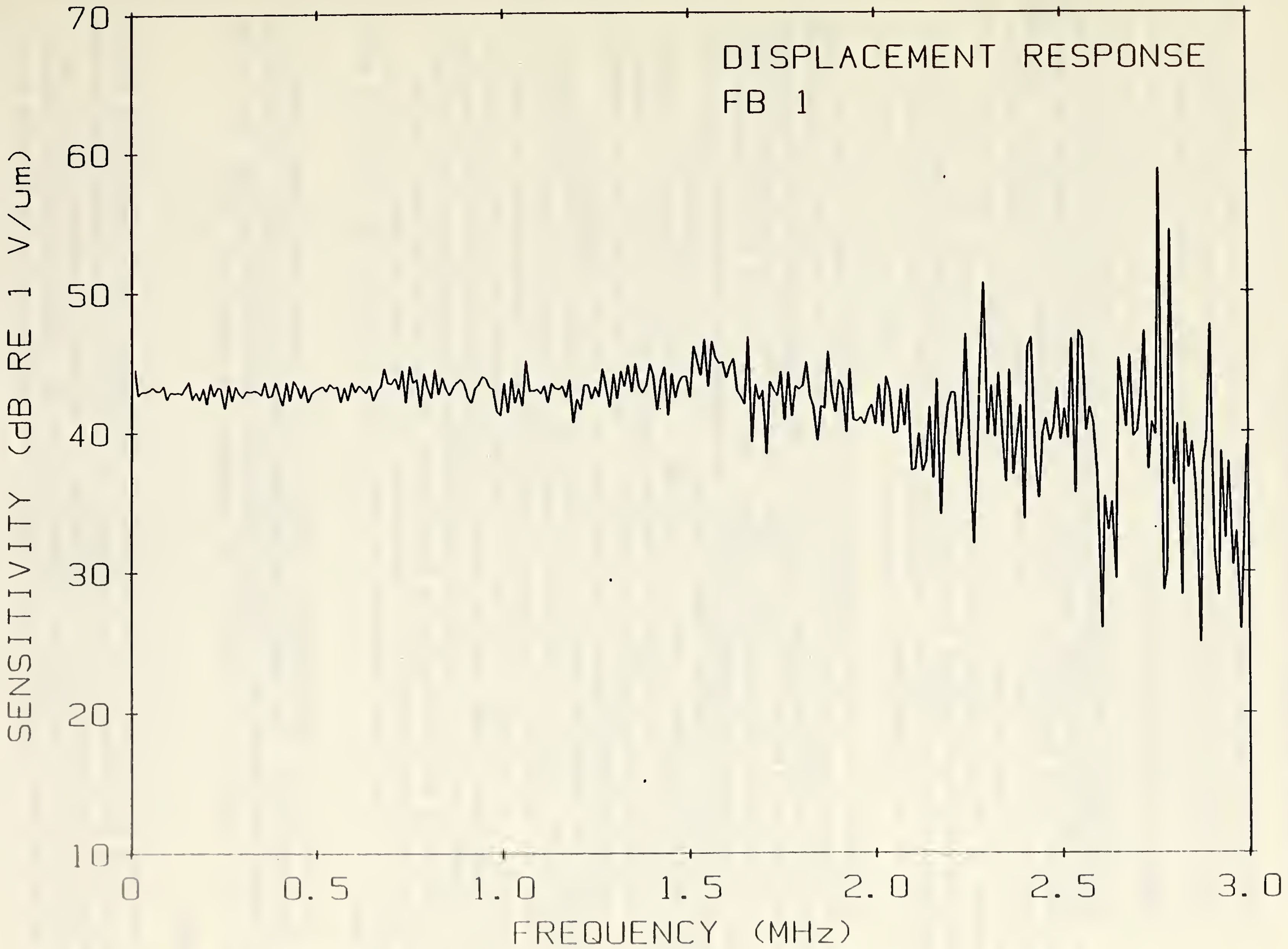

Figure 2. Sensitivity vs. frequency of the modified NBS conical transducer-equalizer combination.

MEASURING RADIOGRAPHIC/RADIOLOGIC SENSITIVITY

Robert C. Placious and Daniel Polansky

Radiation Physics Division

Center for Radiation Research

Traditionally, the measurement of radiographic image quality depends on how well small holes at low constrast are imaged. Since an observer is part of this system, this measurement requires that performance of the eye at different contrast levels be included In the evaluation. Therefore, reference is often made to the classical paper of Rose[1] on fluctuations in the light signal received by the eye and the later paper by Morgan and Sturm[2] where this principle was first applied to medical fluoroscopy. Not surprisingly, it was established that the smallest perceptible hole in the image was inversely proportional to its contrast.

Ultimately, of course, fluctuations in the photon signal to the eye relate back to fluctuations in the incident x-ray photons. For purposes of discussion, however, it is sufficient here to refer to the signal received by the eye and the fluctuations (noise) in that signal. Qualitatively, the relation between contrast and detail detectability, (CDD), can be described as follows. As the signal to noise ratio, (SNR), decreases, corresponding to reduced signal photons, a point is reached where the image of a hole is undetectable regardless of size. This occurs as contrast or density difference is reduced. On the other hand, as one goes to smaller detail (holes) a point is reached where the detail detectability becomes poor due to resolution limits imposed by the complete imaging system. The holes are not detected regardless of contrast. This x-ray/eye system is illustrated in Figure 1. The radiographic CDD curves are based on experimental data.[3] The fluoroscopic curve is based on published curves given in McMaster.[4] Superimposed on these curves are the contrast/hole size ranges provided by the ASTM plaques which were designed to measure equivalent image quality sensitivity.[5] We conclude from this that while the ASTM/NBS system for measuring EIQS sufficiently brackets the film range so that some holes are visible for a given film, the same device would not be suitable for direct industrial fluoroscopy. If this type of device is to be developed for electronic radiology we must obtain accurate CDD curves for such systems.

We have also superimposed on Figure 1 the proposed hole/plaque ranges we are now testing for high energy radiography. This is done only for illustrating that larger hole sizes are required for higher kilovoltages but that the thickness of the plaques, as a function of specimen thickness, are lower.

SUMMARY

We are, at present, in the process of developing a high energy EIQS system based on the design now in use at 200kV. The last report indicated that changes in design of the system-or a re-definition of the way in which we select the numerical value of the EIQS for a given system-was needed. During this reporting period we have received, from outside laboratories assisting in this work, many additional test results with the present design. Our analysis of this data is continuing and we have made arrangements for some additional readings by outside experts. However, based on what we now have, our preliminary conclusion is that the design is suitable and the manner in which the numerical value is determined should be revised. This does not invalidate the proposed system of measuring EIQS at high energies but it does differ from the method used on the 200kV. system. Since this proposed method makes the process of selecting the value of the EIQS somewhat easier, it may eventually lead to a revision in the low energy standard.

REFERENCES

1. A. Rose, J. Opt. Soc. Am., 38 196, (1948)

2. R.E. Sturm, and R.H. Morgan, Am. J. Roentgenol. 62, 617 1949)

3. E.L. Criscuolo, Matls. Res. and Stds. 3, 465, (1963)

4. Nondestructive Testing Handbook, R. C. McMaster, Editor, 1,19.29 (1959) The Ronald Press, N.Y.

5. ASTM Standard E 746-83, Annual Book Of ASTM Standards 03.03, 651 (1984)

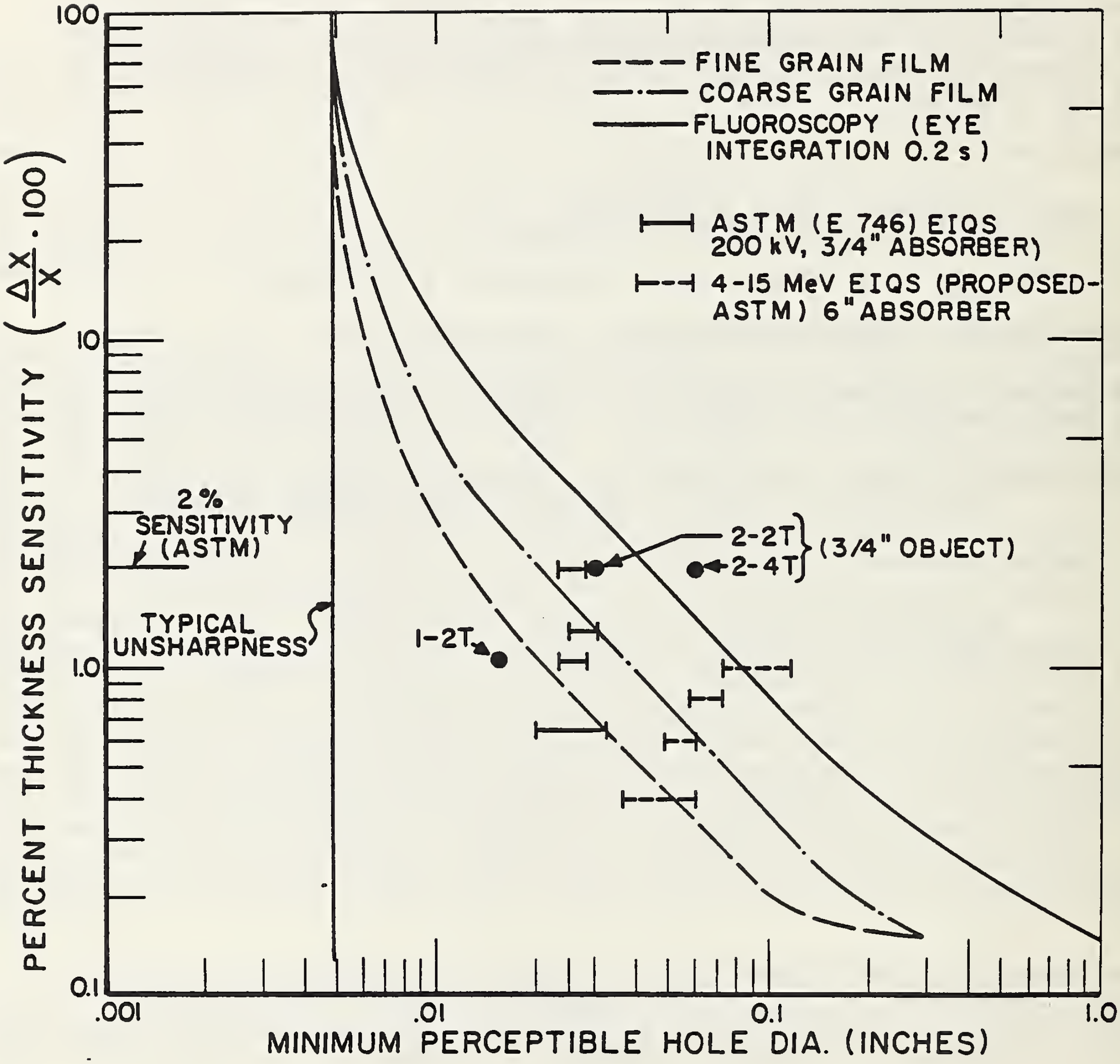

Figure 1. Contrast-detail detectibility curves for two film types and for direct fluoroscopy. Some ASTM image qualities are also shown.

SELF TEST OF VISUAL ACUITY FOR RADIOGRAPHERS

Robert C. Placious

Radiation Physics Division

Center for Radiation Research

As a test for visual acuity for radiographers the detection of slit images of varying width and contrast has been proposed by NBS.[1] The slit image sizes as given in the reference are as follows:

Slit Width	Minutes of Visual Angle (eye/film distance = 40 cm.)
.0089 cm.	0.75
.0119 cm.	1.0
.0178 cm.	1.5

For all widths the length of the slit is 1.24 cm. (0.5"). The contrast range prescribed in the reference is as follows:

Contrast	Film Density Background	slit
0.1	1.70	1.74
0.3	1.70	1.85
0.85	1.70	2.52

The third variable in this test is the edge gradient of the slit image. One series contains a complete set of sharp edged slit images while the other series contains blurred edge images.

At good contrast the normal eye should be able to detect a line having a visual angle of about 1.0 minute. Taking into account all of these conditions, it is prescribed that a person with normal vision should achieve a seventy (70%) percent or better passing grade on this test. The total number of slit images is 72. If, for example, 4 more images containing no slits are included in this test, the total is 76. Of this number, about 12 are judged to be quite difficult to see. Therefore the person with acceptable vision should detect about 64 images-easily achieving the desired passing grade.

We have estimated the signal to noise ratio (SNR) for three of the above cases. This estimate is:

SLIT WIDTH	CONTRAST	SNR
.0089cm.	0.1	21
.0119cm.	0.3	94
.0178cm.	0.85	533

This calculation is based on the x-ray photon signal only. It assumes an emulsion thickness of 6.25 (10^{-4}) cm., an emulsion bulk density of ($3.82 g/cm^3$)[2]

a monoenergetic photon energy of 100 keV. (attenuation coefficient = 0.966 cm^2/gm)[3] and the slope of the exposure/density curve = 0.48 Roentgens per unit change of density.[4] This SNR is for one source of noise only-the fluctuations in the x-ray signal. Other sources of noise, such as x-ray scattering, will reduce these values. The calculation is for a sharp edged slit only.

SUMMARY

We previously reported that a series of slit images had been produced by radiographic means and sent to several DoD laboratories for testing. All of those tested scored better than 90 percent. It was determined howevever that the test was administered to skilled film readers and did not adhere to the exact protocol specified for the test. We are in the process of modifying some of the slit patterns according to some suggestions made by the testing laboratories and to increase the difficulty of detecting some of the patterns. When the entire series of slit images are completed another test test will be made according to the protocol given in the reference.

REFERENCES

1. G.T. Yonemura, NBS Technical Note 1143, U.S. Dept. of Commerce, June 1981

2. S.M. Seltzer, and M.J. Berger, Int. J. Radiat. Isot., 33, 1189 (1982)

3. J.H. Hubbell, Int. J. Radiat. Isot., 33 1269 (1982)

4. Radiography in Modern Industry, Third Edition, Eastman Kodak Co., Rochester, N.Y., 14650

PERFORMANCE ASSESSMENT OF FLUORESCENCE MEASUREMENTS

K. L. Eckerle, J. J. Hsia, S. T. Chang, and K. D. Mielenz

Radiometric Physics Division

Center for Radiation Research

Fluorescent brightness, a visual quantity, is a property of fluorescent penetrants that can be measured quantitatively. This project has as its goal the performance assessment of fluorescent measurements made on fluorescent penetrants. These penetrants are used to detect surface defects of materials by non-destructive evaluations.

Work in the prior year was centered on a reference spectrofluorimeter designed at NBS (ref. 1,2,3). The objective of this work was to characterize the spectrofluorimeter for wavelength scale, stray radiant energy, and linearity. The characterization has been completed.

Further work on the spectrofluorimeter has been aimed at measuring its relative spectral response. This was done by two methods - using a NBS standard lamp, and a NBS standard detector. These were a vacuum tungsten strip lamp and silicon photodiode, respectively. Preliminary technical emission spectra for quinine sulfate dyhydrate have been obtained. Publication of some of this work is anticipated.

Also, a commercial fluorimeter was purchased and modified to conform to ASTM standards. Participation in an ASTM round-robin to evaluate three liquid penetrants was accomplished in collaboration with L. J. Swartzendruber. Solutions of different concentrations were measured. In addition, thermal and ultraviolet fading tests were performed.

Future work will be centered about the NBS reference spectrofluorimeter and the search for a standard material. Also, we will continue to cooperate with committees studying fluorescence and continue to monitor the literature on this subject.

SUMMARY

In FY85, we have successfully obtained preliminary technical emission spectra with the reference spectrofluorimeter, and have obtained data for the ASTM round-robin using the commerical fluorimeter.

REFERENCES

1. K. D. Mielenz, "Photoluminescence Spectrometry", Optical Radiation Measurements, Vol. 3 Measurement of Photoluminescence, pp. 17-19 (Academic Press, Inc., 1982).

2. E. D. Cehelnik, K. D. Mielenz, and R. A. Velapoldi, "Polarization Effects

on Fluorescence Measurements", J. Res. National Bureau of Standards 79 A, 1 (1975).

3. K. D. Mielenz, E. D. Cehelnik, and R. L. McKenzie, "Elimination of Polarization Bias in Fluorescence Intensity Measurements", J. Chem. Phys. 64, 370 (1976).

DEVELOPMENT OF HIGH OPTICAL DENSITY STANDARDS

J. J. Hsia, C. H. Popenoe, and L. E. Fink

Radiometric Physics Division

Center for Radiation Research

Optical density standards are required to calibrate radiographic films. These films are used to detect internal and surface defects of materials by NDE evaluation. The objectives of this project are to develop high optical density standards (up to optical density of 5.8), and to base calibration of master standards on the Inverse Fourth Apparatus (Ref. 1) through development of hardware and software for the Inverse Fourth Apparatus and characterizations of the apparatus and high optical standards.

Realignment of the optical system, refinement of the measurement procedure and modified software resolved the problem of the optical zero-offset distance (Ref. 2). This distance is now a constant and is independent of the optical density of the filter employed.

To conform to the new geometric condition by ISO 5/2-1985 (Ref. 3), "Photography-Density Measurements - Part 2: Geometric Conditions for Transmission Density", an opal-diffuser collection system has been designed and constructed. This system consists of an opal glass, a sample plate with grooves for applying vacuum and pressure, and a specular-aluminum-hemispherical collector for diffuse light.

Measurements of photographic and x-ray step tablets using both opal-diffuser and integrating-sphere collection system have been performed. Preliminary data indicated that, below optical density one, measurements made with the opal-diffuser gave lower optical densities than those made with the integrating sphere. These differences are expected since the opal diffuser introduces interreflections between the sample surface and the opal diffuser. These differences are consistent with the measurements made by PTB, West Germany.

SUMMARY

In FY85, we have resolved the problem of the optical zero-offset distance, designed and constructed the opal-diffuser-collecting system, and intercompared the opal-diffuser and the integrating-sphere collection systems.

REFERENCES

1. D. A. Swyt and J. G. LaRock, "Inverse-fourth apparatus for photometric calibration", Rev. Sci. Instrum. 49(8), pp. 1083-1089 (Aug. 1978).

2. C. H. Popenoe and J. J. Hsia, "Optical Density Determination with an Inverse-Fourth Instrument" in "Technical Activities 1984 Office of Non-

destructive Evaluation", Editor L. Mordfin, NBSIR 84-2944, pp. 92-101 (Nov. 1984).

3. International Standard, "Photography-Density Measurements - Part 2" Geometric Conditions for Transmission Density", ISO 5/2, pp. 1-4, International Organization for Standardization (1985).

INFRARED METHODS OF NONDESTRUCTIVE TESTING

Julius Cohen

Radiometric Physics Division

Center for Radiation Research

The purposes of this project are: (1) to develop expertise and maintain an awareness of infrared methods of NDT, in particular thermography, as they are practiced in industry; (2) to evaluate the current and future needs for standards and traceability for these methods; and (3) to assess the Bureau's role in this area.

Previous work on this project has generated (1) an NBS report "Elements of Thermography for Nondestructive Testing" (ref. 1), (2) a current ASTM activity of compiling a glossary for infrared thermography, and (3) an ONDE sponsored project to develop standard test methods for characterizing performance of thermal imaging systems.

(1) The NBS report presents an elementary review of thermal imaging systems, with emphasis on the application of thermography to nondestructive testing. Topics include heat radiation theory; thermal imaging systems; performance characteristics; effects of emissivity, background temperature, atmosphere, field of view; and examples of applications of thermography to NDE. (2) The glossary cited above is based largely on this NBS report. (3) Draft #1 of ASTM "Standard Test Method for Minimum Resolvable Temperature Difference for Thermal Imaging" has been written; see J. Cohen, "Standard Test Methods for Characterizing Performance of Thermal Imaging Systems," elsewhere in this document.

REFERENCES

1. J. Cohen, "Elements of Thermography for Nondestructive Testing," NBS Technical Note 1177 (May 1983).

STANDARD TEST METHODS FOR CHARACTERIZING PERFORMANCE OF THERMAL IMAGING SYSTEMS

Julius Cohen

Radiometric Physics Division

Center for Radiation Research

The objectives of this new project are to develop standard test methods for characterizing performance of thermal imaging systems for NDE purposes. Specifically, the performance measures, minimum resolvable temperature difference (MRTD), minimum detectable temperature difference (MDTD), and noise equivalent temperature difference (NETD) are to be dealt with.

During FY 1985, the first draft of Standard Test Method for MRTD for Thermal Imaging was completed and presented to ASTM Committee E7.10.04 for deliberation. This method covers the determination of the MRTD capability of the compound observer-thermal imaging system as a function of spatial frequency. Included in the draft are terminology, summary of method, significance and use, apparatus, procedure, reporting requirements, and sample calculations. The second draft is expected shortly to go to committee vote.

For FY 1986, the plans are to complete the drafting of the standard for MRTD and to draft an additional standard, MDTD for Thermal Imaging.

This work is being carried out the the aid and cooperation of Dr. R. Grot, CBT, who graciously permits us to use his thermographic laboratory facilities.

DEVELOPMENT OF LEAK STANDARDS AND CALIBRATION FACILITIES AT NBS

Charles D. Ehrlich and Charles R. Tilford

Temperature and Pressure Division

Center for Basic Standards

The need for improved leak measurement accuracy in a variety of industries, and in some cases for legal traceability to a recognized standards authority, prompted the development of leak standards at NBS. The NBS Leak Standards Program began in FY84 with the objectives of developing primary leak standards, characterizing transfer leaks, and providing a publicly accessible leak calibration service. FY85 has seen significant progress towards these objectives.

An NBS primary leak standard has been developed, and measurements performed on a sintered plug variable-rate leak have shown agreement with measurements made at the Primary Standards Laboratory at Sandia National Laboratories (SNL) of better than 5% over a range of leak rates spanning three orders of magnitude (4×10^{-7} to 4×10^{-10} moles/sec; 10^{-2} to 10^{-5} std cc/sec) for three different gases; helium, argon and nitrogen. The SNL primary standard is of a completely different type than the one at NBS, so that this initial agreement is very encouraging. Measurements made on a second leak of identical design but having a lower leak rate indicate that the leak artifact has undergone some type of mechanical transformation during the course of the year, and the artifact has been returned to SNL for further testing and verification.

Besides the work that has been done characterizing these sintered plug variable-rate leaks, characterization of helium diffusion leaks and sintered silicon carbide leaks has also begun. Helium diffusion leaks of NBS design that will allow variable supply pressures were constructed in FY85. Experiments run during FY85 on a leak comparator device at NBS, designed to provide a systematic study of commercial helium transfer leaks, show an exponential dependence of leakage rate with temperature, contrary to conventional assumption and usage of these leaks.

Work toward providing a publicly accessible leak calibration service in FY86 has proceeded predominantly along two lines, in addition to the work already mentioned. First, documentation of the Primary Leak Standard has begun, a prerequisite toward obtaining calibration status as the detailed error analysis of the system is presented. Second, the NBS Primary Leak and Vacuum Standards Laboratory has expanded in physical space, equipment, and manpower. Floor space has essentially doubled; a dedicated leak rate chamber has been constructed and put into service and a new bellows flowmeter has been designed, constructed, and is ready for test.

As indicated, a substantial part of the FY85 work was done in collaboration with Sandia Labs, who provided a major amount of the support for this program. NBS involvement in the collaboration, besides the work mentioned previously, included on site (at SNL) modification of the leak comparator system to incorporate a temperature control system developed at NBS. Further collaboration will include joint presentation and publication of results in an archival journal.

SUMMARY

FY85 has seen the development of an NBS primary leak standard that has performed well against an established primary standard of different design at SNL. Investigations of the temperature dependence of the most widely used type of commercial leak indicate that conventional assumptions are incorrect. Work continues toward completing the documentation and demonstrating the accuracy required for establishment of an NBS leak calibration service in FY86.

SURFACE METHODS FOR NDE

L.J. Swartzendruber

Metallurgy Division

Institute for Materials Science and Engineering

This activity is involved with the development of procedures and standards for surface methods of NDE. The methods of magnetic particle testing, penetrant inspection, and Barkhausen noise analysis have been of particular interest.

MAGNETIC PARTICLE INSPECTION

A number of the results obtained previously in the area of magnetic particle testing have now been incorporated into a new military standard on magnetic particle inspection, MIL-STD-1949, which supersedes the Air Force document MIL-I-6868E, and the Army document MIL-M-11472 (actual preparation of the document was funded by AMMRC). The new standard includes a method for using Hall-effect probes or equivalent to determine proper magnetization levels for effective inspection. This is possible because we have shown, both theoretically and experimentally, that the tangential value of the H field at the surface of the part being inspected is the primary factor which determines the magnitude of the leakage field from a defect of a given size. Previously it had been assumed that optimum results would be obtained when the value of B/H was a maximum, thus making the best value of applied field very difficult to measure and strongly dependent on the material under test. Our results have shown that, for the majority of materials, the optimum applied fields drive the material well into the saturation region. In this case the material properties are of secondary importance for determining the optimum applied field. Correctly instrumented Hall probes can then be used to test for proper magnetization when using either alternating or direct currents.

Another important factor in improving standards for magnetic particle inspection is testing of magnetic inks and powders for proper physical characteristics, including particle size, shape, and magnetic properties. Current specifications, both in the existing ASTM document, and in the Military Standard are inadequate in this regard. Future work will be concerned with improving this area, primarily in cooperation with the ASTM subcommittee.

DYE PENETRANT TESTING

In the area of dye penetrant testing we have participated in designing and conducting a round-robin test of three proposed new ASTM dye penetrant documents (this was done in cooperation with J.J. Hsia and K.L. Eckerle of the Radiometric Physics Division, Center for Radiation Research). The round-robin results for one of these draft documents were considered encouraging enough to warrant submission for subcommittee balloting. Results for the other two documents, one for measuring thermal stability and the other for measuring ultraviolet radiation stability, appeared unacceptable. Improvements of the techniques spelled out in these two documents and a new round-robin are in the planning stage. This work has pointed out the considerable importance for a strong effort at NBS to provide a mechanism for the calibration of the ultraviolet intensity meters used in NDE and for providing standards against which the fluorescence of dye penetrants (and magnetic inks) may be compared.

BARKHAUSEN NOISE ANALYSIS

Because of the potential need for standards and specifications in the field of Barkhausen noise NDE, an evaluation of this field, its applications, and possible requirements for specifications and standards, is being conducted. Although the field of Barkhausen noise is an old one, serious efforts on NDE applications appear to have started around 1975 with the design of commercial apparatus by the Southwest Research Institute in the United States, by the Technical Research Center in Finland, and by a number of groups in the USSR. Barkhausen noise analysis on metals using inductive sensors is basically a surface technique, being most sensitive to material within approximately 0.3 mm of the surface. A number of studies have shown that Barkhausen noise from deeper regions in a metal can be observed by sensing the acoustic emission which accompanies a Barkhausen discontinuity. This has also been called "magnetomechanical acoustic emission" and is due to the presence of magnetostriction. Although this technique is generally less sensitive than the inductive method, it can be expected to have a number of specialized applications.

Barkhausen noise analysis (BNA) has been shown to be correlated to various material properties including grain size, hardness, internal stress, and microstructure. It has also been suggested that BNA could be used for flaw detection. Besides its evident application in quality control of magnetic material such as silicon steel and ferrites, one of the most interesting possibilities for BNA is in automated on-line testing in a steel mill, heat treating plant, or similar facility.

Several important principles can be enunciated concerning BNA. First, since BNA utilizes a magnetic property of the material, its characteristics will be sensitive to microstructure, internal stress, etc., in a manner similar to other magnetic properties such as coercive force and remanence. Measurement of magnetic properties is a well established method for the NDE and quality control of steel and some other materials. However, in many cases, the sample geometry prevents effective measurement of such properties as the coercive force and, especially, its variation from place to place on a large sample. In this situation BNA can be used effectively. As with many magnetic properties, changes in the Barkhausen noise spectrum result from a number of causes; if several material properties change simultaneously, poor correlation with the Barkhausen noise spectrum and the selected property may result. To carry out BNA it is desirable to sweep repetitively through the hysteresis loop of the material. Of primary interest is the frequency at which this is accomplished. At all but the very lowest frequencies, noise comes in "bursts" with sizes that vary with frequency. Thus, the power density spectrum is a function of the fundamental frequency with which the hysteresis loop is swept. It is generally necessary to keep this frequency below 1000 Hz. Correspondingly, a crucial factor in effective BNA is the design of the probes used to sweep the hysteresis loop, the pickup coils used to sense the noise, and the method by which the noise spectrum is analyzed and correlated to material properties.

There appear to be two important areas where NBS might make a contribution to the field of NDE using Barkhausen noise. One is in the area of coil characterization, and the other the provision of reference materials with well characterized noise spectra which could be useful for system comparison and calibration.

SUMMARY

In cooperation with the Watertown Materials and Mechanics Research Center, a new standard for magnetic particle inspection has been issued. In cooperation with ASTM, a Round Robin in support of a new dye penetrant document was completed. An evaluation of Barkhausen noise NDE was undertaken and possible NBS input areas suggested.

FERROGRAPHIC STUDY OF WEAR DEBRIS

A. W. Ruff

Metallurgy Division

Institute for Materials Science and Engineering

This research has progressed to the point of identifying a primary limitation of the accuracy in the technique of wear particle analysis called ferrography. The technique extracts wear debris from lubricating fluids, or other liquids such as hydraulic fluids, by passing samples through a magnetic field gradient in a specially designed instrument. The ferromagnetic particles are removed from the fluid by the field and caused to deposit on a glass substrate so that they can be subsequently analyzed. The method accomplishes a size separation during the deposition step. The particles can then be microscopically studied in any of several ways. A valid method for handling specimens from the as-received stage as liquid samples to the final stage as particle deposits on the substrate has been developed by a group of interested laboratories. These include the Air Propulsion Lab at Wright Patterson Air Force Base, the Tri-Services Oil Analysis Lab at Pensacola, Florida, the University of Missouri, the Michigan Technological University, and NBS. A method was also proposed to measure the density of deposited particles using optical densitometry. In a series of inter-laboratory comparisons, it was found that the different laboratories disagreed on particle deposit density by as much as 50%. The problem was identified to result from the lack of a method to calibrate the optical densitometer at points other than the two end points, 0% transmission and 100% transmission. NBS has been working on a stepped density plate to be used to calibrate the densitometers used at the laboratories. A prototype plate has been used here with success. However, there has not yet been agreement among the users on either the method to follow or the calibrating specimen to use. A related problem concerns the fact that some operate their densitometer in transmission and others in reflection; this choice determines the nature of the density calibration specimen. Discussions have moved at a slow pace this year in part because of changes of several key personnel at the other laboratories. Plans for next year will continue to follow the path of seeking agreement on a density calibration scheme at least among the principal laboratories.

SUMMARY

A method has been developed to calibrate the density measuring instrument used in ferrographic analysis of wear debris particles. The method is being proposed for widespread use among oil analysis laboratories.

NDE OF CORROSION - GUN BARRELS AND AMMUNITION

A. C. Fraker and A. W. Ruff

Metallurgy Division

Institute for Materials Science and Engineering

The goal of this work is to prepare procedural documents for nondestructive evaluation of corrosion of gun barrels and ammunition. The project is supported by the U.S. Army Materials and Mechanics Research Center, Watertown, Massachusetts. The progress of this past year consists of a further evaluation of the problem and the development of a draft outline for preparing the document for the nondestructive evaluation of the corrosion of ammunition. The corrosion of gun barrels and that of ammunition are considered separately due to the nature of the problems and the need for simplification. Some time was spent visiting ammunition depots and reading reports to get a better understanding of the problem. It is clear that the development of the document for the nondestructive evaluation of corrosion of ammunition would be cost effective and would have the added benefit of providing a standard for increased quality assurance. Nondestructive evaluation of corrosion of ammunition is conducted using visual methods and occasionally, x-radiography. Both of these methods are able to detect corrosion after considerable damage has been done, but they cannot detect the early, initial stages of corrosion. Descriptions of the types of corrosion which occur with different materials and varying circumstances will be helpful for the inspection of ammunition and for early detection of corrosion. The types of corrosion which can be expected to occur with ammunition have been identified, and the draft outline for the NDE document is based on these forms of corrosion.

The types of deterioration which will be evaluated are (1) the condition of painted or coated surfaces, (2) pitting or localized corrosion, (3) stress corrosion, and (4) hydrogen embrittlement. Reference documents cited include military documents, ASTM specification, and NBS reports. Written documentation will be provided to describe materials, exposure conditions and evaluation results. Corrosion damage evaluation will be made based on the materials, their use and one of the four relevant types of corrosion. Expansion of this outline to a more detailed document is in progress now. Test coupons could be packed with ammunition to assist with NDE measurements of initial corrosion and to aid in the development of NDE techniques for corrosion evaluation.

SUMMARY:

The accomplishments of the project for 1985 include an assessment of the procedures of ammunition inspection and ammunition storage and the development of an outline for the nondestructive evaluation of corrosion document.

II. NDE METHODS FOR INTERNAL FLAW CHARACTERIZATION

The work in this section deals with improving or developing new NDE techniques for quantitative flaw evaluation in order to determine suitability and reliability for specific applications. The first group of six reports emphasizes research on measurement methods and the second group of five reports focuses on NDE of specific materials such as concrete, steel and copper. There are several notable advances reported in the section. Two research reports deal with signal inversion for acoustic emission data and another reports on standard methodology for NDE data analysis and assessment of data reliability along with design of a prototype archival computer data base.

ACOUSTIC EMISSION IMAGING

Stephen J. Norton and Melvin Linzer

Metallurgy Division

Institute for Materials Science and Engineering

In ultrasonics, numerous techniques exist for enhancing the signal-to-noise ratio (SNR) of the ultrasonic signals at the receiver, such as increasing the source power or signal averaging. In processing acoustic emission signals, such signal enhancement methods are not possible, and traditional source location techniques based on signal thresholding will fail if the source signals are close to or below the receiver noise.

During the past year, we have continued an investigation into a new inverse-source technique for reconstructing images of random source distributions which, to a considerable extent, overcomes the problem of extracting source information when the receiver signal-to-noise ratio is low. Signal enhancement is achieved by using an array of detecting transducers, and by cross-correlating the emitted source signals recorded at all transducer pairs. An image of the distribution of the source intensity is then obtained by filtering the cross-correlated signals in an optimal fashion and then appropriately summing the filtered signals in the image plane. The filtering and summation operations are similar in principle to the well-known filtered-backprojection algorithm used in medical x-ray tomography. Backprojection, here, refers to the process of adding the signals at each point in the image plane to achieve constructive addition at points where sources exist and cancellation at points where no sources exist. The result is a reconstructed image of the source distribution. We have shown that the point-spread-function of the image reconstruction algorithm can be analytically derived for the case of random and spatially-incoherent sources. Under the latter assumptions, the imaging approach is linear in source intensity and is capable, in principle, of reconstructing quantitative images of extended and complex source intensity distributions. The spatial resolution in the source image is determined by the bandwidth of the emitted radiation.

Under some conditions, acoustic emission signals generated by phase transformations or microcracking may approximately satisfy the assumption of spatial incoherence, and the above technique should be applicable in such cases. Simulations have also indicated, however, that good results may be possible even when the assumption of spatial-incoherence does not hold. This opens the possibility of using the algorithm as a method of crack detection and location.

Work this year has included a completion of the formal analysis, as well as computer simulations of source reconstructions, in which a single experimentally-recorded acoustic-emission waveform was used to simulate multiple signals. As one example, we considered a simulated reconstruction under conditions of significant receiver noise (SNR = 0.5). Figure 1 shows a recorded acoustic-emission signal with no receiver noise, and figure 2 shows the same signal after adding broadband Gaussian noise to achieve a SNR of 0.5. Figure 3 shows a reconstruction of a two point source distribution derived from 32 simulated received signals recorded by 32 hypothetical transducers with uncorrelated noise added to each signal to create a SNR = 0.5. Both sources are clearly discernible in the reconstruction, even though the individual signals are essentially invisible in the receiver noise (figure 2).

This approach may have the potential to radically improve the reliability of acoustic emission monitoring of crack growth in ductile steels where signal amplitudes are often very low and background noise often unavoidably high.

SUMMARY

In summary, we have this past year completed the theoretical development of a new inverse-source reconstruction technique, and demonstrated the resulting reconstruction algorithm by means of numerical simulations. Using an experimentally-recorded acoustic-emission signal, the simulations have shown, as predicted, that the algorithm is capable of reconstructing images of sources whose emitted signals are buried in significant receiver noise.

REFERENCE

S. J. Norton and M. Linzer, Backprojection Reconstruction of Random Source Distributions. J. Acoust. Soc. Amer. (to be submitted).

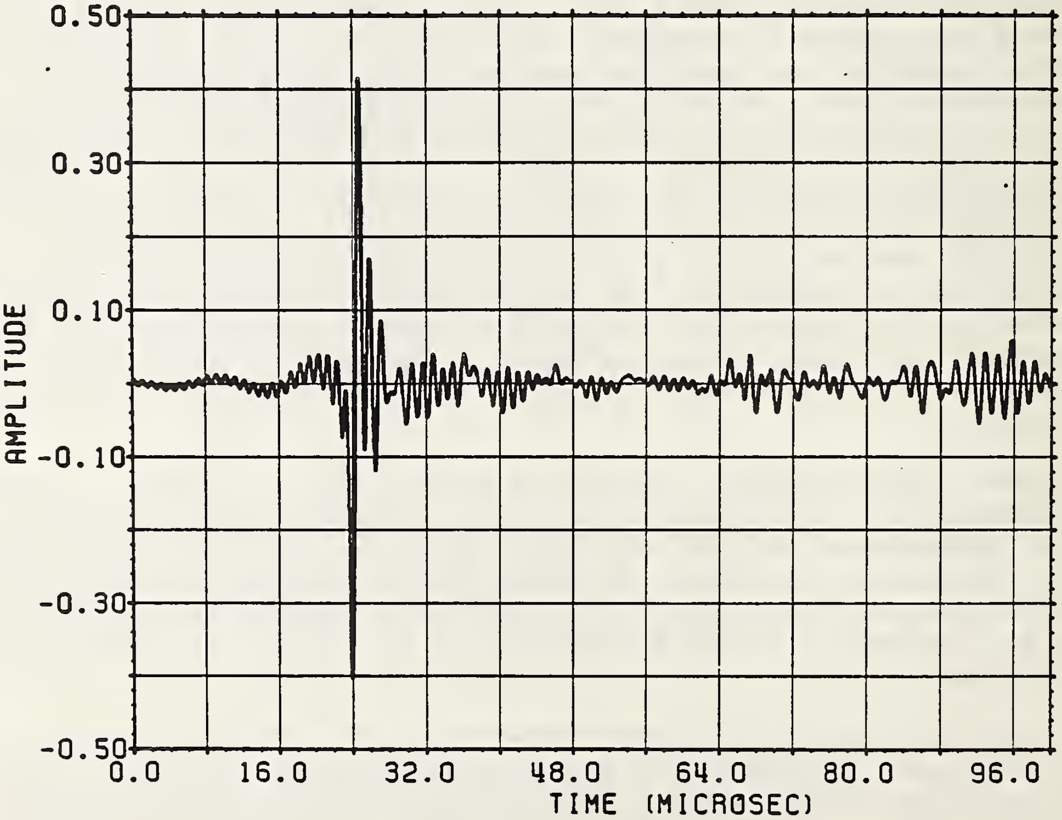

Figure 1. Experimentally-recorded acoustic-emission signal created by breaking a glass capillary on the surface of a steel plate.

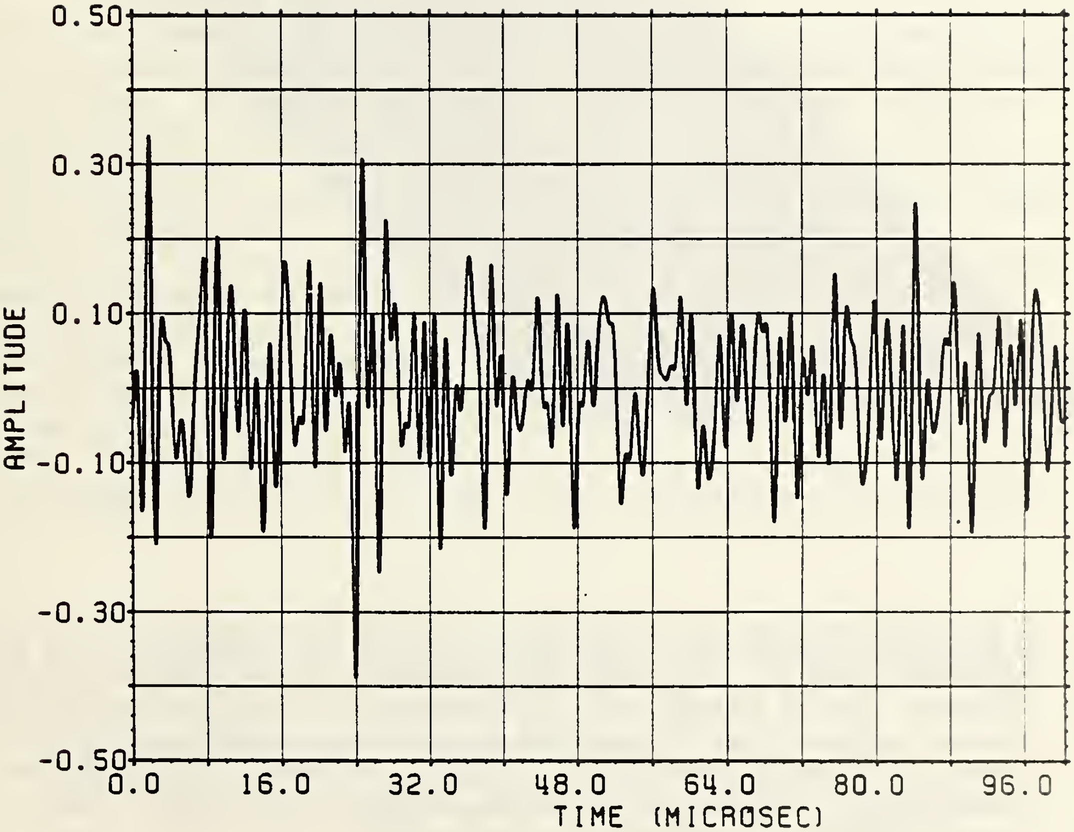

Figure 2. The acoustic-emission signal of figure 1 with broadband, Gaussian noise added (SNR = 0.5).

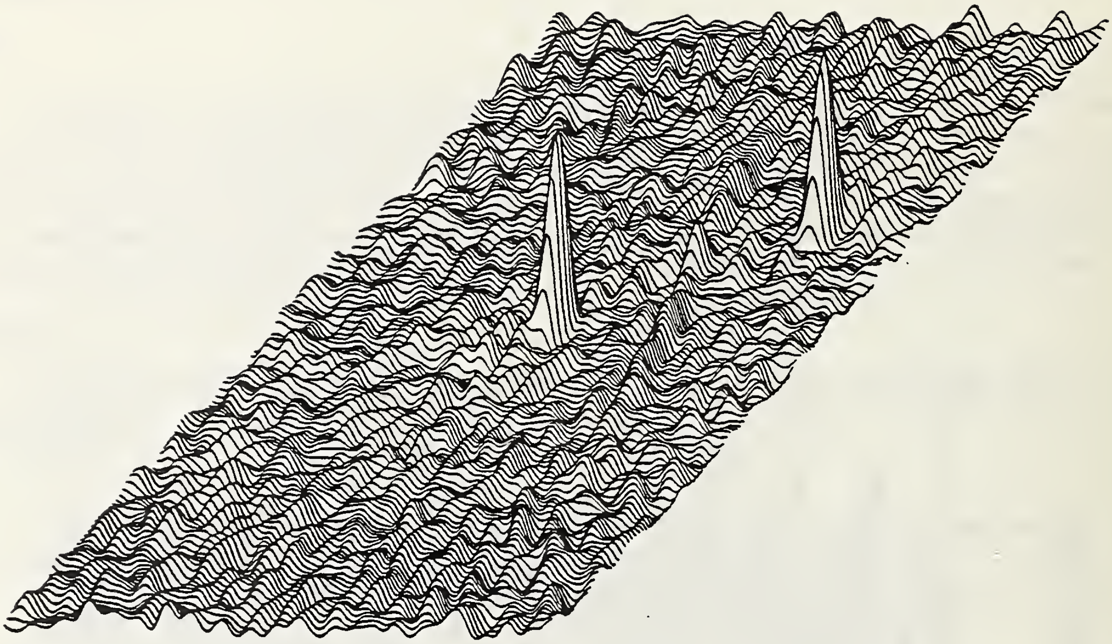

Figure 3. Reconstruction of two point sources using 32 simulated noisy acoustic-emission signals. The algorithm assumed 32 hypothetical transducer elements spaced around the circumference of a circle enclosing the source region. The 32 received signals were simulated by delaying the acoustic-emission waveform of figure 1 and adding uncorrelated, broadband noise, yielding the 32 noise-contaminated signals (each of which being similar in appearance to figure 2).

EXPERIMENTAL GREEN'S FUNCTION AND THE INVERSE PROBLEM

N.N. Hsu, T.M. Proctor and D.G. Eitzen
Mechanical Production Metrology Division
Center for Manufacturing Engineering

and

A. Carasso
Mathematical Analysis Division
Center for Applied Mathematics

INTRODUCTION

The detected Acoustic Emission (AE) signal contains the information about the source, the sensor, and the structure, all mixed together through complicated convolutions. If the sensor transfer function is known and if the details of how the waveform evolves in the structure are known then the detected AE can be predicted by the source waveform and the source waveform may be derived from the detected signal. To know the sensor transfer function, absolute calibration of the sensor is required. To know how the waveform evolves in the structure, however, we have to solve the transient wave propagation problem in detail. The present project is centered on developing techniques to solve the transient wave propagation problem in arbitrary structures by the combination of controlled experiment and digital signal processing. In other words, we are formulating a procedure to determine experimentally the impulse response, represented by the Green's function, of an arbitrary structure. Once the impulse response of the structure is known, AE produced by different sources can be predicted and interpreted.

DISCUSSION

The Green's function is a complete representation for transient wave propagation in a structure due to a point force. For acoustic emission the detected voltage signal, $V(t)$, can be considered the convolution of three time functions: $F(\underline{x}_o,t)$, the source waveform at location $\underline{x}_o$;
$G(\underline{x}_o,\underline{x},t)$, the Green's function for the structure and a fixed configuration with detector at $\underline{x}$ and source at $\underline{x}_o$;
$T(t)$, the transfer function for the receiving transducer.
Letting "*" denote the convolution integral,

$$V = T*G*F.$$

At least in principle, the Green's function of a complex structure can be determined through this formulation if both the source and the transfer function of the sensor are known and if the deconvolution problem can be solved.

Recently we reformulated the problem and developed a new procedure specifically designed for the experimental determination of Green's functions[1,2]. The key to this reformulation is recognizing that the source/sensor are subject to design. We assume that a simulated source is generated by a transducer with transfer function T' acted upon by a voltage pulse V_o. Thus

$$F = T'*V_o$$

and the received voltage becomes

$$V = T*G*T'*V_o.$$

Let

$$L = T*T'*V_o.$$

L represents those functions over which we have control through the design of the sending and receiving transducers and the probing voltage waveform. The received voltage becomes

$$V = L*G.$$

In order to determine G we must solve this equation with measured V and "known L" - a typical ill-posed deconvolution problem. The key question is: what waveform for L will allow an optimum solution for G. We have found one probing waveform which allows us to solve for G systematically and with a good estimate of the errors in G resulting from errors in the measured V. This probing waveform is the inverse Gaussian function, K(σ,t), given by

$$K(\sigma,t) = \frac{\sigma}{2\sqrt{\pi t^3}} e^{-a^2/4t}.$$

K may be considered a special approximation to a Dirac-delta function in which the positive constant σ controls the duration of the probe waveform. Taking L to be an inverse Gaussian function, the problem of determining G has been changed over to one of solving a convolution integral with an inverse Gaussian kernel, a problem for which some powerful tools have been developed. These include partial deconvolution and a strong error estimate[1].

We are now testing this deconvolution technique. The first tests were numerical simulations. The test signal was the calculated surface displacement which would occur if a point force inverse Gaussian waveform were imposed on a plate. This test signal is then deconvolved to obtain an estimate of the Green's function which is compared with the exact Green's function. Figure 1 shows an example for a source and receiver on opposite sides of a plate and two thicknesses apart. The top trace is the test signal (calculated displacement), the middle trace is the estimate of the Green's function obtained by deconvolution and the bottom trace is the exact Green's function.

Encouraged by these results we have begun to test the procedure experimentally. From the definition of L given above, the practical importance of high-fidelity transducers becomes evident. For "perfect fidelity" transducers, the transfer functions T and T' would be "unity". In this case, our desire to probe with L=K only requires that the driving voltage pulse V_o be an inverse Gaussian. Even though the NBS conical transducers are very high fidelity, corrections are necessary to perform the deconvolution.

Experimentally, we have made use of two NBS conical transducers on a plate; one transducer is used as a source, the other as a receiver. A digital to analog waveform generator is programmed with an inverse Gaussian function. The low voltage waveform is amplified using an high power amplifier, developed at NBS, which drives the source transducer. The resulting displacement-time history is measured with the second conical transducer. Since T and T' are not unity for the conical transducers, the transfer functions for the transducers must be accounted for. (An alternative procedure would be to modify V_o to account for T and T' so that L is more nearly inverse Gaussian.) T*T' is accounted for by independently determining the impulse response of the transducer pair using the exact deconvolution available at epicenter[3]. With the transducers transfer function accounted for, the measured displacement is subject to the general deconvolution procedure. An encouraging preliminary result is shown in Figure 2. The curve represents the experimentally obtained Green's function for the sensor and source on opposite sides of a large plate directly facing each other. The experimentally determined curve has the details of the jumps and inflections which match extremely well the known theoretically computed one.

Refinement of the technique such as further improvement of the transducers and amplifiers are underway. However, to simplify the experimental procedure for data acquisition and processing still requires considerable work.

SUMMARY

A procedure to determine experimentally the impulse response of an arbitrary structure is being developed. The concept involves two novel ideas: (1) the theoretical formulation of a probing waveform which facilitates the deconvolution process; (2) the design and construction of a system, a transducer pair together with high speed digital to analog conversion and power amplifier, which introduces a pulse of specified waveform and detects the propagated transient wave without loosing fidelity. Results are encouraging and further tests are in progress.

REFERENCE

1. Alfred S. Carasso and Nelson N. Hsu, "Probe Waveforms and Deconvolution in the Experimental Determination of Elastic Green's Functions," SIAM J Appl. Math 45, No. 3, pp 369-382 (June 1985).

2. D. Eitzen, N. Hsu, A. Carasso and T. Proctor, "Deconvolution by Design - An Approach to the Inverse Problem of Ultrasonic Testing," Review of Progress in Quantitative NDE 4A, pp 179-188 (1985).

3. N. Hsu and S. Hardy, "Experiments in Acoustic Emission Waveform Analysis for Characterization of AE Sources, Sensors and Structures," Elastic Waves and Non-Destructive Testing of Materials AMD-29, Y.H. Pao, ed., ASME, NY.

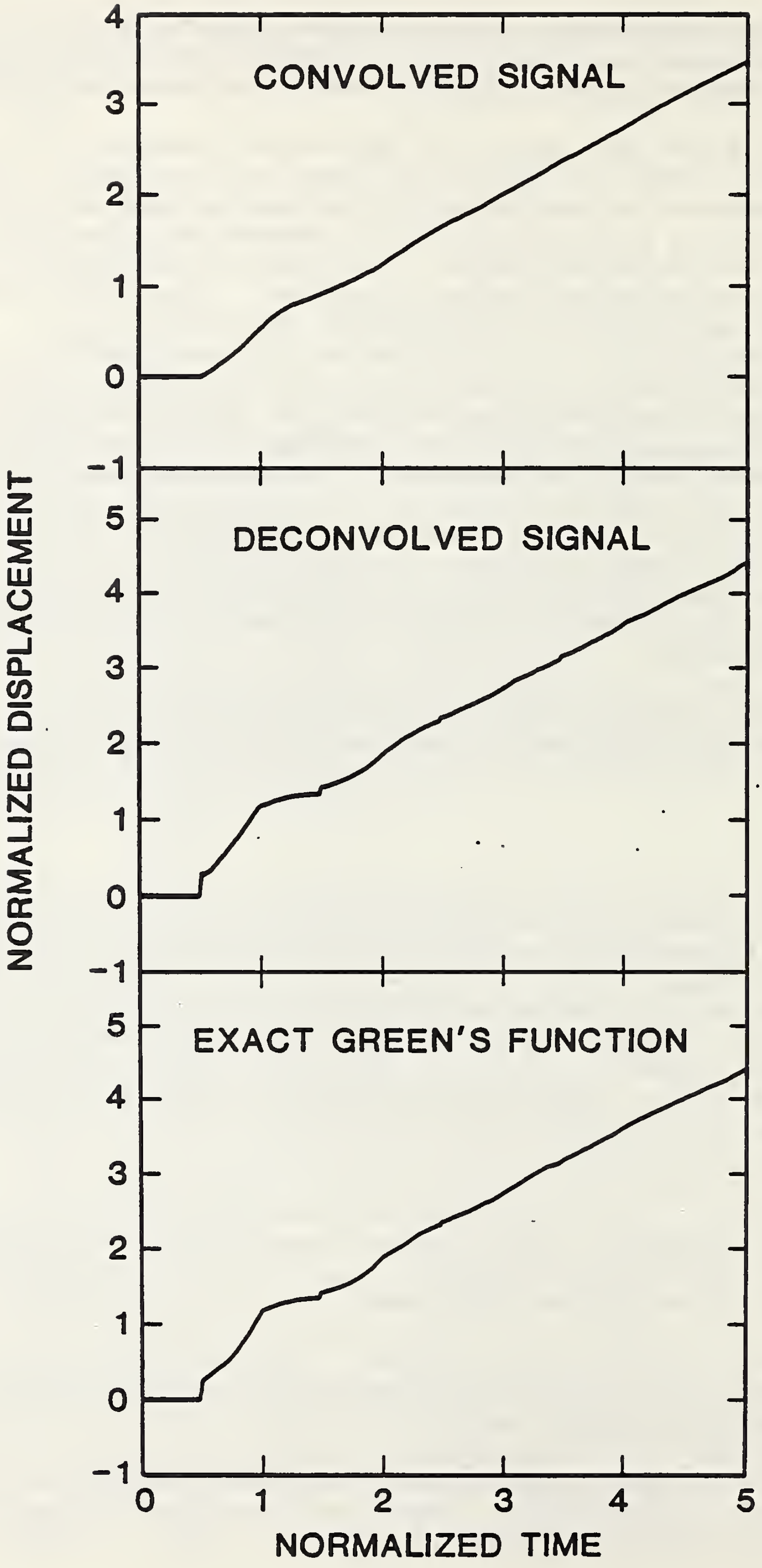

Figure 1. Deconvolution of epicentral response; Heaviside time dependence.

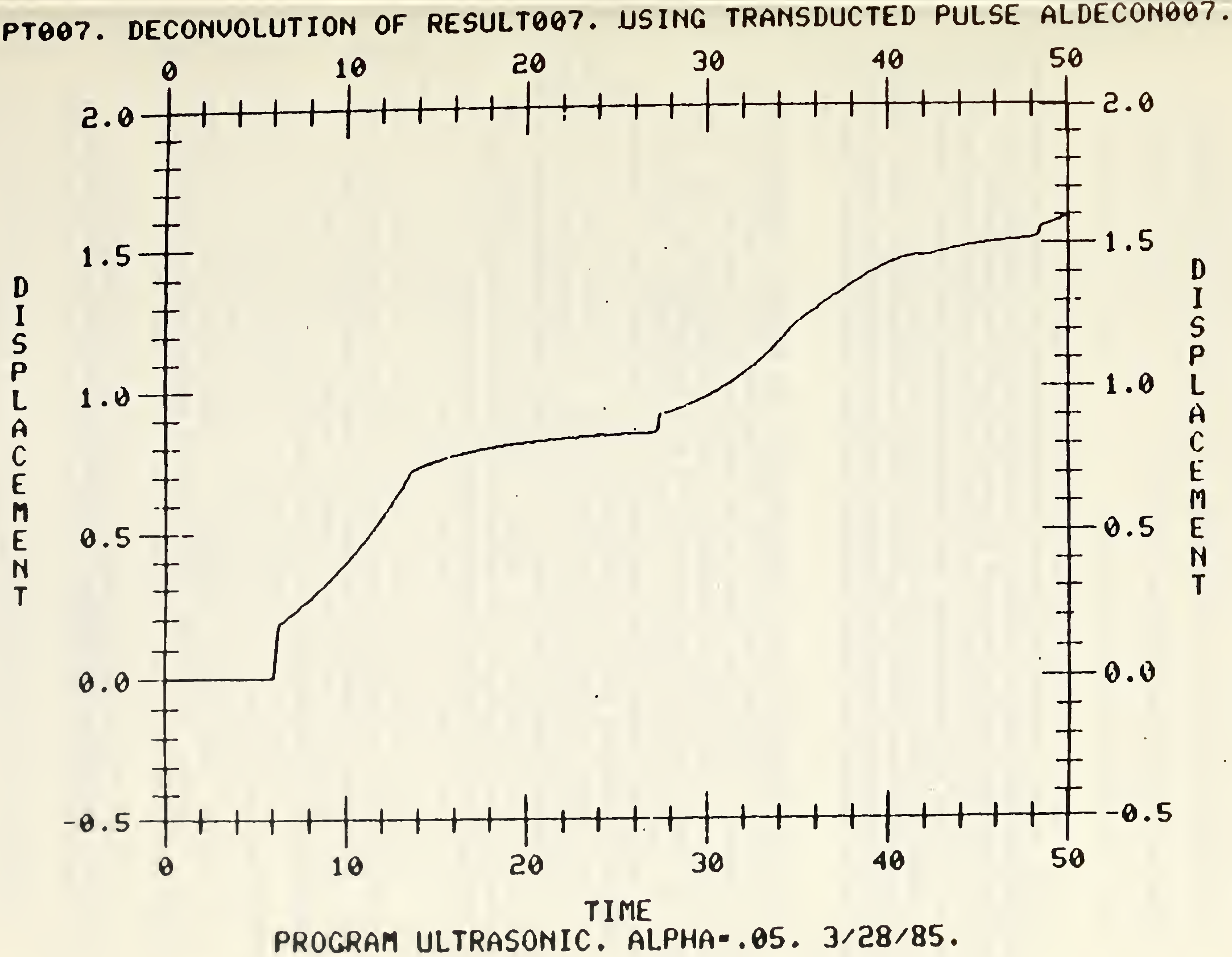

Figure 2. Estimated Green's function using measured signal.

ULTRASONIC POINT SOURCE: THE NBS CONICAL TRANSDUCER AS A DRIVER

T.M. Proctor, N.N. Hsu, and S.E. Fick

Mechanical Procduction Metrology Division

Center for Manufacturing Engineering

The NBS conical transducer[1,2] is an important tool for measuring dynamic, normal surface displacements because of its sensitivity and high fidelity. Reciprocity suggests that it may also be a useful tool for generating prescribed point source ultrasonic waveforms. Conical transducers are being evaluated for this application with very promising results to date. In addition to permitting the prescription of arbitrary waveforms, the approach offers the advantages of repetitive signals over the Breckenridge (cappillary) and Hsu (pencil) sources which are single, transient events. The repetitive signals can be enhanced by signal averaging and more easily displayed upon receipt.

Initial experiments have been performed with two conical transducers on a plate. The desired voltage time waveform is programed into a digital-to-analog converter. This output feeds an NBS developed high power amplifier which drives one of the conical transducers with a voltage pulse of up to 850 volts. The second conical transducer is used as a calibrated receiver to measure the resulting displacement. With the two transducers on epicenter, the exact epicenter deconvolution developed by Hsu has been used to determine the transfer function of the transducer pair.

It is expected that this approach will be used in the experimental determination of unknown Green's functions. With further development conical sources might also be useful in the primary calibration of AE transducers by the surface pulse and through pulse methods; the latter method will require signal averaging to obtain an acceptable signal to noise ratio.

SUMMARY

The NBS conical transducer is extremely useful as a high-fidelity receiver. Preliminary tests indicate that is is also useful as a high-fidelity point source driver and may become an important tool in AE as a simulator and in ultrasonics as a tailored transmitter.

REFERENCES

1. T. M. Proctor, "NBS Conical Transducer: A Quantitative Acoustic Emission Sensor," Technical Activities 1981-Office of Nondestructive Evaluation, H. Berger and L. Mordfin eds., NBSIR82-2449, 23-27, (Dec. 1981).

2. T.M. Proctor, "Further Development of the NBS Conical Transducer." Technical Activities 1982-Office of Nondestructive Evaluation, T. Yolken ed., NBSIR82-2617, 20-24, (Dec. 1982).

THEORETICAL STUDIES OF ACOUSTIC SCATTERING

Raymond D. Mountain

Thermophysics Division

For the last few years, this work has been concerned with the development of moment relations for acoustic scattering data. These studies have lead to some new insights into the relationship between transient (time domain) and steady-state (frequency domain) measurements and thereby into how measurements made in these two domains are related. This was accomplished within the framework of the Born approximation by first expressing the steady-state scattering by an isolated scatterer in terms of a set of volume moments of the scatterer. Next, we examined the time domain scattering by the same scatterer and recognized that moments in time of the amplitude of the scattered signal involved the same volume moments of the scatterer.

This analysis leads to the effective size, a, of the scatterer being given as

$$a^2 = 10\nu^2 R_4/R_2$$

where ν is the sound speed in the material and R_2 and R_4 are the second and fourth time domain moments of the amplitude of the scattered signal provided that the time origin is the instant the incident wave passes through the center of the scatterer.[1]

We have used measurements made by G. Blessing to assess the utility of this relationship. We find that its domain of applicability lies in a region which is difficult to realize experimentally. There exist in the literature, other schemes which employ the Born approximation to obtain size and shape information.[2] However, these procedures involve additional approximations and assumptions[3] which we have not included in our rigorous application of the Born approximation to moment relations.

We anticipate that this type of analysis will be useful in other areas of interest to the NDE community, such as thermal wave studies, by clarifying the connections between steady-state and transient measurements and through the development of specific procedures for analyzing measurements.

REFERENCES

1. R.D. Mountain and G. Birnbaum, "Scattering of sound waves by inhomogenieties: Time domain analysis", Nondestructive Testing Communications 1, pp 219-225 (1984).

2. D.K. Hsu, J.H. Rose and D.O. Thompson, "Reconstruction of inclusions in solids using ultrasonic Born inversion", J. Appl. Phys 55, pp 162-168 (1984).

3. G.J. Gruber, G.J. Hendrix and T.A. Mueller, "Exploratory Development for a High Reliability Flaw Characterization Module", Technical Report No. AFWAL-TR-84-4172, Materials Laboratory, Air Force Wright Aeronautical Laboratories, Air Force Systems Command, Wright-Patterson Air Force Base, Ohio 45433, March 1985.

DESIGN OF AN X-RAY CAMERA USING A CCD SENSOR.

Richard Spal and Masao Kuriyama

Metallurgy Division

Institute for Materials Science and Engineering

This report describes the design of an x-ray camera using a commercial CCD (charge coupled device) area sensor for direct detection of x-rays with energies of about 10 kev. X-ray cameras may be classified as direct or indirect detection devices. A direct detection camera detects the electric charge produced when x-rays strike a photoconductor, while an indirect detection camera detects the visible light rays produced when x-rays strike a phosphor. The latter detection scheme is called indirect since the visible light rays must still strike a photoconductor to produce an electric charge. This scheme has the disadvantages that the spatial resolution is controlled by the phosphor thickness, and the sensitivity is controlled by the efficiency of converting x-rays to visible light rays (typically about 10 percent). While the sensitivity can be improved by inserting an image intensifier after the phosphor, this further degrades the spatial resolution. In comparison, current direct detection cameras based on the x-ray vidicon tube have superior spatial resolution but inferior sensitivity. A direct detection camera based on a CCD area sensor should have spatial resolution comparable to the x-ray vidicon, but much better sensitivity. The resolution is controlled by the CCD photosite size, which is currently as small as 15 by 15 microns for one commercial area sensor. The sensitivity is controlled mainly by the photosite dark current. Since the sensor is small, it is practical to cool it to reduce the dark current enough to detect single x-rays. These advantages of spatial resolution, sensitivity, and size promise to make the device useful for NDE radiography and synchrotron radiation topography.

The CCD image sensor has a rectangular array of square pixels with 490 rows and 328 columns. The pixel dimension, and the center to center distance between pixels, is 24.4 μm. Half of the rows are used for image integration, and the rest for image storage. The integration period may vary from 1/60 sec to about 10 minutes. At the end of the integration period, the charge accumulated in the image integration region is rapidly transferred to the image storage region. During the next integration period, rows of charge in the storage region are shifted through the storage region into a serial register, and charge packets in the serial register are shifted through the serial register to an output amplifier. The output contains a signal component, a clock component, and a dark current component. The output is processed to remove the clock and dark current components, and is converted to a video signal. A commercial frame grabber stores the video signal, and drives a TV during the integration period. Below is a detailed description of the timing and signal processing circuitry.

A block diagram of the timing circuitry is shown in figure 1. A system clock, running at 14 MHz, drives a TV sync generator, the parallel image and storage area clocks, and the serial register clock. The TV sync generator provides horizontal reset (HRST), vertical reset (VRST), and composite sync (CSYNC) signals. The parallel image area clock (ϕ_{PI}) provides a 1 MHz pulse train of 245 pulses to transfer rows of charge through the image region to the storage region. It is activated by VRST, and inhibited by an integration signal (INTGRT) which controls the integration period. Similarly, the parallel storage area clock (ϕ_{PS}) provides a 1 MHz pulse train of 245 pulses, activated by VRST and synchronized with ϕ_{PI} to transfer charge through the storage region. In addition, ϕ_{PS} provides a single pulse, activated by HRST, to transfer a row of charge from the storage region to the serial register. Both ϕ_{PI} and ϕ_{PS} control drivers which must drive a CCD load of 10,000 pF between its high and low voltage levels in 200 nsec. The serial register clock (ϕ_S) provides a 7 MHz signal to transfer charge from the serial register to the output amplifier. It is inhibited by HRST, and controls a driver which must drive a CCD load of 100 pF between its high and low voltage levels in 20 nsec. The high and low voltage levels for the parallel image and storage regions, and the serial register, should be adjusted in the range of -2 to 6 volts for the high level, and -20 to -12 volts for the low level, in order to maximize the charge transfer efficiency.

A block diagram of the signal processing circuitry is shown in Figure 2. The CCD output is amplified and sampled by a fast sample and hold amplifier gated by ϕ_S. The first six pixels of each row, which are not exposed to radiation, are sampled again by another sample and hold amplifier, to determine the clock and dark current components of the CCD output. The outputs of the two sample and hold amplifiers are subtracted in a differential amplifier to get the signal component of the CCD output. The signal is converted to a video signal, captured by a frame grabber, displayed on a TV, and recorded by a tape recorder.

SUMMARY

In summary, we have described the design of an x-ray camera which should have a spatial resolution of about 25 microns and sufficient sensitivity to detect single x-rays. These specifications represent a significant improvement over currently available x-ray cameras. Construction of the camera is in progress, and comprehensive testing is planned.

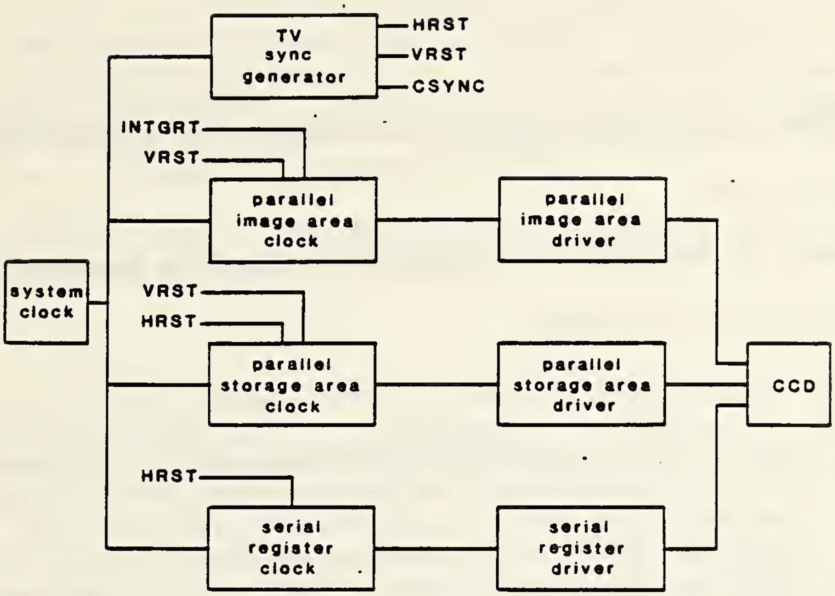

Figure 1 Timing Block Diagram

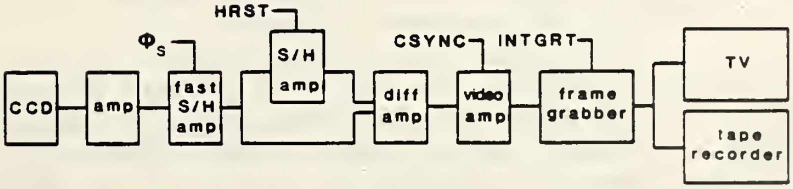

Figure 2 Signal Processing Block Diagram

LONG THERMAL WAVE IMAGING USING HOLOGRAPHIC INTERFEROMETRY

Charles M. Vest

Department of Mechanical Engineering and Applied Mechanics

The University of Michigan

INTRODUCTION

Prior to this year our work has emphasized the use of holographic interferometry as a nondestructive evaluation technique. Emphasis has been on evaluative review of the state-of-the-art of this technique, quantitative aspects of holographic NDE, simultaneous measurement of tilt and displacement, and flaw detection by moiré analysis of interferograms, including digitally-processed moiré patterns. During the present year we initiated investigation of visualization of thermal waves by holographic interferometry.

INVESTIGATION AND RESULTS

A thermal wave is the oscillating and diffusing temperature distribution induced in a material by an oscillating heat input at its boundary. Thermal waves induced by modulated laser beams have been used to image thickness and thermal diffusivity variations in thin objects. Frequencies typically are of the order of 10-100 Hz and specimen thicknesses are typically of the order of millimeters. Images are formed by scanning the object's surface and measuring the temperature amplitude or phase at each point.

In holographic NDE, steady or pulsed heat inputs have been used by several investigators as loading techniques. Holographic interferometry is then used to detect the response of the object's surface to this input and fringe anomalies indicate the presence of flaws.

Our work this year combines the fields of thermal wave imaging and holographic NDE. We have used very low frequency heat inputs (1 Hz or less) to stimulate long wavelength thermal waves in thin aluminum plates. We explored several holographic techniques to visualize the response of surface deformation to these waves. The best results were obtained by stroboscopic holographic interferometry. Fig. 1 is a schematic diagram of the system. Comparison of fringe patterns with those predicted by thermoelasticity clearly indicate that we have succeeded in detecting the oscillating part of the thermoelastic response. This technique therefore enables one to visualize the propagation of long thermal waves in the medium.

In the future we hope to use this technique to learn about the interaction of thermal waves with flaws, and to explore the possible uses of this technique for nondestructive evaluation. If successful, this would lead to a whole-field, analog NDE method. That is, by its very nature, the thermal response is obtained by parallel processing, as opposed to the point by point scanning used in normal photothermal imaging.

A paper in which this work is reported will be presented at the 1985 annual meeting of the Optical Society of America.

SUMMARY

The propagation of long thermal waves in thin aluminum plates has been observed by stroboscopic holographic interferometry. Experimental results are in good agreement with thermoelastic predictions.

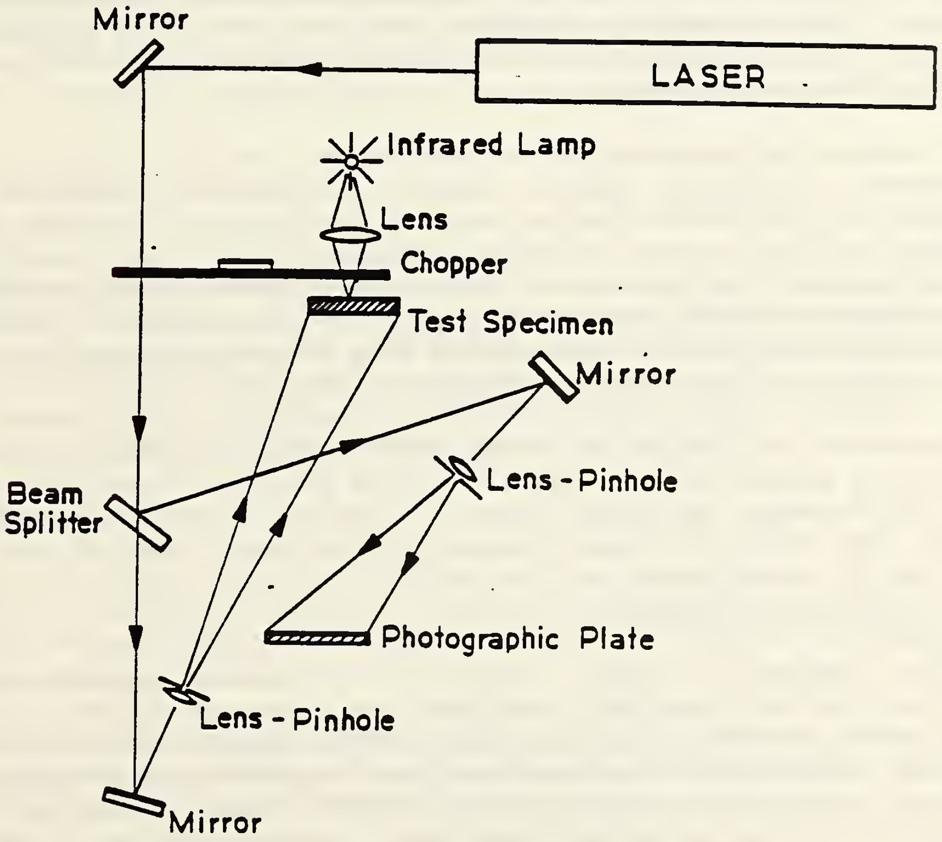

Fig. 1 System for visualization of thermal waves by holographic interferometry.

PULSE-ECHO METHOD FOR FLAW DETECTION IN CONCRETE

Nicholas J. Carino and Mary Sansalone

Structures Division

Center for Building Technology

Nelson N. Hsu

Mechanical Production Metrology Division

Center for Manufacturing Engineering

A cooperative effort between the Structures Division of CBT and the Mechanical Production Metrology Division of CME is focusing on the development of a pulse-echo technique for locating internal defects in concrete structures. The project aims to fill a major need related to the evaluation of existing structures - a necessary first step in repair and rehabilitation of structures. The pulse-echo method can fill this need if a fundamental understanding of wave propoagation in bounded, heterogeneous solids containing internal flaws can be achieved.

Past research has concentrated on developing a reliable point source - point receiver, pulse-echo system. Since a satisfactory transducer for sending pulses into concrete does not exist, an alternate technique was adopted which utilizes a short duration mechanical impact as a point source of spherical waves. The receiver is a broadband, conical, displacement transducer developed at NBS for acoustic emission measurements. Experiments and theoretical analyses have demonstrated that the impact technique can be used to accurately locate planar defects in concrete [1,2].

FY85 research has focused on 1) the development of a fieldworthy system which utilizes a spring-loaded, impactor with a spherical steel tip and a broadband, displacement transducer which is coupled to rough concrete surfaces using a thin lead sheet; 2) signal processing for simple and reliable flaw detection; and 3) experimental and analytical studies of defects within reinforced concrete structures.

Our first approach to signal processing is frequency spectrum analysis. Using the Fast Fourier Transform technique, the frequency content of both theoretical plate responses and experimental echo patterns obtained from concrete plate specimens has been studied as a function of the contact time of the initial elastic impact, the spacing between impact source and receiver, and the location of the reflecting interface. Characteristics of the frequency spectrum can be used to determine the contact time of the impact and the depth of the reflecting interface. For example, the maximum amplitude in the frequency spectrum is related to the depth of the reflector. In a time domain trace, such as that shown in Figure 1a which was obtained from a 0.5 m thick plate specimen, the depth of the reflector must be determined by identifying the arrival time of the first compression wave echo in the trace. The problem is that in the time domain, echo arrivals can be very difficult to identify accurately in bounded structures. However, the maximum amplitude in the corresponding frequency spectrum, which is shown in Figure 1b, allows easy and accurate determination of the depth of the reflector. For comparison, Figure 1c shows the frequency spectrum obtained from the time domain trace of a theoretical infinite plate response calculated for the same contact time and spacing between source and receiver as in the experimental trace.

Currently, we are carrying out experimental studies to deteminine the feasibility of detecting defects (cracks, voids, and honeycombing) within reinforced concrete structures. This experimental work is to be performed in conjunction with two- and three-dimensional finite element studies which will simulate wave propagation in bounded solids containing flaws. Results from a preliminary two-dimensional axisymmetric finite element analysis of a plate subjected to elastic impact are shown in Figure 2. The deformed meshes in this figure represent the displaced shape of the plate at 50 us and 125 us after initial impact. Studies such as these will provide an understanding of the interaction between stress waves and defects within bounded solids.

It is anticipated that the experimental and analytical studies of bounded reinforced concrete specimens containing defects will lead to field testing of the proposed pulse-echo system and eventually lay the groundwork for the development of a standard methodology for pulse-echo evaluation of concrete structures.

SUMMARY

The significant accomplishments of FY85 to date include progress toward the development of a fieldworthy pulse-echo system for concrete and the use of frequency spectrum analysis for simple and accurate flaw identification and depth determination. We anticipate that the remainder of the year will see the development of a methodology for interpreting signals obtained from reinforced concrete structures containing flaws.

REFERENCES

1. N. J. Carino, "Laboratory Study of Flaw Detection in Concrete by the Pulse-Echo Method," Proc. Int. Conf. on In Situ/NDT Testing of Concrete, Oct., 1984, Ottawa, Canada.

2. N. J. Carino, M. Sansalone, and N. N. Hsu, "A Point Source - Point Receiver, Pulse-Echo Technique for Flaw Detection in Concrete," Accepted for publication, April 1985, Journal of the American Concrete Institute.

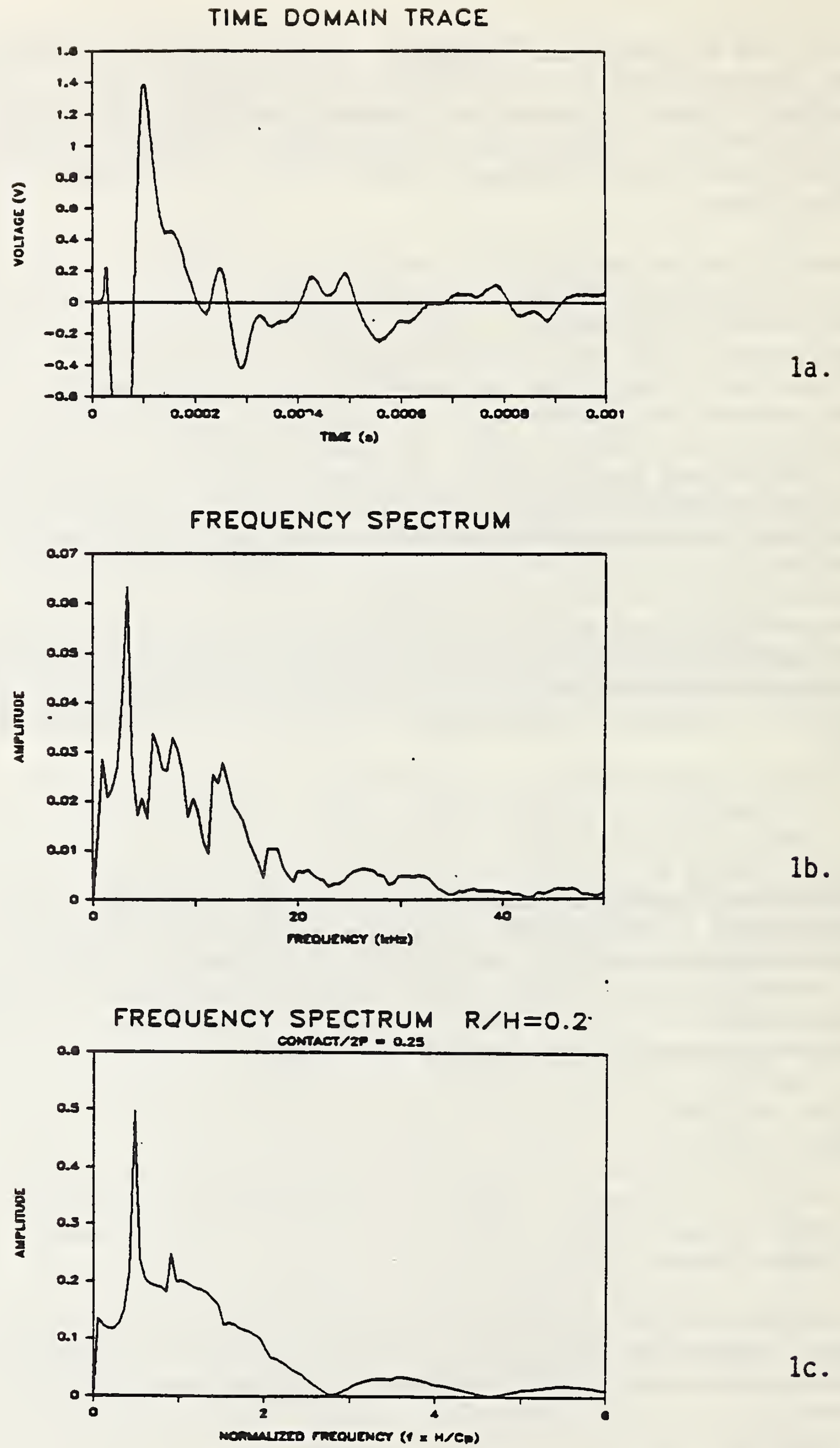

Figure 1. a) time domain trace obtained near the edge of a 0.5 m thick concrete plate specimen; b) frequency spectrum of trace in 1a; and c) frequency spectrum of a theoretical plate response which was calculated for the same contact time and source-receiver spacing as the trace in 1a.

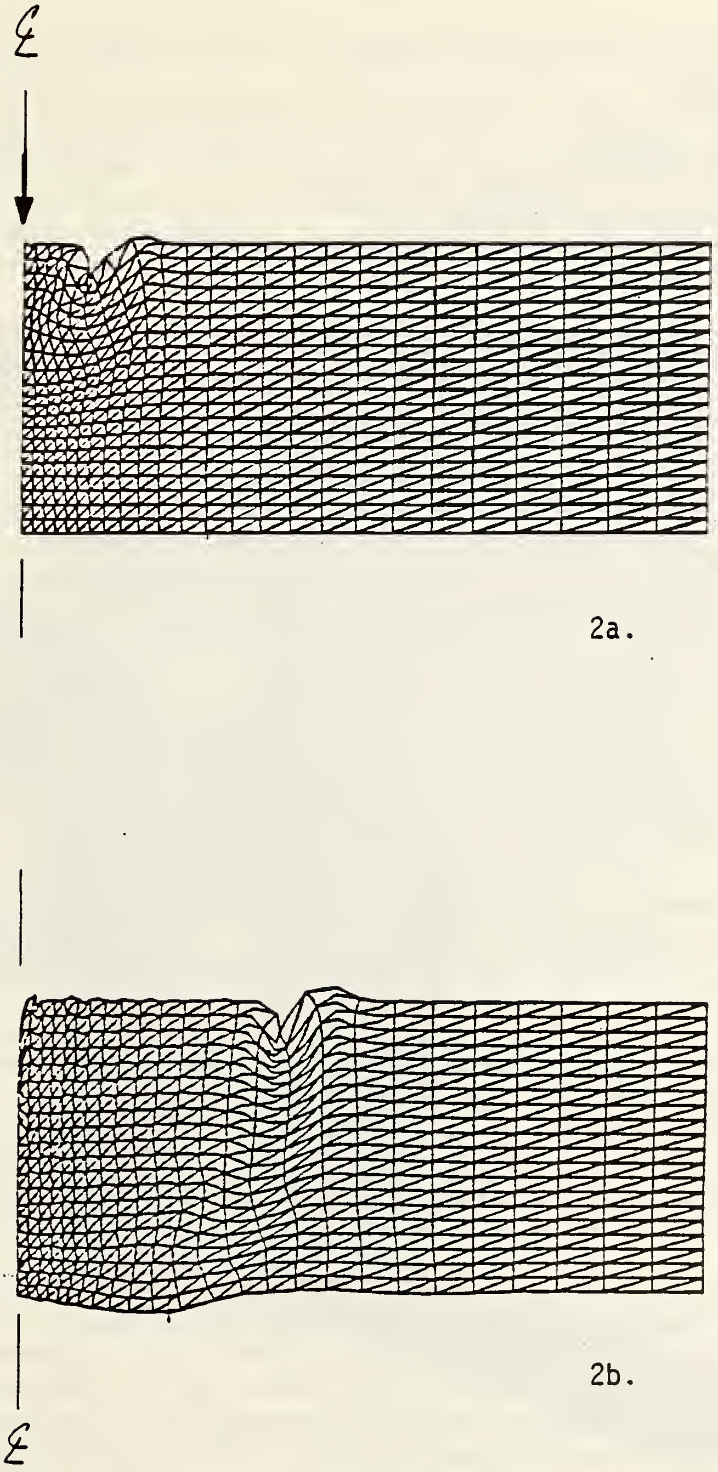

2a.

2b.

Figure 2. Deformed finite element mesh of a plate subject to an elastic impact at its center. a) deformed shape 50 us after impact; and b) deformed shape 125 us after impact.

TRANSDUCER DESIGN FOR ULTRASONIC TESTING OF HIGH ATTENUATION HETEROGENOUS COMPOSITE MATERIALS

N.N. Hsu and T.M. Proctor
Mechanical Production Metrology Division
Center for Manufacturing Engineering

and

N. J. Carino and M. Sansalone
Structures Division
Center for Building Technology

Techniques to evaluate high attenuation, heterogeneous materials such as concrete, polymeric composites, and porous ceramics are needed. Ultrasonic techniques for measuring velocity, moduli, or thickness changes, and echo detection could provide in-process control during fabrication as well as flaw detection information. Because such materials are heterogeneous, they are highly dispersive and absorbing. Traditional ultrasonic techniques are difficult to implement on such materials. Even for simple thickness or velocity measurements, through transmission techniques and the use of massive low frequency transducers are necessary to compensate for the high attenuation loss in such media. These techniques have poor sensitivity and resolution, and are awkward to use.

Based upon our previous laboratory test results, which are summarized in last year's report, we have taken a novel approach to the measurement problems commonly encountered in testing high attenuation heterogenous material. The basic concept consists of:

(1) use of a point impact source and piezoelectric wide band detection;
(2) use of digital recording and digital signal processing;
(3) use of computed theoretical Green's functions as a basis for comparison and as a guide for feature extraction; and
(4) design of field applicable transducers with selected band width and sensitivity for specific applications.

As an example of the above approach, a prototype transducer for measuring the thickness of concrete slabs up to a meter thick is shown in Figure 1. The transducer is a hollow thick-walled brass cylinder with a ring-shaped piezoelectric ceramic disk on one end which serves as the detecting element. A spherical tipped steel impactor, which is inserted into the hollow axis of the cylinder, is used as a point-impact source. The impact occurs at the center of the hole in the ring-shaped ceramic element. The detected echo is digitized and further processed to yield the thickness information. Some preliminary results indicate that the prototype is quite adequate for its intended application. Further improvement to the transducer will be made by modifying the shape of the brass cylinder to reduce the unwanted echoes from the backing material.

SUMMARY

We have designed and constructed a transducer which generates and detects deep penetrating spherical waves for measuring the thickness of high attenuation heterogeneous composite materials. The concept of the transducer design is different from the conventional approach of generating planar waves. The combination of theoretical Green's functions and digital processing techniques makes the interpretation of the signal tractable and reliable.

Figure 1. Picture showing the prototype point impact transducer for thickness/velocity measurement of concrete.

NDE OF DISTRIBUTED DAMAGE IN METALS

R.J. Fields and H.M. Ledbetter

Fracture and Deformation Division

Progress in the NDE of distributed damage in metals has been made in the following areas: wave velocity studies in creep damaged copper; measurement of cavity size distributions in 304 stainless steel; preparation of a cast copper specimen for SANS evaluation; and ferromagnetic susceptibility studies in creep damaged stainless steels.

ULTRASONIC STUDIES ON CREEP DAMAGED COPPER

Copper bars containing known amounts of creep cavities (oriented cracks that are randomly distributed spacially) were prepared for elastic wave velocity measurements. The preparation of the cavitated material was described in the previous Annual Report of ONDE (Ref. 1). A photomicrograph of the typical microstructure is shown in Figure 1. The elastic wave velocities and moduli were determined as a function of density (or void concentration) for the various specimens. The technique employed for these determinations involved determining the time for an elastic wave to travel from one end of a bar of known length to the other end, be reflected, and return. Standard ultrasonic transducers produced the pulse and recorded its return. These results were monitored on an oscilloscope whose time base could be determined with high precision.

For both axial (z) and transverse directions, Figures 2, 3, and 4 show

c_1 vs x
v_1 vs x
c_1 vs ρ

where v_1 = longitudinal sound velocity
ρ = mass density
$c_1 = \rho v_1^2$ = longitudinal modulus
x = volume fraction of voids = $1 - \rho/\rho_0$

The different intercepts show the effect of texture. Probably a <111> rod texture that shall be verified by calculations.

The large slope suggests that the voids are not spheres. For spheres, Hashin's (Ref. 2) model predicts, approximately,

$$\frac{1}{c_1}\frac{dc_1}{dx} = -\frac{21}{8} = -2.63$$

For the x-direction slope, we find, approximately,

$$\frac{1}{c_1}\frac{dc_1}{dx} = -7.87$$

The difference in slopes (x and z directions) suggests that the disc-shaped voids do not orient randomly, but in some preferred way.

That $\left(\frac{dc}{dx}\right)_{z\text{-dir}}$ exceeds $\left(\frac{dc}{dx}\right)_{x\text{-dir}}$ suggests that the discs tend to align perpendicular to the z axis (the stress axis).

Thus, all these sound-velocity measurements are consistent with the metallography and with the model of void growth (Ref. 3).

QUANTITATIVE MICROSCOPE STUDIES OF CREEP DAMAGED 304 STAINLESS STEEL

Creep damaged 304 stainless steel had been prepared for characterization by the SANS technique (Ref. 4) prior to ultrasonic NDE characterization. Some of the more highly damaged specimens contained cavities that are visible in the optical microscopy. It is not appropriate to use SANS in this size range. These cavities have been measured using automated quantitative microscopy.

We report here some of the measurements on a large number of creep cavities in AISI type 304 stainless steel. The data were obtained through the use of an automatic image analyzing computer, a device which is capable of scanning large numbers of microscopic fields on polished metal surfaces and making measurements on individual creep cavities in each field. The techniques used, as well as some preliminary results, are reported in greater detail in [5]. All raw data is available on IBM-PC compatible magnetic media (floppy disks).

The test program utilized flat, plane stress tensile specimens fabricated from strip stock of a commercial heat of AISI type 304 stainless steel. All specimens were tested in air at 600°C under constant load creep conditions. Two series of tests were conducted. The first was a set of replicate tests in which four groups of three specimens were tested under conditions which were identical for each group. The second set of tests involved a group of specimens which were tested at various loads and test durations, analyzed, retested at the same load for an additional period of time, and then reanalyzed. In all cases the central 3-4 cm of the specimen test section was carefully polished after removal from the testing machine. The specimens were then analyzed on an image analyzing computer. With the magnification used in the present study (406x), this device is capable of measuring cavity areas down to 1.7 μm^2. A sufficient number of fields were examined on each specimen so that at least 1000 cavities were measured per specimen. The results were corrected for the presence of inclusions by measuring the inclusion size distribution on an uncavitated specimen, and subtracting this distribution from the measured cross-sectional area distribution.

Figure 5 is a histogram showing the measured distribution of cavity cross-sectional areas on a typical specimen. A well-defined peak in the distribution may be seen in the neighborhood of 15 μm^2, with the distribution falling off fairly smoothly with increasing area. Figure 6 shows the same distribution plotted on Weibull probability axes. It can be seen that the probability distribution function for the measured cavity cross-sectional area is reasonably well represented by a Weibull cumulative distribution function over most of the range. Of interest is the fact that the slope of the distribution appears to flatten towards the extreme upper end of the curve. Because the coefficient of variation is inversely related to the slope of the curve, this indicates a substantially greater degree of scatter in the size variations of the largest cavities as compared to the much more numerous smaller cavities. We believe that this result suggests that the small cavities can be treated deterministically using models similar to those developed in Ref. 3. The large cavities apparently behave stochastically and would require a different type of formalism.

The results of both test series indicate that the mean measured cavity area (A) varies with time (t) and applied stress (σ) according to the relation $A = Ct\sigma^{\alpha}$ where C and α are constants. Figure 7 shows the results of the series of replicate tests, with the error bars indicating the standard deviation of the measured vales. The correlation coefficient for the linear fit is greater than 0.99. The hypothesis that the mean cavity area increases linearly with time is supported by some recent SANS observations on type 304 stainless steel due to Fuller et al [3] and also by earlier work on alpha-iron by Cane and Greenwood [6].

It should be noted that the above results were obtained on metallographic specimens. As such, they represent a two-dimensional cut through a three-dimensional distribution. We have developed a computer program which numerical converts the 2-D distribution to the 3-D distribution using the theory of R.T. DeHoff (7) and the algorithm of Visscher and Goldman (8). This program still requires further development to run correctly.

The present geometrical shape of the reference specimen of 304 stainless steel is not conducive to the same procedural approach applied to the copper specimens. We are now evaluating the best NDE approach to studying these reference specimens.

PREPARATION OF A CAST COPPER SPECIMEN FOR SANS CHARACTERIZATION

SANS studies on the creep damaged copper, reported in the previous ONDE Annual Report (1), were complicated by a texture effect in the original, copper bar stock. In order to quantify this effect, untextured copper of the same purity would have to be analyzed in the SANS instrument. A copper cylinder 25 mm in diameter and 25 mm long was heated in a quartz vessel under a reducing atmosphere (CO) to 1200°C for one hour. The resulting ingot was cut and polished to the same dimensions as the preceding SANS specimens and given to the researchers in the Reactor Division for evaluation. Their report on this specimen will be issued separately.

FERROMAGNETIC SUSCEPTIBILITY OF CREEP DAMAGED AUSTENITIC STAINLESS STEELS

In the course of a routine investigation of several superheater tubes from a coal-fired power plant, it was discovered that they were ferromagnetic in certain areas. These austentic stainless steel tubes had failed after about 120,000 hours (13.5 years) service at 540°C, sustaining a steam pressure of about 1850 psi.

It is very significant that the magnetic regions were those that also exhibited abundant creep cavities and cracks. Since austenitic steels are not normally magnetic to the extent found here, further work was undertaken to detect the source of the ferromagnetism. Optical and electron microscopy revealed the presence of sigma phase (non-magnetic) and ferrite (magnetic) at grain boundary triple junctions (Figures 8 and 9). Evidently, a certain percentage of the FCC alloy can transform slowly at steam plant temperatures to the BCC structure. The interesting questions are: why is the creep damaged regions much more ferromagnetic than the sound areas of the tubes and can these observations be used to develop a simple NDE technique for steam plant opeators that will detect severely degraded austenitic superheater tubes in situ? Such an NDE technique would be useful because it would alert field engineers to the presence of aged components during scheduled down-times rather than have them fail during operation of the plant. A correlation between magnetic susceptibility and extext of optically visible creep damage in 321 stainless steel is shown in Figure 10. Futher work has detected increased magnetic susceptibility in crept 304 and 347 stainless steels.

SUMMARY

Progress in the NDE of distributed damage in metals has been made in the following areas: wave velocity studies in creep damaged copper; measurement of cavity size distributions in 304 stainless steel; preparation of a cast copper specimen for SANS evaluation; and ferromagnetic susceptibility studies in creep damaged stainless steels.

REFERENCES

1. L. Mordfin, editor, "Office of Nondestructive Evaluation, Technical Activities 1984," NBSIR 84-2944 (November 1984).

2. Z. Hashin "The Elastic Moduli of Heterogeneous Materials," J. Applied Mechanics 29 pp. 143-150, (1962).

3. E.R. Fuller, Jr., R.J. Fields, T.-J. Chuang, and S. Singhal," Characterization of Creep Damage in Meals Using Small Angle Scattering," J. of Research of NBS, 89, pp 35-45, (1984).

4. R.J. Fields, R.C. Dobbyn, and C.I. Glinka, "Microstructural Characterization by Small Angle Neutron Scattering," to be published in In Process, Nondestructive Microstructure Characterization, A.S.M. Symposium, Sept. 1984.

5. T.S. Liu, R.J. Fields, D.G. Harlow, and T.J. Delph, "Statistical Observations of Creep Cavitation in AISI Type 304 Stainless Steel," Scripta Metallurgica, 19, pp 299-304, (1984).

6. B.J. Cane and G.W. Greenwood, "The Nucleation and Growth of Cavities in Iron during Deformation at Elevated Temperatures," Metal Science 9, pp 55-60, (1975).

7. R.T. DeHoff, "The Determination of the Size Distribution of Ellipsoidal Particles from Measurements Made on Random Plane Sections," Trans. A.I.M.E., 224, pp 474-477, (1962).

8. W.M. Visscher and A.S. Goldman, "Estimating the Distribution of Spherical Particles from Plane Sections. An Optimal Algorithm for Solution of the Abel Integral Equation," J. of Scientific and Statistical Computing, 4, pp 280-290, (1983).

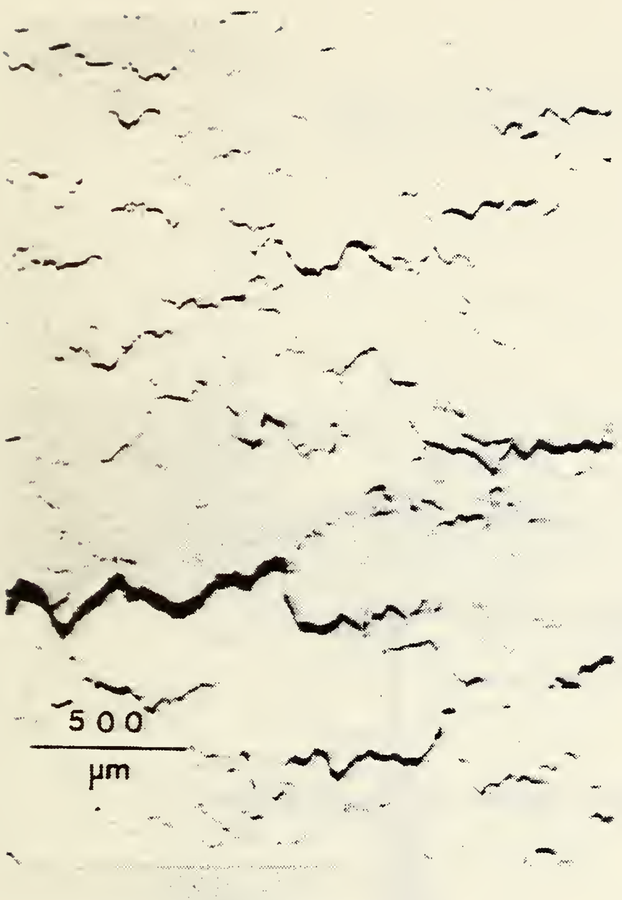

Figure 1. Creep damage in copper consists of cavities (or oblate spheroidal voids) oriented with the major axis perpendicular to the applied tensile stress.

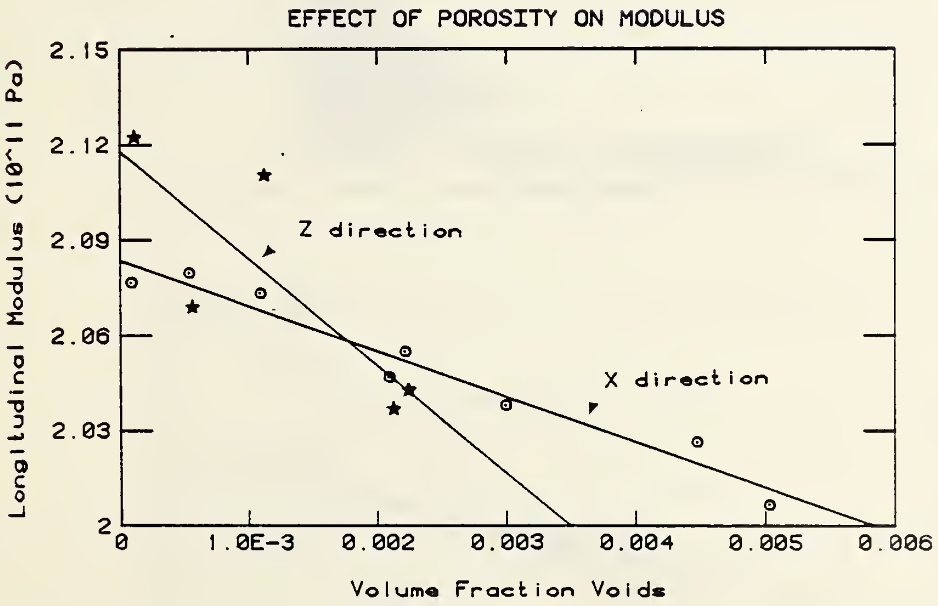

Figure 2. Longitudinal modulus versus volume fraction of voids in copper.

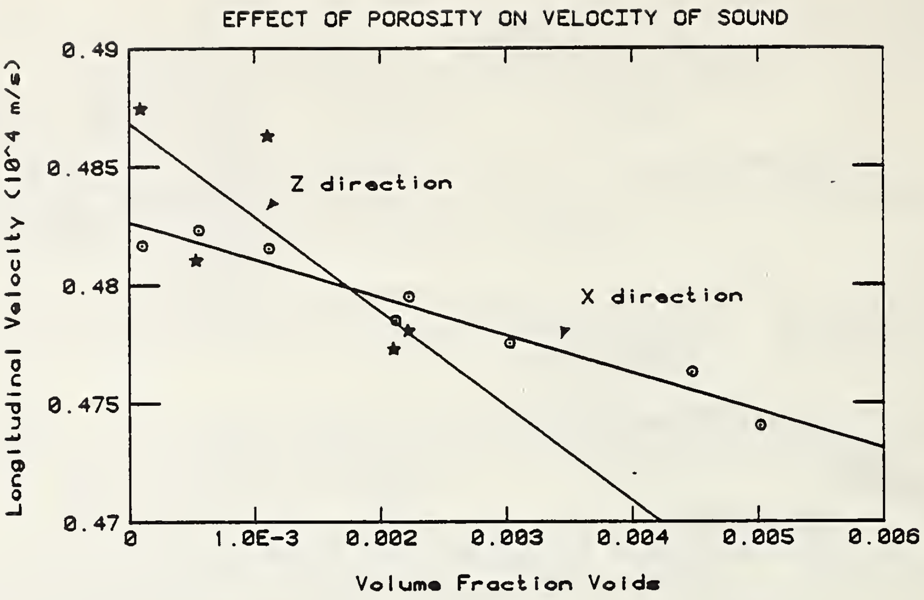

Figure 3. Longitudinal sound velocity versus volume fraction of voids in copper.

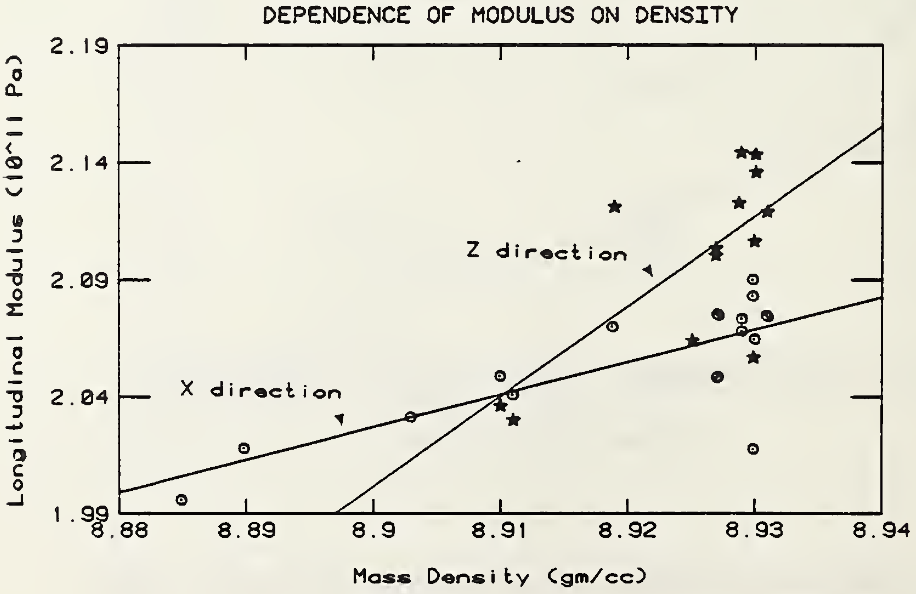

Figure 4. Longitudinal modulus versus mass density in cavitated copper.

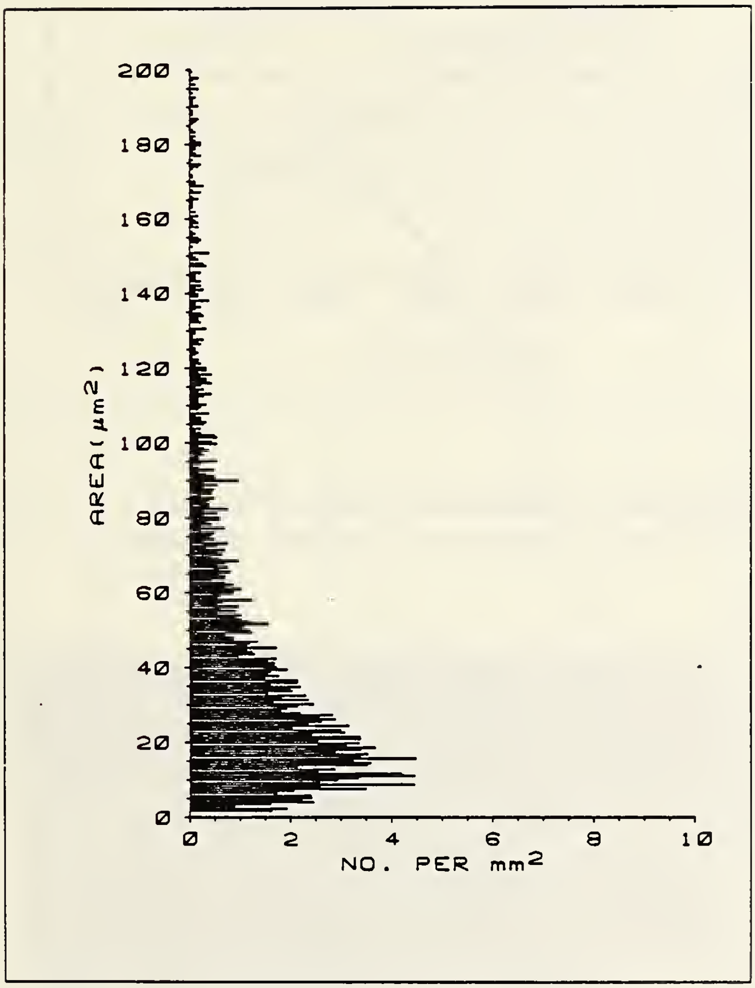

Figure 5. Histogram showing distribution of cavity cross-sectional areas on a typical specimen of cavitated stainless steel.

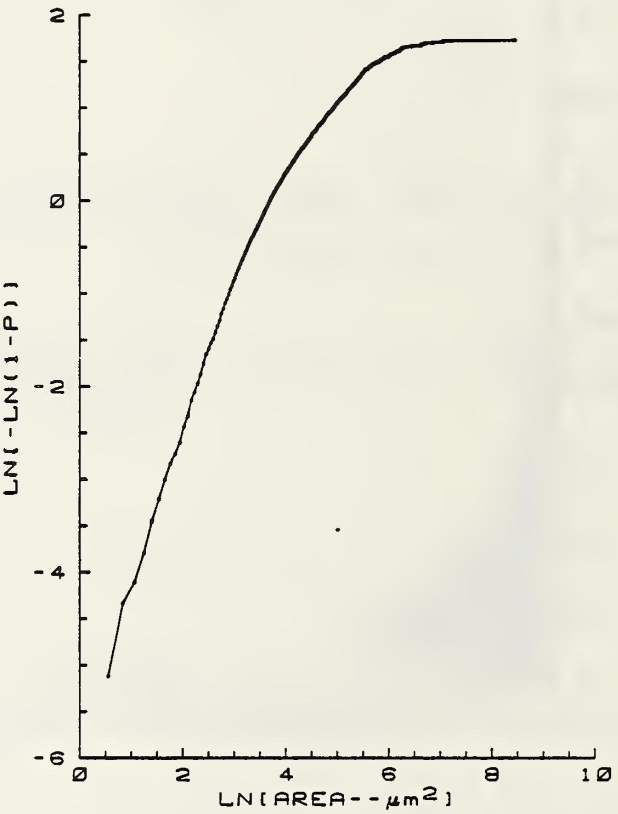

Figure 6. Distribution of cavity cross-sectional areas plotted on Weibull probability axes.

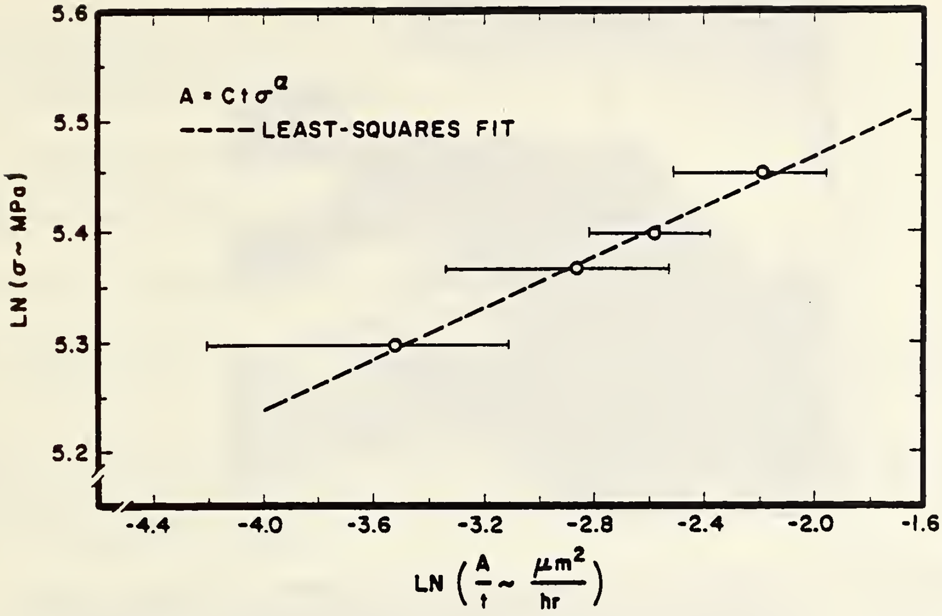

Figure 7. Evaluation data from numerous tests with model-based equation results in straight line fit, thus supporting model.

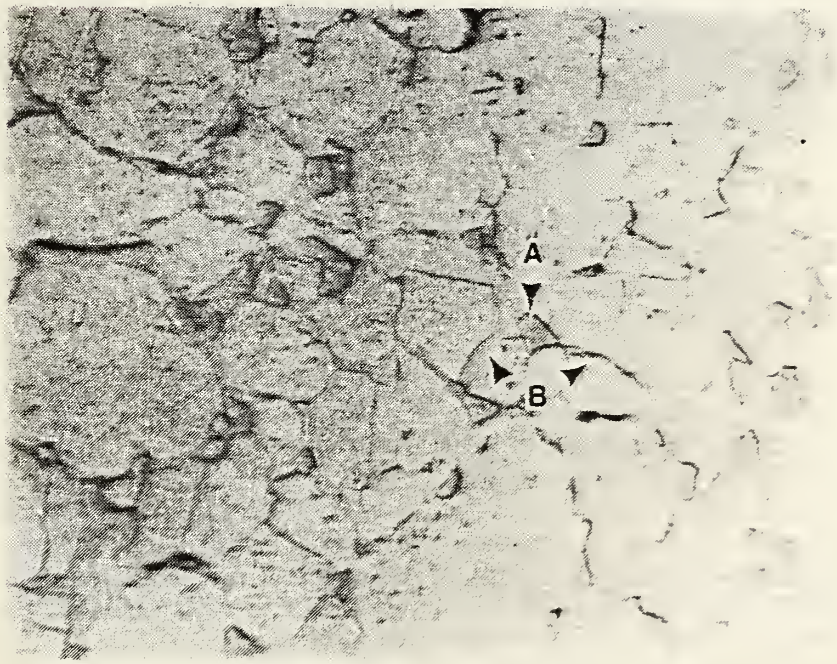

Figure 8. Optical micrograph of degraded 321 stainless steel showing (a) ferrite and (b) sigma phase.

Figure 9. Electron micrograph of degraded 321 stainless steel showing ferrite (identified by electron diffraction).

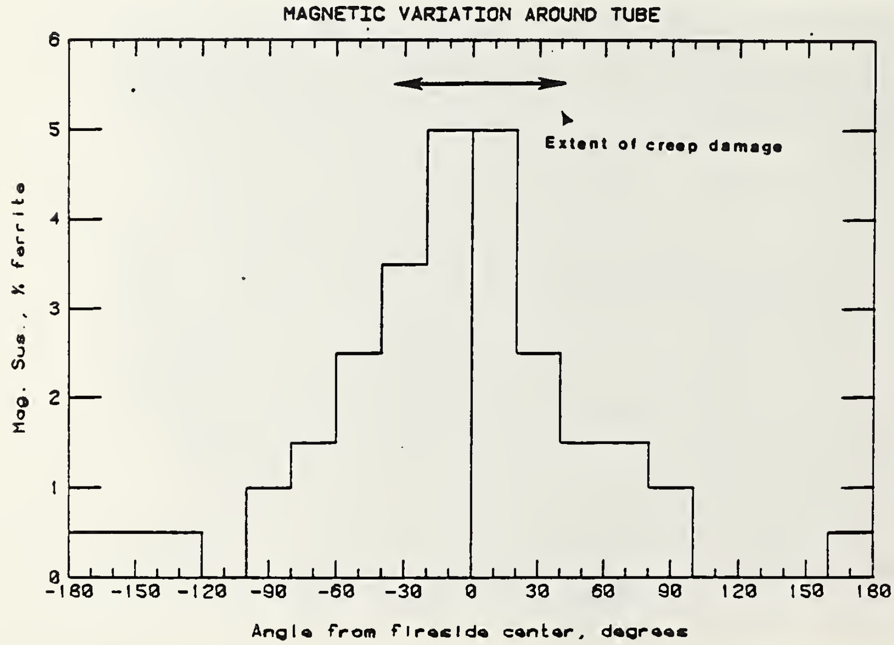

Figure 10. Variation of ferromagnetic susceptibility (in terms of equivalent % ferrite) around perimeter of failed tube. Extent of visible creep damage is indicated.

CREEP CAVITIES IN COPPER: AN ULTRASONIC-VELOCITY AND COMPOSITE-MODELING STUDY

H. M. Ledbetter and R. J. Fields

Fracture and Deformation Division

Institute for Materials Science and Engineering

When copper suffers tensile loading at high temperatures, voids nucleate at grain boundaries. These voids grow, coalesce, and cause failure.

These voids (or creep cavities) pose problems for many people: the nde specialist, who wants to detect them; the materials engineer, who wants to improve resistance to failure; and the materials scientist, who wants to understand the material behavior.

The present study used ultrasonic methods to determine longitudinal-mode sound velocities and elastic constants in crept copper rods. We considered two directions: axial and radial, that is, parallel and perpendicular to the rod (stress) axis. We denote these directions x_3 and x_1, respectively.

The study produced five principal conclusions:

1. The copper rods contain considerable texture. To quantify this, we assume the usual [111] - [100] duplex rod texture observed in copper. From copper's well-known monocrystal elastic constants, from an averaging model given by Gairola and Kröner, and from the two sound velocities, v_1 and v_3, one can calculate the relative [111] and [100] contributions. For the as-received material, we obtained $x(111) = 0.56$, the volume fraction of grains with [111] orientations.

2. Heating the copper alters the texture. By the same analysis used above, using v_i values measured after heating, we found $x(111) = 0.71$. The proportion of [111] texture increases. Metallography shows grain growth during heating. Presumably, this explains the texture transition.

3. The voids are not spherical. Figure 1 shows the variation of both v_1 and v_3 with void volume fraction (determined by measuring mass density). The figure also shows a theoretical line for spherical voids. Both other theories and measurements support this prediction. The strong departure of observation from this line suggests that the voids have oblate-spheroidal (disc) shape. Datta and Ledbetter showed that disc-shaped voids soften a material much more than do spherical voids. The extent of softening depends on the disc's aspect ratio: flatter discs cause more softening. Metallography confirms that sets of small spherical voids coalesce and form disc-shaped voids along grain boundaries.

4. The disc-shaped voids do not orient randomly. If they did, the slopes dv_1/dx and dv_3/dx would not differ.

5. Probably the disc-shaped voids tend to orient perpendicular to the stress axis, x_3. This accounts for the slope dv_3/dx exceeding dv_1/dx. Again, metallography confirms this orientation tendency.

We plan to use composite-property-modeling methods to verify quantitatively the void geometry described above. Our model will include several variables: (a) copper's elastic constants, (b) void volume fraction, (c) void shape, and (d) void orientation.

In any related future studies, we want to consider two other properties: (a) shear-wave sound velocity, and (b) internal friction.

Usually, both of these properties provide more information about internal structure than the longitudinal-wave sound velocity used in the present study.

SUMMARY

By measuring longitudinal-mode ultrasonic velocity, we studied creep cavities in copper. Using a model by Ledbetter and Datta, we interrelated several variables: cavity volume fraction, cavity shape, and cavity orientation. Also, we made some deductions concerning texture.

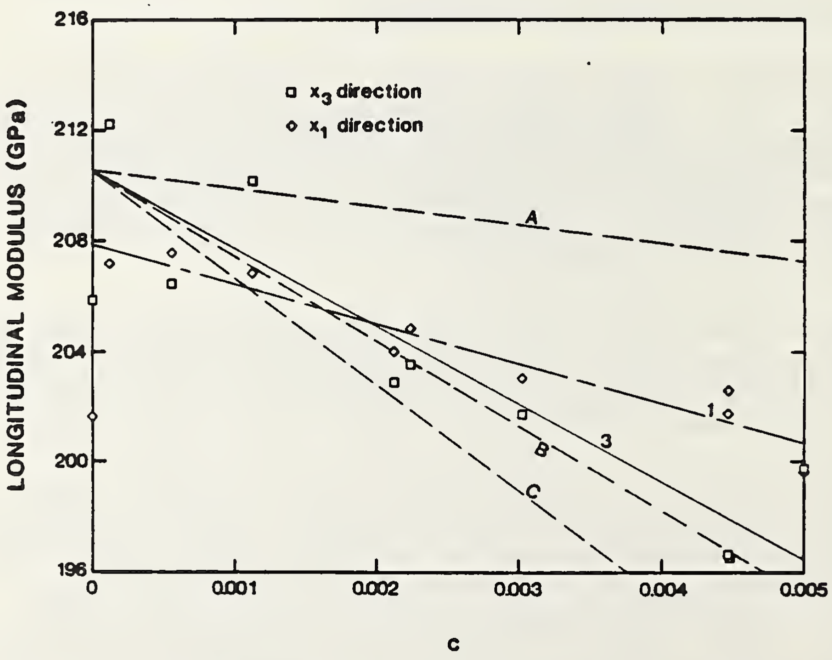

Figure 1. Longitudinal modulus $C_\ell = \rho v_\ell^2$ versus volume fraction of voids in creep-cavitated copper. The rod (stress) axis is denoted 3. Dashed lines represent Ledbetter-Datta model calculations for (A) spherical voids, (B) 10:1-aspect-ratio disc-shaped voids oriented randomly, and (C) identical discs oriented perpendicular to 3 axis. Symbols show measurements.

NDE DATA ANALYSIS, RELIABILITY MODELING, AND PC-BASED SOFTWARE RESEARCH

J. T. Fong, R. S. Cramer, D. F. Redmiles, M. R. Knapp-Cordes

Mathematical Analysis Division, and

J. J. Filliben

Statistical Engineering Division

Center for Applied Mathematics

This project grew out of a consulting request in 1976 by the U. S. Department of Transportation to the National Bureau of Standards (NBS) for a comprehensive evaluation of the structural integrity of a large number of girth welds in an oil pipeline then under construction at Alaska.

The study identified a research need on the development of an "acceptable industry standard" for analyzing round robin inspection data and for estimating the detection, location, and sizing reliabilities of a field nondestructive evaluation (NDE) procedure.

To address this need, the NBS Center for Applied Mathematics initiated in 1977 a long-term research project with two specific goals as follows:

(a) To develop an analysis and modeling methodology for estimating the detection, location, and sizing reliabilities of ultrasonic and radiographic examination of weld flaws with or without post-examination sectioning data.

(b) To design a prototype archival database and personal-computer-based software for collecting, evaluating, and disseminating field inspection and round robin NDE data for on-line operational, maintenance, and design decision support.

Since 1978, this work has also been supported by the NBS Office of NDE. During 1982-84, an industry-based Pressure Vessel Research Committee (PVRC) of the Welding Research Council in New York, NY, provided partial support for the analysis of round robin and sectioning data of PVRC specimen 251J. Two technical reports, one for each of the above two goals, are being prepared for discussion and publication during 1985-86. The titles of those two reports are:

(a) "Reliability Analysis of Round Robin NDE Data for PVRC Weld Specimen 251J," by J. T. Fong, NBS Technical Report to Pressure Vessel Research Committee of the Welding Research Council, New York, NY, Oct. 1985.

(b) "How to Manage Engineering Data with a Personal Computer (PC)," by J. T. Fong, ASME Special Technical Publication for 1986 Joint PVP and Computer Engineering Conference Tutorial at Chicago, IL, July 1986.

TYPICAL ANALYSIS RESULTS

To illustrate the analysis methodology and the significance of a typical result, the reliability of a flaw fabrication procedure used by PVRC about 20 years ago when specimen 251J was made, is selected for discussion in this report. As shown in Fig. 1, a block of A533 Grade B thick-section steel (28 cm or 11 in thick) had 15 flaws of 4 different types built into the butt weld during a 159-pass submerged-arc welding procedure. The actual dimensions of those flaws, as determined by Yukawa in 1981 (Ref. 1), are compared with the intended dimensions in Table 1.

To bring the data into a more manageable form for interpretation and modeling, we consider a normalization procedure where the maximum dimension of each intended flaw is assigned the uniform value of 1.00. The actual dimensions of the 15 flaws as determined by Yukawa in his sectioning experiment are presented in a normalized box plot (Fig. 2) using a software package known as DATAPLOT (Ref. 2).

A qualitative observation of Fig. 2 shows that the flaw fabrication procedure is (a) dimensionally stable (up to 50% oversizing) for long slags and short slags, (b) consistently exaggerating in dimensions by a factor of 2.2 for cross cracks, and (c) generally unreliable for longitudinal cracks. This "inhomogeneity" in data provides an opportunity to conduct an analysis of variance (ANOVA) (Refs. 2 and 3) and a more accurate assessment of the fabrication reliability than hitherto attempted by previous investigators (Ref. 4). A comparison of the traditional univariate analysis of 15 flaw size data versus the use of ANOVA for 4 types of flaws is given in Fig. 3. An interval estimate of the so-called mean amplification factor as a measure of the effectiveness of the flaw fabrication procedure for confidence levels between 50% and 95% is given in Fig. 4. The chi-square distribution of the total variance using a one-way analysis of variance procedure for 50% to 95% confidence levels is given in Fig. 5. More detailed results of the reliability study of the flaw fabrication and detection procedures are given in the Oct. 1985 NBS report to PVRC.

REFERENCES

1. S. Yukawa, "Sectioning of PVRC NDE Specimen 251J," Progress Report to PVRC dated Jan. 15, 1981 and May 25, 1983.

2. J. J. Filliben, "DATAPLOT - An Interactive High-Level Language for Graphics, Nonlinear Fitting, Data Analysis, and Mathematics," Computer Graphics, 15, No. 3, pp. 199-213 (1981).

3. H. E. Daniels, " The Estimation of Components of Variance," J. Royal Statistical Soc., Supplement 6, No. 2, pp. 186-197 (1939).

4. Buchanan, R. A., "Analysis of the NDE of PVRC Plate-Weld Specimen 251J," WRC Bulletin 221, Nov. 1976.

Table 1. Sectioning Results for PVRC 251J

Flaw	Type*	Actual Flaw Location Coordinates (in.) X	Y	Z	Intended Flaw Location Coordinates (in.) X	Y	Z
A	CC	26.1-25.5	2.4-4.2	1.0-1.3	25.5-26.3	3.0	1.0
B	LS	26.3-26.4	16.1-18.1	0.6-1.1	26.3	16.0-18.0	1.0
C	LC	25.9-26.6	29.7-33.4	0.7-1.2	26.3	30.0-32.0	1.0
D	LC	25.1-25.6	2.2-5.5	2.4-3.1	25.0	2.0-4.0	2.75
E	CC	25.3-25.5	17.1-19.0	2.8-3.2	25.0-25.8	17.0	2.75
F	SS	25.1-25.2	30.6-31.8	1.9-2.7	25.0	30.6-31.4	2.75
G	LS	26.2-26.4	2.2-4.8	4.6-5.4	26.3	2.0-4.0	5.5
H	LC	25.7-25.4	16.1-21.9	5.0-5.7	26.3	16.0-18.0	5.5
I	CC	26.0-26.4	30.2-31.9	5.2-5.7	25.5-26.3	31.0	5.5
J	CC	25.1-25.8	3.1-4.6	7.7-8.2	25.0-25.8	3.0	8.3
K	SS	25.1-25.5	17.1-18.1	8.0-8.3	25.0-25.8	17.0	8.3
L	LC	25.1-25.7	29.1-33.9	7.6-8.2	25.0	30.0-32.0	8.3
M	LC	25.7-26.3	1.0-5.0	9.3-10.0	26.3	2.0-4.0	10.0
N	CC	25.8-25.3	16.7-18.7	9.3-9.8	25.5-26.3	17.0	10.0
O	LS	26.0-26.2	29.8-32.2	9.6-10.2	26.3	30.0-32.0	10.0

*Type of Flaw: CC = Cross Crack
LS = Long Slag
LC = Long Crack
SS = Short Slag

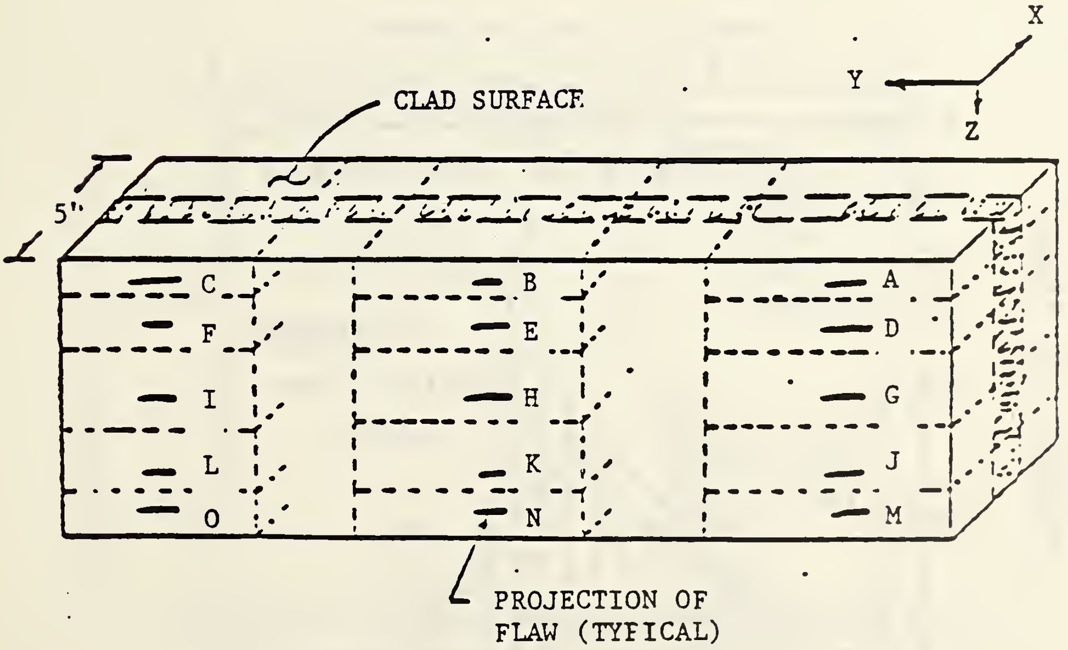

Figure 1 - Principal sectioning cuts of PVRC 251J. The block is 11 inches high (z-direction) by 36 inches long (y-direction)

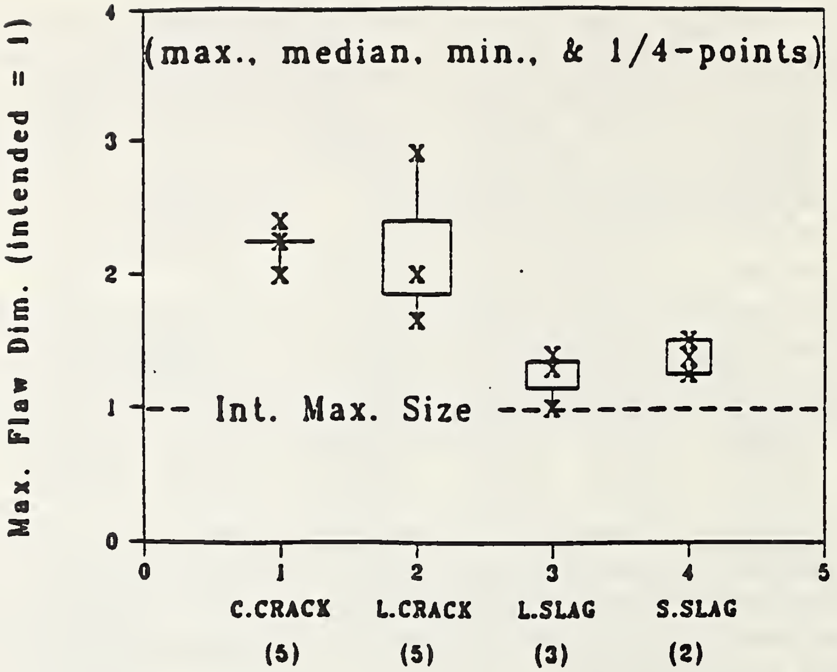

Figure 2. Box plot for four (4) types of flaws

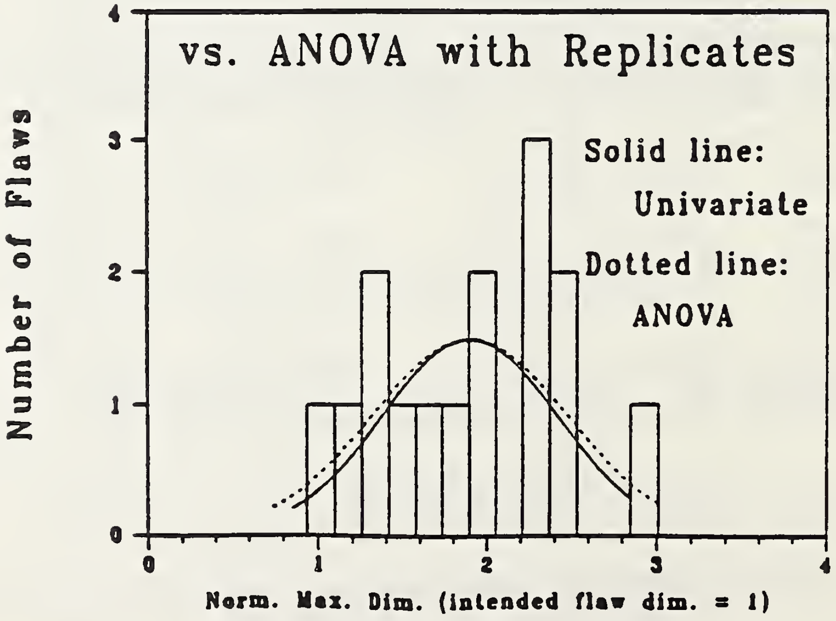

Figure 3. A comparison of univariate anal. vs. ANOVA with replicates

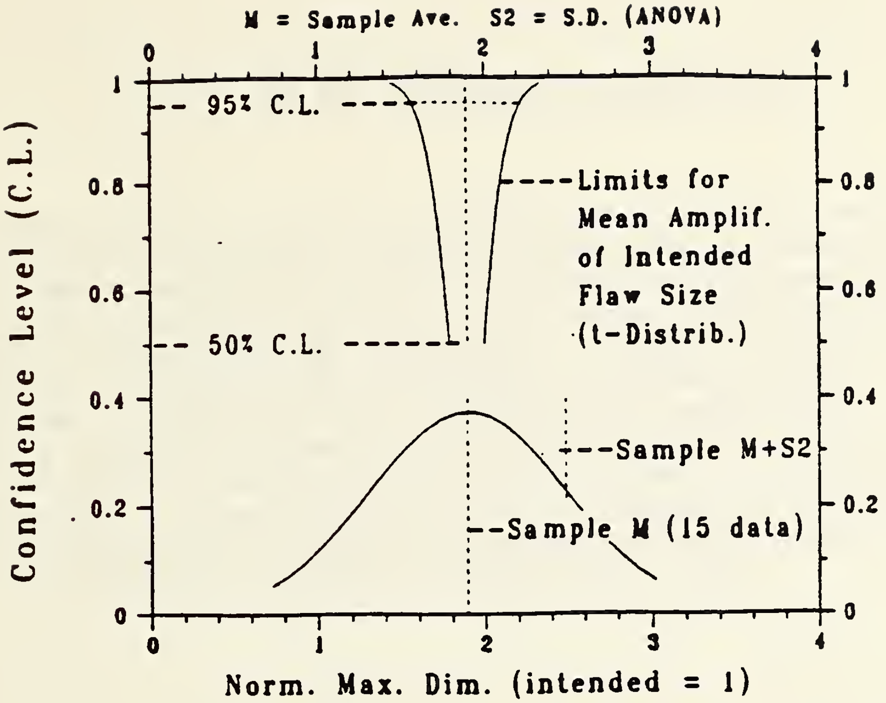

Figure 4. t-distribution limits mean amplif. of intended flaw size

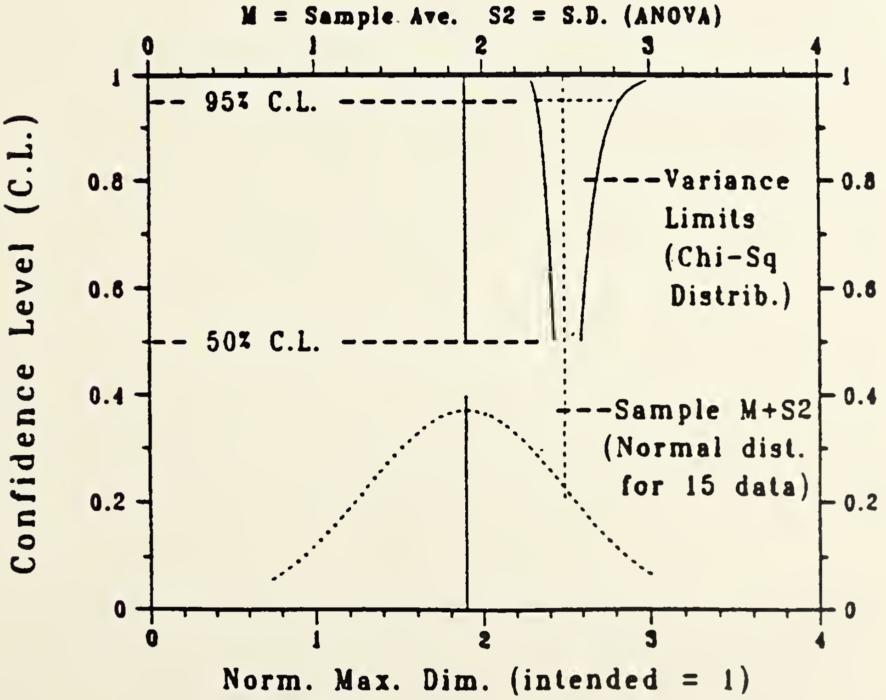

Figure 5. Chi-Sq distribution limits

III. NDE FOR INTERFACES AND COMPOSITES

The topics for this section, interfaces and composites, were chosen primarily because of the major technical importance of interfaces and composites in modern engineered systems. They were also chosen because of the continuing difficulty and scientific and technical challenge facing NDE when applied to interfaces and composites. Although the focus of most of the activities in this section are on NDE for process control, the work is also important to in-service and post-manufacture inspection. In the first group of six papers on composites, three papers of particular interest deal with monitoring of polymer cure rate by fluorescence, dielectric and ultrasonic techniques. In the second group of five papers on interfaces, the theoretical and experimental work on eddy current conductivity profiling and the associated data inversion process deserve note.

CURE MONITORING OF COMPOSITES USING FLUORESCENCE SPECTROSCOPY

Bruno M. Fanconi, Francis W. Wang and Robert Lowry

Polymers Division

Institute for Materials Science and Engineering

The manufacture of polymer matrix composites involves complex chemical and physical changes that must be adequately controlled to produce desirable products. Monitoring of resin viscosity during cure is a key step towards improved process control. A technique is under development that uses the sensitivity of the fluorescence intensity of some organic molecules to the local viscosity. Optical fibers are used to bring the excitation light into the interior of a curing composite component, as well as to collect and transmit the emitted light for detection. The light in the fiber excites probe molecules that are located within the penetration depth of the evanescent wave. This distance depends on the refractive indices of the waveguide and surrounding matrix, as well as the angle of incidence that the propagating light makes with the optical fiber-matrix interface. Thus, this approach is particularly sensitive to the interfacial region that is of critical importance in achieving desirable mechanical properties and performance.

The current focus of this work has been the identification of suitable probe molecules, and calculations of the effect of viscosity profiles on fluorescence intensities excited by evanescent waves. Two types of probe molecules have been examined. The excimer-type fluorescence probes are attractive owing to the presence of the monomer fluorescence that can be used as an internal standard. This feature is attractive since factors other than viscosity change can affect the observed fluorescence intensities. Curing studies of amine-cured epoxy resins had shown that the excimer-fluorescence technique was insensitive to viscosity changes in the later stage of curing. For this reason, other probe molecules with fluorescence sensitivity over a wider viscosity range have been investigated. The lack of an internal standard for these probe molecules lead to use of a second molecule which has a viscosity <u>insensitive</u> fluorescence intensity at a frequency distinct from that of the viscosity probe. Figure 1 shows the fluorescence intensities as a function of cure time of the probe molecule 1-(4-dimethylaminophenyl)-6-phenyl-1,3,5 hexatriene and the internal standard 9,10-diphenylanthrancene dissolved in an epoxy resin. The ratio of these two intensities is related to the viscosity developed at that stage of cure.

An advantage of the use of probe molecules is that their concentrations can be extremely low. The concentration of the probe molecule and internal standard used to obtain the data shown in Figure 1 were $5*10^{-5}$M and $2*10^{-5}$M, respectively. At these exceedingly low concentrations the probe molecules are not expected to have an effect on the resultant mechanical properties of the composite part.

A significant advantage of waveguide spectroscopy for composites is that the sampled material lies near the fiber-matrix interface, and by varying the penetration depth of the evanescent wave it may be possible to profile the viscosity distribution or chemical change in the interfacial region. We have calculated fluorescence intensities excited by the evanescent waves of the various cavity modes of thin-film waveguides. The calculated intensities of the emitted light were evaluated for sensitivity to distributions in the probe-molecule concentrations within the penetration depths. Various concentration profiles were examined to include likely distributions of viscosity and chemical effects in the interfacial region.

The calculations were conducted for thin film type waveguides in which prisms are used to couple the light into the waveguides. The thin film waveguide modes that can be activated depend on the refractive indices of the film, substrate, and coupling prism, as well as the film thickness, the wavelength of the excitation light, and the angle of incidence. The electric field magnitudes within the matrix material were determined for these allowed modes, and together with an assumed concentration profile of probe molecules, the relative fluorescence intensities excited by the waveguide modes were calculated. The concentration profile was assumed to be of the form $C(x)=C_o(1-\exp(a_ox^2))$ where x is the distance into the matrix from the waveguide-matrix surface, C_o in the concentration in the bulk and a_o is a parameter that controls the distance near the surface over which the concentration differs appreciably from that of the bulk. Figure 2 shows the ratio of the fluorescence intensities of the two allowed modes assuming a substrate refractive index of 1.46, a waveguide refractive index of 1.56, and an excitation light frequency of 488nm. The ratio is sensitive to the concentration profile over a distance of about 30nm.

The model calculations support the notion that information about viscosity profiles and chemical variability near the waveguide-matrix interface can be elucidated using fluorescence spectroscopic studies of probe molecules excited by the evanescent waves.

SUMMARY

Suitable probe molecules for monitoring viscosity changes occurring during composite cure have been identified. Calculations of the fluorescence intensity as a function of probe molecule concentration near the waveguide-matrix interface indicated sensitivity over distances from 2 to 50nm.

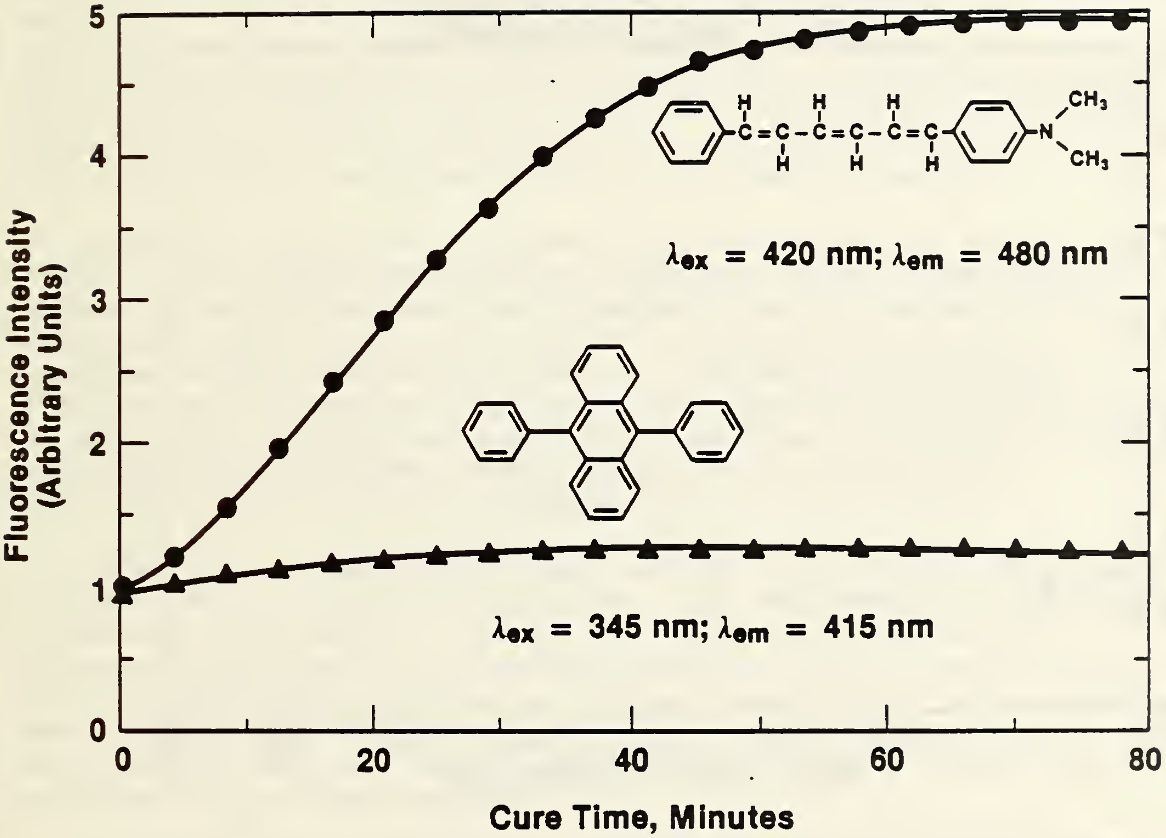

Figure 1. Fluorescence intensities of viscosity probe (top curve) and reference standard (bottom curve) in an epoxy resin as a function of cure time.

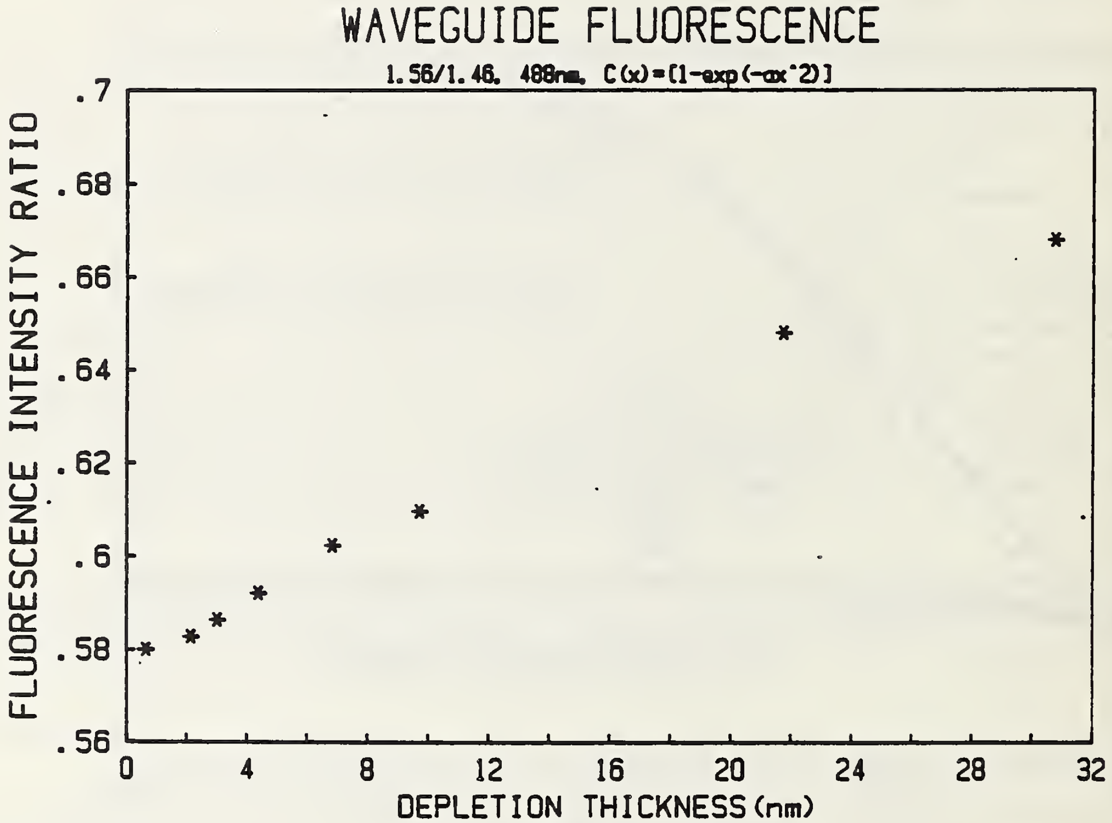

Figure 2. Ratio of the calculated fluorescence intensities of two waveguide modes as a function of the distance from the waveguide-matrix interface at which the concentration is 1/2 that of the bulk.

CURE MONITORING IN EPOXY RESINS BY ELECTRICAL MEASUREMENTS

Frederick I. Mopsik

Polymers Division

Institute for Materials Science and Engineering

The processing of epoxy resin based composites has been rapidly expanding. These composites, especially those using high strength fibers, are being considered as advanced, light weight replacements for metals in many high technology applications. A major need in furthering the application of these composites is a means for monitoring and controlling the cure reaction so that it can be optimized for high cure rate and better quality control. Monitoring of the cure cycle through dielectric measurements offers the possibility of an easily implemented technique that could readily be automated for on-line process control.

When this project was initiated last year, it was not clear as to whether ionic conduction or dipolar relaxation would be the dominant process in monitoring cure. An automated system for measuring AC conductance over a very wide range of values as a function of time was developed to help resolve this issue. A reproducible, disposable electrode set was also developed since the cured resin bonds very strongly to any metal. In addition, a previously developed dielectric spectrometer that used rapid time-domain measurements provided a basis for investigating any dipolar loss mechanisms.

This past year measurements were carried out on several epoxy base resins using an imidazole curing agent. The measurements at the beginning of the cure were made at 50 Hz with the conductivity system where conductance is clearly the dominant contribution to dielectric loss. As the cure approached completion at constant temperature, the measurements were extended both in frequency and in sensitivity using the spectrometer. Modifications were made to the spectrometer to allow a precise time reference for the measurements.

A sample cure curve is shown in Fig. 1. The solid curve shows the data at 50 Hz with the extensions from the spectrometer shown as crosses. The initial rise at short times is the increase in conductance as the sample was heated in the oven. The strong decrease is the result of cure. The smooth monotonic decrease in conductance after the maximum indicates that conductance is the main contributor to dielectric loss. If a dipolar loss process that moved to lower frequencies during cure were important, it would appear as either a shoulder or second peak in the conductance curve, since for a given frequency the conductance is proportional to dielectric loss and a dipolar loss process must have a maximum as a function of frequency. The data in Fig. 1 clearly show no shoulder or second peak once the conductance starts to decrease.

There is, at the end of the cure, evidence of a relaxation process. This is seen in Fig. 1 by the lower conductance values at 0.01 Hz taken from spectrometer data. This loss is mainly at higher frequencies and is relatively featureless. This can be seen in Fig. 2, where a complete spectrum is presented in the complex plane. The points increase in frequency to the left. The strong upsweep to the right is from conductance. A relaxation would be definitely peaked and is not seen.

One unexpected result from these measurements was found when a sample was preheated prior to filling the cell. The results for this cure are shown as the lower curve in Fig. 3 which is shifted by 50 minutes to the right from the upper curve, the data from Fig. 1. The preheating partially cured the sample as evidenced by the shorter cure time. What is even more significant is that the strong decrease in conductance at the end of the cure is unaffected, since the two curves run in parallel. This result suggests that a standardized conductivity measurement could be used to evaluate the state of the resin prior to cure, establish its useful life and help determine processing conditions.

For next year, more systems must be studied to establish firmly the dominance of conductance as a contribution to dielectric loss. The results already show that conductance can be used to follow the cure rate, but it is possible that low conductance resins may show a relaxation phenomenon near cure completion. Also, the use of conductance measurements to establish shelf-life must be pursued. A series of partially cured samples must be studied to confirm the results found this year. Such a study could lead to a standardized test method for monitoring the initial state of a cure. Also, a tie-in must be made to other, more traditional measurements so that electrical measurements can be related to more conventional measures of cure. Already, it has been found that the conductivity decrease comes after the exotherm as measured by DSC.

SUMMARY

Conductivity and dielectric loss measurements have been made on curing epoxy resin samples. Conductance as a function of time shows great promise as an inexpensive and easily automated method for monitoring cure.

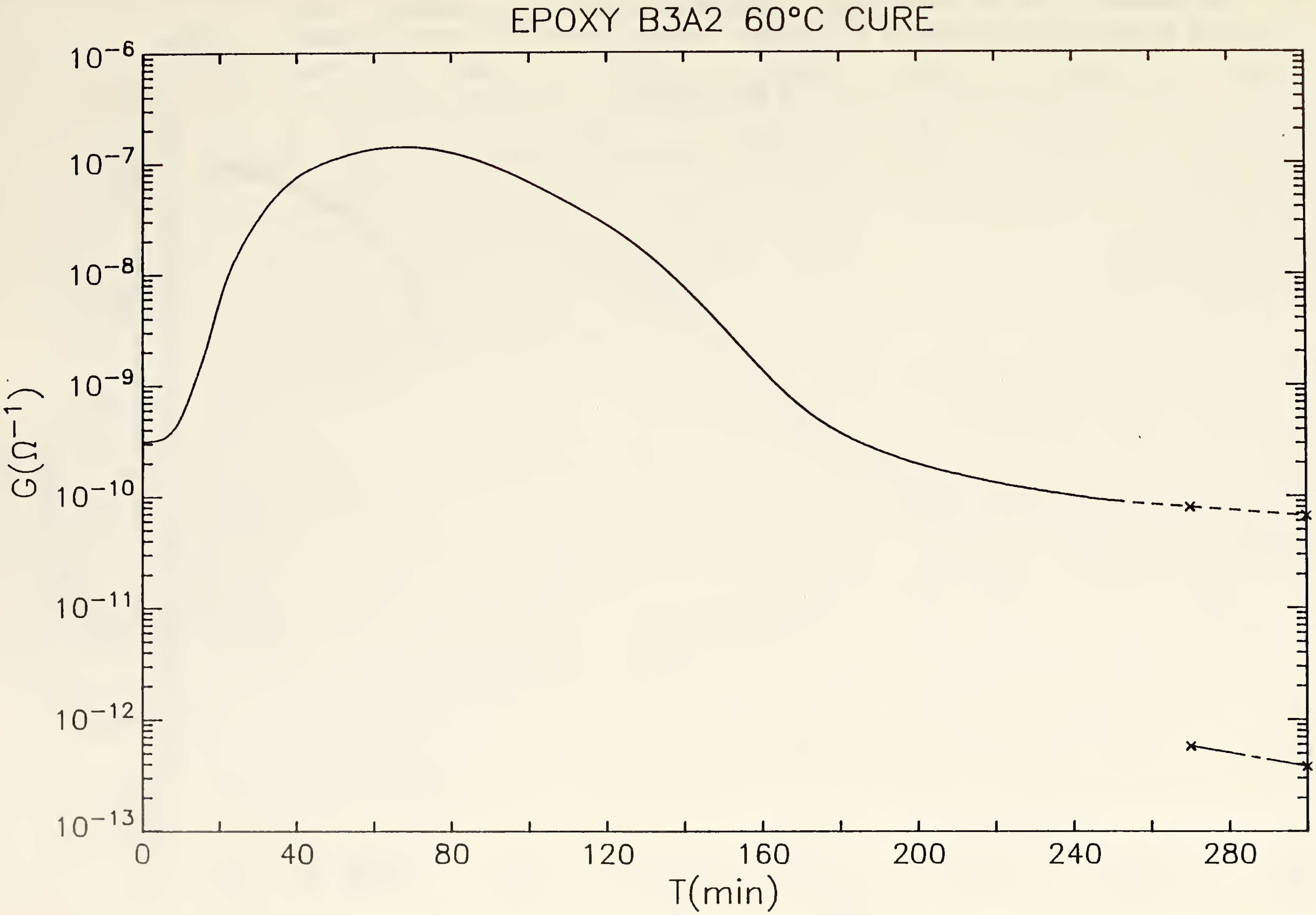

Figure 1. Conductance vs time for a curing epoxy. The main upper curve is for 50 Hz while the small lower curve is for 0.01 Hz. The crosses are data taken from the dielectric spectrometer.

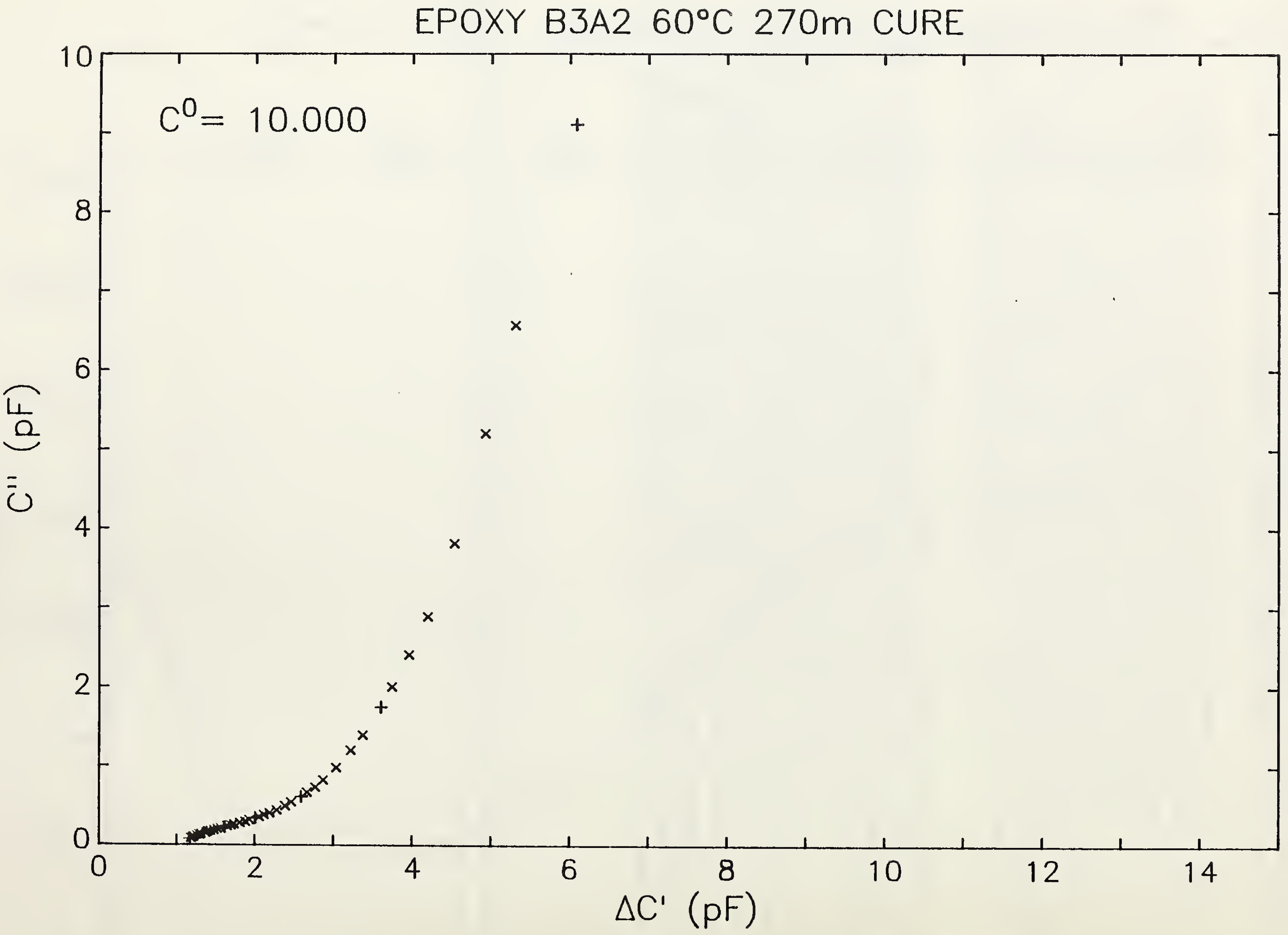

Figure 2. Complex plane plot for the complex capacitance measured at 270 minutes into the cure. Frequency decreases to the right. The upsweep is due to conduction.

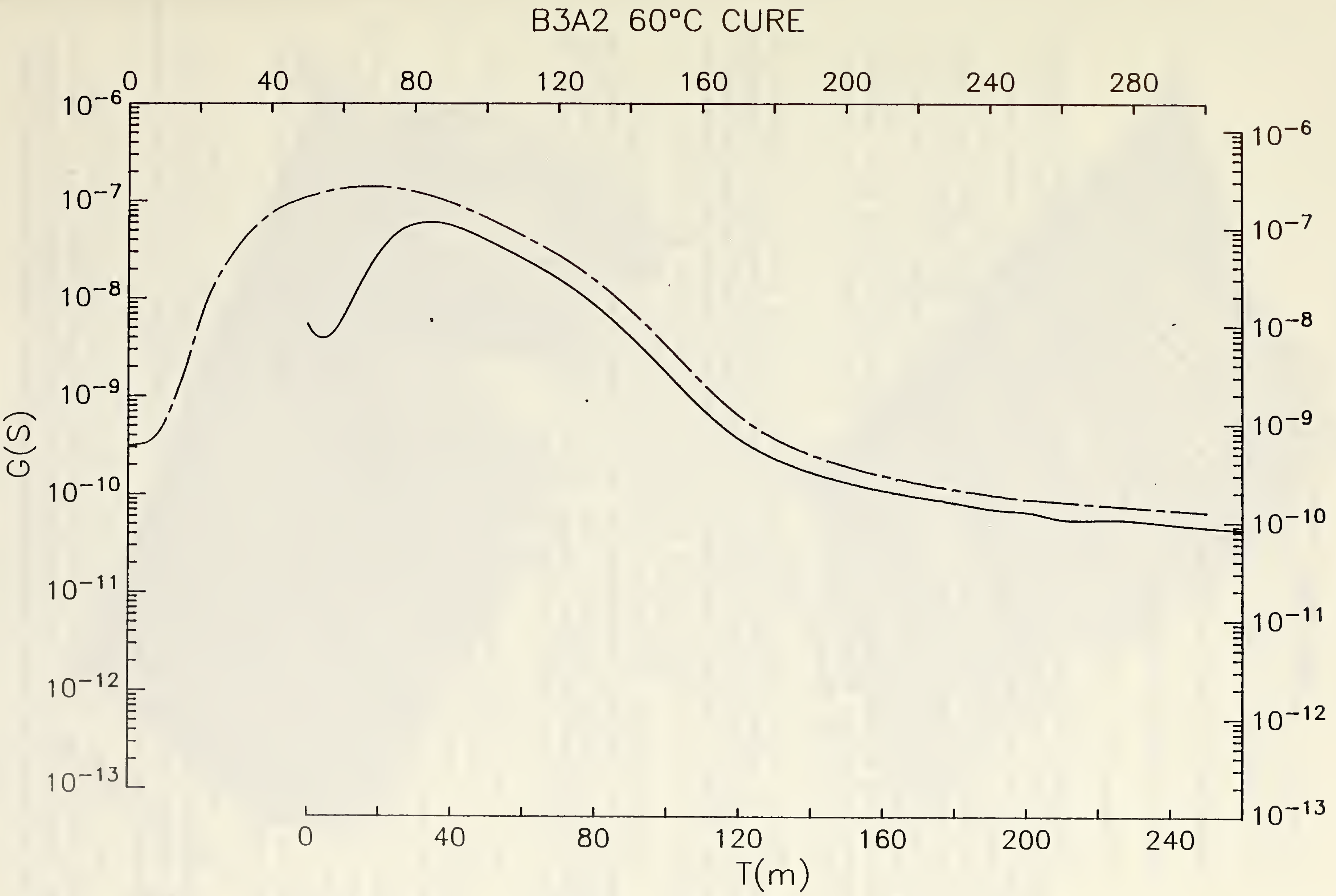

Figure 3. The upper curve is the 50 Hz cure data of Figure 1. The lower curve is data taken for a preheated sample and is displaced by 50 minutes from the upper curve.

ULTRASONIC CHARACTERIZATION OF POLYMERS

S. I. Rokhlin, K. Lewis, F. K. Graff

Department of Welding Engineering

The Ohio State University

Columbus, Ohio 43210

Thermosetting resins are widely used as matrices for advanced composite materials and structural adhesives. Fabrication of composite materials or adhesive joining consists of curing (polymerization) under proper thermal and pressure conditions of resin-impregnated fiber fabrics. During the curing reaction, the thermoset resin transforms from the visco-liquid state to the gel and then vitrified to the gelled glass. This transformation is accompanied by strong changes of the viscoelastic properties of the materials which are related to the molecular network. Therefore, measurements of velocity and attenuation of ultrasonic waves during cure may give important information on the extent of the thermoset curing reaction and the mechanical properties of the material.

Several authors used ultrasonic waves for curing study of thermosetting resins. In spite of these studies not much work has been done to understand the nature of the ultrasonic wave interaction with thermosetting resins during curing. The key issue here is the curing time-frequency-temperature behavior of the ultrasonic wave velocity and attenuation during cure.

In this work we applied an ultrasonic spectroanalysis technique to measure the frequency dependence of the ultrasonic velocity and attenuation, continuously during the cure of the epoxy resin. During the experiment we monitor amplitude and phase changes in the time and frequency domains of the first signal transmitted through the epoxy resin in an experimental cell.

The three dimensional plot of the attenuation coefficient data is shown in Fig. 1. From this data we come to a very important conclusion: the attenuation coefficient behaves linearly with frequency at all stages of the curing reaction from the viscous liquid to the solid state. The slope of the attenuation factor as function of frequency is strongly dependent on time of cure (on degree of cure). The linear behavior of attenuation versus frequency suggests that the attenuation effect cannot be explained by classical viscothermal absorption or relaxation theory. Such type of behavior (so-called hysteresis behavior) is poorly understood on the molecular level and was found previously for some highly viscous liquids, for solid polymers and for biological tissue.

The phase velocity data were evaluation from the phase spectrum of the transmitted signal. These data are shown in Fig. 2. It is seen that there are substantial changes in ultrasonic velocity changes with time and a moderate dependency on the frequency.

The analysis of experimental data suggests that epoxy thermosetting resin behaves as a polymer glass in the MHz frequency range in all stages of the curing reaction. The ultrasonic wave feels the liquid-solid transformation during curing as a transformation in a glassy state, the rate of which of course depends on temperature.

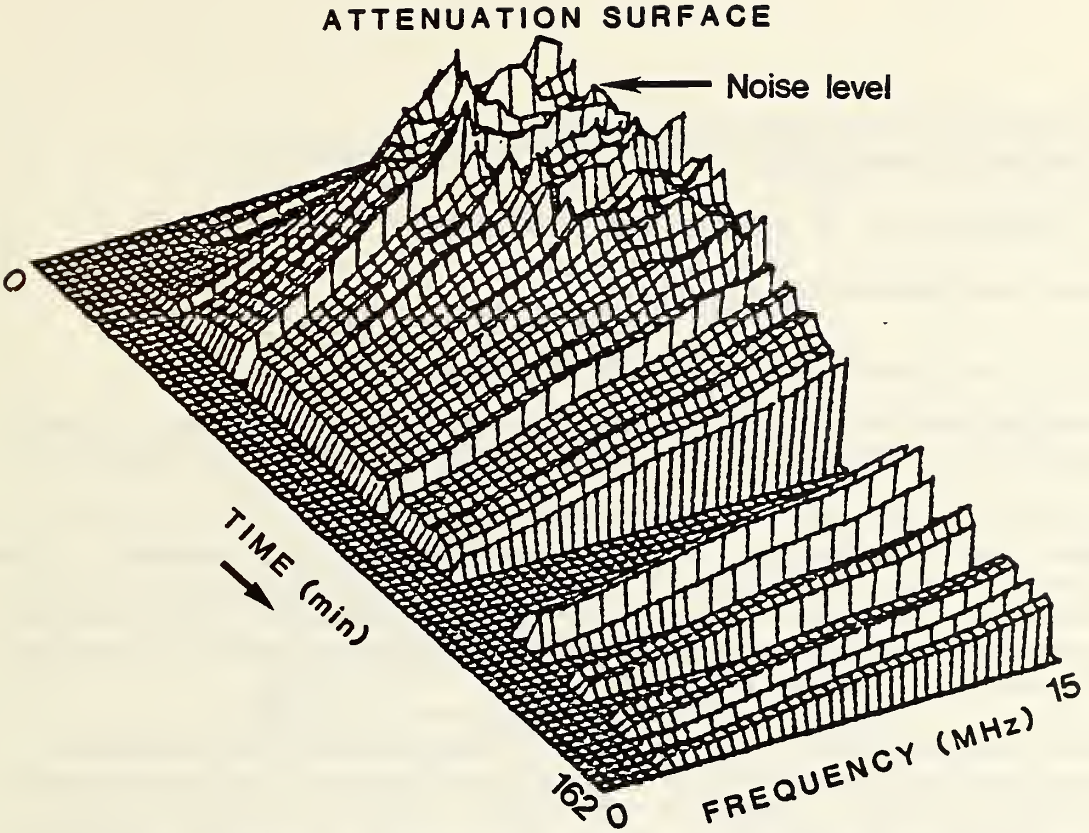

Fig.1 Attenuation coefficient versus frequency and time of curing.

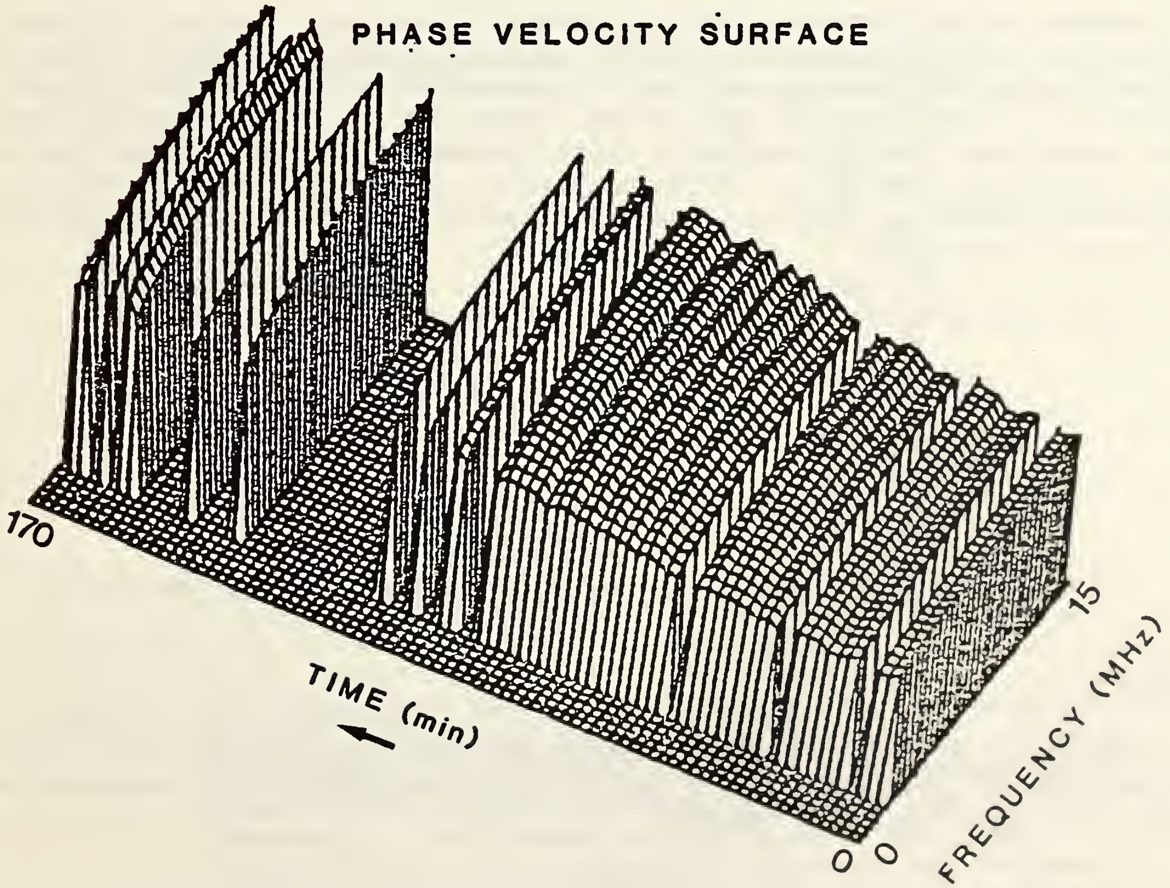

Fig.2 The phase-velocity of ultrasonic wave versus frequency and time of curing.

SOUND VELOCITIES AND ELASTIC CONSTANTS OF REINFORCED COMPOSITES

H. M. Ledbetter, M. W. Austin, and R. D. Kriz

Fracture and Deformation Division

Institute for Materials Science and Engineering

Our studies continue on sound velocities and elastic constants of reinforced composites. These studies involve both measurements and modeling.

A physical property of a composite material depends mainly on three ingredients: matrix property, inclusion property, and phase geometry. Phase geometry includes many variables: volume fraction, inclusion shape, inclusion orientation, inclusion size, and inclusion distribution. For some composites, especially at higher temperatures, the inclusion-matrix interface affects an apparent physical property.

Elastic constants enter many aspects of composite-material behavior: stiffness-weight ratio, load-deflection, elastic instability, thermoelastic stress, residual stress, sound-wave velocities, material characterization, relationship to other physical properties (for example, thermal expansivity and specific heat), plastic deformation, theoretical strength, and nondestructive evaluation.

Because one can measure elastic constants accurately, typically within one percent, they provide good tests of physical-property models. Although isotropic materials possess only two independent elastic constants, a bulk modulus and a shear modulus, composites (depending on their symmetry) possess up to twenty-one elastic constants. Most composites exhibit at least orthotropic macroscopic symmetry, thus nine elastic constants. Uniaxial fiber-reinforced composites exhibit transverse-isotropic (hexagonal) symmetry, thus five elastic constants.

During the last year, we focused on several types of composites:

	reinforcement	matrix
1.	SiC particle	$A\ell$
2.	SiC fiber	$A\ell$
3.	$A\ell_2O_3$ fiber	$A\ell$
4.	graphite cloth	epoxy
5.	glass fiber	epoxy
6.	graphite	ferrite, pearlite (cast iron)
7.	voids	Cu

SUMMARY

We continue to study, both by measurement and modeling, the sound velocities and elastic constants of various two-phase materials. The accompanying figures show some selected results.

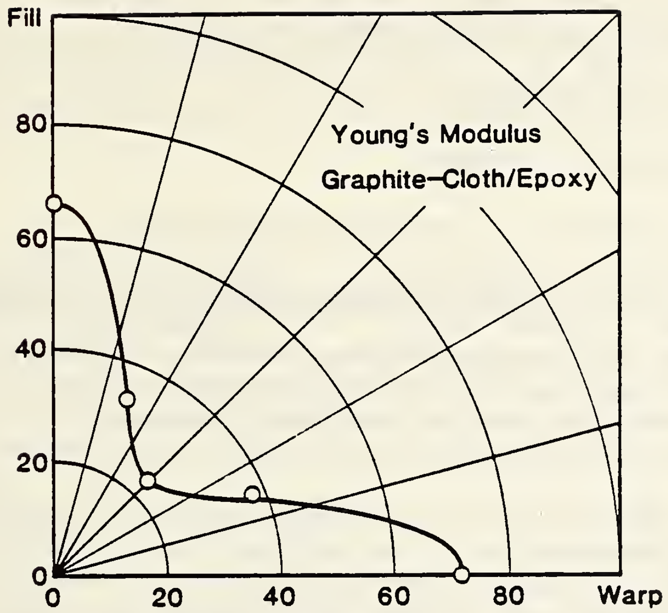

Figure 1. Angular variation of Young's modulus (in GPa) for a graphite-fabric-reinforced epoxy-matrix composite. Curve through measurements represents theory.

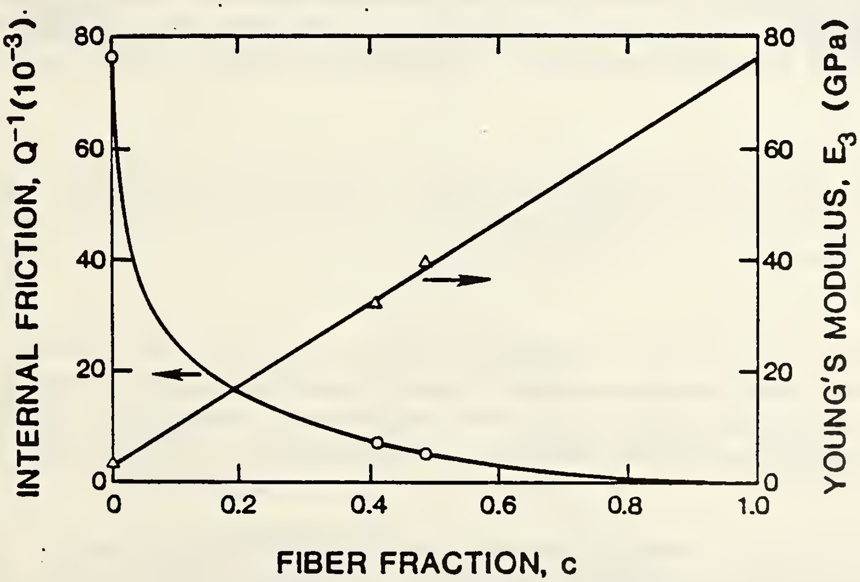

Figure 2. Young's modulus along fiber direction, E_3, and internal friction, Q^{-1}, versus fiber volume fraction, c. Straight line assumes linear rule-of-mixture and represents least-squares fit to three measurements. Curved line for Q^{-1} represents a free damped-oscillator model and linear rules-of-mixture for mass, force constant, and resistance constant. The model contains one adjustable parameter.

INTERNAL STRAIN (RESIDUAL STRESS) IN AN SiC/Al PARTICLE-REINFORCED COMPOSITE: AN X-RAY DIFFRACTION STUDY

H. M. Ledbetter and M. W. Austin

Fracture and Deformation Division

Institute for the Materials Science and Engineering

Silicon carbide and 6061 aluminum alloy possess very different thermal-expansion coefficients: 3.3 and $22.5 \cdot 10^{-6} K^{-1}$, respectively. Thus, one expects large internal strains and stresses in these composites because the two constituents form interfacial bonds at high temperatures and are cooled to ambient temperatures. The studied composite consisted of 30 volume percent SiC particles, approximately 5 μm in size, and shard-shaped.

In principle, one can measure the internal strain by conventional Bragg-Brentano-focusing and $\sin^2\psi$-method x-ray diffraction and compute the internal stress from the elastic constants. One determines the strain by measuring the unit-cell dimensions of both phases, both unmixed and mixed in the composite. If a denotes the unit-cell dimension, then the linear strain is

$$\varepsilon = \Delta a/a = (a_c - a_o)/a_o \qquad (1)$$

where subscript o denotes the unmixed state and subscript c the composite state. Table 1 gives the results of these measurements. Being face-centered cubic, the aluminum alloy possesses one lattice parameter. Being hexagonal, SiC possesses two. The table also contains the bulk modulus, B, and the stress, σ, calculated from the isotropic hydrostatic-stress relationship

$$\sigma = B \Delta V/V \qquad (2)$$

where ΔV/V denotes the volume strain, the sum of the three principal strains:

$$\Delta V/V = \sum_{i=1,3} (\Delta a/a)_i \qquad (3)$$

As expected from the relative thermal expansivities and an elastic sphere-in-hole model, the aluminum matrix shows tensile stress, averaging 259 MPa. The SiC particles show a compressive stress, averaging -219 MPa. The stress in the aluminum matrix amounts to approximately 95 percent of the yield strength, 274 MPa.

Finally, we note that, based on transmission-electron microscopy, some authors suggest enormous dislocation densities in these composites. The diffraction patterns in Fig. 1 do not support this claim. High dislocation densities amount to a high distortion strain, which manifests itself as x-ray-diffraction-peak broadening. Figure 1 suggests only moderate peak broadening, thus only a moderate dislocation density. We intend to study this question quantitatively.

SUMMARY

By x-ray diffraction methods, we studied the internal-strain/residual-stress problem in a particle-reinforced SiC/Aℓ composite. The particles exist in compression, the matrix in tension, approximately 95 percent of the yield strength.

Table 1. Measured strains and computed stresses for Al and SiC

	Al	SiC
$\Delta a/a$ (10^{-3})	1.15	-0.32
$\Delta c/c$ (10^{-3})	-	-0.33
$\Delta V/V$ (10^{-3})	3.45	-0.98
B(GPa)	74.9	223.4
σ(MPa)	259	-219
σ_{yield}(MPa)	274	-

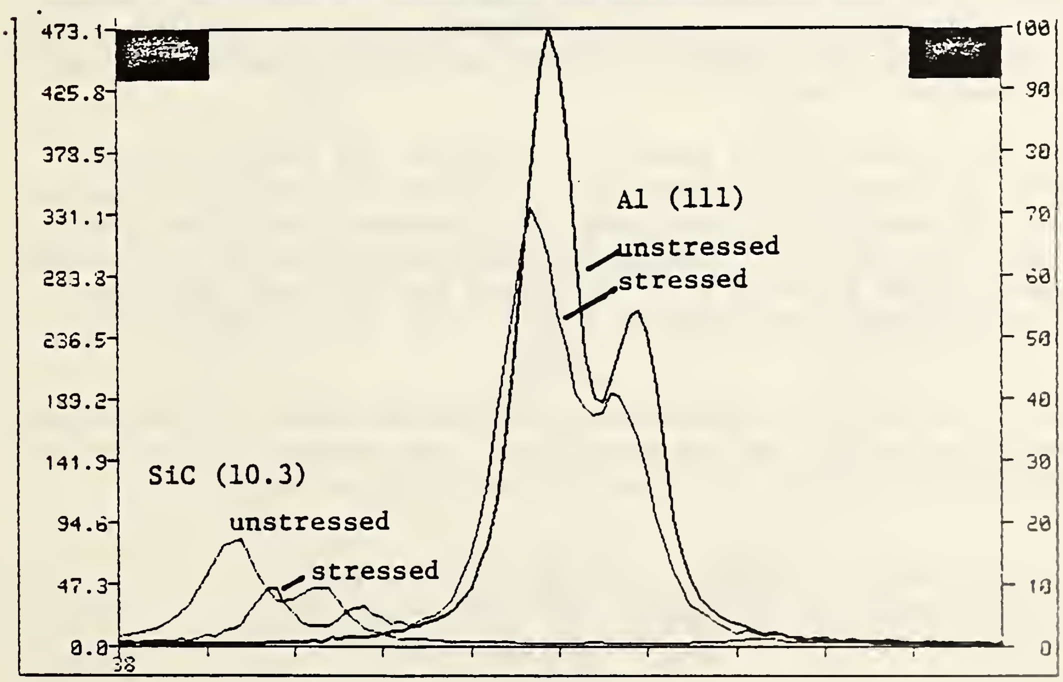

Figure 1. X-ray diffraction pattern for the aluminum (111) line (on right) and for the silicon-carbide (10.3) line. The higher-intensity curves represent the unstressed cases.

EFFECT OF INTERFACE PROPERTIES ON WAVE PROPAGATION IN A MEDIUM WITH INCLUSIONS

S. K. Datta (consultant to NBS)

Department of Mechanical Engineering

University of Colorado, Boulder

Much current practical interest exists concerning wave propagation through a composite medium with a random distribution of inclusions: particles, flakes, or long continuous fibers in a homogeneous matrix. Several theoretical studies report wave speeds and attenuation of coherent plane elastic waves propagating through an elastic homogeneous medium containing spherical or ellipsoidal elastic inclusions. All these studies assume that the inclusions bond perfectly with the surrounding matrix material. Recently, Sayers [1] examined the effect of a distribution of thin elastic spherical shells in a homogeneous matrix material of different elastic properties.

In the present study, we analyze a problem different from the one considered in [1]. We assume that the inclusions possess elastic properties different from those of the matrix. Also, we consider the effect of a thin boundary layer or material through which the elastic properties vary either continuously or discontinuously from those of the inclusions to those of the matrix. Results for the case without a thin layer are obtained by letting the layer thickness go to zero.

The principal object of this study is to explore the practicality of using ultrasound to characterize properties of interface layers in a particulate composite. Ultrasound is a practical tool for measuring properties of, and characterizing the state of, a material with microstructure. References to these various studies occur in [1]. We derive the equations governing scattering by an inclusion surrounded by a thin layer of variable elastic properties. (See Fig. 1.)

We find that the effective phase velocities and attenuation coefficients can be modified substantially by the thin layer. For example, the effective speed of propagation of a plane longitudinal wave is given by

$$\frac{k_1^{*2}}{k_1^2} = \frac{(1 + 9cP_1)\,(1 + 3cP_o)\,\{1 + \frac{3c}{2} P_2\,(2 + 3\tau^2\,)\}}{1 - 15cP_2\,(1 + 3cP_o) + \frac{3}{2}\,cP_2\,(2 + 3\tau^2)} \tag{1}$$

where P_o, P_1, and P_2 depend on material properties. Considering the example of SiC spherical particles in an Aℓ matrix, we find P_1 in this case is 0.02.

Thus, for small h/a we find that the percentage changes in P_0 and P_2 are approximately 174(h/a)% and 88(h/a)%, respectively. These changes should be discernible in phase-velocity measurements. In Eq. (1), k denotes wavenumber, c denotes the volume concentration of inclusions, τ denotes the matrix-material wave-speed ratio, and subscript 1 denotes longitudinal wave.

SUMMARY

This study considers propagation of effective plane longitudinal and shear waves through a medium with a random distribution of spherical inclusions. We assume that inclusions and matrix possess different elastic properties and that a thin layer of elastic material with still different properties separates the inclusions from the matrix. Also, we assume same-size inclusions and same-thickness layers. We find that the layers substantially affect the phase velocities and attenuation of coherent plane waves propagating through this composite medium.

REFERENCES

1. C. M. Sayers, Wave Motion, 7(1985) 95-104.

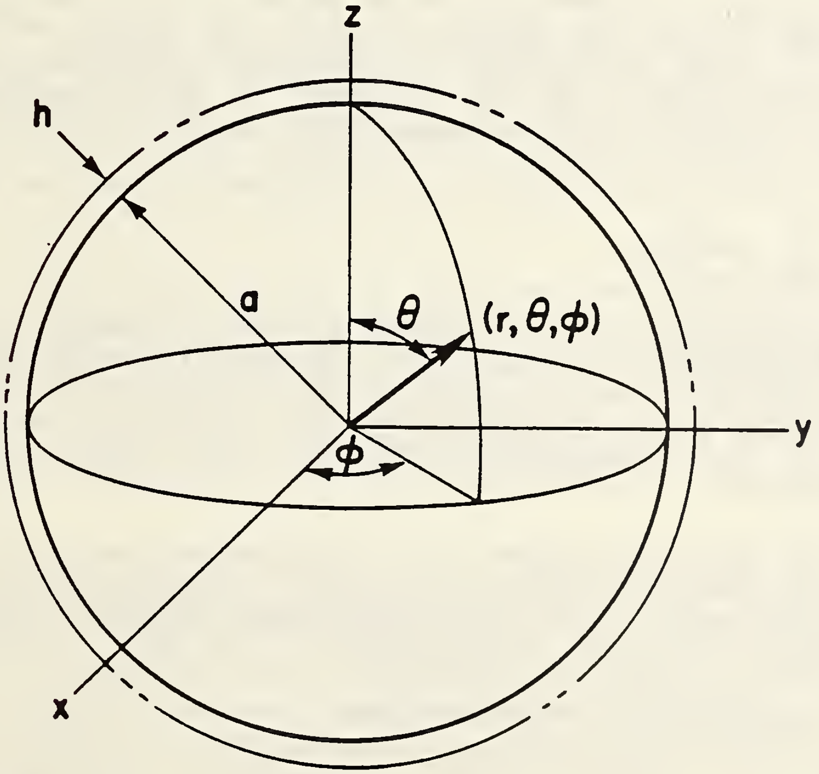

Figure 1. Schematic diagram showing spherical polar coordinates for a spherical particle of radius a surrounded by a layer of thickness h.

CONDUCTIVITY PROFILING BY EDDY-CURRENT MEASUREMENTS

Arnold H. Kahn and Kevin R. Long

Metallurgy Division

Institute for Materials Science and Engineering

The purpose of this project is the development of a theoretical and experimental basis for the determination of electrical conductivity profiles of metallic materials by eddy current methods. Such conductivity profiles are of interest because they are associated with surface hardening processes; traditional eddy current testing, based on a comparison with selective calibration samples is commonly used for quality control but measures only some average depth. This research is aimed at introducing quantitative profiling methods.

In solving the inverse problem of determining conductivity profiles, the quantity of greatest interest, called the admittance function, ref. 1, is given by

$$c(\omega) = E(\omega)/(i\omega\mu_o H(\omega)), \tag{1}$$

where ω is the angular frequency of the ac currents, $E(\omega)$ and $H(\omega)$ are respectively the electric and magnetic fields at the surface of the test material, and μ_o is the permeability of free space. Impedance measurements allow one to determine $c(\omega)$, as will be shown. By general methods of electromagnetic theory, it may be demonstrated that for a finite sample $c(\omega)$ has the form

$$c(\omega) = \sum_{n=1}^{\infty} \frac{A_n}{\lambda_n - i\omega} , \tag{2}$$

where the A_n and λ_n are real. The λ_n are the inverse time constants of the eddy current normal modes of decay; the A_n may be interpreted as the mode strengths. These parameters characterize the test material. They are obtained by fitting the measured values of $c(\omega)$ to a truncated sum of the form of Eq. (2). The truncated sets of λ_n and A_n are used to establish the inversion profile.

The present approach is based on the observation that if $c(\omega)$ consists of N terms, it represents the exact solution of a forward problem of N conductive shells, ref. 1. The shell conductances and their spacings are given by the continued fraction expansion

$$c(\omega) = -h_o + \cfrac{1}{i\omega\mu_o\tau_1 + \cfrac{1}{-h_1 + \cfrac{1}{i\omega\mu_o\tau_2 + \ddots + \cfrac{1}{-h_N}}}} , \tag{3}$$

where the h_i are the spacings between shells with conductances τ_i. h_0 is the distance from the measuring point to the first shell. Finally, we recognize that the model of shells is a discretized representation of a continuous profile. The shells are then smoothed by spreading the conductances of each shell half way to its neighbors, to give a step-like rendition of the profile.

The proposed inversion process consists of the following steps:

1. Perform impedance measurements to obtain $c(\omega)$ at numerous values of the (real) frequency ω, over a range such that the corresponding skin depths span the dimensions of interest.

2. From the measurements of $c(\omega)$, obtain a best fit to a truncated series of the form of Eq. (2).

3. Transform $c(\omega)$ into the continued fraction form of Eq. (3), so as to display the conductances and spacings of the shells.

4. Smooth the representation by shells into a quasi-continuous distribution by spreading the conductances over the region between shells, while keeping the integrated conductivity unchanged.

In testing the outlined inversion procedure, it is important to learn the effects of the finite truncation of the series of Eq. (2). For this purpose a computer simulation was performed for the profile reconstruction of a uniformly conducting slab, for which $c(\omega)$ is known exactly. The series was truncated for $N = 4$, 8, and 16 terms; the reconstructed profiles are shown in Fig. 1. The data are appropriate for an aluminum slab 1 cm thick. The input conductivity is shown as a dashed line.

Several characteristics seen in Fig. 1 are generally observed in inversions by this method. The profiles are ragged at the outer surface, then they are true for roughly half the region, and finally the accuracy deteriorates near the midpoint of the slab. The deterioration is understood to be caused by the symmetry induced vanishing of the interrogating electric field at the midpoint. Since the exciting field is weak in this region, there is little information to be obtained there from a small number of terms in the series.

To demonstrate the inversion process, we performed computer experiments for the inversion of data corresponding to a non-uniform profile. As an example, we present the case of a profile with a step in the conductivity. (In principle, the method could be applied to any profile.) The forward problem was solved and the admittance calculated at 20 frequencies from 1 kHz to 200 kHz. These data were then used as input to the four-step inversion process outlined above. In Fig. 2 we show the results. The input conductivity is drawn as a dashed line. The best fit to the data was obtained with 9 terms in the series of Eq. 2. The horizontal steps give the reconstructed conductivity profile and the vertical lines show the locations of the shells. This is typical of the best performance by this method. More subtle deviations from uniformity would be poorly detected.

The approach has been extended to cylindrical geometry. When the following substitutions are made the complete calculation algorithm still applies:

$$c(\omega) \dashrightarrow Rc(\omega)$$

$$\tau_i \dashrightarrow \tau_i/R_i$$

$$-h_i \dashrightarrow (R_i^2-R_{i+1}^2)/2,$$

where R is the sample radius, the R_i are the shell radii, and the τ_i are the cylindrical shell conductances.

The admittances are obtained from the experimental data by the following relation

$$Rc(\omega) = \frac{1}{2} R^2 + \frac{i}{2} \frac{(Z(\omega) - Z_o(\omega))a^2}{\omega L_o} , \qquad (4)$$

where

$Z_o(\omega)$ = impedance of empty coil
$Z(\omega)$ = impedance of coil with sample
R = radius of sample
a = radius of coil
L_o = inductance of empty coil.

Experimental tests using cylindrical coils have been performed. It was found that the results determine the positions of conductivity change with good accuracy, but that the magnitudes are only qualitatively represented.

While this work initially had been intended to address the characterization of surface modification processes, the methods are generic and may be used for the study of a conductivity profile, no matter how produced. One area of emerging interest is that of temperature profiling, since in many materials the conductivity is a unique strong function of temperature. Discussions with the Aluminum Association have indicated that such an approach could be very useful for determining temperature profiles during the extrusion of aluminum.

SUMMARY

The method of depth profiling the electrical conductivity of a sample material by measuring the frequency dependence of a surrounding coil's impedance has been studied and tested by computer simulation. The theory was extended from planar to cylindrical geometry. Experimental verification was undertaken.

REFERENCES

1. R. L. Parker, J. Geophys. Res. 85, 4421 (1980).

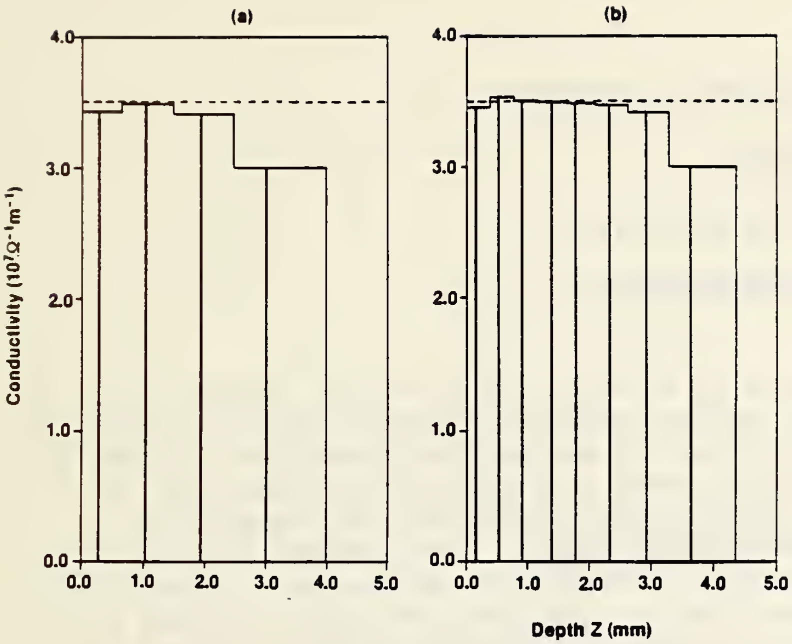

Figure 1. Profile reconstruction of a uniform slab of 1 cm thickness, using exact but incomplete data in Eq. (2). Graphs (a), (b), and (c) have 4, 8, and 16 terms. The vertical lines show the locations of the computed shells; horizontal solid lines show the computed conductivity. The dashed line gives the input conductivity.

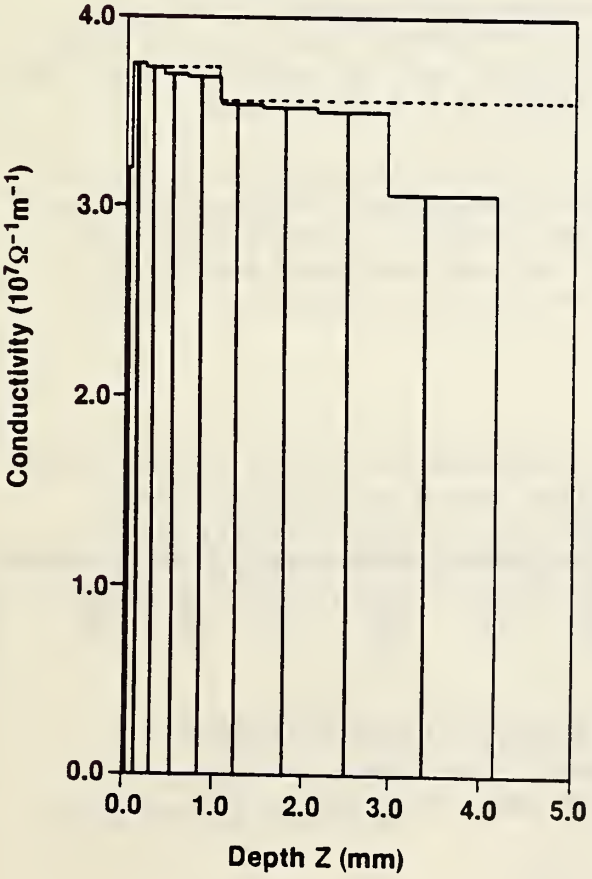

Figure 2. Results of inversion computation for a profile with a step in the conductivity. Input data were for 20 frequencies between 1 kHz and 200 kHz.

ULTRASONIC MEASUREMENT OF SURFACE ROUGHNESS

G.V. Blessing and D.G. Eitzen

Mechanical Production Metrology Division

Center for Manufacturing Engineering

The purpose of this research is to study the effect of surface part roughness on the scattering of incident ultrasonic waves; and then in turn to address the inverse problem of evaluating surface part condition by means of the scattered wave. Related studies were initiated several years ago in support of an ASTM project to evaluate the relationship of roughness to (apparent) material attenuation in steel plate[1]. The program has since evolved to developing the ultrasonic technique for monitoring roughness features on static and moving parts. Both liquid and air-coupled schemes are being investigated. While the amplitude of reflected echoes at normal incidence is being given principle attention, off-angle and multi-transducer schemes are also being investigated.

Figure 1 illustrates recent ultrasonic results on a flat aluminum strip with five increments of roughness ranging from to 0.8 to 37 µm rms. Each roughness section was nominally 5 cm square on the 25 cm long specimen. The peak-detected echo amplitudes of the back scattered pulses are recorded as a function of transducer position along the sample length. (The time for this transducer sweep was a few seconds.) The sharp (step) boundary between roughness sections is evidenced by the sudden drop in signal amplitude due to boundary scattering. The pulse-echo measurements were made at normal incidence, with a water squirter system coupling transducer and part via a one cm water jet path (0.6 cm diameter) between nozzle exit and part surface. The ultrasonic frequency was 5 MHz, for a wavelength of 0.3 mm in water.

This approach has also been successfully applied to curved surfaces, on stationary and rotating cylindrical parts with roughnesses comparable to the strip values above. In the case of the (7 cm diameter) rotating part, the detected echo amplitude faithfully recorded the same scattered amplitude as was obtained on the stationary part, up to the tested rotation rate of 200 rpm.

SUMMMARY

A good correlation between rms surface roughness and reflected ultrasonic echo amplitude has been obtained. The coupling medium can be air, water immersion, or a squirter (similar to a machine tool coolant stream). The interrogated surface can be flat, curved, stationary, or moving. We will seek to direct the work toward in-process control of the surface finish of parts produced by automated machining.

REFERENCE

1. G.V. Blessing, P.P. Bagley, and J.E. James, "The Effect of Surface Roughness on Ultrasonic Echo Amplitude in Steel," Materials Evaluation 42, pp 1389-1400 (Oct. 1984).

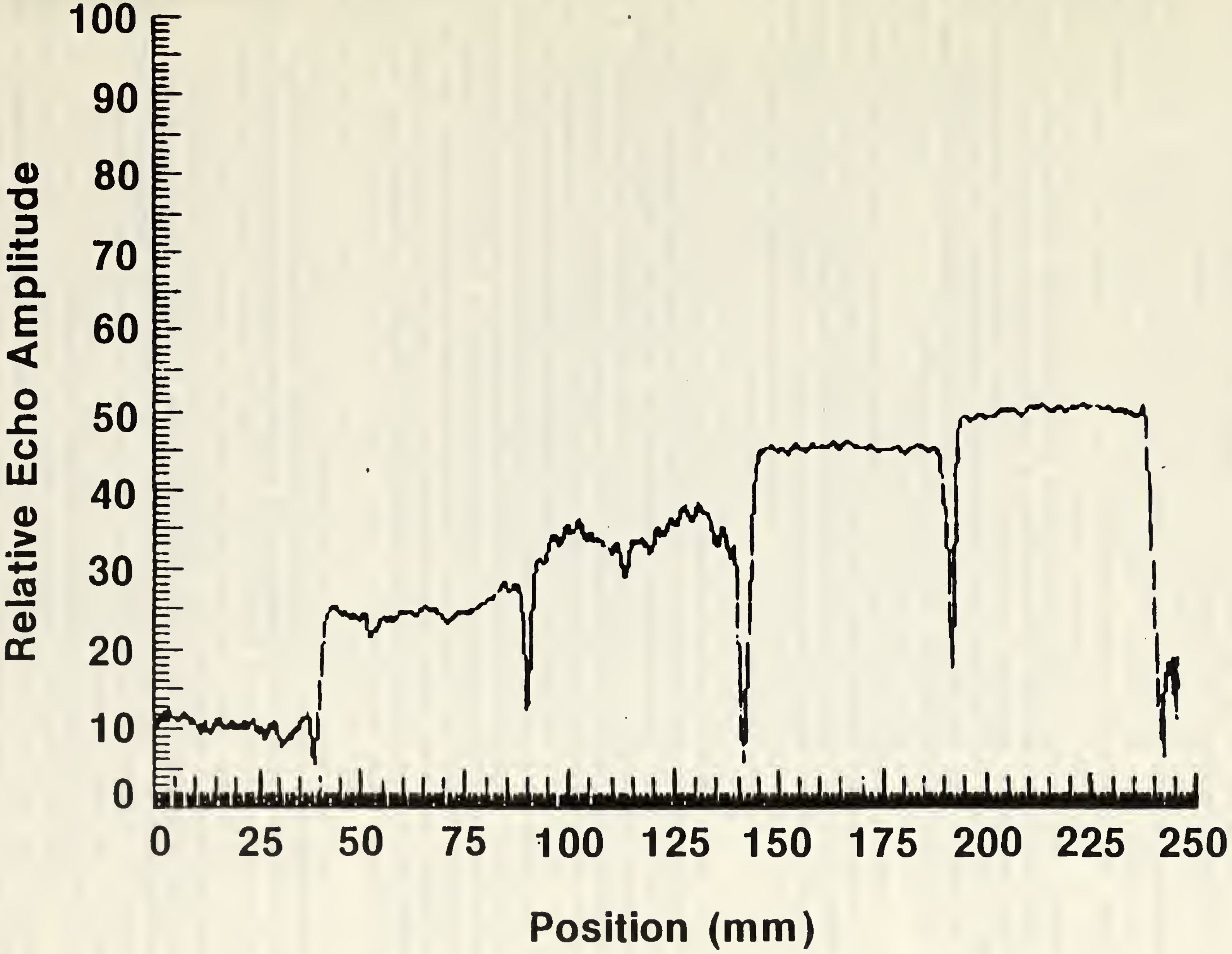

Figure 1. Ultrasonic echo amplitude versus transducer position as a function of decreasing surface roughness for five increments of roughness: 37, 20, 14, 7, and 0.8 μm rms.

OPTICAL MEASUREMENT OF SURFACE ROUGHNESS

T. V. Vorburger, D. E. Gilsinn, E. C. Teague, M. J. McLay,
F. E. Scire and C. H. W. Giauque

Mechanical Production Metrology Division

Center for Manufacturing Engineering

Optical scattering techniques are being used extensively to study and monitor the surface roughness of a variety of optical, semiconductor, and mechanical components produced by industry. However, the successful development of these techniques carries the need for a better understanding of the physics of optical scattering from rough surfaces as well as for standardization of some of the more practical approaches for on-line measurement.

Our research in optical scattering is directed along two lines. First, we are performing basic research into the quantitative understanding of the relationship between rough surface topography and the resulting optical scattering patterns. Second, we are working on practical approaches for the use of the optical scattering method in an automated inspection station and as a manual tool for inspecting the roughness of components with unusual shapes.

On the basic research side, we have completed a study of the inverse scattering problem for six sinusoidal surfaces with varying amplitudes and spatial wavelengths. Table I shows a comparison of values for roughness average R_a and spatial wavelength D calculated from the optical angular scattering measurements with R_a and D values measured by a stylus instrument on samples machined in the same batch runs as those measured optically. The agreement between the results is well within the uncertainties of the measurements which were on the order of 1-3 percent. Our main conclusion from these results is that for the wide range of wavelengths and roughnesses represented by these surfaces the straightforward optical theory that we used is sufficiently valid to be useful for measuring geometrical roughness parameters of surfaces. We have now begun the work of building a surface statistical model that will allow for successful application of inverse scattering techniques for measuring realistic, random rough surfaces.

On the applied research side, we are developing instruments for measurement of surface roughness in the two practical situations mentioned above. Both of these use a commercial optical sensing unit with a 20 element detector array to measure the optical scattering distribution. Figure 1 shows the on-line optical instrument (termed the ragun) for monitoring surface roughness in operation at the Automated Inspection Station in the NBS Automated Manufacturing Research Facility. The robot moves each part to be measured in front of the ragun for roughness inspection. The instrument is at an early stage of development. At later stages we plan to direct the optical alignment of the part with data presented to the robot controller by the ragun and to quantify the measured scattering results in terms of standard roughness parameters.

Towards that end, we have compared results measured with this instrument with measurements of rms roughness R_q using the stylus profiling instrument and with angular distributions measured by our research optical instrument named

DALLAS,[1] that has been discussed in previous reports. Measurements were taken on three hand lapped stainless steel specimens of varying roughness.

The scattering geometry of the on-line instrument is somewhat different from that of the DALLAS instrument (Fig. 2). In both cases the surface is oriented with respect to the instrument in such a way that the detector array intercepts the planar pattern of scattered light. The on-line instrument has been discussed by Brodmann, et al.[2] and is shown schematically in Figure 2a. It consists of an optical source with an infrared wavelength of about 800 nm and a 20-detector photodiode array that spans a scattering angle (2ϕ) of 30°. The angle of incidence α is equal to 8.4°, just far enough off normal so that the optics for collecting the scattered radiation do not interfere with the incident beam. Under proper alignment, the long axis of the detector array is parallel to the roughness direction on the surface, i.e., perpendicular to the lay of the machining marks. In the DALLAS setup, the angle of incidence θ, which may be varied, was set at 40°, and the roughness direction and the plane of the semicircular detector yoke were oriented in the plane of incidence. The detector yoke consists of 87 detectors separated by 2°, which span a total scattering angle of ±86° with respect to the surface normal. Therefore, the scattering angle range of the DALLAS detection system is a little less than three times that of the on-line instrument.

The two sets of angular scattering results are shown in Figure 3. As the rms roughness measured by the stylus instrument increases, the angular scattering pattern broadens for both instruments. In particular, the DALLAS result for the surface #14 with 0.078 μm R_q clearly shows a strong specular beam at a scattering angle of -40°. This peak disappears and the diffuse scattering curve broadens for the two rougher surfaces. The on-line sensor data do not show a narrow specular beam because the angular resolution of this instrument is broader owing to the finite convergence angle of the incident beam. Nevertheless, these scattering patterns also show increasing width as R_q increases. In addition, a scattering pattern index, shown as S_N, tracks the R_q roughness values. S_N is a nonstandard parameter introduced by the manufacturer of the on-line instrument, that is directly proportional to the variance of the bell-shaped scattering pattern. In Figure 3, the S_N value tends to increase with the rms roughness. Figure 3, therefore, shows a clear correlation between roughness and scattering for this small number of specimens and this correlation may be exploited to measure the roughness of hand lapped specimens.

Our future work in this area will include research on the appropriate statistical model for optical scattering from industrial surfaces and continued development of the on-line instruments.

For practical use of the on-line instrument we are working to obtain a reliable relationship between S_N and one of the standard profile parameters. For the manual version of the on-line instrument, we must develop mechanical adapters that will enable it to be aligned with curved surfaces.

We also plan to interface the on-line instrument to a desktop computer and perform the inverse calculation with the appropriate statistical models to derive the surface roughness parameters directly.

SUMMARY

During FY 85 we have completed a comparison of optical and stylus measurements of roughness parameters on sinusoidal surfaces and find excellent agreement between them. We have also installed an optical scattering instrument in an on-line system to monitor surface roughness on parts manipulated by a robot and correlated results from this instrument with results obtained from a research angular scattering instrument and from a stylus instrument.

REFERENCES

1. T. Yolken and L. Mordfin, editors, "Office of Nondestructive Evaluation - Technical Activities 1984," NBSIR 84-2944 (Nov. 1984) p.3.

2. R. Brodmann, O. Gerstorfer, and G. Thurn, Opt. Eng., "Optical Roughness Measuring Instrument for Fine-Machined Surfaces," Opt. Eng. 24, No. 3, pp. 408-413 (May/June 1985).

Table 1

Comparison of Stylus and Optical Measurements of Roughness Parameters

(D = surface wavelength, all units in μm)

Surface	Measured by Stylus		Deduced From Optical Scattering	
	R_a	D	R_a	D
Brass 1	1.02	40.1	1.013	40.0
Brass 2	1.02	100.2	1.013	100
Brass 3	1.01	801	0.98	794
Nickel 1	1.03	100.2	1.011	100
Nickel 2	0.31	100.2	0.311	100
Nickel 3	2.98	100.1	3.008	100

Figure 1. The ragun optical roughness instrument in operation at the NBS AMRF.

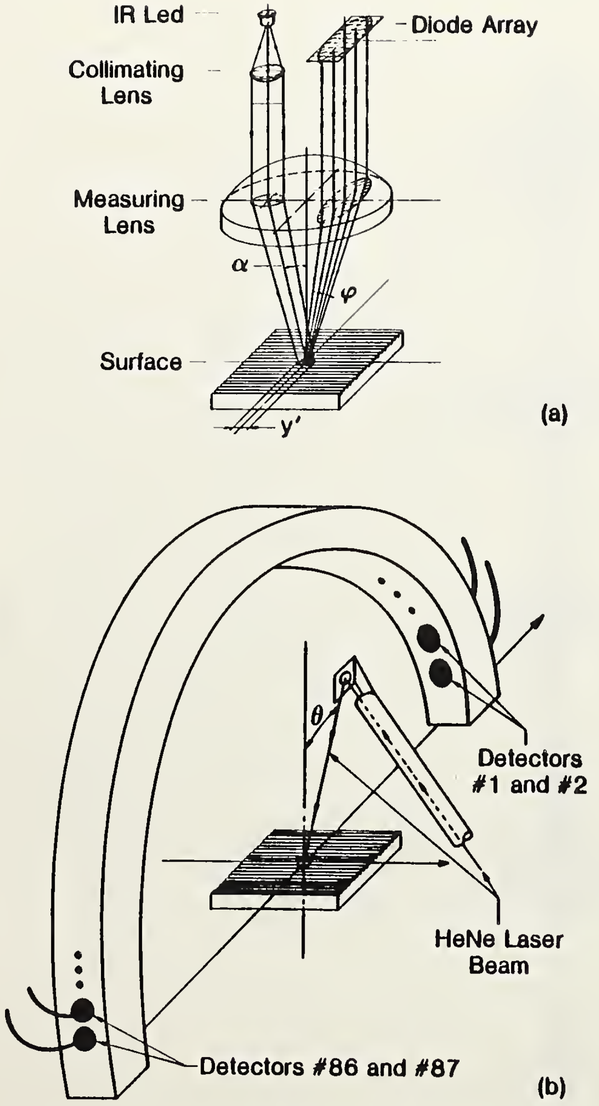

Figure 2. Scattering geometries for the on-line instrument (a) and the DALLAS instrument (b). (a) is taken from Ref. 2.

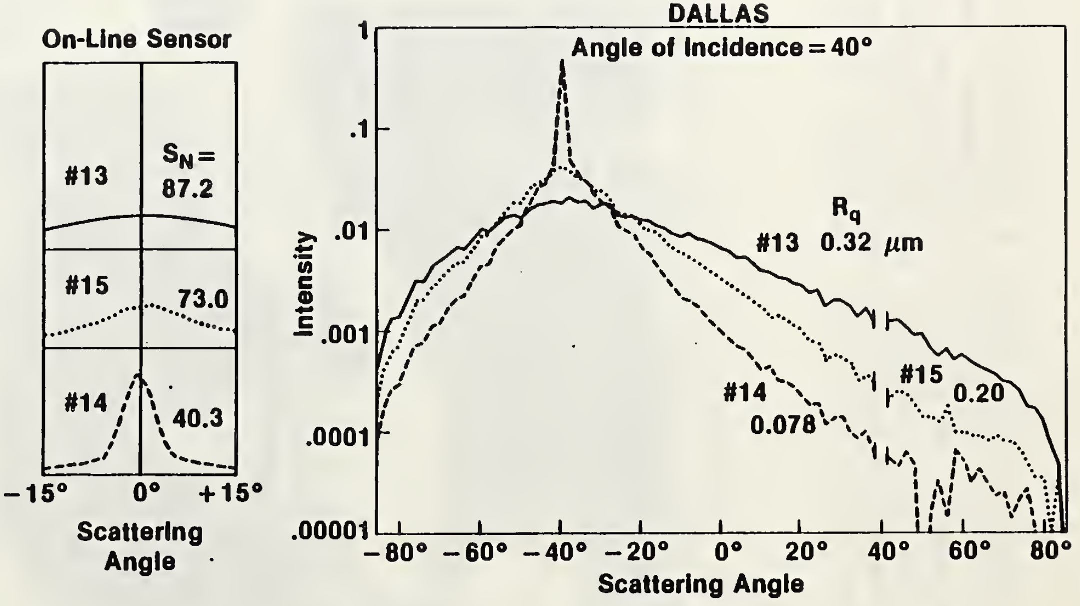

Figure 3. Measured optical AD's with the on-line sensor (left) and the DALLAS instrument (right) for hand lapped stainless steel roughness specimens. The DALLAS data are plotted on a logarithmic scale that spans five orders of magnitude whereas the data for the on-line instrument are plotted linearly with intensity. The scattering index S_N is proportional to the variance of the scattering pattern about the mean.

NONDESTRUCTIVE EARLY DETECTION OF CORROSION AND DELAMINATION UNDER PROTECTIVE COATINGS USING THERMAL WAVE MICROSCOPY

T. Nguyen and M. E. McKnight

Building Materials Division

Center for Building Technology

Thermal wave (TW) microscopy has proven to be an excellent method to image microfeatures beneath the surface of both transparent and opaque samples. The main objectives of this study are to determine the feasibility of thermal-wave imaging as a sensitive nondestructive method for detecting early corrosion and defects at the steel/coating interface and to propose a procedure for using the method. The information obtained, can, however, be applied to numerous areas of materials science. In 1984, the research results demonstrated that thermal wave microscopy is capable of imaging the microstructure of steel with or without a corrosion layer. The results also showed that TWM could be used to image corrosion spots of $\geqslant$ 5μm in size under a clear coating. In 1985, we utilized the technique to 1) detect corrosion of metal under an opaque (pigmented) coating and 2) investigate how far thermal waves can penetrate through a protective coating to detect the corrosion of metal underneath.

In addressing the first area, both rough and polished cold-rolled, SAE 1010 steel samples, which had been corroded during exposure to 90 % RH and 40° C, were employed. The thermal wave imaging system used has been described previously (1,2). The scanning electron microscope backscatter (SEM) and TW images of these corroded (uncoated) steel samples are shown in Figure 1 and 2. As shown in these figures, both SEM backscatter and TW were able to image regular type of corrosion on both polished and rough steel. However, close examination of these micrographs reveals that it is quite difficult to distinguish between the corrosion from the surface roughness features in the SEM backscatter images (Figure 1a). Indeed, our computerized image analysis was not able to distinguish differences in gray levels between the corrosion and surface roughness on this image. As a result, the area and the percentage of corrosion could not be computed. In contrast, corrosion clearly stands out in the TW images; and this is most pronounced at 142 kHz frequency. Based on this image, the thickness of the corrosion layer was estimated to be about 7μm. The sharp contrast on the TW images also allowed rapid and reliable calculations of the area and percent of corrosion on steel by image analysis.

After taking the images, the uncoated samples were washed repeatedly with acetone and ethyl alcohol (to ensure a wettable surface), then dried with hot air before application of the pigmented coating. An orange alkyd coating (125 cps viscosity) was flooded on these specimens and spun horizontally using a spin coater to obtain uniform opaque coatings of $\simeq$ 2.5μm in thickness (thickness was calculated based on spin speed and coating viscosity). The samples were cured at 150° C for 30 minutes. TW and backscatter SEM images of the samples, which were taken after conditioning for two weeks at room temperature, are shown in Figures 3 and 4. These figures demonstrate clearly that TWI is capable of imaging very early corrosion of steel under an opaque coating. The contrast due to corrosion is also visible in the SEM image. In the SEM image, however, the image is due to the contour of the corrosion spot (where the resin follows as a result of the spinning action) rather than to a difference in thermal properties between the corrosion products and steel substrate (as is the case with TWI).

To address the problem of the depth of penetration of thermal waves in organic coatings, a clear, crosslinked network epoxy coating on rough, corroded cold-rolled steel samples was employed. 25 mm x 25 mm steel samples were divided into 6 sections. After covering one of the 6 sections with a pressure sensitive adhesive tape, a coating layer of 2μm thick was applied. The thickness was estimated based on a calibration curve established by using reflection/absorption Fourier transform infrared technique. The coated sample was then cured at 180°C for 30 minutes. The taping and coating procedure was repeated until coating thickness of 0, 2, 4, 6, 8, and 10μm were obtained on 25 mm x 25 mm corroded samples (Figure 5). Gold coatings of 200 and 400 A° were evaporated on the samples to protect the organic coatings because our preliminary investigation indicated that organic coatings of ⩾ 3μm thick on steel substrate underwent charging and/or burning at 30 kv power. Representative TW and SEM images of these samples are shown in Figures 6 - 10. The micrographs showed that corrosion under coatings, up to 10μm thickness, could be imaged by TWI. It should be noted, however, that in some cases bubbling and charging were observed on gold coatings (Figure 11) and that there was no noticeable difference of these effects between the 200 and 400 A° Au films. These burning and bubbling problems could affect the "effective thickness" to be imaged above the corrosion spots. Nevertheless, SEM micrographs of the same area of some imaged sections did not show the corrosion, indicating that the organic coatings on these sections were still preserved. We shall investigate the use of lower power (20 and 25 kv) and/or carbon coating in place of gold as possible solutions to eliminate the gold bubbling problem. We will also investigate the use of laser thermalwave, thereby possibly eliminating the elaborate specimen preparation requirements and also possibly providing imaging to greater depths. The results obtained indicated that TWM is capable of imaging corrosion of steel beneath an opaque, ≃ 2.5μm organic coating and quite thick clear coating. However, for complete assessment of the potential of TWI as a nondestructive method to detect corrosion under protective coatings and paints, additional studies on the effects of type of coatings (organic, inorganic and metallic) and particle size and type of pigments on the imaging capability of TWM are needed.

SUMMARY

The results obtained indicated that TW provides sharper contrast of the corrosion of steel than conventional SEM. The results also showed that TW can image the corrosion under both clear and pigmented coatings. For clear coating, TW was able to image corrosion of steel under organic coating up to 10μm thick. For both clear and pigmented coating of greater than 3μm, a gold film must be employed to protect the organic coating from burning or charging. However, gold films do not seem to always protect effectively the organic coatings. The use of lower power or laser thermal waves should be considered to alleviate the burning problem caused by electron TW at high power.

REFERENCES

1. T. Nguyen and M. E. Mcknight, "Office of Nondestructive Evaluation," NBSIR 84-2946, pp. 17 - 24 (Nov. 1984)

2. T. Nguyen and A. Rosencwaig, "Thermal-wave Microscopy and Its Applications to Imaging the Microstructure and Corrosion of Cold-rolled Steel," Appl. Surface Sci., 24, No. 1 (1985).

3. T. Nguyen, "Thermal-wave Imaging of the Microstructure and Corrosion of Cold-rolled Steel under Protective Coatings," J. Industrial Engineering Chemistry Product R and D, Accepted for publication, June/1985.

ACKNOWLEDGEMENT

We wish to thank Craig Olson, Metallurgy Division for helping to obtain the backscatter SEM and TW images.

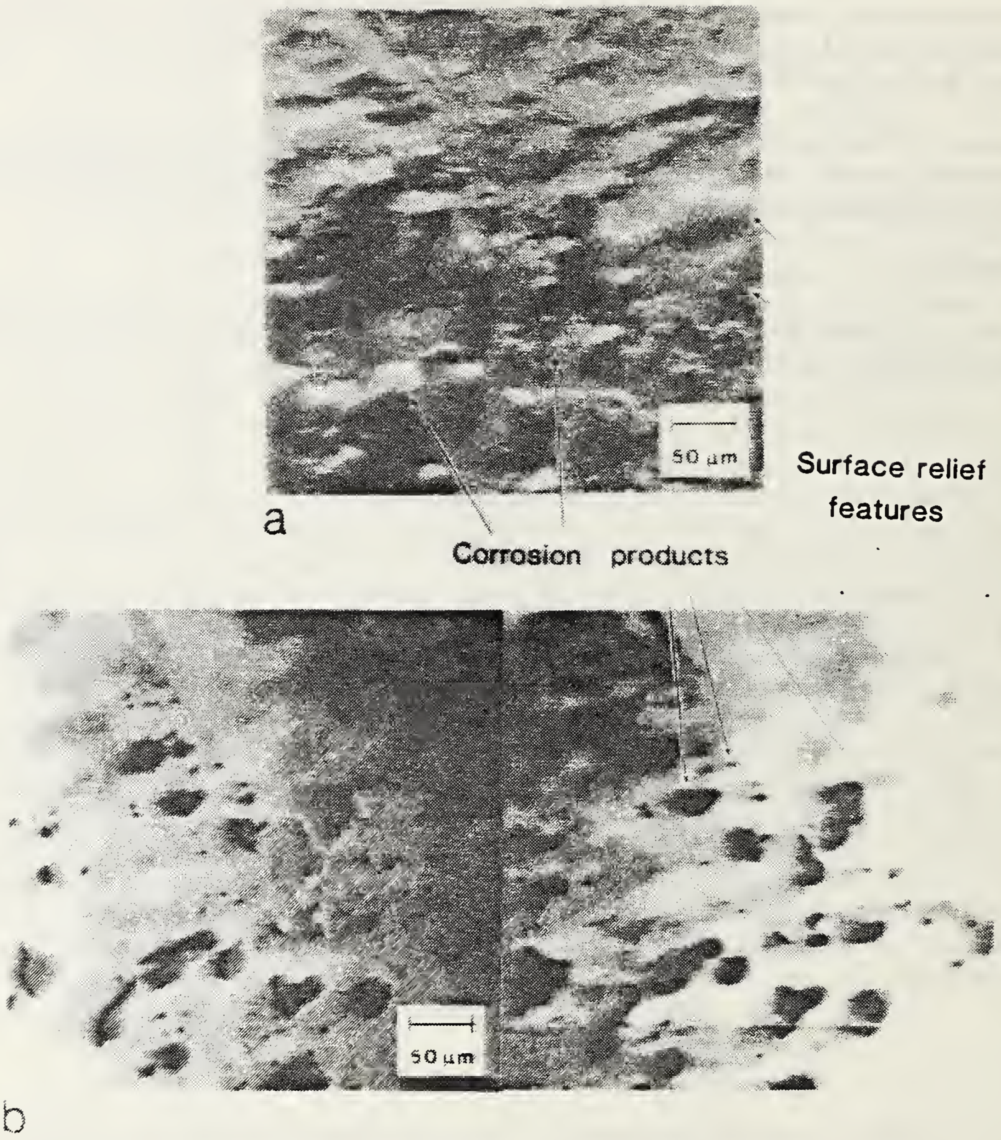

Figure 1. Images of corrosion on uncoated, rough, cold-rolled steel a) SEM b) Thermal Wave (TW) at 79 kHz modulation frequency, and c) TW at 142 kHz, showing well-resolved contrast between corrosion products and surface roughness by TW.

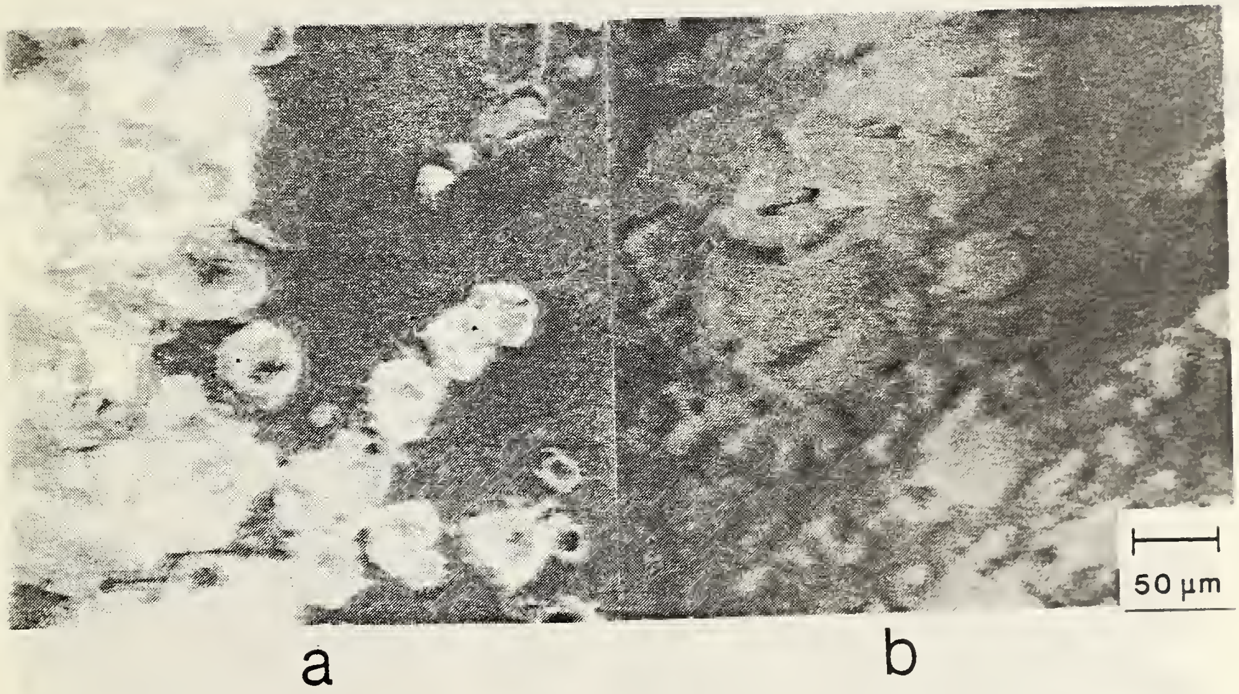

Figure 2. SEM (a) and TW (b) images of corrosion of uncoated, polished, cold-rolled steel, showing less constrast of the corrosion products on polished steel by TW.

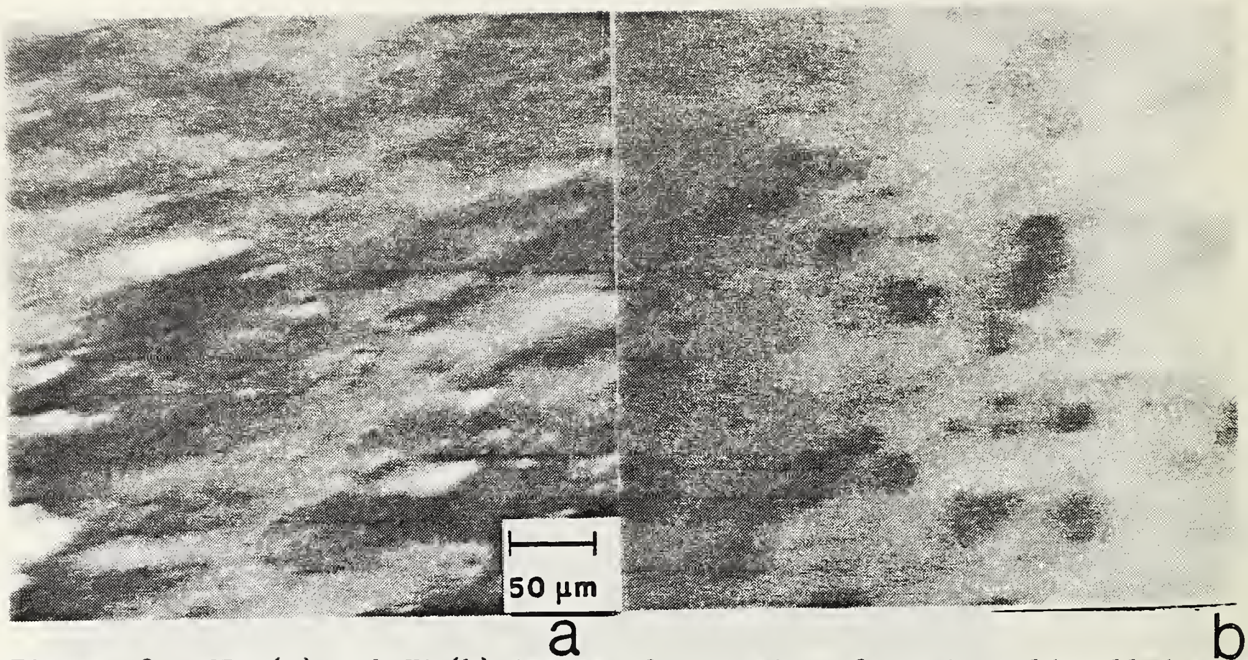

Figure 3. SEM (a) and TW (b) images of corrosion of rough, cold-rolled steel under a 2.5μm pigmented (orange) organic coating, showing the imaging capability of corrosion underneath an opaque coating by TW.

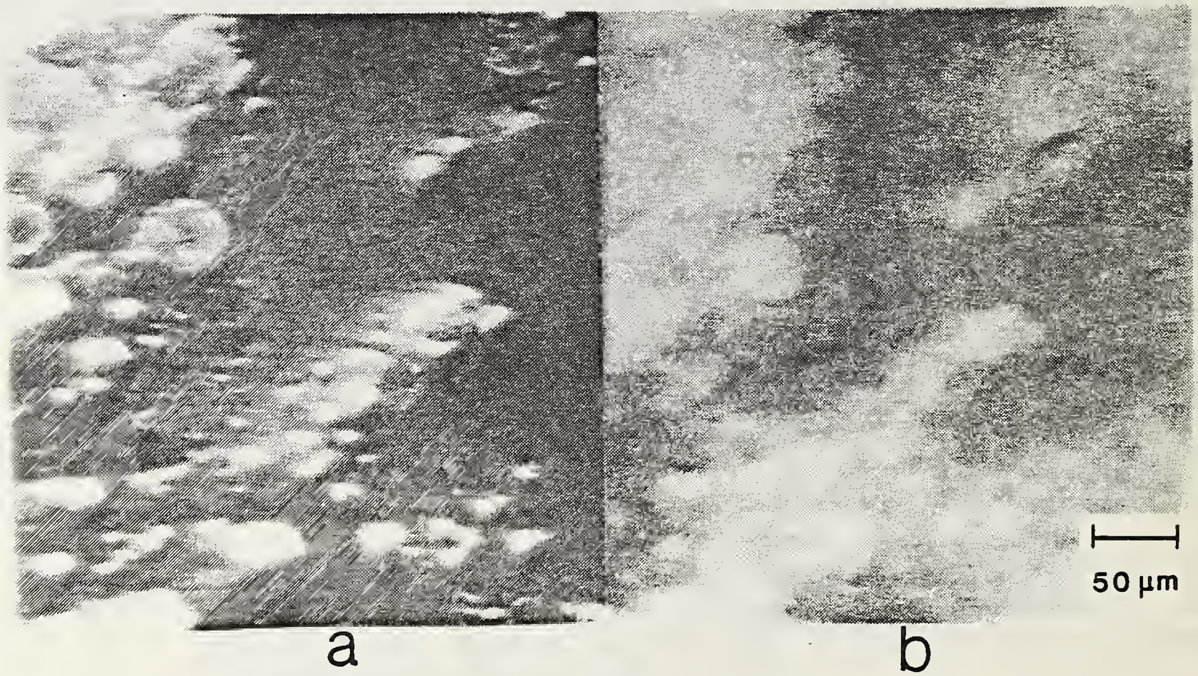

Figure 4. As figure 3 but on polished steel sample.

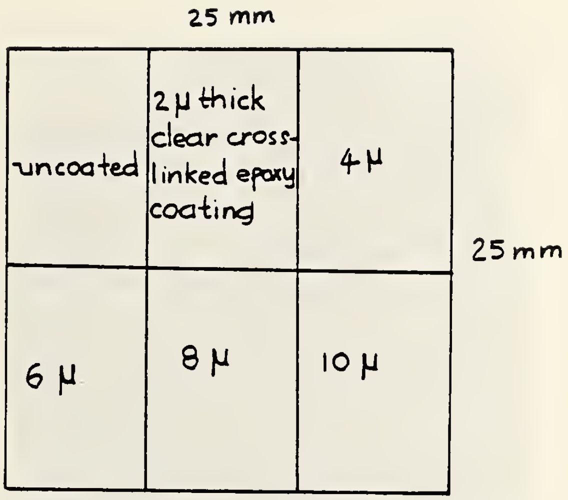

Figure 5. Corroded steel sample with different organic coating thickness for studying the effect of coating thickness on the TW imaging of corrosion beneath coating.

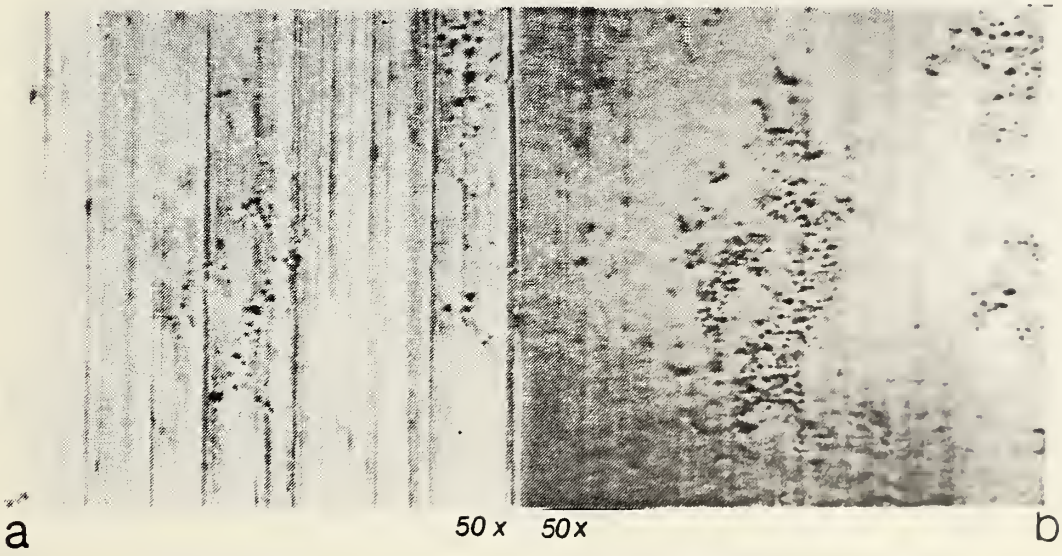

Figure 6. SEM (a) and TW (b) images of corrosion of steel coated with a 200 A° Au film.

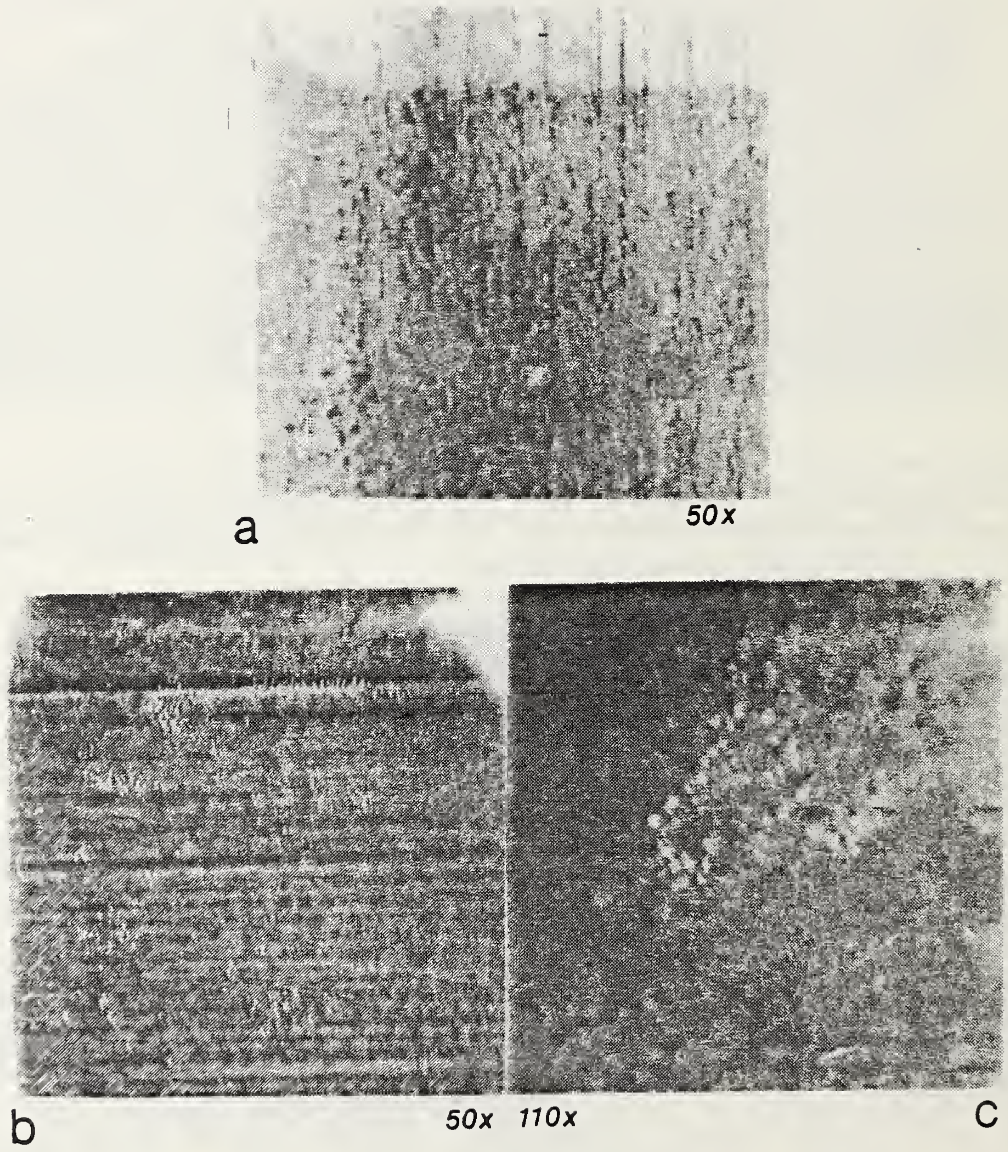

Figure 7. SEM (a) and TW (b and c) images of corrosion of steel underneath a 8 μm organic coating which was protected by a 200 A° Au film on top, showing very well the corrosion under rather thick organic coating by TW.

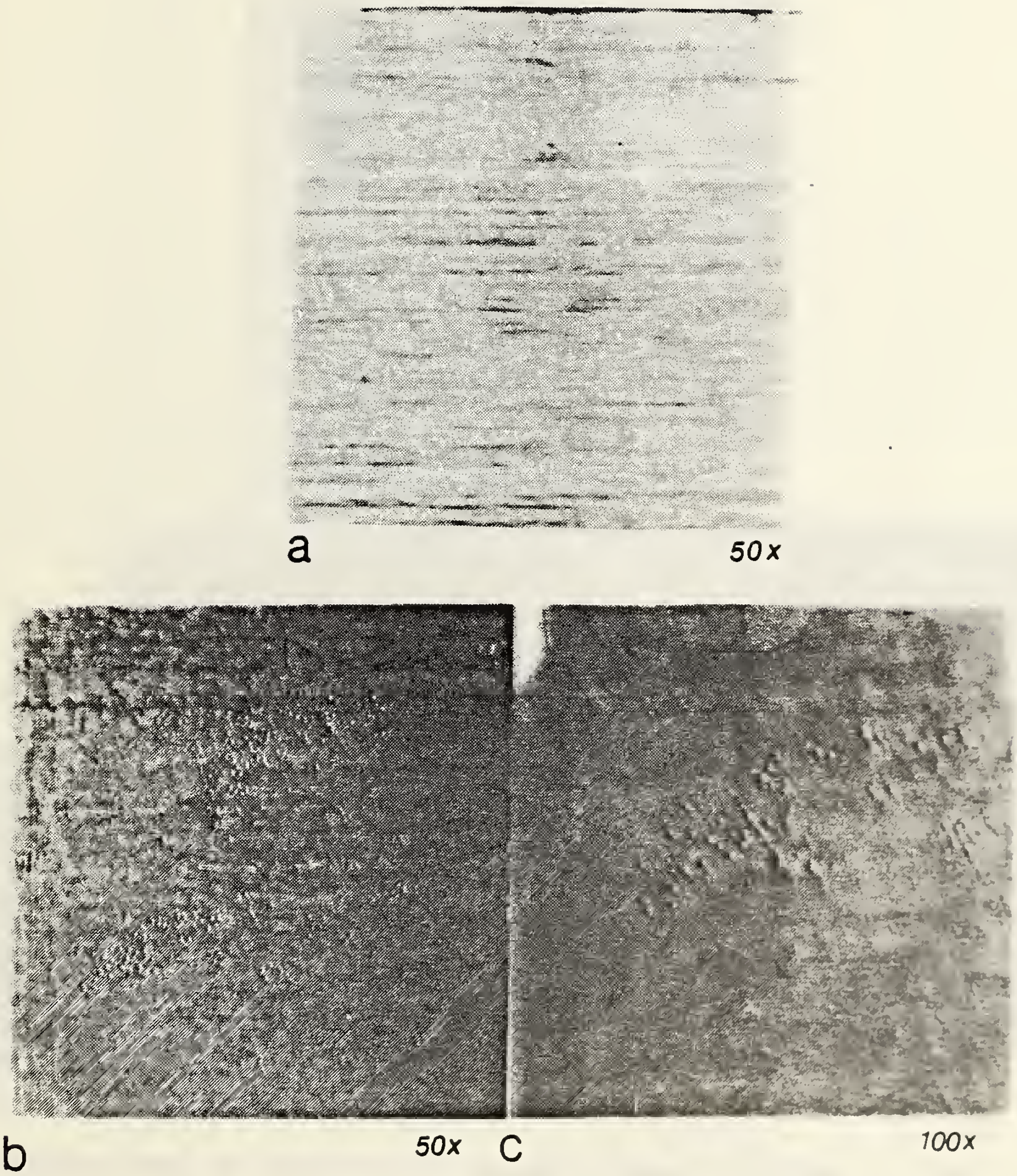

Figure 8. As figure 7 but the thickness of organic coating is 10µm. The corrosion products are visible in the SEM image indicating that probably some gold and organic coatings have been burned.

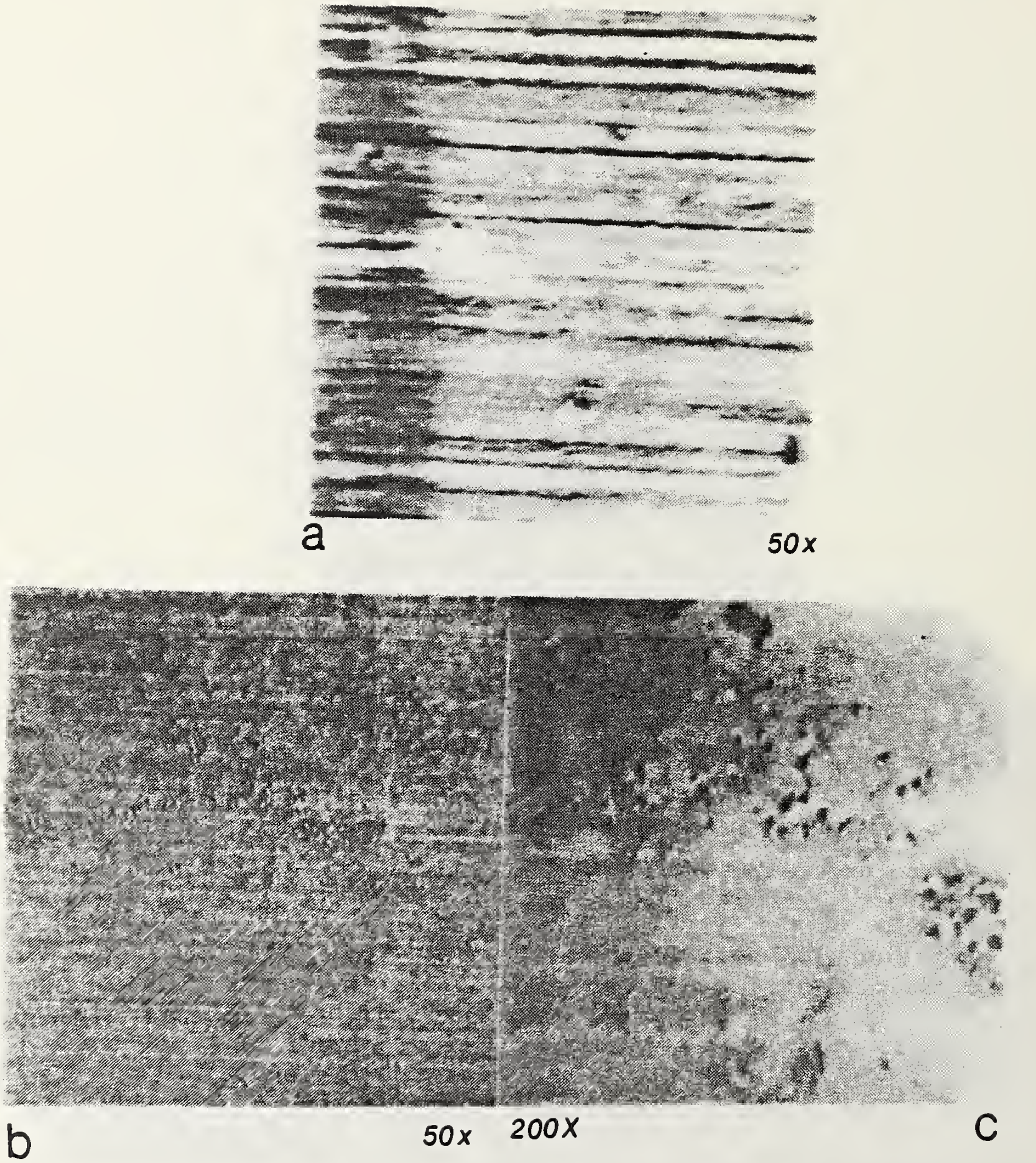

Figure 9. SEM (a) and TW (b and c) images of corrosion of steel underneath a 6 μm organic coating which was protected by a 400 A° Au film on top.

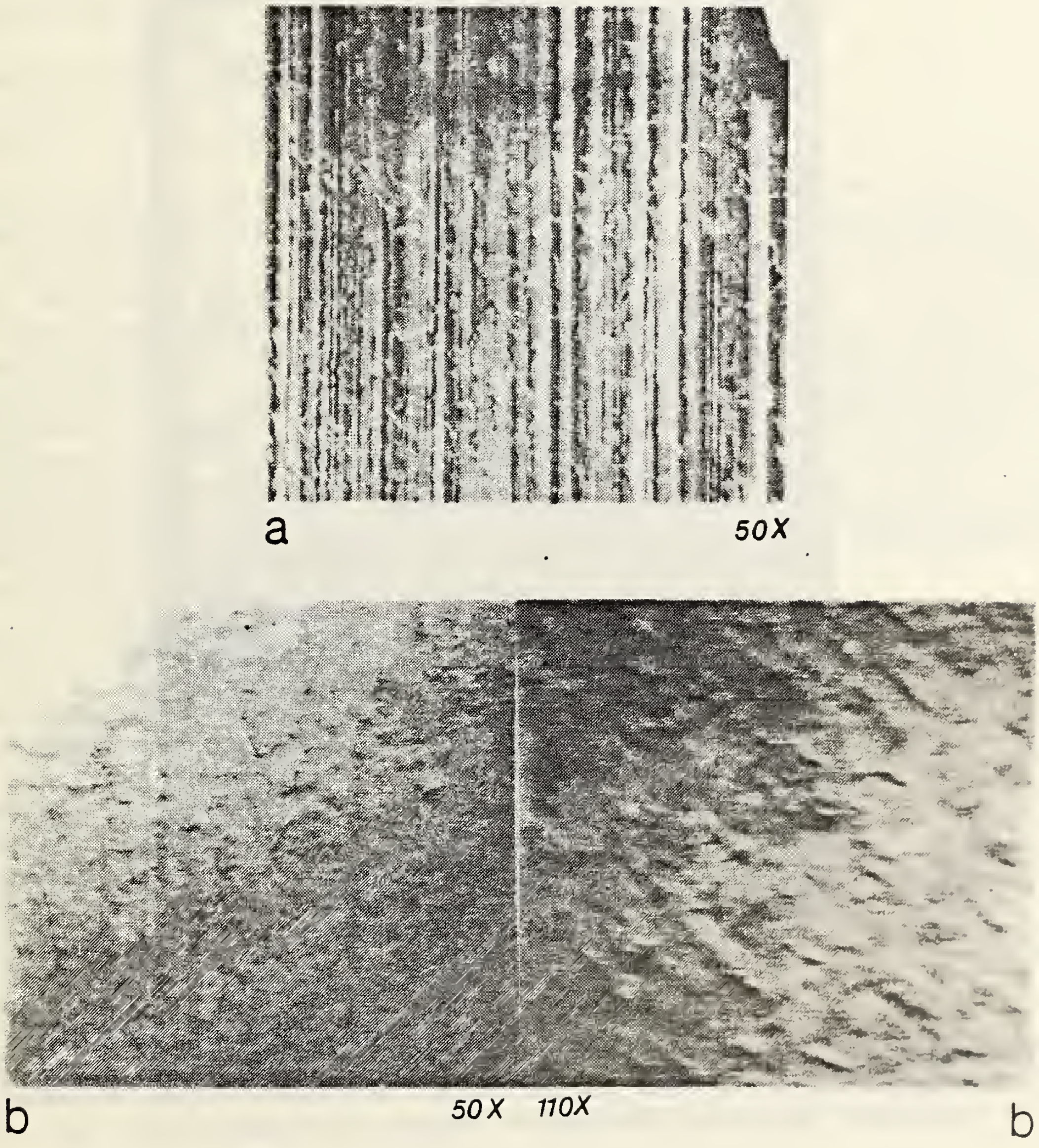

Figure 10. As 9 but the thickness of the organic coating is 10μm.

Figure 11. Polarized light microscopy at 600x showing the bubbling and cracking of gold films on some of the imaged sections. (Gold films were employed to protect the thick organic coatings).

THERMAL WAVE MICROSCOPY FOR USE IN NEAR SURFACE CRACK DEPTH AND ORIENTATION DETERMINATION IN METALLIC MATERIALS

Peter J. Blau and Craig D. Olson

Metallurgy Division

Institute for Materials Science and Engineering

INTRODUCTION

The purpose of this project is to develop and examine metal calibration specimens containing near-surface cracks using the Thermal Wave Microscope (TWM). The TWM uses a pulsed electron beam in a specially-modified Scanning Electron Microscope (SEM) to generate near surface thermally excited regions. Within these regions, acoustic signals due to thermal expansion are generated. These can be detected with an acoustic transducer on which the sample is mounted. Differences from place to place on the specimen surface in thermal conductivity, microstructural homogeneity, and thermoelastic properties affect the contrast in the TWM image. The FY'85 work on this project involved the fabrication of specimens containing detectable defects and produced a study of the TWM operating conditions required to detect and characterize these defects. Associated with this work were investigations of specimen mounting and beam damage to the surfaces being examined in detail by the TWM.

RESULTS

Several types of candidate specimens for TWM calibration were obtained and/or fabricated. The most instructive one was produced by drilling small holes in a brass coupon and rolling them closed to form a closed "crack". Fig. 1 shows how this was done. The simulated defect specimen (SDS) was systematically examined in the TWM while operating conditions were varied. Only certain specific operating conditions resulted in satisfactory images. These are given in Tables 1 and 2. For other types of specimens with different shapes, mounting methods, and materials compositions it is likely that another set of imaging conditions would be found. The reasons why some specific conditions worked better than others in producing images are not yet known.

Figure 2 presents a curve of thermal diffusion length versus frequency for brass using an expression given by Rosencwaig [1]. The frequencies giving satisfactory images for the brass SDS on the TWM have been indicated on the plot.

Figure 3 shows that the TWM could detect the direction of inclination of the subsurface crack if it were oriented properly with respect to the electron beam scanning direction. The "shadow" in the image was clearly observed when the plane of the crack in the SDS was at 90 degrees to the scanning direction (the beam scanned from left to right on the photograph.) A similar effect of defect orientation was obtained for operating frequency and phase and is shown in Figure 4. Tilting the specimen surface away from normal to the electron beam also affected the ability of the TWM to obtain satisfactory images.

Figure 5 shows the nature of the scanned area after prolonged examination (about 20 hours on the same area at various raster sizes - i.e. magnifications.) A film of carbon was apparently deposited on the heated examination area. Attempts at chemically etching this area to study whether beam damage (such as recrystallization of the brass) had occurred were not successful due to the presence of the deposited film. There were no obvious signs of heating effects in the microstructures surrounding the area of prolonged beam rastering.

CONCLUSIONS

The following conclusions were drawn based on TWM studies of a brass simulated defect specimen:

(1) The ability of the TWM to detect and image subsurface defects was affected by beam voltage and current, specimen tilt, and specimen orientation.

(2) The presence of a subsurface crack and the fact that it was inclined in a particular direction to the surface plane was detectable. The angle of its inclination and depth of the crack at a given surface location could not be ascertained.

(3) TWM worked better on the metallic specimens than on other materials investigated during the course of the year. These included specimens of partially stabilized zirconia, glass, and polymers.

(4) There was no clear evidence for beam heating damage to the microstructure because etch-resistant carbon films were deposited in the scanned regions of the brass specimen after prolonged exposure to the beam.

RECOMMENDATIONS

Based on results for the metallic specimens examined during the past year, TWM may aid in the detection, location, and orientation of defects, but would require substantial improvements and significant progress both in instrumentation and theory in order to become more quantitative. Because related work using the TWM on wear specimens during the past year [2] has shown some promising results in detecting the locations of phase boundaries, areas of elastic incompatibilities, and the density of compressed compacts, it is recommended that work be redirected from the quantification of crack depths into another area of considerable technological importance. This new effort involves the detection of localized areas of residual stress in metallic assemblies.

REFERENCES

1. A. Rosencwaig, Science 218 (1982) 223.
2. P. J. Blau and C. D. Olson, Proc. Wear of Materials, ASME, NY, (1985), 424.

TABLE 1. THERMAL WAVE IMAGING CONDITIONS FOR BRASS

(SIMULATED DEFECT SPECIMEN)

Accelerating Voltage (kV)	Current (μ A)	Imaging Frequencies (kHz)
20	1.9	143, 144, 150, 211, 214
30	1.8	64, 72, 74, 76, 81, 83, 84, 86, 87, 97, 140
30	1.9	64, 72, 74, 85, 87, 106, 143, 144, 209, 213, 214

TABLE 2. BEST PHASE SELECTIONS FOR IMAGING AT FREQUENCIES OF EITHER 143 or 144 KHZ ON THE BRASS SIMULATED DEFECT SPECIMEN

Accelerating Voltage (kV)	Current (μ A)	Phase (degrees)
20	1.9	002, 091, 188, 308
30	1.9	001, 002, 008, 060, 068, 100, 160, 170, 181, 300

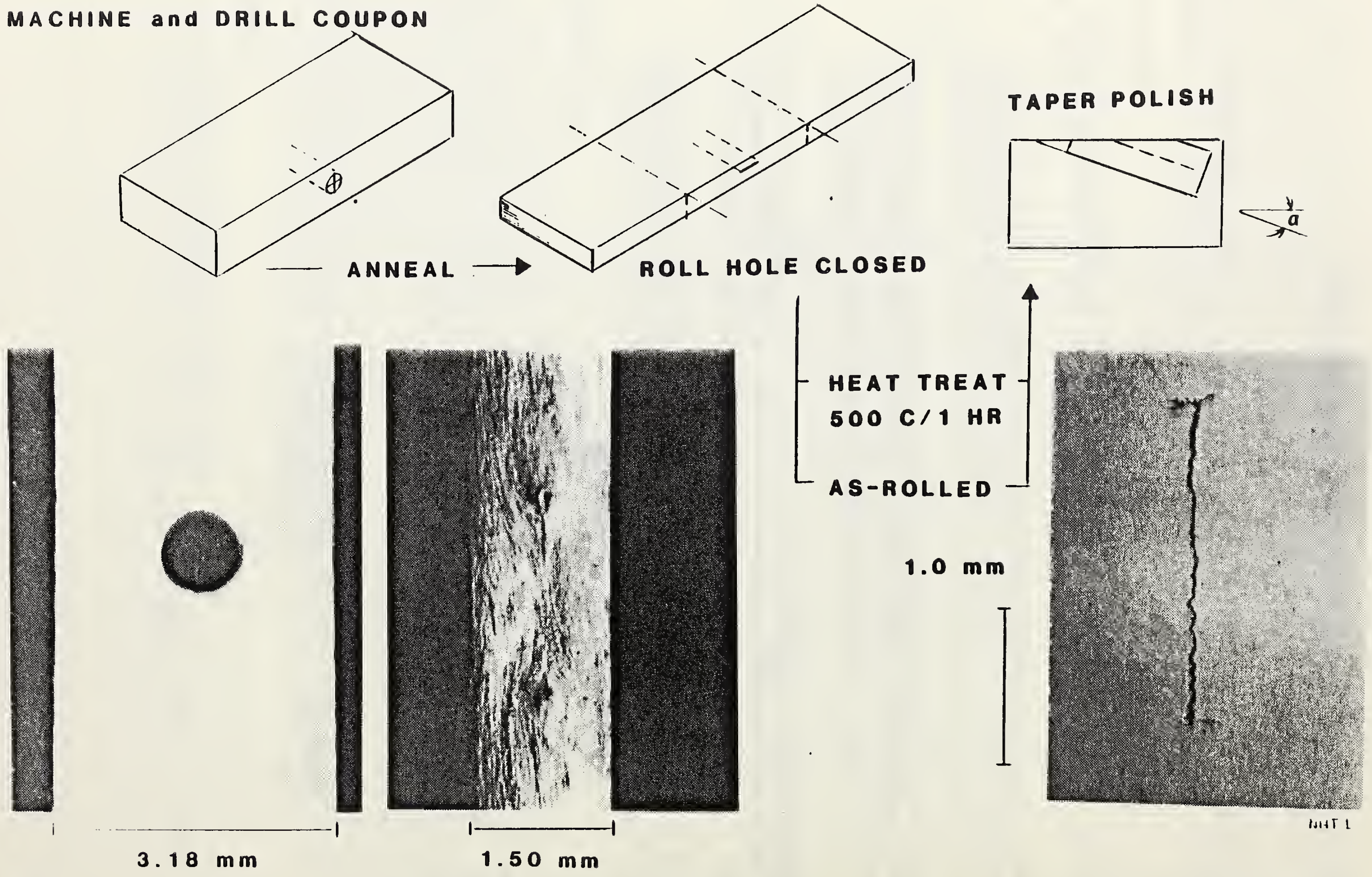

Figure 1. Fabrication method for the brass simulated defect specimen.

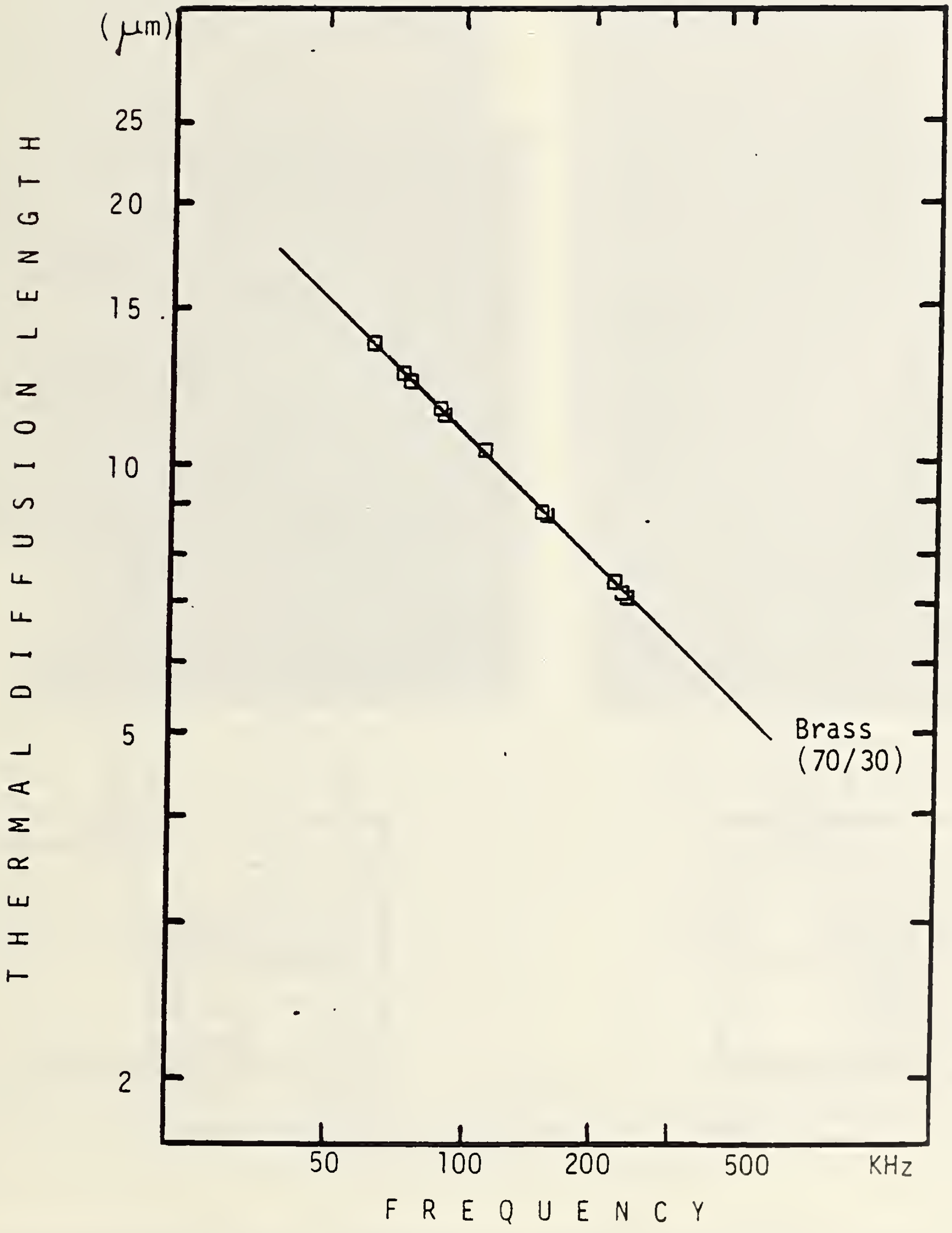

Figure 2. Calculated thermal diffusion length in brass (solid line) and specific values of the imaging frequency which gave satisfactory results.

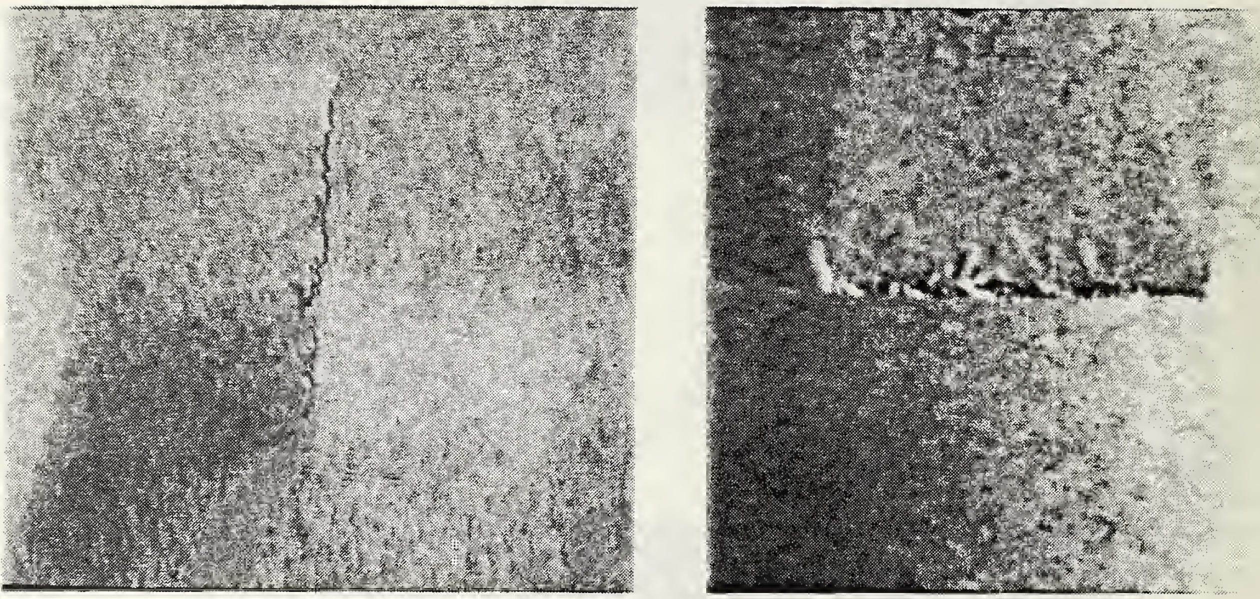

IMAGE DATA

kV 30 Curr 1.8 μA
Mag 40 X
Freq 76 kHz
Phase 097
Date 2 1 85
Matl BRASS

IMAGE DATA

kV 30 Curr 1.8 μA
Mag 40 X
Freq 76 kHz
Phase 097
Date 2 1 85
Matl BRASS

Figure 3. Orientation of the crack with respect to the beam scanning direction (left to right) affected defect detectability.

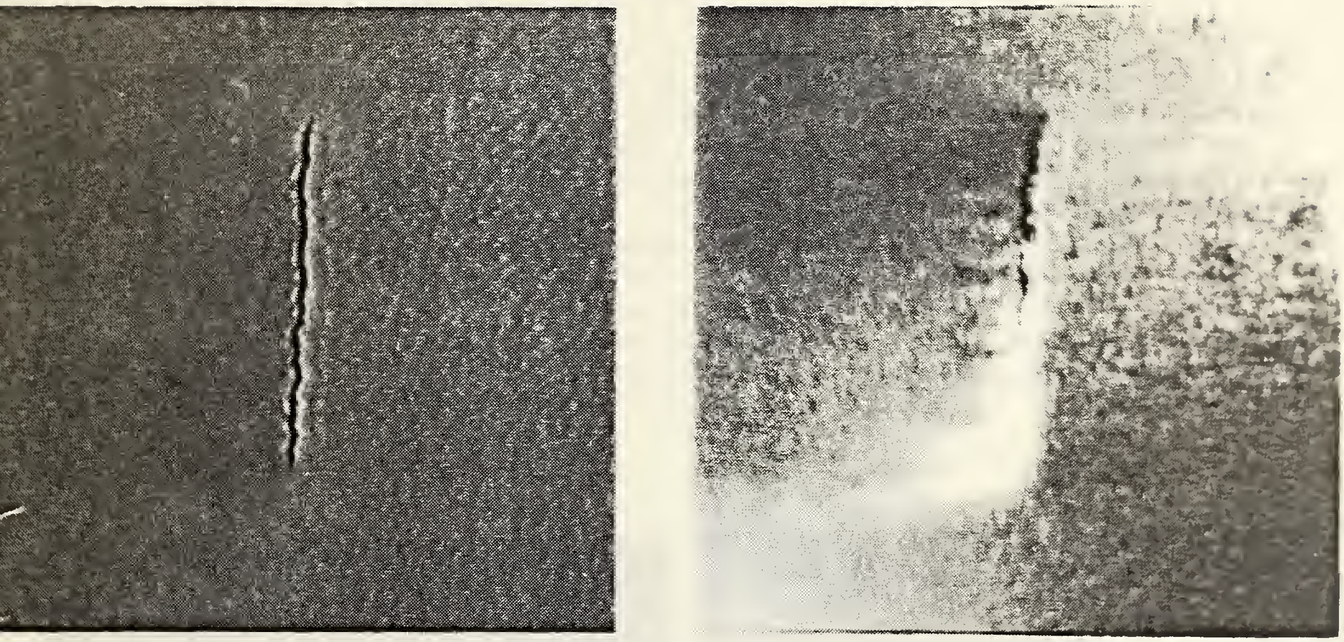

IMAGE DATA

kV 30 Curr 1.8 μA
Mag 40 X
Freq 87 kHz
Phase 097
Date 2 1 85
Matl BRASS

IMAGE DATA

kV 30 Curr 1.8 μA
Mag 40 X
Freq 97 kHz
Phase 002
Date 2 1 85
Matl BRASS

Figure 4. Ability to detect the simulated crack was affected by both frequency and phase settings on the TWM.

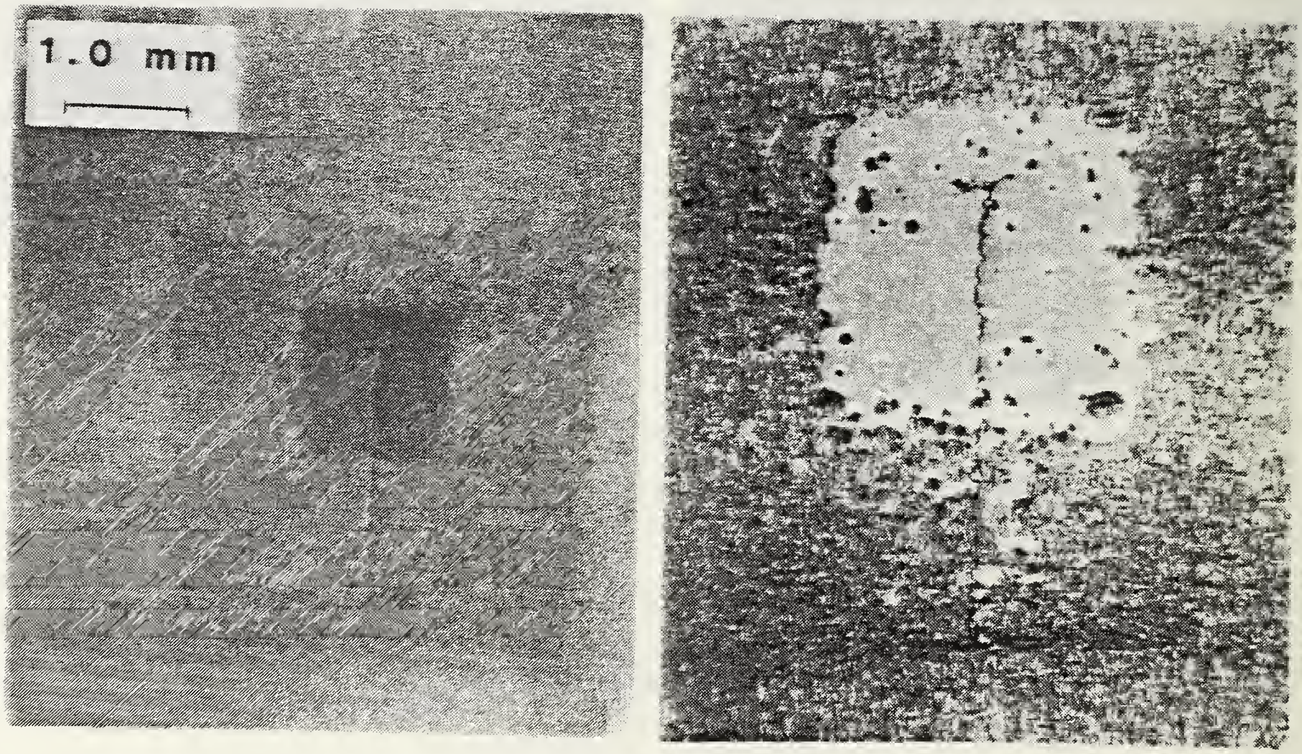

(a) (b)

Figure 5. Carbon deposition during prolonged examination was observed. (a) specimen surface as-removed from the chamber, (b) after etching to reveal the grain structure in the vicinity of the crack area.

IV. NDE FOR PROCESS CONTROL

NDE for process control is the focus for this section of the report. In contrast to Section III's focus on interfaces and composites, this section emphasizes NDE of metals and ceramics for process control. The five reports on ceramic processing NDE document an advance in this important application of process technology. The report on ultrasonics in metallurgy also is notable in that important progress has been made in developing an ultrasonic internal temperature sensor for hot metals. The work on developing an ultrasonic technique to evaluate thermal insulation both during manufacture and for inspection after installation is also notable. This technique (patent applied for) is expected to find widespread application in the building industry.

NONDESTRUCTIVE EVALUATION OF DISTRIBUTED DAMAGE IN CERAMIC MATERIALS USING SMALL ANGLE NEUTRON SCATTERING TECHNIQUES

K. A. Hardman-Rhyne

Inorganic Materials Division

Institute for Materials Science and Engineering

The problem of measuring pore size distributions as a function of sintering conditions has long plagued material scientists. A non-destructive small-angle neutron scattering (SANS) technique, sensitive to defects (sizes up to 3 μm) and their size distribution has been developed at NBS. Theoretical advances relating to those problems are reported by N.F. Berk in the Reactor Radiation Division [1], however, the experimental and material issues are addressed here.

The sintering process for ceramic materials includes studies of both unfired compacted powder samples ("green" ceramics) with 50 percent porosity and sintered materials with 2 percent porosity (generally consisting of closed pores). These volume fractions and pore sizes (~1.0 μm) are much larger than can be seen with traditional single particle diffraction techniques in small angle scattering. Multiple scattering techniques have been employed to elucidate microstructural information including pore size, size distribution, porosity, and surface areas [2,3]. The analysis procedure utilizes the strong wavelength dependence of the small Q incoherent multiple scattering data to determine the scattering radius of curvature, r_c at Q=0. In addition a Porod analysis is used to determine the total surface area of the pores from the large Q data.

Multiple Scattering arises from thick samples or a high concentration of powder particles or voids in the material. The scattered neutron intensity is measured on a two dimensional detector. Since the neutron intensity contours are generally circular in multiple scattering experiments, the intensity data are circularly averaged and plotted as a function of the scattering vector, Q where in the small angle limit $Q = 2\pi\theta/\lambda$ for θ, the scattering angle and λ, the neutron wavelength. Q is proportional to the distance on the detector between the incident and and scattered beam. The shape of the curve is described by the scattering radius of curvature r_c at Q = 0, and is related to the full width at half maximum, q, as $q = 2.355r_c$. Qualitatively, the shape dependence of the multiple scattered curve can be called beam broadening. This beam broadening effect is strongly wavelength dependent and is most apparent at greater wavelengths. If multiple scattering is not present the shape of the intensity (r_c) as a function of Q exhibits no wavelength dependence.

Compacts of sub-micron spray-dried spinel ($MgAl_2O_4$) powder (approximately 0.76 µm in size) were uniaxially pressed at 69 GPa and then isostatically pressed at 207 GPa. The "green" pressed disks were calcinated at 700°C to remove organic binders and will be referred to as the "green" state (G.S.) sample. This sample was fired at 1300°C for 12 hours to obtain a partially sintered material referred to here as the sintered sample.

As expected, the small-Q scattering from the G.S. compact showed a strong wavelength dependence due to the high porosity. Analyses of the samples indicated that the G.S. sample is 53.6% dense (or 46.4% porosity) and the sintered sample is 97% dense (or 3% porosity).

The small-Q regime of the scattering curves were fit to a gaussian function and the incident beam values were substracted to obtain $r_c[Q]$ (the notation means radius of curvature at the origin in Q units) as a function of wavelength. The $R_{eff}(0)$ or effective void radius measured from the small-Q data [3] for the G.S. and sintered samples are 440 and 800nm, respectively. The theoretical and experimental values of $r_c[Q]$ versus wavelengths are shown in Figure 1. The error bars are shown or are less than the size of the symbol. Excellent agreement of the data with theory can be seen. The $R_{eff}(\infty)$ or effective void radius measured by the large-Q data [3] and surface area of the voids were determined from the analyses of the Porod regime. The $R_{eff}(\infty)$ for the G.S. sample is 160nm and for the sintered material, 690nm. The surface area for the G.S. sample is $4.5m^2/gm$ which is in good agreement with gas adsorption results.

SUMMARY

The two R_{eff} values obtained for the "green" state could suggest a distribution of void sizes but the large difference here suggests that two different size characteristics are being measured; that of "neck" and "bottles" of ink-bottle type connected porosity. In the sintered material the SANS measures both closed and open porosity. With the completion of the cold source at the reactor this year, higher wavelengths will be obtainable which will allow measurements of pores or inclusions up to 30 µm. This is particularly significant in that the size range of 5 to 30 µm will allow SANS results to be compared with other techniques such as thermal waves and ultrasonics which can be used as sensors for on-line process control.

REFERENCES

1. N. F. Berk, 1985 Annual Report submitted to ONDE.

2. N. F. Berk and K.A. Hardman-Rhyne, J. Applied Cryst. 18, in press 1985.

3. K. A. Hardman-Rhyne and N. F. Berk, J. Applied Cryst. 18, in press 1985.

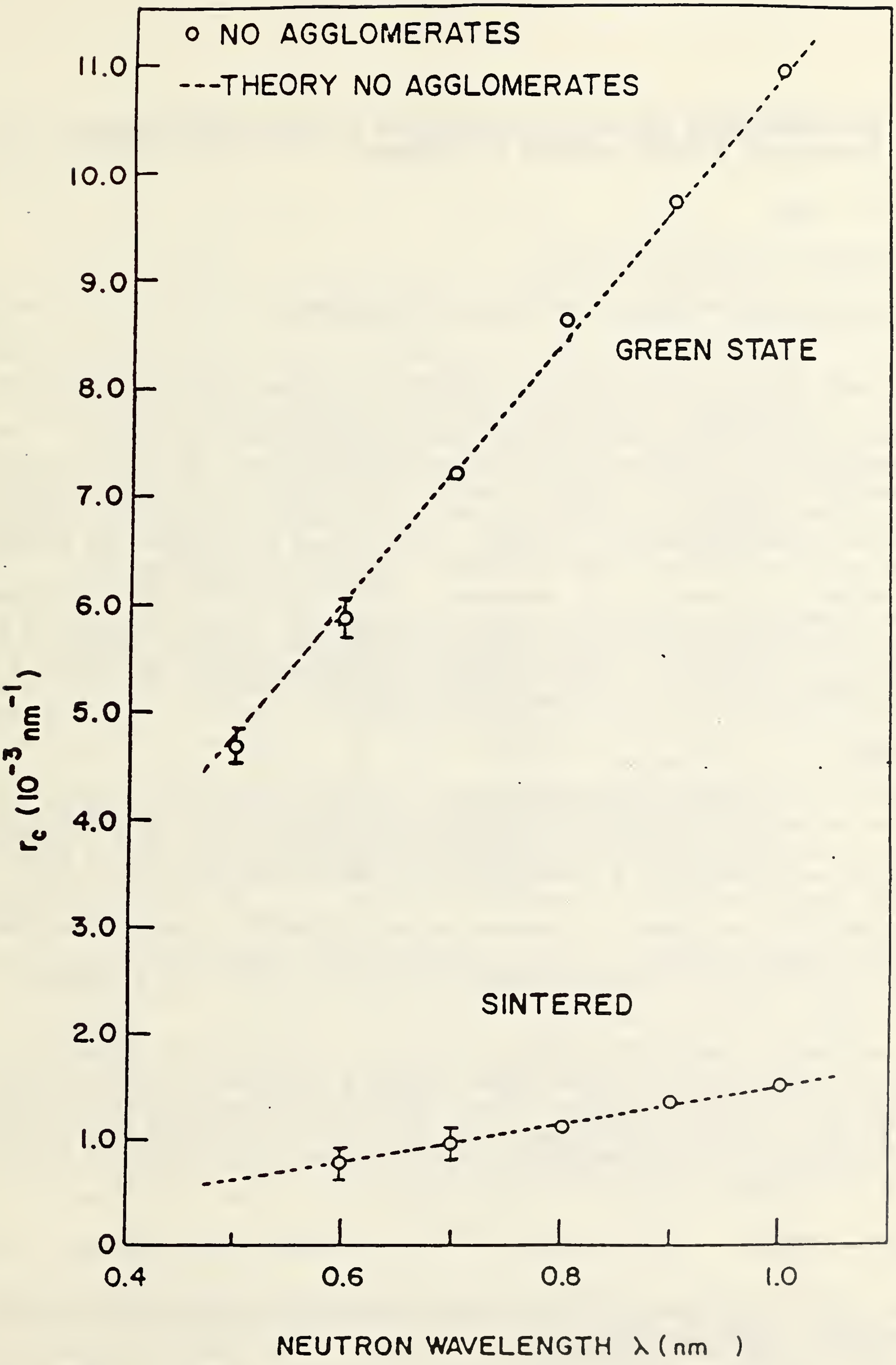

Figure 1. The theoretical (dotted lines) and experimental (squares) $r_c[Q]$ versus neutron wavelength both green state and sintered spinels.

THE PHASE SHIFT AND MULTIPLE SCATTERING IN SMALL ANGLE NEUTRON SCATTERING: A THEORY FOR NDE OF CERAMICS .

N.F. Berk

Reactor Radiation Division

Institute for Materials Science and Engineering

Small angle neutron scattering (SANS) from ceramic materials in early stages of processing, including the powder and green state, usually is characterized by the observation of "beam broadening"--an apparent broadening of the incident beam well beyond instrumental resolution and the absence of a weakly scattered component, in contrast to the typical SANS diffraction experiment. Since this behavior is generally observed to depend strongly on the wavelength, λ, of the incident beam it is sometimes assumed to be describable as multiple refraction. In fact, λ-dependent beam broadening is a signature for incoherent multiple scattering which, in terms of the underlying single-particle cross-section, may be far removed from the refractive regime of very large single-particle phase shifts. Indeed, for particle or void sizes of typical concern in such materials, say radii, R, encompassing the range 0.1-10 μm, the phase shift

$$\nu = 2R\rho\lambda, \tag{1}$$

where ρ is the scattering length density, will tend to lie in a regime (0.1-10) not evidently characterized as either refraction, $\nu \to \infty$, or diffraction, $\nu \to 0$. Thus it is important to incorporate the ν-dependence of the single-particle scattering into a formalism for incoherent multiple scattering (MSANS) from a population of particles or voids [1]. While such an approach falls short of the complete dynamical scattering theory ultimately required for such complex systems, it does provide a powerful quantitative tool for nondestructive evaluation of ceramics processing and distributed damage [1,2].

We have assumed that the MSANS intensity is the result of incoherent multiple scattering from monodisperse, randomly distributed, structureless spheres in a uniform background. Then, the neutron cross-section per unit of area from a sample of thickness z and area A, as a function of wavevector $\vec{Q}$ in the plane of a two-dimensional, position sensitive detector, and with pinhole collimation, is [1,3,4]

$$W(Q,z) = e^{-\bar{z}}\delta(\vec{Q}) + \frac{kR}{2\pi}\int_0^2 \zeta J_0(QR\zeta)\left[e^{-\bar{z}(1-q(\zeta))} - e^{-\bar{z}}\right]d\zeta, \tag{2}$$

where $q(\zeta)$ in the exponent is completely determined by the single-particle, ν-dependent, cross-section,

$$\sigma(Q,\nu) = k^2R^4\left|\int_0^1 J_0(xu)\left[e^{i\nu\sqrt{1-u^2}} - 1\right]u\,du\right|^2. \tag{3}$$

In lowest order, $O(\nu^2)$, the right hand side of (3) easily reduces to the Born approximation or diffraction limit. Also in (2), the scattering power $\bar{z} = z/\ell$, where ℓ is the scattering mean-free-path.

Numerical evaluations of $q(\zeta)$ are shown in Fig. 1 for a range of ν. For $\nu \leqq 1$ the curves are indistinguishable to within 0.1% from the diffraction limit ($\nu \rightarrow 0$)

$$q^{0}(\zeta)= \Theta(2-\zeta)\{(1 + \xi/2)\sqrt{1 - \xi} - 2\xi(1 - \xi/4)\ln[\frac{2}{\zeta}(1 + \sqrt{1 - \xi}]\}, \qquad (4)$$

with $\xi = \zeta^{2}/4$. Even for $\nu \approx 2$ the Born approximation is effectively stable but breaks down quickly for larger values, as shown. The leading singularity of $q(\zeta)$ at $\zeta = 0$ is determined entirely in $O(\nu^{2})$ and is thus the same as in the diffraction limit, which from (4) is given by $1/2\zeta^{2}\ln\zeta$. It is this singularity which fixes the asymptotic fall of $\sigma(Q)$ as $Q \rightarrow \infty$ and gives the Porod law, which is thus seen to be invariant in ν [1,6]. Moreover, the N-fold single-particle limit, where N is the number of particles, defines the $Q \rightarrow \infty$ behavior of the multiple scattering since the asymptotic behavior of (2) is determined by the leading singularity of the integrand at the origin. Since $q(\zeta) \rightarrow 1$ as $\zeta \rightarrow 0$, this is established in $O(\bar{z})$ and is the singularity of $q(\zeta)$ [1]. Thus, for $Q \rightarrow \infty$, $NAW(Q,z)/V \rightarrow N\sigma(Q,\nu)/V \sim P/Q^{4}$, where $P = 2\pi(S/V)$ is the Porod constant, and S is the total surface area of the N particles.

These ideas have been successfully applied to a SANS beam broadening study of high purity alumina (Al_2O_3) powder [2]. Eq. (2) was used to fit the curvature κ of measured intensity curves at $Q = 0$ for several incident neutron wavelengths, allowing the determination of ϕ and R--interpreted as an effective radius, see below. Parameters were in the ranges: $\lambda = 0.45\text{-}1.0$ nm, $z = 2.0\text{-}10.0$ mm, $\phi = 0.25\text{-}0.33$, and $\bar{z} = 5\text{-}400$. The corresponding phase shifts, $\nu = 0.15\text{-}.0.30$, were well within the limit shown above, Fig. 1, to justify analysis as multiple diffraction. To apply the method to polydispersed powder, the radius measured from the small-Q data was interpreted as an effective radius, R(0), defined by the extension,

$$\bar{z} = N\sigma/A \rightarrow z\phi\langle\sigma\rangle/\langle v\rangle \rightarrow z\phi\nu^{2}\lambda^{2}R(0), \qquad (5)$$

where $\langle\cdot\rangle$ denotes the average over the particle-size distribution (PSD). The last equivalence in (5) applies only to the diffraction regime, where $\sigma \rightarrow \sigma^{0} = (1/2)\bar{\nu}^{2}\pi R^{2}$ and $R(0) = \langle R^{4}\rangle/\langle R^{3}\rangle$. The best-fit value of R(0) from all data was found to be 265 nm within a 2-5% uncertainty. Once R(0) is known, all the small-Q data can be represented on a universal curve for multiple diffraction, $r_c[QR]$ vs $\bar{z}$, where $r_c[QR] = 1/\sqrt{-\kappa}$ is the radius of curvature of the scattered intensity at $Q \cong 0$ in dimensionless units and is effectively a measure of the width of the intensity curve near the origin [1]. This is shown in Fig. 2, comprising the results from 25 data sets, where the theoretical curve is well-approximated in the range shown by

$$r_c[QR] = 0.92\,[\bar{z}\ln 0.85\bar{z}]^{0.5} \qquad (6)$$

For the limit of single-particle scattering by a sphere, $r_c[QR] = \sqrt{(5/2)}$. Large-Q data were analyzed using the Porod law, expressed in terms of the effective particle radius $R(\infty) = \langle R^{3}\rangle/\langle R^{2}\rangle$, which results from its extension to polydispersed systems. The result [2] was $R(\infty) = 232$ nm within 15%. The values of R(0) and $R(\infty)$ were rationalized by assumption of a lognormal PSD, from which $\langle R\rangle = 171$ nm and dimensionless width parameter $\beta = 0.382$ were derived. These results were found to be in very good agreement with powder size determinations by laser light scattering and by x-ray sedigraph methods. Application to MSANS NDE of unfired "green" state compacts and sintered materials is also in progress [7].

SUMMARY

Significant progress has been made toward the development of an analytical methodology for deriving quantitative particle-size information from multiple small angle neutron scattering (MSANS). Application to alumina powder has indicated the potential of the approach for reliable NDE of ceramic materials, and ongoing measurements also point in this direction. Theoretical work continues with emphasis on extending the formalism, analytical methodology and computer software to the determination of larger particle-size ranges and the development of more systematic approaches to data analysis.

REFERENCES

1. N.F. Berk and K.A. Hardman-Rhyne (1985). J. Appl. Cryst., 18, in press.

2. K.A. Hardman-Rhyne and N.F. Berk (1985). J. Appl. Cryst., 18, in press.

3. H.S. Snyder and W.T. Scott (1949). Phys. Rev. 76, 220.

4. H.A. Bethe (1953). Phys. Rev. 89, 1256.

5. R.J. Weiss (1951). Phys. Rev. 83, 379.

6. N.F. Berk and K.A. Hardman-Rhyne (1986). Proceedings of the International Conference on Neutron Scattering, 1985, Santa Fe; Physica B, to be published.

7. K.A. Hardman-Rhyne, K.G. Frase, and N.F. Berk (1986). Proceedings of the International Conference on Neutron Scattering, 1985, Santa Fe; Physica B, to be published.

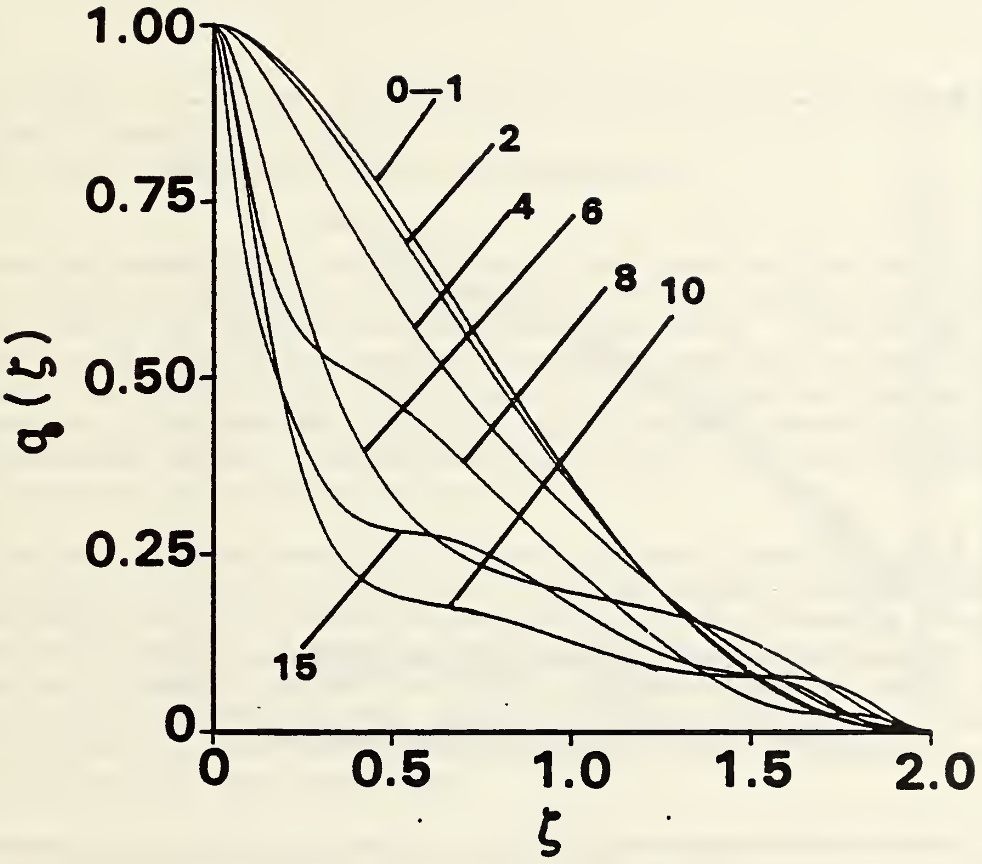

Figure 1. The function q(ζ) for several values of the phaseshift ν.

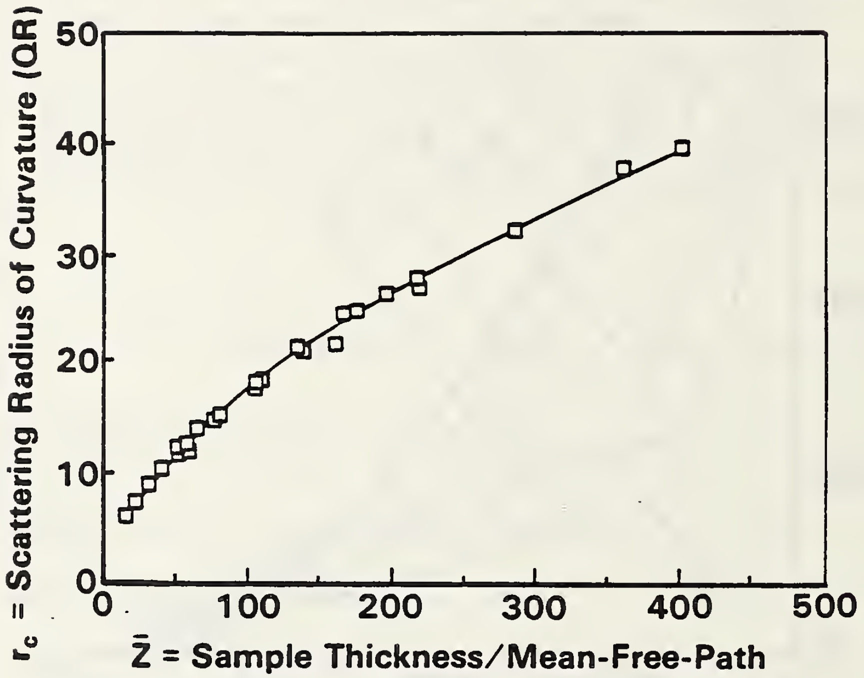

Figure 2. Radius of curvature of multiple scattering intensity at Q = 0.

ULTRASONIC MEASUREMENTS OF CERAMICS

G.V. Blessing
Mechanical Production Metrology Division
Center for Manufacturing Engineering

and

M.P. Jones
Inorganic Materials Division
Institute for Materials Science and Engineering

Substantial materials research interest continues for the development of effective ceramic processing procedures, and for the nondestructive evaluation of ceramic properties both during and after processing. This is evidenced by the expanded efforts at NBS in the ceramics area, and has led to a collaboration between the Institute for Materials Science and Engineering and Manufacturing Engineering to nondestructively monitor specific ceramic properties at various processing stages. The approach being taken for the ultrasonic nondestructive technique is presented here.

The purpose of this study is to relate pertinent material properties of sintered ceramics to their green-state elasticity using ultrasonic methods. This relationship would be useful to monitor and control ceramic processing, permitting the rejection of ceramics possessing poor green-state elastic properties and thereby avoid further costly processing. While many ultrasonic studies have been made on sintered ceramics, few have been made on the green state, and apparently none have systematically correlated green-state elasticity with final sintered properties.

By means of ultrasonic longitudinal and shear wave velocity measurements, the degree of isotropy, homogeneity, and inter-sample elasticity variations will be determined as a function of processing parameters on both the green and sintered states for a series of alumina ceramic samples. To evaluate material elasticity in particular as a candidate for a process-control parameter, dynamic modulus values will be calculated from these velocity measurements on samples in which the binder has been removed (producing hard agglomerates and subsequent low strength materials) before pressing and sintering. These green-state elastic values will then be compared with those obtained on samples that yield good (high strength) properties. It is conjectured that hard agglomerates will act as elastically uncoupled particles due to a lack of binder, and lead to lower sample moduli. The lower green-state moduli would then be expected to correlate with a low-strength sintered state.

To avoid sample contamination by couplant absorption into the porous ceramics (especially in the green state), dry coupling techniques have been developed for use with both longitudinal and shear waves. A novel polymeric coupling material permits dry coupling of shear waves to fragile green-state and sintered ceramics with minimal pressure in a two-transducer through-transmission technique. With these techniques, order-of-magnitude differences in elasticity have been observed between green-state and sintered-state samples.

SUMMARY

A joint CME/CMS study designed to relate ultrasonic measurements of green-state elasticity to the final sintered properties of ceramics was undertaken in mid FY 85. Dynamic modulus measurements have been identified as one possible process-control parameter. A novel coupling technique necessary for dry coupling to green-state ceramics has been developed using a special polymeric material. Initial measurements showing an order-of-magnitude difference in elasticity have been carried out.

THERMAL WAVES

Grady White, Lorretta Inglehart, Marty Jones, Anne Wilson,
and Christie Nguyen

Inorganic Materials Division

Institute for Materials Science and Engineering

The technique of thermal waves involves the periodic application of heat to a specimen and the monitoring of the resulting heat flow. Periodicity not only increases the signal to noise ratio but also allows the heat flow process to be treated as a highly damped traveling wave. The physics involved in the generation and detection of thermal waves has been studied by a number of groups over the past several years but the systematic application of thermal waves to the investigation of NDE applications is a recent development. Because thermal waves scatter from thermal discontinuities in a manner analagous to the scattering of sound waves from elastic discontinuities, thermal waves should provide an alternate probe for the NDE of materials. Therefore, we are beginning to apply the thermal wave technique to the study of certain well defined defects in brittle materials.

The work this year has been divided into three categories porosity investigation, equipment construction and development, and cement investigation. Each of these topics will be considered separately below.

POROSITY INVESTIGATION

The major thrust this year has been the investigation of porosity in alumina. Porosity in ceramics has long been a source of concern, but no practical techniques for determining porosity in a reliable nondestructive manner have yet been developed. Microscopy, both optical and SEM, and porosimitry measurements have been used in the past but these approaches are both time consuming and destructive to the specimens being investigated. Moreover, porosimitry measurements detect only the open, or connected, pores in the material. Therefore, closed, or isolated, pores are not detected by this technique. In addition, there have been several papers in the literature reporting correlations obtained between ultrasonic velocities and porosity in ceramics. However, the specimens in these papers generally have been poorly characterized both in terms of sample preparation and porosity analysis. Therefore, it has not been possible for a model to be developed accurately relating the velocity and the porosity. For these reasons, we have chosen to study porosity in a well controlled, well characterized manner. We chose thermal waves as our probe both because we expect changes in porosity to be strongly reflected in variations in thermal conductivity and because we wish to understand better the relationship between thermal waves and materials. In this work, we are collaborating with various people at NBS: Gerry Blessing in the Fabrication Technology Division, and Carl Robbins and Kay Rhyne in the Inorganic Materials Division.

The specimens were made from alumina powders which had been spray dried by Carl Robbins of the Inorganic Materials Division and were pressed at 30,000 psi. The first set of specimens were then divided into three categories: green state, bisque fired, and dense fired. The temperature treatments for the three categories were, respectively, no firing, 1100 C for 20 hours, and 1500 C for 20 hours. Density measurements using the Archimides Principle, light scattering measurements at 10.6 um wavelength, and ultrasound velocity measurements were then made on the specimens. Table 1 summarizes the results.

Table 1. Specimen Parameters

	% density	I/I(dense)	velocity (xE5 in/s)	
			long.	trans.
green	.58	.142	.661	.422
bisque	.60	.200	1.482	.902
dense	.98	1.000	4.492	2.010

A second set of specimens is currently being pressed and fired at conditions duplicating those described above. In addition, a set of specimens is being made up of alumina powder which has been calcined (fired at 1000 C for 12 hours) after being spray dried. The calcined powder is expected to provide specimens which maintain their porosity through various firing treatments. This will allow us to test porosity in two materials which are nominally the same but in which the network of aluminum oxide surrounding the pores has been fired at different temperatures. Table 2 lists the thermal treatments for the second batch of specimens.

Table 2. Thermal Treatment

	Uncalcined	Calcined
powder	RT	1000 C/12 hr
green	RT	RT
bisque	1100 C/20 hr	1100 C/20 hr
dense	1500 C/20 hr	1500 C/20 hr

The thermal wave measurements have been made in a photoacoustic system (ref. 1) in a modified cell which allows measurements to be made upon all three types of specimen, green, bisque fired, and dense fired, without unsealing the cell. This eleminates a major source of error in the photoacoustic effect (PAE). The measurements are being made with a carbon dioxide laser since, at 10.6μm, alumina absorbs very strongly, providing a heat source localized at the surface of the specimen. The specimens are mounted at a position where the laser beam diameter is ~2mm rather than at the focus of the beam. This not only reduces the chances of thermally damaging the specimens but provides a signal which is averaged over a range of pore sizes.

Figure 1 is a plot of the PAE signal for the three uncalcined specimens as a function of frequency. There is a clear distinction among the three specimen treatments as viewed by the PAE which we are beginning to study. The linear dependence of signal magnitude on $1/\omega$, Fig. 1a, is consistant with thermally thick, optically opaque specimens, as modeled by Rosencwaig and Gersho (ref. 2). The increase in signal magnitude as the interrogated specimen is changed from the green to the dense specimen is expected since the increasing porosity should increase the resistance to heat diffusion. However, in the plot of the signal phase, Fig. 1b, the turn over for the dense fired specimen which occurs at low frequency is unexpected. This effect is currently under investigation to determine if it is an anomaly of the PAE system or is a real effect.

EQUIPMENT CONSTRUCTION AND DEVELOPMENT

We are constructing a mirage thermal wave system at NBS which is designed to be compact and self contained, except for the laser heat source. We have now obtained a 4-watt argon ion laser, a 1.5 watt carbon dioxide laser, a vector lock-in amplifier, optical beam steering equipment, an acousto-optic modulator, and a position sensitive detector. The two lasers give us the ability to operate at widely different wavelengths to take advantage of the optical absorption properties of various specimens which we wish to investigate.

The mirage system will provide a noncontact thermal wave capability and will be free of the constraints imposed by the PAE cell. In addition, the mirage system is designed to be completely computer controllable, which is necessary if mapping or imaging is to be done on any regular basis. We expect the mirage system to be operative near the beginning of FY86.

CEMENT INVESTIGATION

We have also used the PA system to investigate epoxy impregnated cement samples fabricated in the Center for Building Technology. The initial purpose of this work was to determine if the photoacoustic effect (PAE) could map out defects, in particular microcracking, in such a complicated structure of varying materials and voids.

The experimental procedure consisted of mounting the cement specimen onto the PA cell as outlined in reference (1). Twenty scans of 7mm in length were made at 50μm separations. The signal was processed in a vector lock-in amplifier and then fed into a chart recorder. The phase information was used, rather than the magnitude information, to minimize contributions from optical and surface effects. The change in phase of the signal is related to the time delay of the thermal wave and, therefore, to the depth the signal penetrated into the specimen. The data from the chart recorder was hand digitized and entered into a computer from which a two dimensional map of the interrogated surface was obtained. After comparison of this map with an investigation of the surface made with an optical microscope, we determined that changes in the thermal wave signal in this specimen were due to variations in the epoxy filler rather than to structural variations in the cement. However, data from this work have not yet been fully analyzed and further investigations upon specimens which have not been epoxy impregnated are planned in an attempt to find surface microcracking.

FUTURE PLANS

We plan to continue the work on the porosity, including developing a model to interpret the interaction of thermal waves with porous materials. We also intend, in collaboration with Drs. John Murphy and Grover Wetsel of the Johns Hopkins Applied Physics Laboratory and Prof. Robert Green of Johns Hopkins University, to place inclusions in alumina specimens to determine the sensitivity of thermal waves to the detection of such flaws. Finally, we intend to use the mirage system to try to detect and quantify surface and near surface defects which serve as sources of failure for brittle materials. All three defects, pores, inclusions, and cracks pose serious problems for use of ceramics in load bearing applications.

SUMMARY

We have used the PAE system built last year to obtain preliminary signal magnitude and phase data upon alumina specimens which are 58%, 60%, and 98% of theoretical density. Clear differences in both magnitude and phase are observed among all three specimens. The specimens are being made at NBS and are being characterized by a number of tests, e.g. light scattering, SANS, porosimitry, and ultrasound, in addition to the thermal wave measurements, to provide as thorough an understanding of their properties as possible. Such an understanding is vital to the developement of a quantitative model relating thermal waves to the measurement of porosity.

A mirage thermal wave system is being built at NBS to provide imaging capabilities. The mirage system is designed to be computer controlled and will allow detection and mapping of closed vertical cracks, inclusions, and other localized defects.

REFERENCES

1. T. Yolken and L. Mordfin, editors, "Technical Activities 1984 Office of Nondestructive Evaluation," NBSIR 84-2944 (Nov. 1984).

2. A. Rosencwaig and A. Gersho, J. Appl. Phys. 47, 64-69 (1976).

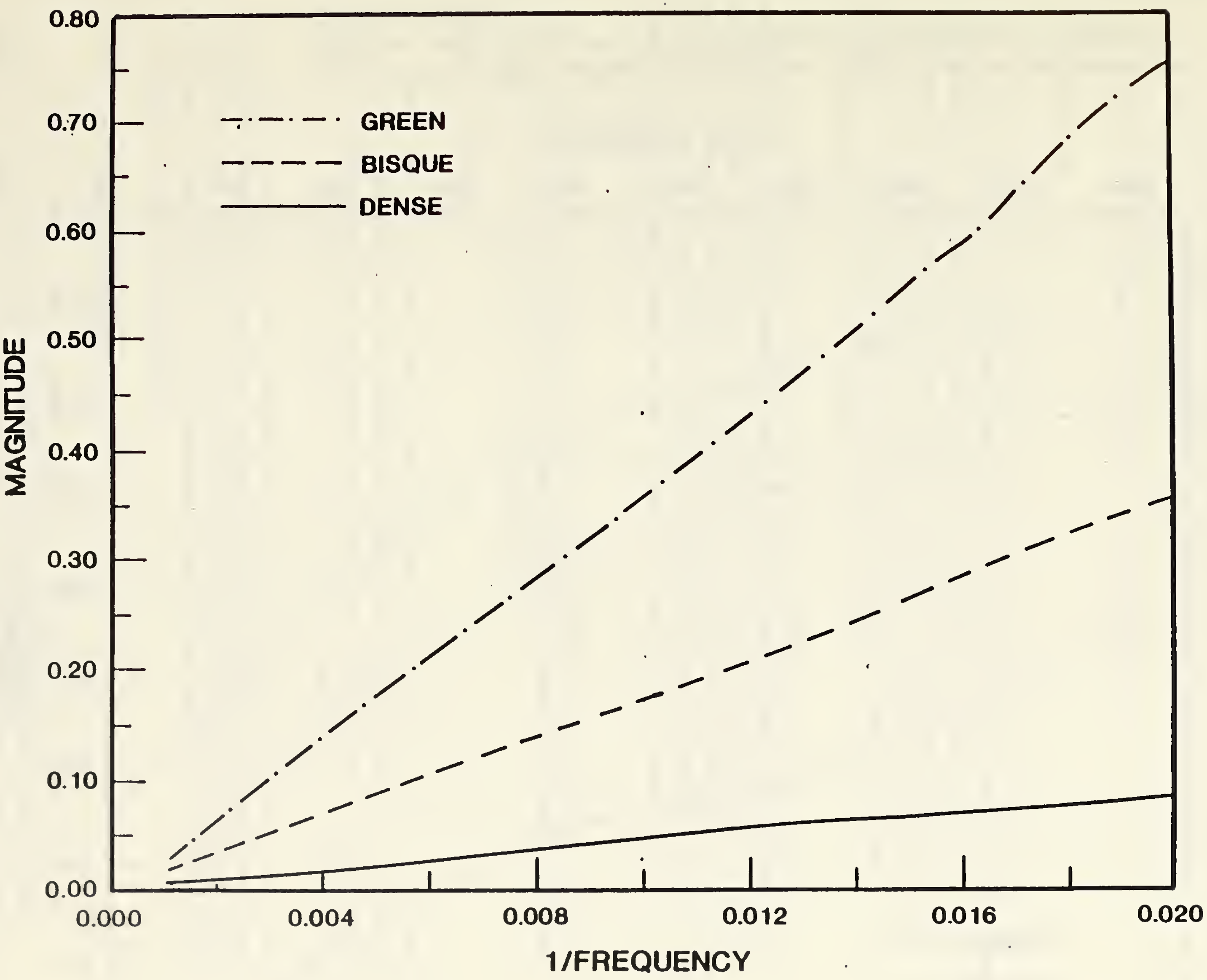

Figure 1a. Plot of PAE magnitude vs 1/ω for three alumina specimens: green, bisque, and dense. Straight lines are in agreement with the theory of Rosencwaig and Gersho (ref. 2).

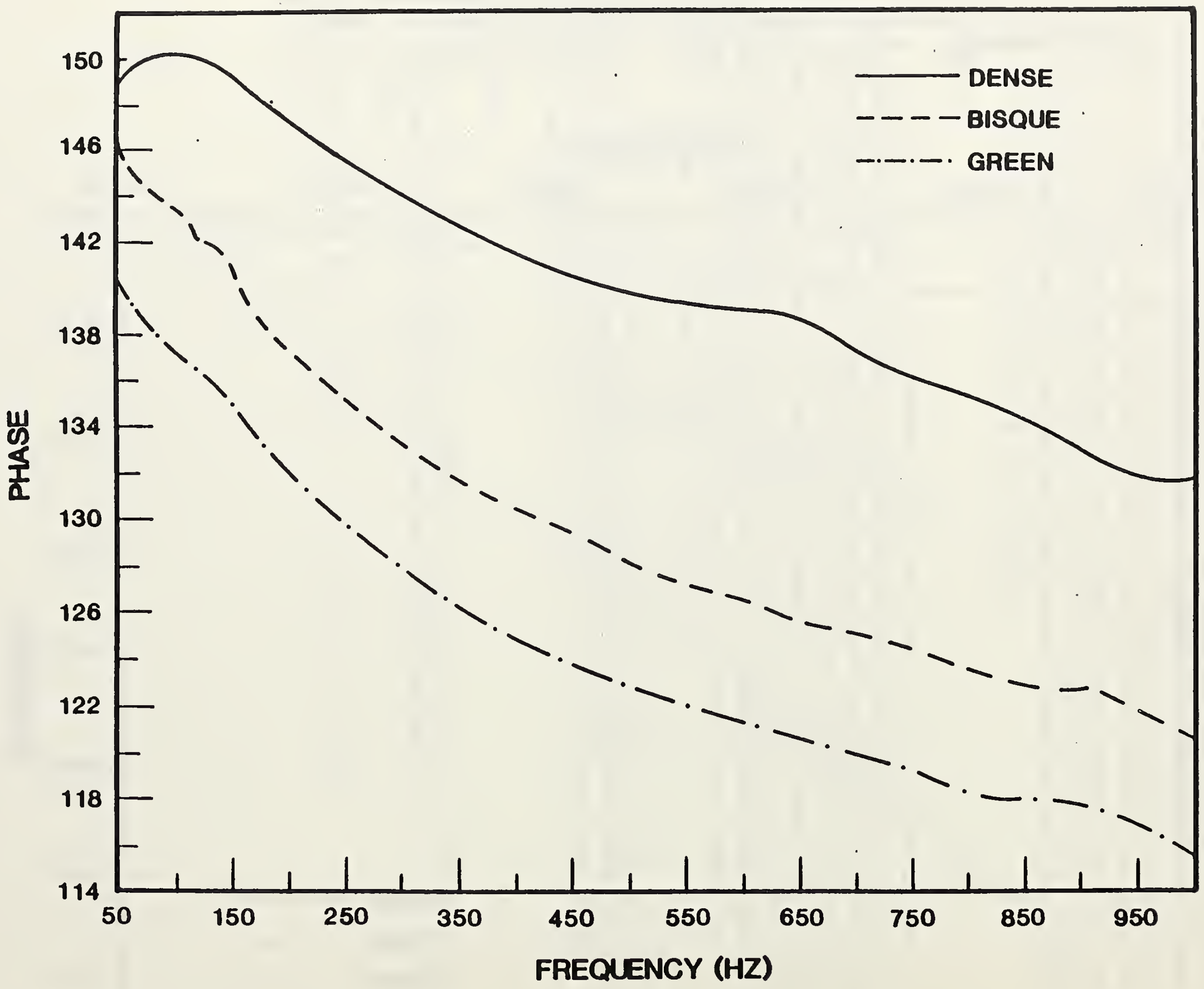

Figure 1b. Plot of PAE signal phase vs ω for the three alumina specimens in Fig. 1a. The turn over for the dense fired specimen is currently under investigation.

NONDESTRUCTIVE EVALUATION-GREEN STATE CERAMICS

C. Robbins, W. Coblenz and M. Jones

Inorganic Materials Division

Institute for Materials Science and Engineering

INTRODUCTION

"The ability to form advanced ceramics with the required level of reliability requires extreme levels of microstructural control over powder characteristics, particle packing, and pore size uniformity."[1] "It is increasingly evident that the starting powder characteristics and the details of the consolidation process (prior to densification) are the origins of many of the limiting defects that are found in these technologically important ceramic materials."[2]

The task of this project is to prepare "green" (unfired) and selectively sintered ceramic compacts with known flaws for exploratory study and characterization by nondestructive and destructive analytical methods. Powders selected for the compacts must be thoroughly characterized, processing conditions documented and some destructive tests made on the ceramic compacts at selected intervals between "green" and fully densified states.

During this year, work was continued at NBS and at Argonne National Laboratory (ANL) on a group of spinel ($MgAl_2O_4$) compacts, and work was initiated on a new group of Al_2O_3 compacts.

SPINELS ($MgAl_2O_4$)

These materials were characterized both at NBS and at ANL. At NBS the pore size distribution was measured using small angle neutron scattering (SANS). Both green and sintered specimens were measured. Experimental results are presented elsewhere in this annual report by K. Hardman-Rhyne.

Initial results from Argonne National Laboratory have detected density gradients in some of the green compacts using both x-ray tomography and x-ray microradiography. Surface scratches produced during processing, which were visible by light microscopy, were also seen by microradiography as slight density differences.

ALUMINA COMPACTS (Al_2O_3)

A high purity alumina powder (purity, 99.99%) from Baikalox was selected to prepare green compacts with known flaw sizes and number density. Particle size distribution by x-ray sedigraph shows a median particle diameter of 0.55 µm (Figure 1). Measurements of surface area (gas adsorption technique of Brunauer, Emmett, and Teller [BET]), porosity (mercury porosimetry), and crystallite size (x-ray analysis) are currently in progress on this powder.

Three sets of compacts prepared from the as-received powder were bisque fired at 1000°C for 18, 42, and 66 hours in an initial study. These specimens have been examined at NBS by SANS and ultrasonic methods. Ultrasonic data for the compacts are given in Table 1. The samples have been returned for porosimetry measurements for correlation of the ultrasonic results.

A large quantity of the powder has been spray dried to produce soft agglomerates (Figure 2) for die pressing 100-150 compacts. In addition, a quantity of this spray-dried powder has been calcined to produce hard agglomerates. Green compacts prepared from the soft agglomerates should have interconnected pores. Compacts prepared from hard agglomerates should have large interagglomerate pores and when sintered at low temperatures should produce a bimodal pore size distribution (interparticle and interagglomerate).

Microstructure will be documented by microscopy and porosimetry. Currently, on the order of seventy compacts have been prepared for the following studies: SANS measurements; thermal wave studies; acoustic measurements; and microscopy and mercury porosimetry studies.

SUMMARY

Initial work at ANL on spinal samples provided by NBS demonstrate that x-ray tomography and microradiography may be used to detect flaws in green ceramics. These samples have been characterized at NBS for pore size distribution using SANS. Work at NBS on alumina has shown that ultrasonic methods are sensitive to initial sintering in near green state ceramics. A quantity of soft agglomerates of Al_2O_3 has been prepared for die pressing 100-150 green compacts. The compacts are currently being studied by NDE and DE methods.

FUTURE PLANS

Plans are to introduce controlled flaws in the form of highly sintered Al_2O_3 spheres into the green die pressed compacts prepared from the soft agglomerates. It is also planned to generate spherical voids of known size in the compacts by the addition of styrene spheres to the powder before die pressing, and then removing the former by low temperature calcination. We have demonstrated that this is a feasible method of sample preparation.

Table 1.

Wave Speeds in Bisque Fired Al_2O_3, Die Pressed at 28 MPa (4,000 psi)

Treatment	Thickness (mm)	Longitudinal (mm/μs)	Shear (mm/μs)
Green	8.02±.03	0.823	0.620
1000 °C-18 hrs.	7.95±.02	1.882	1.341
1000 °C-42 hrs.	7.88±.08	2.360	1.519
1000 °C-66 hrs.	7.87±.06	2.324	1.651

REFERENCES

1. H. K. Bowen, "Basic Research Needs on High Temperature Ceramics for Energy Applications," Mat. Sci. and Eng., 44, 1-56 (1980).

2. M. Yelazquez and S.C. Danforth, "Pressure Filtration of Monosized Colloidal Silica," to be published in "Proceedings of the Symposium on Surface and Colloid Science in Computer Technology," Potsdam, NY, June 1985.

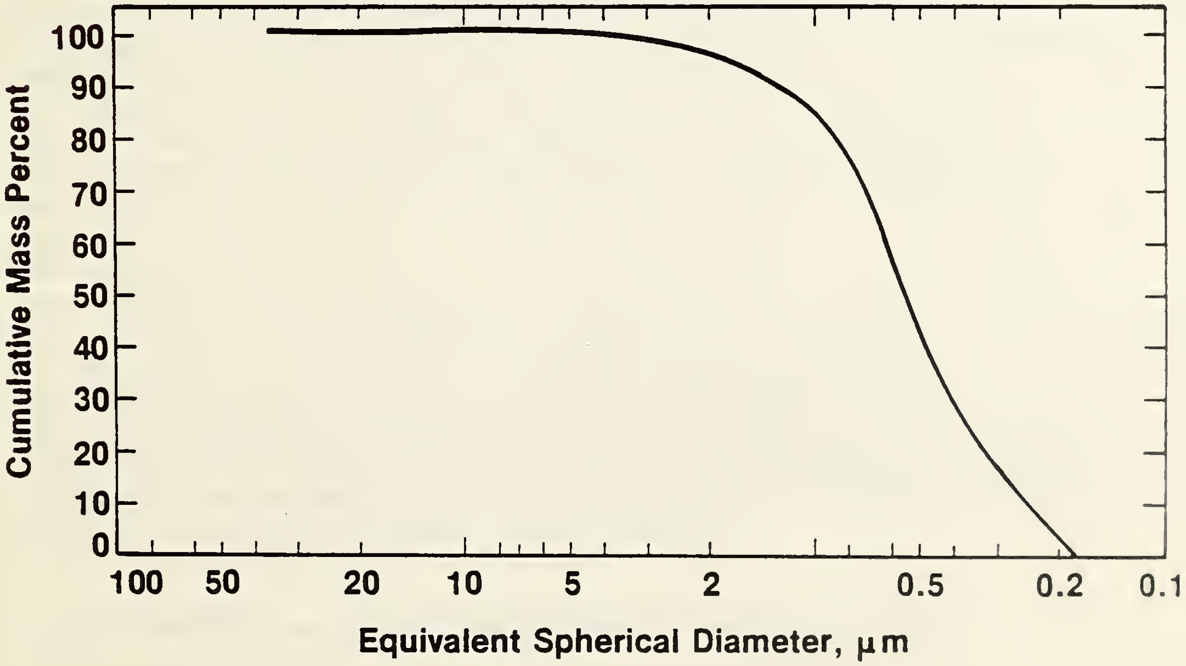

Figure 1. X-ray sedigraph of Al_2O_3 showing a median particle size of 0.55 μm.

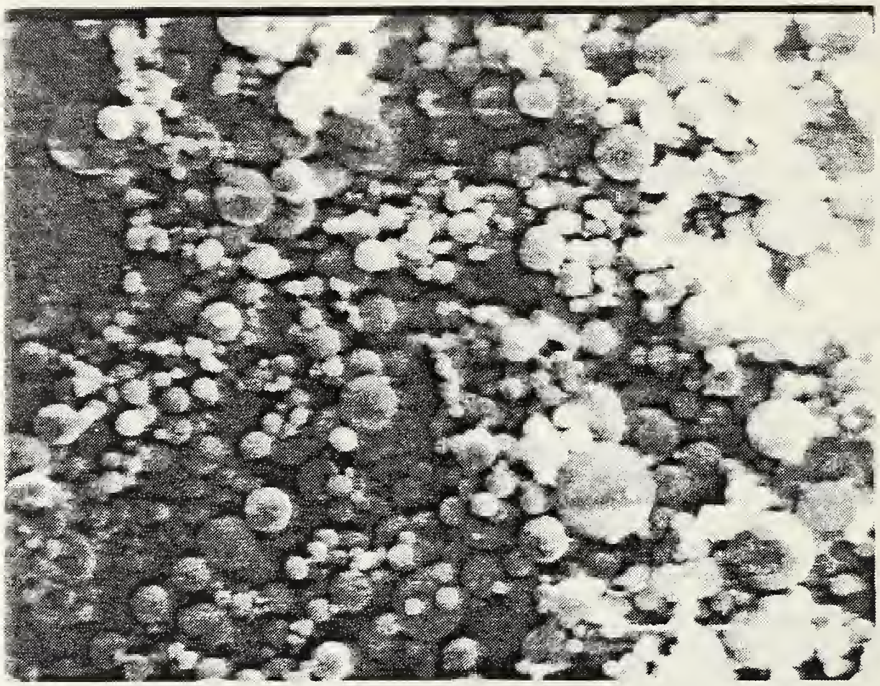

Figure 2. SEM photograph of spray dried agglomerates of Al_2O_3 before die pressing. Long scale bar = 10 μm.

ULTRASONICS IN METALLURGY

Bernard Droney*, Melvin Linzer, Jeffrey Martinez, Floyd Mauer,
Stephen Norton, Kurt Sandstrom, Christian Turner and Haydn Wadley

Metallurgy Division

Institute for Materials Science and Engineering

INTRODUCTION

In FY 85, significant progress was made in perfecting measurement techniques and obtaining velocity-temperature data needed for accurate reconstruction of temperature profiles in hot steel by ultrasonic tomography.

Ultrasonic tomography involves determining the time of flight and path length along a number of paths within one cross section of a hot steel body. Techniques based on computerized tomography are then used to reconstruct the ultrasonic velocity profile. Theory has recently been extended to include reconstructions in square as well as circular cross sections and to make use of heat flow constraints in order to reduce the number of measurements required. The velocity-temperature dependence for each type of steel under investigation is then needed in order to convert velocity profiles to temperature profiles. Progress in obtaining this type of data is reported here.

VELOCITY-TEMPERATURE MEASUREMENTS

Last year we described an improved method for obtaining ultrasonic velocity data at high temperatures for steel samples. A one-piece, stepped rod was used to provide both a test section and buffering rod. An ultrasonic wave could be generated by focusing a laser pulse onto the outer end of the test section or the step where it joined the buffering section. The difference in time of flight gives the TOF in the test section, which is at a uniform temperature in the hot zone of an argon-atmosphere furnace. This method, which was first used for obtaining velocity-temperature data on 304 stainless steel, has now been used for measurements on AISI 1018 plain-carbon steel (0.18 wt % C, 0.74 wt % Mn). This being a ferritic steel, the results are complicated by the bcc to fcc phase transition and the magnetic transition at the Curie point, as well as microstructural changes associated with precipitation/dissolution of carbon. In particular, it is not possible to use handbook values of the thermal expansion when making the necessary corrections for changes in the length of the test section. We have, therefore, modified our equipment to obtain dilatometer measurements on the same test section and under the same heating and cooling conditions used for ultrasonic measurements. Curves for thermal expansivity and longitudinal velocity are shown in Figure 1 and Figure 2.

---

* AISI Research Associate from Bethlehem Steel Corporation

The transition temperatures determined by thermal analysis are also shown. A_1 and A_3 represent the low-temperature and high-temperature limits of the two-phase region over which the alpha phase (bcc) and gamma phase (fcc) coexist. To differentiate between heating and cooling, the letters c for "chauffage" and r for "refroidissement" are added.

On heating, the expansion is nearly linear until the A_1 boundary is crossed and austenite begins to form. The reduction in volume accompanying the bcc to fcc transition results in contraction of the sample until the transformation to austenite is completed at the A_3 boundary. Above the A_3 temperature, the curve is again linear. On cooling, there is considerable hysteresis, causing a 50° to 60° C shift in the transition region. Ultrasonic velocity, on the other hand, shows surprisingly little effect due to the crystallographic transformation. What it does show is considerable nonlinearity starting about 250° C below the transition. The curve is remarkably reproducible on successive heating and cooling cycles. In fact, within the heating and cooling rate limitations of our furnace, it is difficult to show any hysteresis. These observations indicate that limitations on ultrasonic temperature sensing that might have resulted from a non-unique velocity-temperature relation in ferritic steels are not as serious as once thought.

The origin of the steep velocity-temperature gradient between about 720° and 820° C is unclear. One explanation advanced by Papadakis et. al. (reference 1) is based upon the dissolution of carbides. However, data of Kurz and Lux (reference 2) on high-purity Armco iron show the same phenomenon over a similar temperature range even though this material contained no carbides. They also show that the bcc-fcc transition at 910 °C has a negligible effect on the velocity-temperature relation. The Curie temperature for iron is 768° C and the possibility exists that the effects we observe are a manifestation of the loss of the magneto-striction contribution to the modulus.

A source of high purity iron is now being sought to enable us to unambiguously isolate the effects of phase transitions from those associated with magnetostriction and carbide formation.

SUMMARY

Reference data relating ultrasonic velocity to temperature has been obtained at temperatures up to 1110 ° C for AISI 1018 plain carbon steel. The uncertainty in these measurements is roughly 1 part in 10^3, which corresponds to an uncertainty of ±7° C in temperature. The data will be used in reconstructing temperature profiles in hot steel bodies from time-of-flight measurements.

REFERENCES

1. E. P. Papadakis, L. C. Lynnworth, K. A. Fowler, and E. H. Carnevale, "Ultrasonic Attenuation and Velocity in Hot Specimens by the Momentary Contact Method with Pressure Coupling, and Some Results on Steel to 1200° C, "The Journal of the Acoustical Society of America 52 No. 3 (Part 2) pp. 850-857 (1972).

2. W. Kurz and B. Lux, "Die Schallgeschwindigkeit von Eisen und Eisenlegierungen im festen und flussigen Zustand," High Temperatures-High Pressures 1 pp. 387-399 (1969).

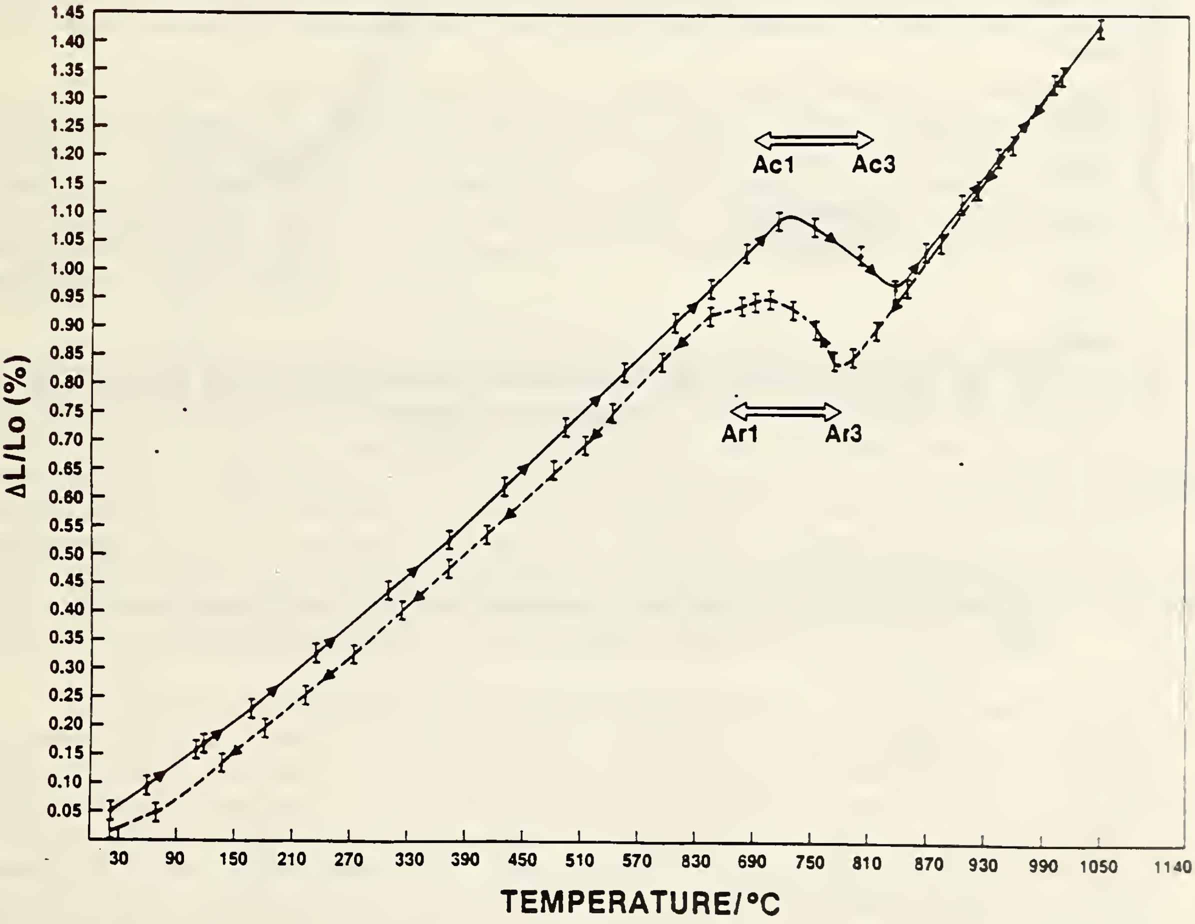

Figure 1. Linear expansion in percent for AISI 1018 carbon steel. The transformation range on heating (Ac1-Ac3) and cooling (Ar1-Ar3) was determined by thermal analysis.

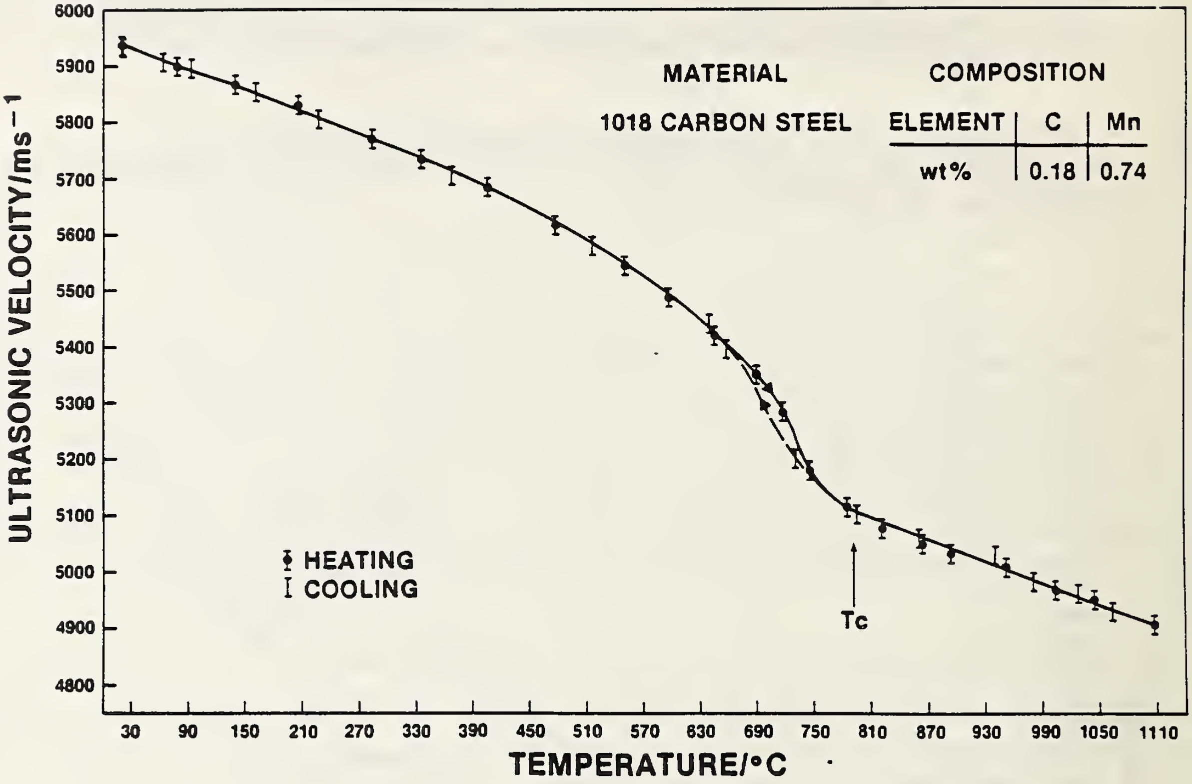

Figure 2. Ultrasonic velocity versus temperature for AISI 1018 carbon steel. T_C is the Curie temperature, 768° C for iron.

ACOUSTIC EMISSION AS AN NDE TECHNIQUE FOR CHARACTERIZING MARTENSITIC TRANSFORMATIONS

Y. Berlinsky[1], H. N. G. Wadley, R. B. Clough, J. A. Simmons and M. Rosen[2]

Nondestructive Characterization Group

Metallurgy Division

Institute for Materials Science and Engineering

Acoustic emission is an elastic transient generated by a change of stress within a body. As such this technique has remarkable potential in monitoring and characterizing various microscopic phenomena such as dislocation motion, microcrack growth and martensitic phase transformations.

Traditional acoustic emission instrumentation measures, among other things, the acoustic emission energy of an event. The measured energy of an acoustic emission signal cannot as yet be theoretically related to the elastic energy of source. Therefore, to quantitatively measure this quantity, we have used calibration sources of known strain energy to relate the data measured during experiments with traditional instruments to the energy of the natural sources.

Two types of energy calibration sources, whose time dependences bound those of most natural sources, have been used. One is that of a dropping ball and the second is the absorption of an infrared laser pulse. The calibration system is described in Figure 1. By varying the height of the dropped ball or the energy of the laser pulse, [ref. 1], a calibration curve is obtained. This calibration curve relates the envelope strength (relative energy units) of a commercial acoustic emission system with the source elastic energy. The envelope strength is corrected for bandwidth due to the difference between the source spectrum and the AE system response. Such a curve is shown in Figure 2.

Once having calibrated our measurement system, we were then able to proceed with an investigation of the kinetics and mechanisms of martensitic phase transformations. The Fe-30.5 wt. % Ni system was chosen as a model alloy system because its transformation conveniently began just below ambient temperature and the transformation itself has been intensively studied by numerous other techniques. It was found from the acoustic emission signals emitted that upon cooling this alloy just below room temperature, a few martensitic plates were formed. The stress field induced by these plates in the surrounding matrix then catalytically induced a "burst" of martensitic transformation with concomitant more intense emission. This was then followed, on further cooling, by numerous emissions as the sample underwent a complete transformation to martensite. A typical acoustic emission activity is shown in Figure 3.

---

[1] Guest Worker from Israel, Ministry of Defense

[2] Guest Worker from the Johns Hopkins University, Material Science Department and Center for NDE

Interestingly, the M_s temperature (martensitic start temperature) is very clearly defined by acoustic emission and is substantially higher than that reported in the literature from electrical resistivity measurements. Using the calibration procedure described earlier, the elastic energy of an acoustic emission could be converted to that of the source from whence it came, i.e., a martensitic lath. We are presently investigating the relationship of this energy to the shape change of a martensitic plate - a key parameter in the description of a martensitic transformation.

Work has also begun to investigate the martensitic phase transformation of rapidly solidified ribbons of Fe-30.5 wt. % Ni. A typical acoustic emission activity (events rate) of the ribbon is shown in Figure 4. Being more sensitive than electrical resistivity, the acoustic emission technique detects the early stages of a martensitic transformation. That is because only a few martensitic plates do not cause a detectable change in the electrical resistance of the sample.

By comparing the acoustic emission activity of the bulk and the ribbon samples, a different transformation mechanism was evident. It was found that the M_s temperature in the ribbon was lower than that in the bulk sample. There was no burst at the early stages of the transformation, and the activity had only one distinct envelope, in the temperature range of -50 °C to -100 °C.

Future efforts will be directed towards getting a better understanding of the energy calibration procedure, and its sensitivity to various parameters. Also the kinetics and mechanism of martensitic phase transformations will be investigated, using the calibrated acoustic emission technique.

SUMMARY

New calibration methods are being developed to facilitate quantitative use of acoustic emission data recorded with traditional instrumentation. The procedures are based upon calibration and standardization of analysis methods. They have been applied to the study of martensitic transformations and show promise of quantifying the dynamics of this important class of metallurgical transformations.

REFERENCES

1. Y. Berlinsky, R. B. Clough, H. N. G. Wadley, and M. Rosen. "Acoustic Emission as an NDE Technique for Characterizing the Martensitic Phase Transformation in a Fe-Ni Alloy," to be published in the proceedings of the conference: Reviews of Progress in Quantitative NDE, June 23 - 28, 1985.

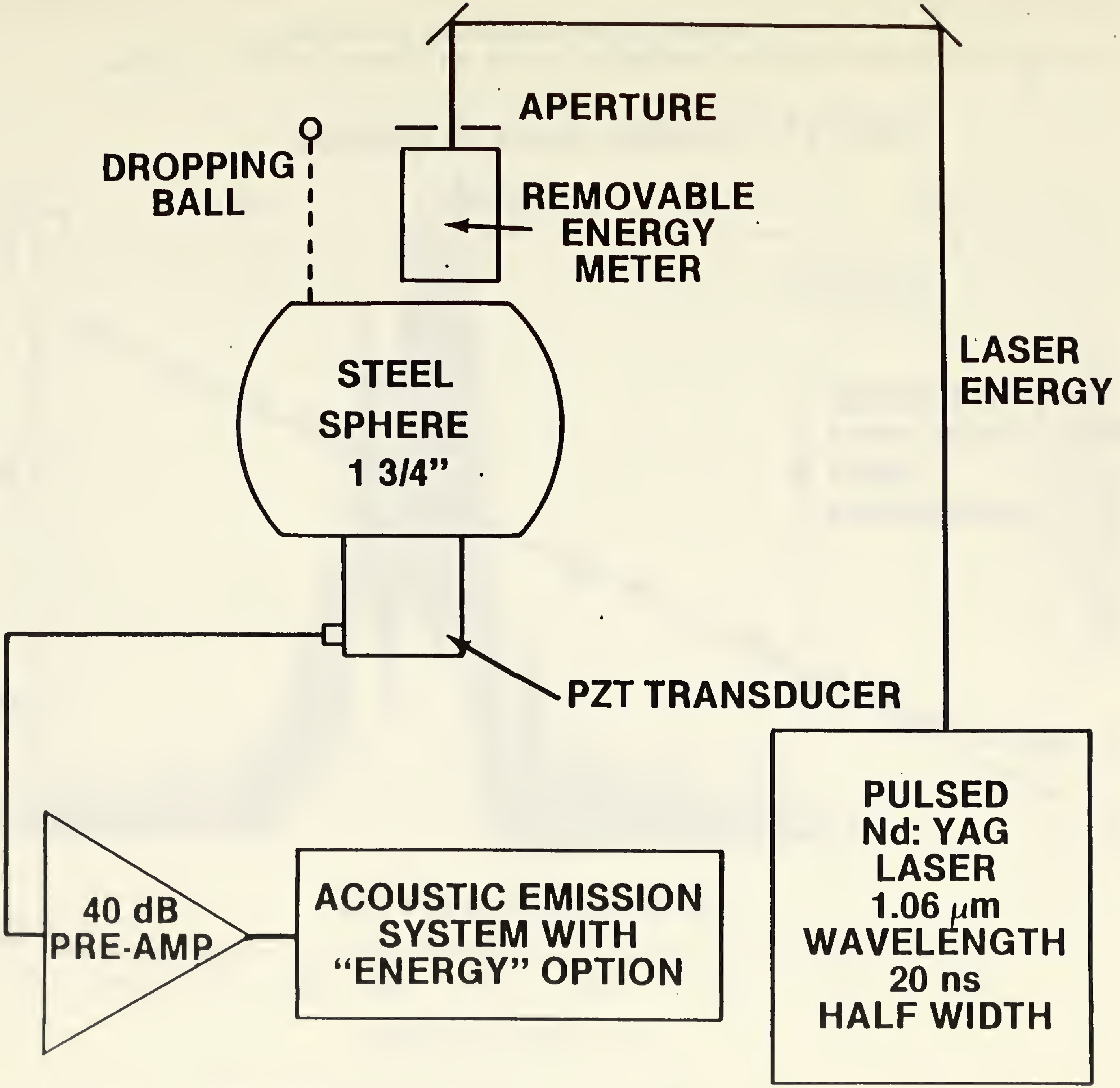

Figure 1. System for acoustic emission calibration.

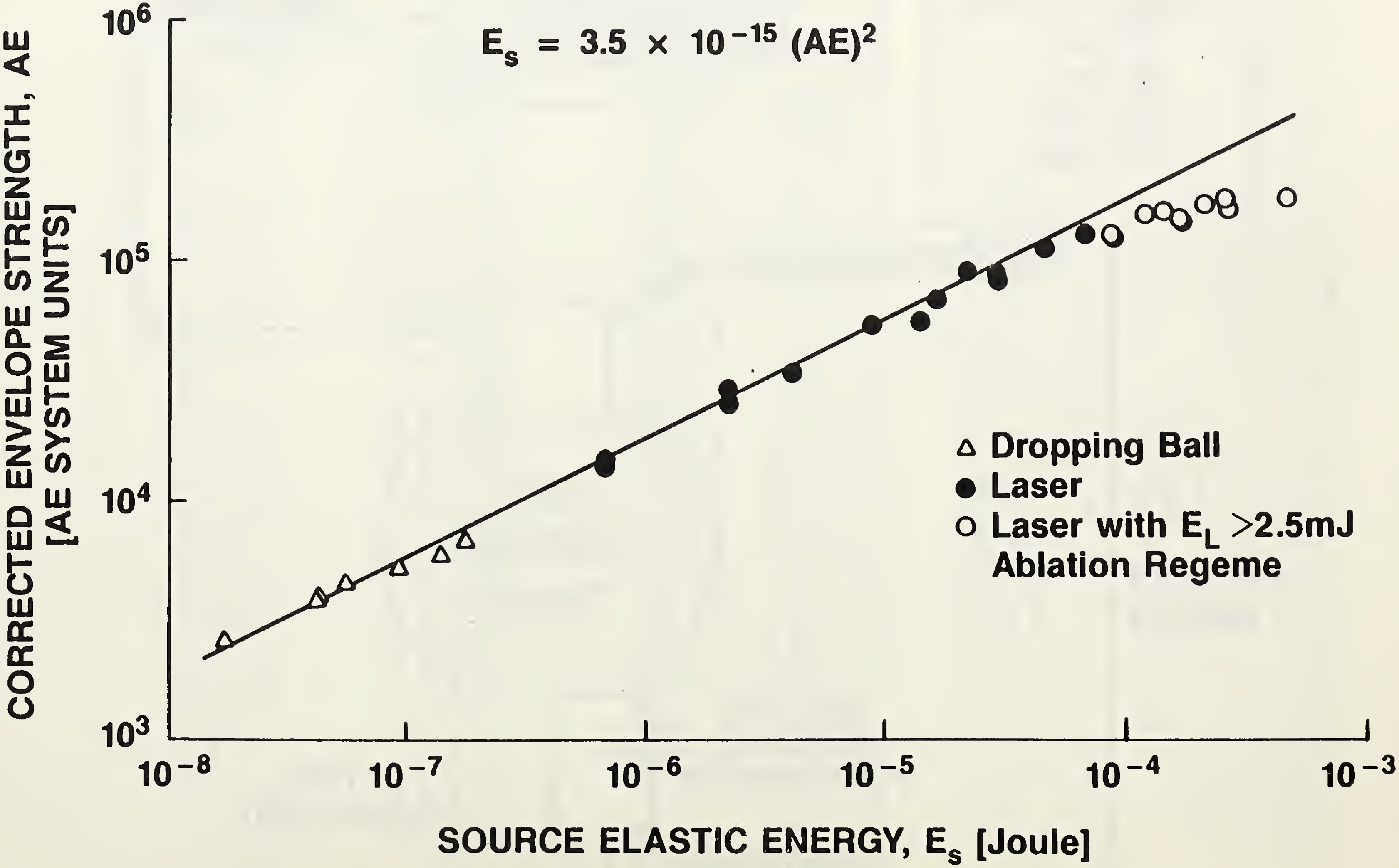

Figure 2. Energy calibration of the AE system--corrected envelope strength as a function of the source elastic energy.

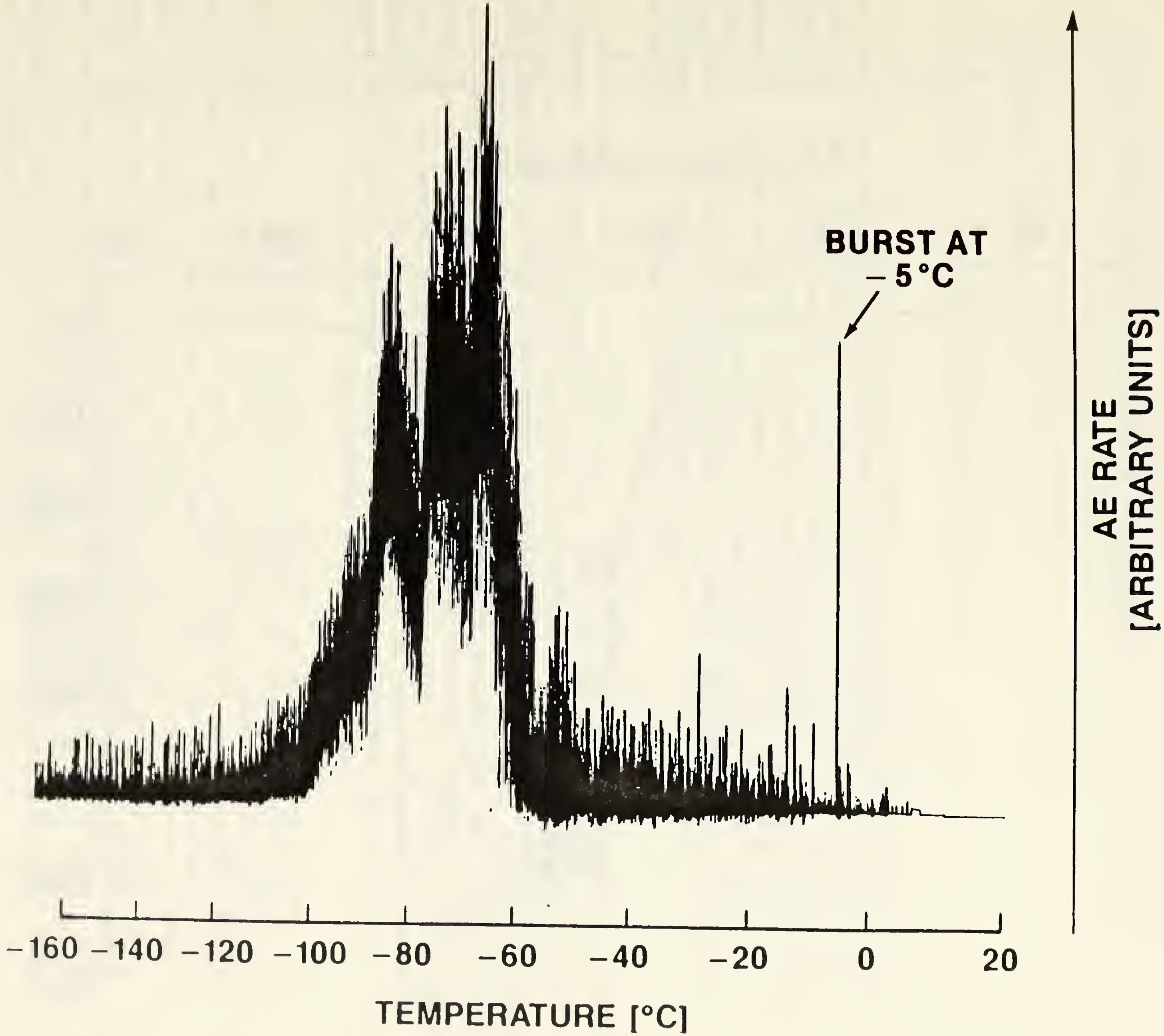

Figure 3. Typical AE activity during cooling of Fe –30.5 wt. % Ni from room temperature to –170 °C. A sharp burst is observed at –5 °C.

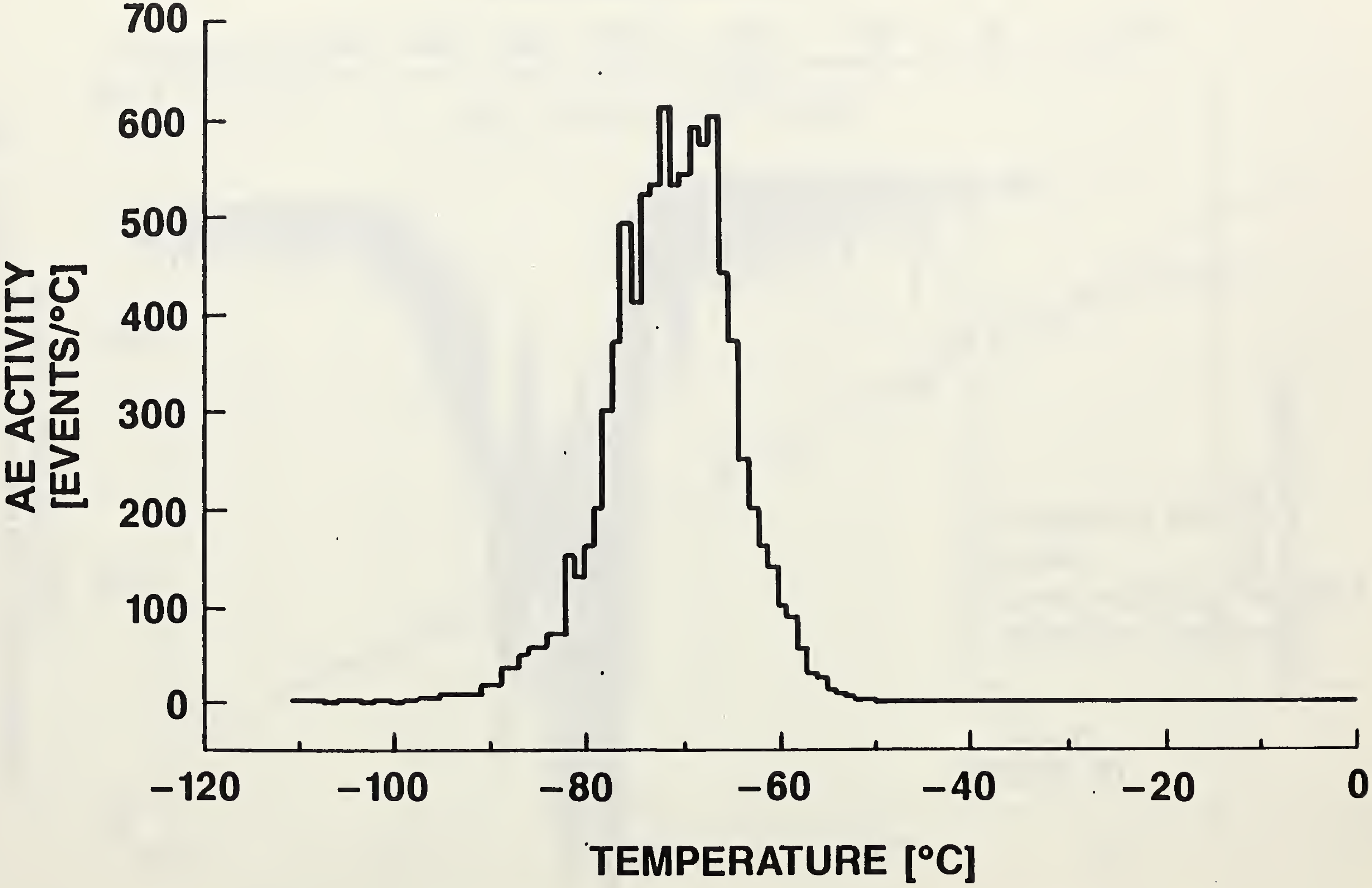

Figure 4. Event rate during cooling of rapidly solidified Fe -30.5 wt. % Ni ribbon from room temperature to -140 ^{o}C.

DYNAMIC MICROINDENTATION EVALUATION OF MATERIALS

Robert S. Polvani

Metallurgy Division

Institute for Materials Science and Engineering

Facing many different end uses, designers of industrial parts and equipment need data bases and test methods for measuring the mechanical properties of metals, especially their dynamical capabilities. Structural supports and piping require creep strengths, while bearing, cams and gears involve impact and sliding wear strengths. A sensitivity to the rate of loading is found in all polymers and some metals. A new and nondestructive approach to dynamic mechanical testing is being developed. Derived from conventional "hardness" there are two important innovations. The indentation is described in terms of the instantaneous applied load and penetration depth. Secondly, indentation can be performed over a range of loading times, from hours down to milliseconds.

The Dynamic Microindentation Tester was extensively revised to improve three features of its dynamic capability. First, the test event recorder, a storage oscilloscope, was replaced with a transient digital oscilloscope. Doing this required completely revising the system software, but markedly increased the detailing of the test event. Potentially, a 10X improvement is available. Second, the load and displacement transducers were revised; the measurements are now directly coupled to the sample itself. Before displacement was measured with respect to the main frame, and converting to penetration required correction for the compliances of the sample and main frame. Lastly, as a means of determining the extent of anelastic recovery, a pause of variable duration was introduced between the recording of the test event and measurement of the residual indentation depth.

Figures 1 a and b report actual test data for a typical dynamic test. The specific result is for a test of an O-2 hardened and tempered tool steel. Figure 1 b is the load-displacement curve for the indent; it combines the results of both the up-loading and down-loading of the sample. Figure 2 is a schematic explanation of this curve. Because the two results are reported, load-displacement curves can serve two different and important functions. First, the indentation deformation energy can be partitioned into its elastic, plastic and anelastic components. For example the total work to indent the O-2 steel was 430 gf-um; of that total 26 percent was elastically recoverable. This partitioning of the indentation energy has been used as a means of understanding the wear resistance of "hard" coated metals, and should be even more useful if a different property, formability for example, were the primary interest.

Second, the load-displacement curve is interchangeable with the stress-strain curve. The convertibility has been already shown for copper, but except for specific cases cannot be generally made. A primary goal of this task is to develop a way for making that general conversion.

Lastly, Table I offers preliminary data illustrating the importance of using a dynamic loading. The sample is a metal matrix composite of 6061 aluminum and 15 volume percent SiC particulate. These are dynamic Knoop hardness data, and show an effect of loading time on the apparent hardness. The determinations were all made in the loaded condition, and reflect both the elastic and plastic deformation responses of the material.

TABLE I. A comparison of the Knoop Hardness as a function of the duration of the applied loading.

LOAD DURATION (SECONDS)	100	10	1	0.1	0.01
KNOOP HARDNESS (kg/mm^2)	80	156	160	147	113

To explain the relative softening at the extremes of the duration requires conjecture. At the slowest rate, creep is a significant factor that has the time necessary for an observable effect. At the highest rate, the input of deformation energy is dissipated as both plastic deformation and local heating. For near impact conditions, theory predicts about an 80 percent conversion of the deformation energy into local heating.

SUMMARY

The apparatus has been extensively revised for improved dynamic performance and preliminary testing has been performed. Samples are now being prepared for a demonstration of the general dynamic capabilities.

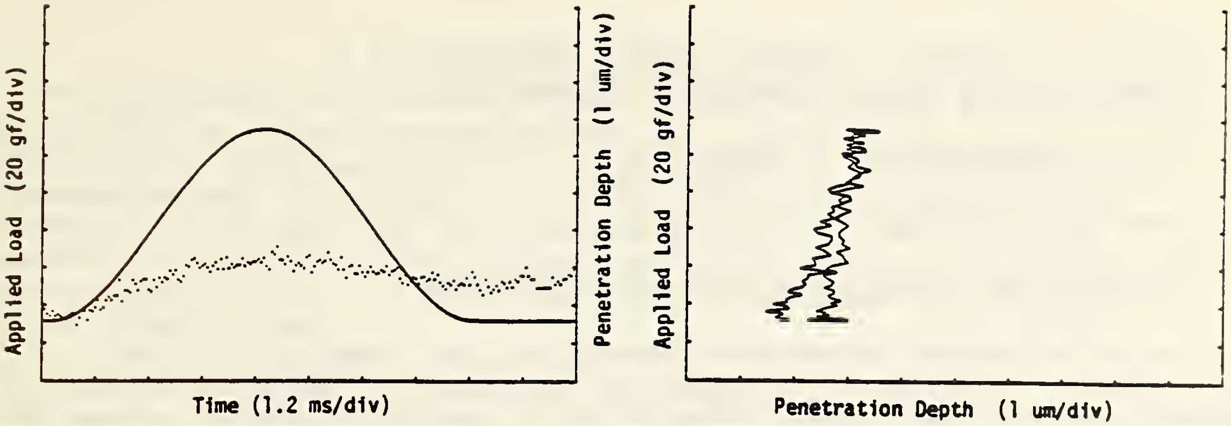

Figure 1. Dynamic results for a 100 gram Knoop indentation of a hardened and tempered 0-2 tool steel.

(a) Applied load, A, and penetration depth, B, curves versus time.

(b) The load-displacement curve for loading, L and unloading, U.

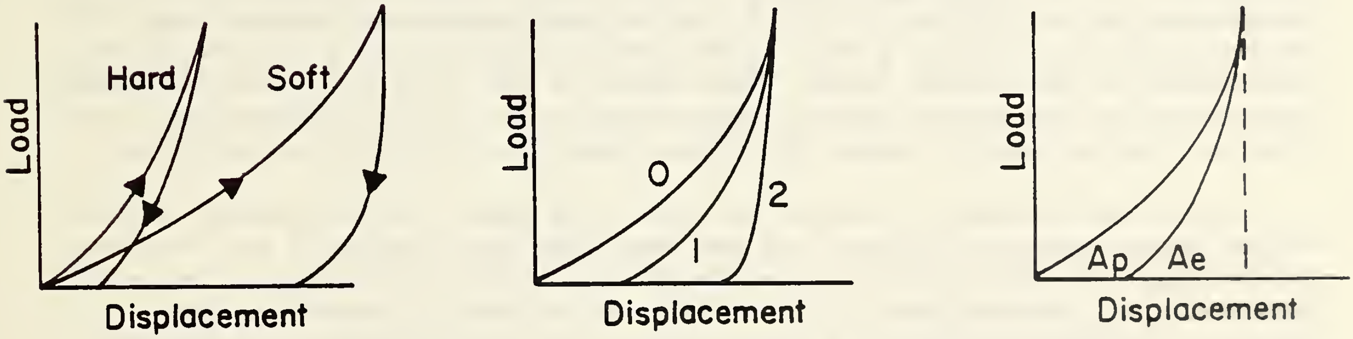

Figure 2. Schematic representations of the load-displacement curve.

(a) Hard materials have smaller indentation energies, Ap.

(b) After up-loading, 0, recovery can be largely elastic, 1, or plastic, 2.

(c) This characteristic can be quantified by the relative elastic energy, Ae and plastic energy, Ap, or area under the curves.

USE OF A COMMERCIAL HARDNESS TESTING INSTRUMENT AS A NONDESTRUCTIVE PROBE OF MECHANICAL PROPERTIES

D. S. Lashmore and J. L. Mullen

Metallurgy Division

Institute for Materials Science and Engineering

The microhardness indentation process involves a sampling of a very small volume of material in the region of the indentor. The kinetic values of hardness and load displacement characteristics provide information related to microdeformation and contain information related to the elastic properties and yield strength of the material(1). This project was designed to develop the instrumentation to characterize this process and to measure microindentation charcteristics of important alloys. Characteristic of this project is the use of commercially available instruments because of the desirability of rapidly transferring to industry a new technology. The development of this kind of a NDE technique is particularly important to the electrodeposition area because of the typically small volumes of material available for the measurement of mechanical properties.

As in many instrumentation projects, one of the more serious problems is signal to noise ratio. In the system described here two sources of noise exist; the first is the signal to noise ratio of the analog signals from the displacement and the load measuring instruments and the second is the digitizing noise or uncertainty in the voltage resulting from limitations in the digitizing equipment. The ideal system should not be digitizing noise limited. Unfortunately, at the start of this project only an 11 bit A/D converter was available. As the signal was about 1 volt, this yielded a digitizing uncertainty of about 400μ volts. By making some changes in the hardware, it became possible to obtain a full 12 bits which improved the situation to an uncertainty of about 240μ volts. This error in the ability to read the signal is marginally acceptable; however, converting to a 16 bit A/D converter would give us a noise value of about 15μ volts, which is below the analog noise.

Major improvements in signal to noise were made with the advice of John Mandel whose scheme to improve the raw data involves fitting of the raw data and determining the standard deviation of the collection of data. Then each data point is compared with a statistical value which incorporates the residual standard deviation, a noise factor, and the difference between the raw data and the fitted data.

Other important developments in the instrumentation included the procurement of a commercial hardness testing instrument specifically for this project. In the past, all the development of instrumentation and software has to be on a shared instrument which severely limited the time available. Major improvements were made to the apparatus to improve its rigidity. A load displacement curve for a NBS standard reference material of copper is shown in Fig. 1. Simple hardness values using this instrumentation compared with the traditional technique are shown in Fig. 2 and the instantaneous Vickers harbdness as a function of displacement is shown in Fig. 3. The latter curve confirms Tabor's statement (1), that the Vickers hardness number is independent of displacement and that the strain will always be 8% which is exactly what was measured.

The unloading curve provides a means of determining the modulus of the material. For the copper specimen we have been indenting, the slope corresponds to 1,4100 kg/mm^2(20 million psi) which is consistent with the literature values. Significantly the strain measured was exactly 8% in agreement with the empirical value assumed by Tabor (1) for a Vickers indentor. An estimate of the Ultimate Yield Stress can also be obtained from the data using a value of 2.9 for ratio of Vickers Hardness to Ultimate tensile strength, then

$$UTS= 135\ Kg/mm^2/2.9=46\ kg/mm^2\ (65{,}320psi). \qquad (1)$$

This value is in good agreement with the values reported by Lamb(2) for copper electrodeposited from the same electrolyte as the sample we are using.

SUMMARY

It has been demonstrated that commercial hardness testing instruments have the potential to provide important information concerning ultimate tensile strength and elastic modulus. This capability is important for those concerning with coatings or alloy development where only small amounts of material are available for testing. When existing limitations in equipment are overcome, then data will be obtained on copper single crystals to confirm and further develop the theory of the microindentation process.

REFERENCES

1. D. Tabor. J. Inst. Metals 1951 Vol 79, pg. 1-18.

2. V. Lamb, C. Johnson and D. Valentine. J. Electrochem. Soc. Vol. 117, No. 9, (Sept. 1970).

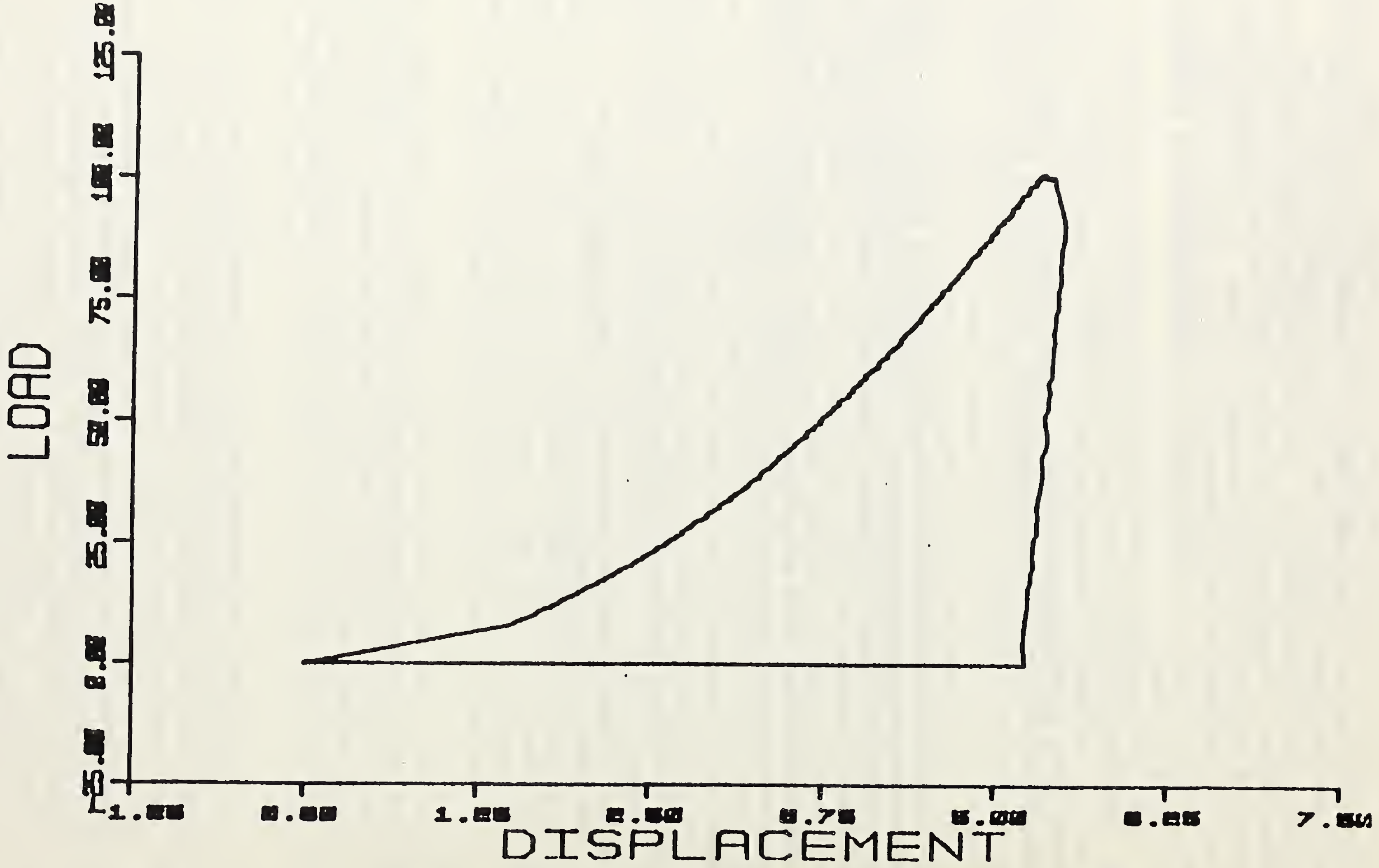

Figure 1. Load in grams as a function of displacement in microns displacement for copper with a Vickers diamond indentor.

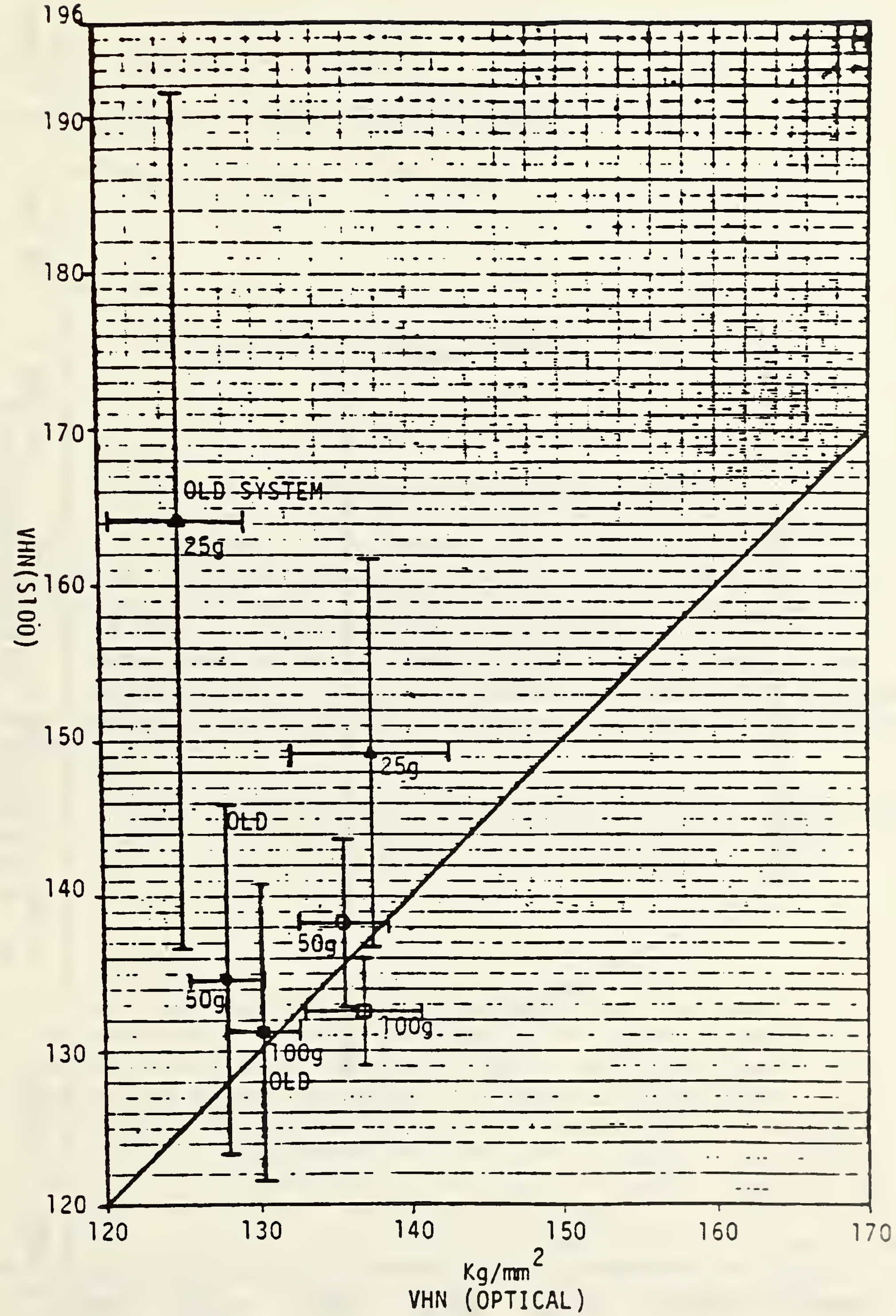

Fig. 2 Vickers Hardness Measured by the Automated Hardness Measurement System as a Function of the Optical Vickers Hardness. The error bars represent ± 1 Standard Deviation.

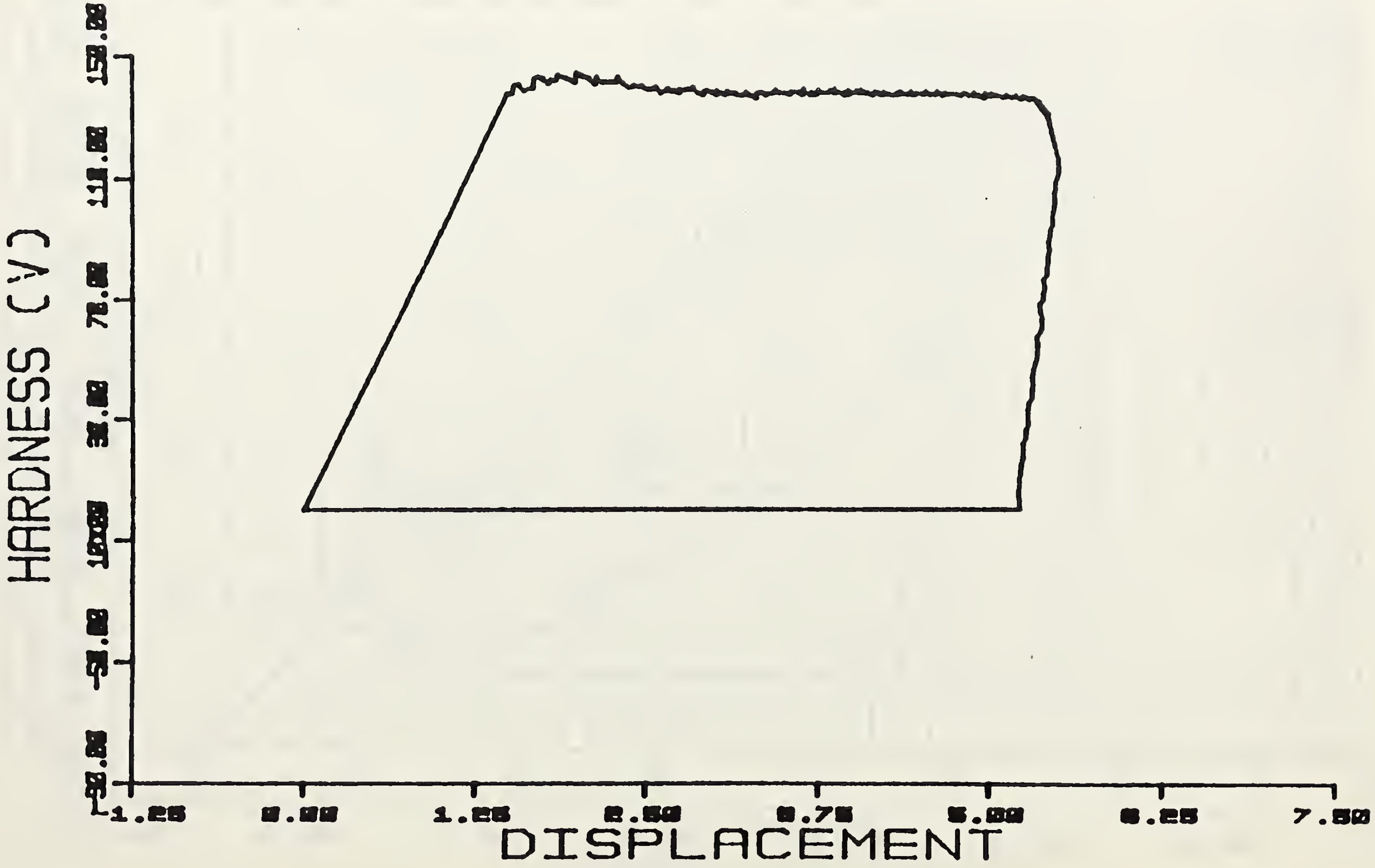

Figure 3. Vickers hardness as a function of indentor displacement in microns for copper.

NONDESTRUCTIVE EVALUATION OF TOOL WEAR AND CHIP FORMATION

Kenneth W. Yee and Laurie Evans

Automated Production Technology Division

Center for Manufacturing Engineering

and

David Dornfeld

University of California, Berkeley

INTRODUCTION

With the upswing in automated manufacturing - especially untended manufacturing - the detection of worn or dull tooling, and the maintenance of small, manageable chips become very important elements in the machining process. The continued use of worn or dull tools can result in the production of unfit parts, or broken tools, and the formation of continuous chips can cause entanglement and clogging of the machining center. This means that in an untended operation, where there is no operator to stop and check the machining center, tool and chip management is extremely important since the machining center itself can be damaged by worn tooling and chip congestion.

Progress in tool wear prediction in milling operations is described in this report as well as continued work in the area of chip form management.

TOOL WEAR

On-line tool wear sensing is more important now than ever in automated manufacturing. Without an operator to determine when tooling must be changed, an imprecise method in itself, worn tools must be changed based on the amount of cut or the number of parts made. This is an inefficient method since the life of tools, even from the same lot, varies significantly. This means that tools would have to be changed after the shortest life expectancy of any tool in a lot. Much of the useful life will be wasted for the majority of tools, and there is a loss of time and money in making excessive tool changes due to the additional time required to change tooling. Worse still, a machine tool might not have enough locations in the tool magazine to operate untended for the required length of time.

Drill-Up is an instrument which was originally designed at the National Bureau of Standards to prevent breakage of small-diameter drills used on automatic-feed drilling machines. This application and the measurement methods involved are described in reference 1; a description of the use of Drill-Up to monitor tool wear in large diameter drills is given in reference 2. Based on time-domain analysis of vibration, Drill-Up has a calibration routine which automatically adjusts to the amplitude of the vibration signal due to normal machining. Large amplitude accelerations, synchronous with the tool rotation, have been found to be indicative of improper machining, and it is this increase in signal level which Drill-Up monitors as the tool wears to detect worn-out tooling.

The use of Drill-Up as an alternative to monitoring feed force and spindle power consumption has been investigated for detecting tool wear in end-milling in three hardnesses of steel; this has been described in reference 3. Because they are commonly-employed tools, 1/2 in. (approx. 12 mm) diameter high speed steel end mills were used in heavy cuts in AISI 4150 (290 Brinell Hardness Number, BHN), 4130 (245 BHN), and 1015 (180 BHN). Drill-Up parameters were altered to provide two instruments, an original circuit and a more sensitive circuit, for monitoring end-mill wear. Feed force and spindle cutting power, defined as total spindle motor power consumption while machining minus spindle motor power consumed while the spindle motor is rotating but not cutting, were also examined as tool wear detection parameters. The results of the experiments conducted are shown in Figure 1. Linear regression fits of feed force and cutting power are plotted versus maximum flank wear of the four cutting flutes, for the average of four tools in each of the three steels. The wear values at which the Drill-Up circuits determined worn tooling are plotted on the feed force versus wear plot. It can be seen that the change in the cutting power with increasing flank wear (the slope of the curve) is very similar for all three steels, and is large enough that cutting power might be a viable method for detecting wear. The change in feed force with flank wear varies with the increasing hardness of the steel. This means that feed force may be less applicable than cutting power for a wide range of materials, but may not be ruled out as a wear monitoring method yet. The original Drill-Up circuit was found to be capable of detecting wear in the two harder steels, and the sensitive circuit was able to detect a suitable degree of wear in the softer steel. (A worn-out tool is considered to have roughly 5-7 milli-inches, or 125 to 175 micrometers flank wear.) The performance of Drill-Up in these experiments indicates that it is a useful method of determining tool wear for one size of end mill in several steels.

Feed force and cutting power methods show promise in the area of tool wear detection for end-milling. Drill-Up has shown potential in detecting tool wear in drilling, has been successful in preventing breakage of small diameter drills, and with minor modifications can predict tool wear in end-milling.

CHIP FORMATION

The goal of this research is to investigate the applicability of acoustic emission (AE) to the study of chip formation in single-point turning. The results of this research have both theoretical and practical interest since some of the limitations of present untended manufacturing operations are related to a lack of knowledge of the chip conditions. In some metal operations this can lead to deterioration of the surface finish, dimensional variation, or severe damage to the workpiece and tooling due to chip tangle.

In order to predict chip formation, an acoustic emission event (rate) counter was constructed which was designed expressly as an experimental tool to be used for the counting of acoustic emission (AE) signal bursts which exceed a selectable threshold voltage during a predetermined time interval. Tests using this device were performed on a turning center with coated carbide insert tooling. An AE transducer was mounted at the rear of the tool holder. The materials machined were 6061-T651 aluminum rod, and two types of steel rod: AISI 1215 and 4340. The AE signal was analyzed using the acoustic emission event counter. Each significant burst event in the AE signal can be related to the chip breaking process due to the instantaneous large energy release at chip fracture compared to the AE generated during normal cutting. The count rate of burst events above a certain threshold excludes the continuous-type AE signal contributed by normal cutting and is a good indicator of the chip-breaking frequency. This is shown in Figures 2 and 3 which are plots of the events per second versus the feed rate for the two types of steel bars. The transition from continuous to discontinuous chip formation occurs at about 0.006 inches per revolution for the 4340 and, for the 1215, at around 0.004 inches per revolution. For the alloy steel there is a detectable change in slope; for the low carbon steel there is a less discernable change. For two materials (the aluminum and the alloy steel) one can predict the formation of chips; it may also be possible to predict chip formation in the low carbon steel although with less certainty. Further development is needed in this area with a wider range of materials in order to produce suitable chip management algorithms.

SUMMARY

During FY85, progress has been made in tool wear monitoring via development of power, force, and time-domain vibration (Drill-Up) methods, as applied to end-milling. Chip formation detection in turning has proceeded in several new materials, including low carbon steel (AISI 1215) and mild alloy steel (AISI 4340).

REFERENCES

1. K. W. Yee, and D. S. Blomquist, "An On-Line Method of Determining Tool Wear by Time-Domain Analysis," Technical Paper MR82-901, Soc. Mfg. Eng'rs, Dearborn, MI, 1982.

2. K. W. Yee, "On the Use of Drill-Up for On-Line Determination of Drill Wear," Technical Paper MR84-914, Soc. Mfg. Eng'rs, Dearborn, MI, 1984.

3. K. W. Yee, and L. Evans, "Drill-Up, An Alternative for On-Line Determination of End-Mill Wear," Proc. of the 13th N. A. M. R. C., Berkeley, CA, Soc. Mfg. Eng'rs, Dearborn, MI, May, 1985.

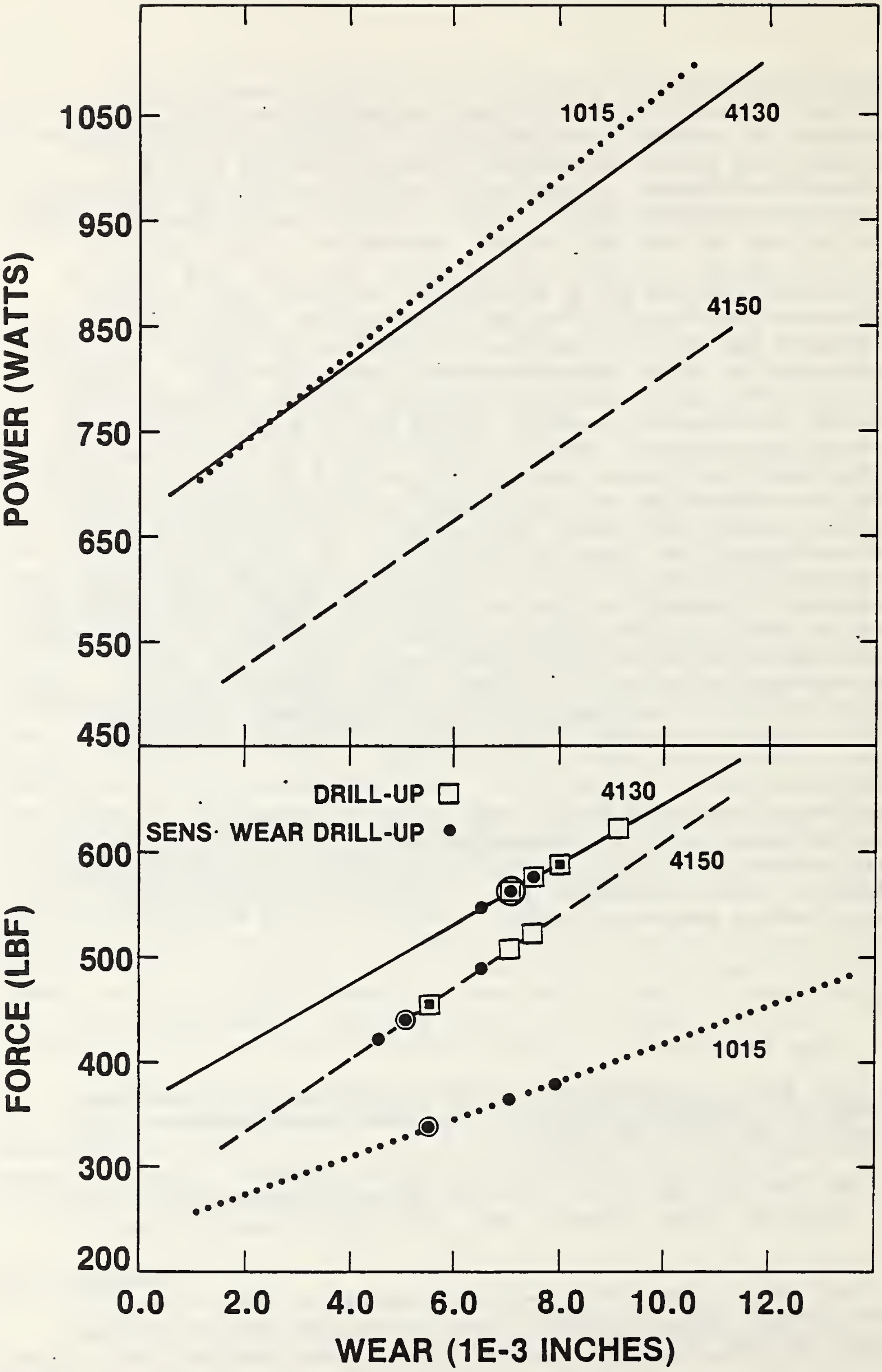

Figure 1. Feed Force and Cutting Power vs. Wear for Three Steels

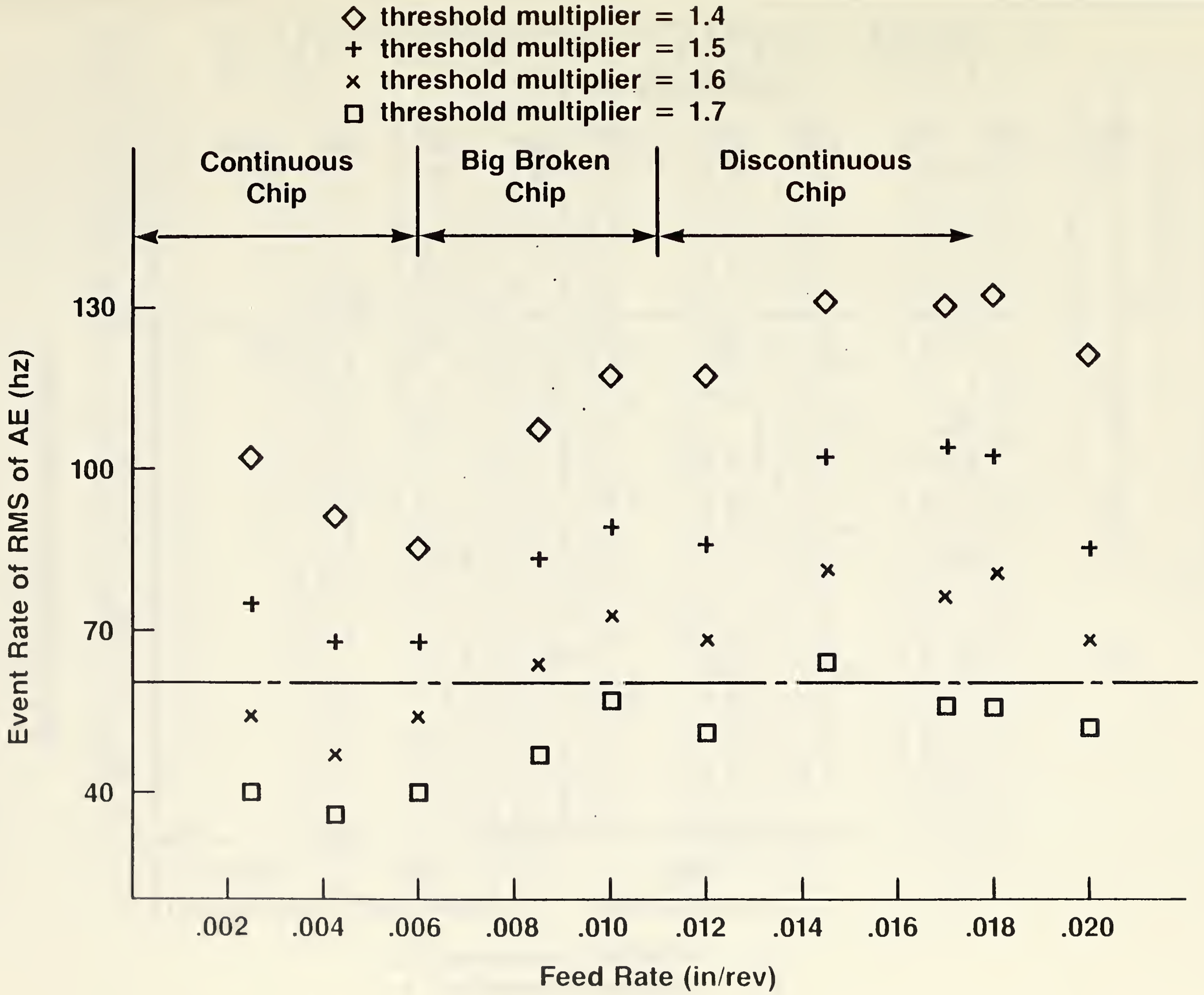

Figure 2. Event rate of RMS of AE vs. feed rate for AISI 4340 steel

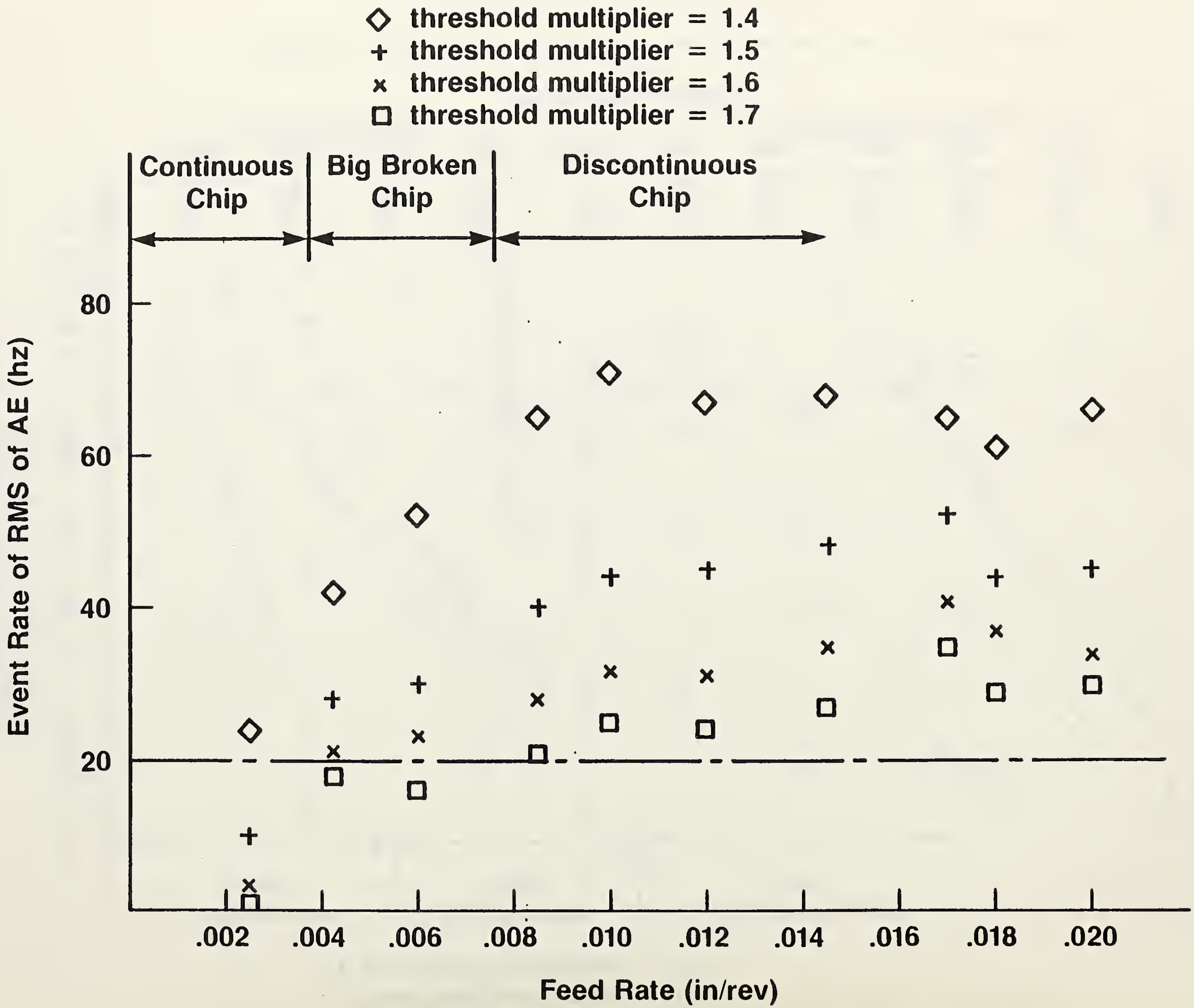

Figure 3. Event rate of AE vs. feed rate for AISI 1215 steel

ULTRASONIC MEASUREMENTS ON THERMAL INSULATION

G.V. Blessing and D.R. Flynn

Mechanical Production Metrology Division

Center for Manufacturing Engineering

A recent request from the thermal insulation sector of the building industry to NBS, for innovative methods to measure insulation quantity, has resulted in feasibility tests using ultrasonic waves. The scattering sensitivity of air-borne ultrasound at 40 kHz to the average density of commercially available fiberglass batt material has been demonstrated in these tests.

A two transducer transmit-receive continuous wave system was used, with the transmitter facing the receiver and separated by about 15 cm. Figure 1 illustrates the received amplitude obtained at 40 kHz respectively for (a) no insulation, (b) one R-11 batt thickness, and (c) two R-11 batt thickness between transmitter and receiver. The R-value is the commercially-used measure for heat flow resistance. Home ceiling insulation values may range from zero to R-40 or greater, depending on the region of the country and other factors.

Two significant features may be observed for the signals in Fig. 1 as a function of increasing R-value. The most prominent is the (expected) reduction in signal amplitude with increasing insulation due to increased ultrasonic scattering. Less evident, but perhaps of equal significance as a practical measurand, is the phase shift (later in time) with increasing insulation. It may be conjectured that this shift is due to an increased sound path the waves must travel on the average through the multiply-scattering fiberglass medium. This is based on the assumption that fiberglass, possessing a significantly different acoustic impedance from air, acts to scatter rather than absorb the wave front.

A patent application covering this technique for inferring thermal insulation values from ultrasonic measurements has been submitted to DOC. It is expected to be useful for process control in manufacture of insulation and for determining the value of installed insulation.

SUMMARY

The feasibility of a new method of inferring the R-value of installed attic insulation using air-borne ultrasound has been demonstrated. The technique promises to be orders of magnitude faster, less expensive, and less intrusive than other methods. It may also be used for process control of insulation manufacture.

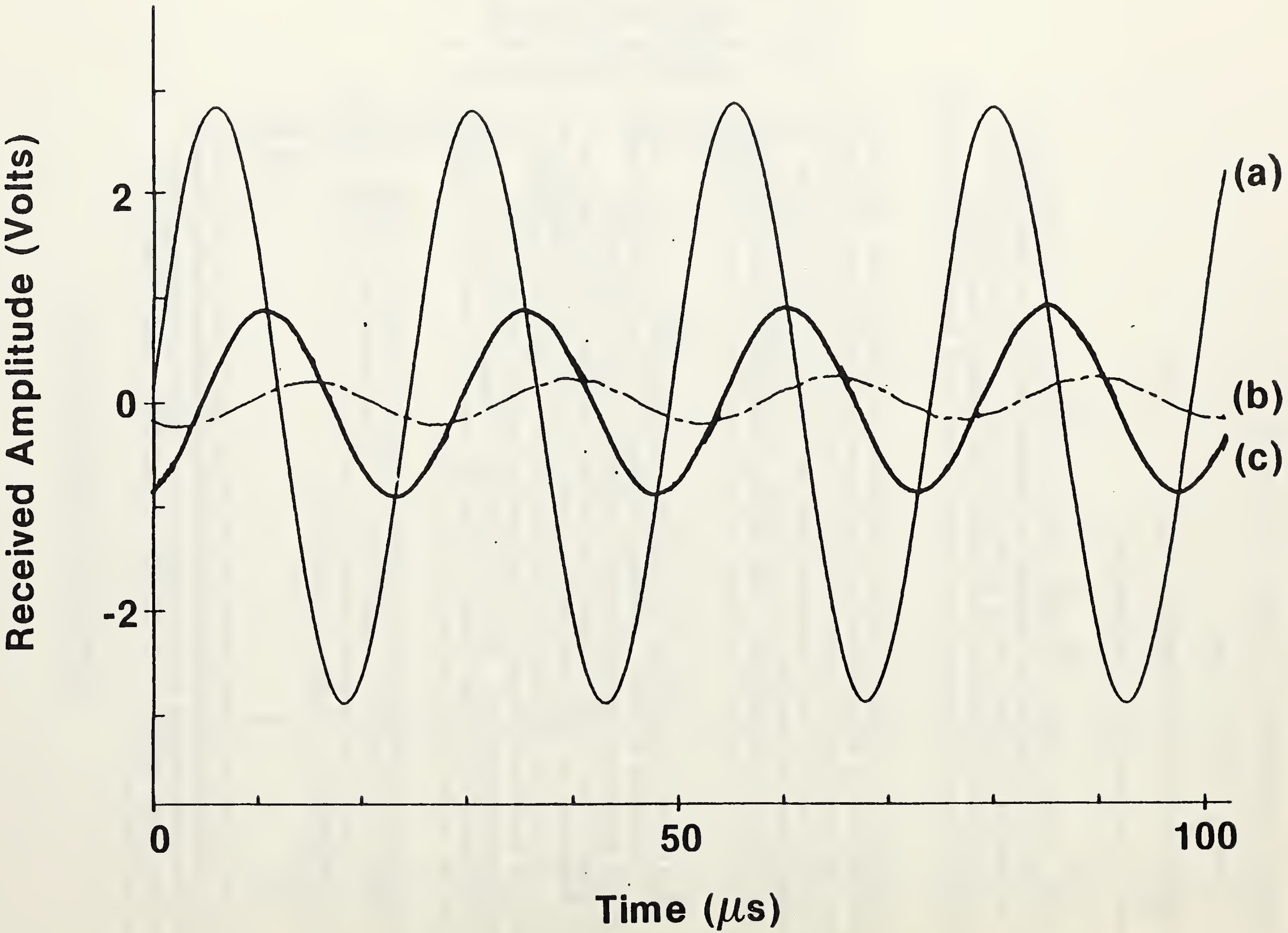

Figure 1. The received 40 kHz ultrasonic wave amplitude as a function of time for three quantities of fiberglass insulation between transmitter and receiver: (a) none, (b) one, and (c) two R-11 batts.

APPENDICES

A. NDE SEMINARS AT NBS

Dr. Erkhardt Schneider, Fraunhofer Institut für Zerstörungsfreie Prüfverfahren, Saarbrücken, FRG

"Evaluation of Stress States with Ultrasonic Techniques"

October 16, 1984

Mr. James J. Yavelak, Babcock & Wilcox Co., Alliance, Ohio

"Sensing Residual Stresses and Microstructure with Magnetic Barkhausen Noise Analysis"

December 10, 1984

Dr. David A. Hutchins, Queen's University, Kingston, Ontario, Canada

"Non-Contact Ultrasonic Transducers for NDE"

March 11, 1985

Ms. Susan N. Vernon, Naval Surface Weapons Center, Silver Spring, Maryland

"Eddy Current Inspection of Composites with Conducting Fibers in a Non-Conducting Matrix"

March 28, 1985

Dr. Eva Krasicka, University of Illinois

"Ultrasonic Study of Tunneling of Trapped Hydrogen in Niobium"

May 23, 1985

Dr. B. N. Ranganathan and associates, Martin Marietta Aerospace, New Orleans, Louisiana

"Nondestructive Evaluation at the Michoud Division of Martin Marietta Aerospace"

July 16, 1985

Professor Richard Klaus, Virginia Polytechnic Institute and State University, Blacksburg, Virginia

"NDE of Composite Materials Using Optical Fibers"

August 6, 1985

Dr. William N. Reynolds, Atomic Energy Research Establishment, Harwell, United Kingdom

"Ultrasonic and Thermographic Characterization of Composite Materials"

August 13, 1985

B. INVITED TALKS BY ONDE STAFF

"NBS Research on NDE Sensors for Manufacturing Process Control," H. T. Yolken, Bethlehem Steel Corporation, Research Seminar, Bethlehem, Pennsylvania, October 18, 1984.

"Quantitative NDE and Quality Improvement," L. Mordfin, Fairmont State Section, American Society for Nondestructive Testing, Fairmont, West Virginia, November 8, 1984.

"Quantitative NDE and Quality Improvement," L. Mordfin, Hampton Roads Section, American Society for Nondestructive Testing, Newport News, Virginia, January 8, 1985.

"International NDE Standards and the GATT Code," L. Mordfin, 7th International Conference on NDE in the Nuclear Industry, Grenoble, France, February 1, 1985.

"Quantitative NDE and Quality Improvement," L. Mordfin, Lynchburg Section, American Society for Nondestructive Testing, Lynchburg, Virginia, February 20, 1985.

"The Challenge of Advanced NDE," H. T. Yolken, luncheon address, 1985 Spring Conference, American Society for Nondestructive Testing, Washington, D.C., March 11, 1985.

"Advanced NDE for Manufacturing Process Control," H. T. Yolken, 17th Symposium on Nondestructive Evaluation, San Antonio, Texas, April 24, 1985.

"NDE Sensors for Manufacturing Process Control: Developing National Strategy and Policy," H. T. Yolken, Review of Progress in Quantitative NDE, Williamsburg, Virginia, June 25, 1985.

"Automated Materials Processing," H. T. Yolken, National Science Foundation, Planning Workshop for Senior Management, Washington, D.C., July 15, 1985.

C. PUBLICATIONS

Following is a partial listing of NBS reports and publications on NDE and related topics that have been issued since last year's Technical Activities report was prepared. A more complete compilation will be presented in ONDE's annual bibliography with abstracts.

B. A. Auld, G. McFetridge, M. Riazat and S. Jefferies, "Improved Probe-Flaw Interaction Modeling, Inversion Processing, and Surface Roughness Clutter," Review of Progress in Quantitative Nondestructive Evaluation 4A, pp. 623-634 (1985).

M. Barsky and N. N. Hsu, "A Simple and Effective AE Source Location System," *Materials Evaluation* *43*, No. 1, pp. 108-110 (Jan. 1985).

H. Berger, D. C. Cutforth, D. A. Garrett, J. Haskins, F. Iddings and R. L. Newacheck, "Neutron Radiography," *Nondestructive Testing Handbook* *3*, 2nd edition, Section 12, pp. 532-563 (ASNT, 1985).

G. Birnbaum, G. S. White, and C. M. Vest, "Laser Generated and Detected Ultrasound and Holographic Methods," *Pressure Vessel and Piping Technology 1985--A Decade of Progress*, pp. 661-669 (ASME, NY, 1985).

P. J. Blau, "Investigation of the Nature of Micro-indentation Hardness Gradients Below Sliding Contacts in Five Copper Alloys Worn Against 52100 Steel," *J. Materials Science* *19*, p. 1957 (1984).

P. J. Blau, "Relationship Between Scratch and Knoop Micro-indentation Hardness and Implications for Abrasion of Metals," *Microstructural Science* *12*, p. 293 (1985).

P. J. Blau and T. R. Shives, "Microindentation Hardness Testing," *ASTM Standardization News* *13*, No. 1, pp. 47-51 (1985).

G. V. Blessing, N. N. Hsu and T. N. Proctor, "Ultrasonic-shear-wave Measurement of Known Residual Stress in Aluminum," *Experimental Mechanics* *24*, No. 3, pp. 218-221 (Sept. 1984).

G. V. Blessing, P. O. Bagley and J. E. James, "The Effect of Surface Roughness on Ultrasonic Echo Amplitude in Steel," *Materials Evaluation* *42*, No. 11, pp. 1389-1392 (Oct. 1984).

T. E. Capobianco and F. R. Fickett, "Precision Measurement of Eddy Current Coil Parameters," *Review of Progress in Quantitative Nondestructive Evaluation* *4A*, pp. 491-498 (1985).

A. S. Carasso and N. N. Hsu, "Probe Waveforms and Deconvolution in the Experimental Determination of Elastic Green's Functions," *SIAM J. Appl. Math.* *45*, No. 3, pp. 369-383 (June 1985).

A. S. Carasso and N. N. Hsu, "The Inverse Gaussian Pulse in the Experimental Determination of Linear System Green's Functions," ARO Report 85-1, pp. 389-404 (Army Research office, Research Triangle Park, NC, 1985).

E. L. Church, T. V. Vorburger and J. C. Wyant, "Direct Comparison of Mechanical and Optical Measurements of the Finish of Precision Machined Optical Surfaces," *Opt. Eng.* *24*, pp. 388-395 (1985).

R. B. Clough, H. N. G. Wadley and F. S. Biancaniello, "Acoustic Emission Studies of Electron Beam Melting and Rapid Solidification," *Nondestructive Evaluation: Application to Materials Processing*, pp. 27-40 (ASM, 1984).

R. B. Clough and H. N. G. Wadley, "Acoustic Emission Monitoring of Dislocation Motion and Microfracture During Electron Beam Melting and Rapid Solidification of Aluminum Alloys," *Review of Progress in Quantitative Nondestructive Evaluation* *4B*, pp. 661-669 (1985).

K. L. Eckerle, J. J. Hsia and V. R. Weidner, "Transmittance MAP Service," NBS SP 692, 44 pp. (1985).

[D. G. Eitzen], "Glossary of Terms and Definitions for Acoustic Emission Testing Procedures," Military Standard MIL-STD-1945, 5 pp. (DOD, 24 October 1984).

D. G. Eitzen, N. Hsu, A. Carasso and T. Proctor, "Deconvolution by Design--An Approach to the Inverse Problem of Ultrasonic Testing," Review of Progress in Quantitative Nondestructive Evaluation 4A, pp. 179-188 (1985).

F. R. Fickett and T. E. Capobianco, "Magnetic Field Mapping with a SQUID Device," Review of Progress in Quantitative Nondestructive Evaluation 4A, pp. 401-410 (1985).

C. L. Friant, M. Rosen, R. E. Green, Jr. and R. Mehrabian, "Ultrasonic NDE of Rapidly Solidified Products and its Application to Process Control," Nondestructive Evaluation: Application to Materials Processing, pp. 51-59 (ASM, 1984).

C. L. Friant and M. Rosen, "Ultrasonic Materials Characterization of Melt Spun Metallic Ribbons," Nondestructive Methods for Material Property Determination, pp. 301-314 (Plenum Press, NY, 1984).

D. E. Gilsinn, T. V. Vorburger, F. E. Scire, E. C. Teague and M. J. McLay, "Surface Texture Characterization by Angular Distributions of Scattered Light," Review of Progress in Quantitative Nondestructive Evaluation 4B, pp. 779-788 (1985).

M. Gvishi, M. Rosen and H. N. G. Wadley, "Acoustic Emission Characterization of the Martensitic Phase Transformation in NiTi," Review of Progress in Quantitative Nondestructive Evaluation 4B, pp. 651-659 (1985).

K. Hardman-Rhyne, N. F. Berk and E. D. Case, "Porosity Study of Sintered and Green Compacts of $YCrO_3$ Using Small Angle Neutron Scattering Techniques," Nondestructive Evaluation: Application to Materials Processing, pp. 103-108 (ASM, 1984).

N. N. Hsu and D. G. Eitzen, "Analytical Approach to Acoustic Emission Signal Processing: Problems and Progress," Proc. 7th International Acoustic Emission Symposium, pp. 326-334 (Japan Soc. Non-Destructive Inspection, 1984).

S. Kim, J. R. Weertman, S. Spooner, C. J. Glinka, V. Sikka and W. B. Jones, "Microstructural Evaluation of a Ferritic Stainless Steel by Small Angle Neutron Scattering," Nondestructive Evaluation: Application to Materials Processing, pp. 169-176 (ASM, 1984).

D. S. Kupperman, H. B. Karplus, R. B. Poeppel, W. A. Ellingson, H. Berger, C. Robbins and E. Fuller, "Application of NDE Methods to Green Ceramics: Initial Results," Nondestructive Evaluation: Application to Materials Processing, pp. 89-101 (ASM, 1984).

H. M. Ledbetter, S. K. Datta and R. D. Kriz, "Elastic Constants of an Anisotropic, Nonhomogeneous Particle-Reinforced Composite," Acta Metallurgica 32, pp. 2225-2231 (1984).

M. Linzer, editor, Ultrasonic Imaging 7 (Academic Press, 1985).

T. S. Liu, R. J. Fields, D. G. Harlow and T. J. Delph, "Statistical Observations of Creep Cavitation in AISI 304 Stainless Steel," Scripta Metallurgica 19, pp. 299-304 (1984).

R. Mehrabian and H. N. G. Wadley, "Needs for Process Control in Advanced Processing of Materials," Review of Progress in Quantitative Nondestructive Evaluation 4B, pp. 839-858 (1985).

L. Mordfin, editor, "Office of Nondestructive Evaluation: Technical Activities 1984," NBSIR 84-2944, 163 pp. (Nov. 1984).

L. Mordfin, editor, "NDE Publications: 1982," NBSIR 85-3183, 32 pp. (May 1985).

J. C. Moulder, J. C. Gerlitz, B. A. Auld, M. Riaziat, S. Jefferies and G. McFetridge, "Calibration Methods for Eddy Current Measurement Systems," Review of Progress in Quantitative Nondestructive Evaluation 4A, pp. 411-420 (1985).

T. Nguyen and A. Rosencwaig, "Thermal-wave Microscopy and Its Applications to Imaging the Microstructure and Corrosion of Cold-rolled Steel," Appl. Surface Sci. 24, No. 1 (1985).

S. J. Norton and H. N. G. Wadley, "Tomographic Reconstruction of Internal Temperature," Review of Progress in Quantitative Nondestructive Evaluation 4A, pp. 309-318 (1985).

R. L. Parker, "Ultrasonic Measurement of Solid/Liquid Interface Position During Solidification and Melting of Iron and Steel," Nondestructive Evaluation: Application to Materials Processing, pp. 23-25 (ASM, 1984).

T. M. Proctor, F. R. Breckenridge and D. G. Eitzen, "The Development of High Fidelity Acoustic Emission Transducers," Proc. 6th Intl. Conf. on NDE in the Nuclear Industry, pp. 329-337 (ASM, Metals Park, OH, 1984).

R. E. Schramm and J. C. Moulder, "EMAT/Synthetic Aperture Approach to Thick-Weld Inspection," Review of Progress in Quantitative Nondestructive Evaluation 4A, pp. 225-232 (1985).

J. J. Smith, M. Rosen and H. N. G. Wadley, "Nondestructive Characterization of Rapidly Solidified Al-Mn Alloys by Ultrasonic and Electrical Methods," Nondestructive Evaluation: Application to Materials Processing, pp. 61-69 (ASM, 1984).

J. J. Smith, "Nondestructive Characterization of Rapidly Solidified Aluminum-Manganese Alloys," Report CMR-NDE-14, 48 pp. (Johns Hopkins University, Baltimore, MD, 1984).

P. L. Swanson, "Subcritical Fracture Propagation in Rocks: An Examination Using the Methods of Fracture Mechanics and Non-Destructive Testing," NBS-GCR-85-491, 268 pp. (April 1985).

L. R. Testardi, S. J. Norton and T. Hsieh, "Determination of Inhomogeneities of Elastic Modulus and Density Using Acoustic Dimensional Resonance," *Review of Progress in Quantitative Nondestructive Evaluation 4B*, pp. 877-880 (1985).

H. N. G. Wadley, chairman, "Acoustic Emission--Open Discussion," *Review of Progress in Quantitative Nondestructive Evaluation 4B*, pp.727-737 (1985).

H. N. G. Wadley, S. J. Norton, F. S. Biancaniello and R. Mehrabian, "Ultrasonic Measurement of Internal Temperature Distribution," *Nondestructive Evaluation: Application to Materials Processing*, pp. 3-11 (ASM, 1984).

H. N. G. Wadley, editor, *Proceedings, 6th International Conference on NDE in the Nuclear Industry* (ASM, Metals Park, OH, 1984).

H. N. G. Wadley and R. Mehrabian, "Acoustic Emission for In-Process Monitoring and Microstructure Control?," *Nondestructive Methods for Material Property Determination*, pp. 207-236 (Plenum Press, NY, 1984).

H. T. Yolken and L. Mordfin, "Strategic Plan for Nondestructive Evaluation for the Period 1985-1989," 41 pp. (Office of Nondestructive Evaluation, NBS, December 1984).

D. AWARDS

AEWG Publication Award

Frank Breckenridge, Carl Tschiegg and Martin Greenspan, all associated with the Center for Manufacturing Engineering, received the coveted Publication Award of the Acoustic Emission Working Group for their landmark paper, "Acoustic Emission: Some Applications of Lamb's Problem," which appeared in the Journal of the Acoustical Society of America, Volume 57. The citation states, in part, that the paper ". . . laid the foundation for the standardized calibration of acoustic emission sensors and stimulated the development of quantitative theories of the wave-propagation aspect of acoustic emission."

Department of Commerce Silver Medal

Department of Commerce Silver Medals, which are bestowed for meritorious contributions of unusual value to the Department, were awarded to Dr. Bruno M. Fanconi of the Polymers Division, Dr. Frederick R. Fickett of the Center for Electronics and Electrical Engineering, and Dr. Hassel M. Ledbetter of the Fracture and Deformation Division. All three are principal investigators in the NDE Program.

Industrial Commission on Illumination (CIE)

Dr. Jack Hsia of the Center for Radiation Research was named associate director of CIE Division 2 on "Physical Measurement of Light and Radiation," by the Council of the Commission. A principal investigator in the NDE Program, Hsia has been developing measurement standards for the fluorescence of liquid penetrant and magnetic particle materials, and for the light transmittance of high-density radiographs.

Department of Commerce Bronze Medal

Dr. Anna C. Fraker of the Metallurgy Division and Dr. Maurice B. Kasen of the Fracture and Deformation Division were recipients of the Department of Commerce Bronze Medal Award for superior federal service. Fraker is the NDE Program's principal investigator for NDE of corrosion; Kasen was cited, in part, for ". . . his innovative, definitive studies on how defects affect pipeline structural integrity. . . ."

NBS Unit Safety Award

The Office of Nondestructive Evaluation is proud to announce its receipt of the NBS Unit Safety Award, "for an exceptional safety performance record for a continuous period beginning July 1, 1979." Dr. George Birnbaum has served as the Office's safety officer for this entire period.

E. PRINCIPAL INVESTIGATORS

Berk, Norman F.	Small-angle neutron scattering Condensed matter theory
Berlinsky, Yoram	Acoustic emission Wave propagation and instrumentation
Blau, Peter J.	Thermal waves Tribology
Blessing, Gerald V.	Ultrasonics Experimental physical acoustics
Breckenridge, Franklin R.	Acoustic emission and transducers Transducer calibration
Capobianco, Thomas E.	Eddy current NDE Electromagnetic technology
Carasso, Alfred S.	Acoustic emission Applied mathematics; inverse problems; image analysis; deconvolution
Carino, Nicholas J.	Pulse echo Concrete technology and structural analysis
Clark, Alfred V.	Ultrasonics and eddy currents Mechanical properties

Clough, Roger B.	Acoustic emission Mechanical properties
Cohen, Julius	Thermography Fourier optics
Droney, Bernard	Steel processing sensors Metallurgy
Eckerle, Kenneth L.	Fluorescence Spectrophotometry
Ehrlich, Charles D.	Calibrated leaks and leak detection Surface physics
Eitzen, Donald G.	Acoustic emission Engineering mechanics
Fanconi, Bruno M.	Optical wave guide techniques Polymer science
Fick, Steven E.	Specialized measurement Electrical engineering
Fickett, Frederick R.	Electromagnetic methods Solid state physics, superconductivity, and magnetism
Fields, Richard J.	Quantitative metallography Mechanical metallurgy
Fong, Jeffrey T.	Reliability Mathematical analysis
Fraker, Anna C.	Microstructures, microscopy, and standards development Corrosion processes
Free, George M.	Eddy current measurements AC impedance measurements
Hardman-Rhyne, Kay A.	Small-angle neutron scattering Ceramics
Hsia, Jack J.	Spectrophotometry Spectrophotometry and thermal radiation properties
Hsu, Nelson N.	Acoustic emission and ultrasonics Experimental solid mechanics
Hunston, Donald L.	Ultrasonics Polymer science

Inglehart, Lorretta	Thermal waves Physics
Kahn, Arnold H.	Eddy currents Solid state physics
Kriz, Ronald D.	Ultrasonics and fiber optics Mechanical properties of composites
Kuriyama, Masao	X-ray diffraction Solid state physics
Lashmore, David	Microhardness measurements and micromechanical properties Alloy deposition
Ledbetter, Hassel M.	Elastic properties and internal friction Physical properties of solids
Linzer, Melvin	Ultrasound instrumentation Signal processing
Mauer, Floyd A.	Ultrasonic temperature sensing Ultrasonic measurement
Mielenz, Klaus D.	Fluorescence Optical instrumentation and optics
Mopsik, Frederick I.	Electrical measurements Dielectrics
Moulder, John C.	Eddy current; ultrasonics using EMATS Materials research
Mountain, Raymond	Acoustic scattering Statistical physics
Norton, Stephen J.	Ultrasonic imaging Inverse modeling
Nguyen, Tinh	Thermal wave imaging and infrared thermography Corrosion under coatings
Placious, Robert C.	Radiological imaging Radiation physics
Polansky, Daniel	Radiographic inspection of materials Physics
Prask, Henry J.	Neutron diffraction Residual stress
Proctor, Thomas M.	Acoustic emission, transducers Transducer calibrations and design

Robbins, Carl R.	Ceramic powder preparation and characterization X-ray diffraction
Rosen, Moshe	Ultrasonics, eddy currents Materials characterization
Ruff, Arthur W.	Wear condition monitoring Tribology/metallurgy
Simmons, John A.	Defects and elastic propagation; materials characterization Applied mathematics and theoretical mechanics
Spal, Richard D.	X-ray imaging Synchroton radiation
Swartzendruber, Lydon W.	Surface methods Physical metallurgy
Teague, E. Clayton	Non-contacting optical measurements of surface roughness Surface metrology and physics
Tilford, Charles R.	Leak and pressure standards Vacuum technology
Vorburger, Theodore V.	Optical scattering techniques Surface roughness measurement
Wadley, Haydn N. G.	Acoustic emission Fracture and deformation
Wang, Francis W.	Fluorescence spectroscopy Polymer characterization
White, Grady S.	Thermal waves Mechanical properties of brittle materials
Yee, Kenneth W.	Machine tool sensors Electronic instrumentation

NBS-114A (REV. 2-80)

U.S. DEPT. OF COMM. **BIBLIOGRAPHIC DATA SHEET** *(See instructions)*	1. PUBLICATION OR REPORT NO. NBSIR-85/3187	2. Performing Organ. Report No.	3. Publication Date November 1985

4. TITLE AND SUBTITLE

Institute for Materials Science and Engineering
Nondestructive Evaluation - Technical Activities 1985

5. AUTHOR(S)

Yolken, H.T., Mordfin, L., Birnbaum, G. (Editor)

6. PERFORMING ORGANIZATION *(If joint or other than NBS, see instructions)*

NATIONAL BUREAU OF STANDARDS
DEPARTMENT OF COMMERCE
WASHINGTON, D.C. 20234

7. Contract/Grant No.

8. Type of Report & Period Covered

Annual, FY85

9. SPONSORING ORGANIZATION NAME AND COMPLETE ADDRESS *(Street, City, State, ZIP)*

National Bureau of Standards
Rte. 270 & Quince Orchard Road
Gaithersburg, Maryland 20899

10. SUPPLEMENTARY NOTES

☐ Document describes a computer program; SF-185, FIPS Software Summary, is attached.

11. ABSTRACT *(A 200-word or less factual summary of most significant information. If document includes a significant bibliography or literature survey, mention it here)*

A review of the Nondestructive Evaluation Program at NBS, for fiscal year 1985, is presented in this annual report.

12. KEY WORDS *(Six to twelve entries; alphabetical order; capitalize only proper names; and separate key words by semicolons)*

acoustic emission; eddy currents; leak testing; magnetics; neutrons; nondestructive evaluation; optics; penetrants; radiography; standards; thermal testing; ultrasonics

13. AVAILABILITY

☒ Unlimited
☐ For Official Distribution. Do Not Release to NTIS
☐ Order From Superintendent of Documents, U.S. Government Printing Office, Washington, D.C. 20402.
☒ Order From National Technical Information Service (NTIS), Springfield, VA. 22161

14. NO. OF PRINTED PAGES

225

15. Price

$22.95